REPORT DOCUMENTATION PAGE

Form Approved
OMB No. 0704-0188

Public reporting burden for this collection of information is estimated to average 1 hour per response, including the time for reviewing instructions, searching existing data sources, gathering and maintaining the data needed, and completing and reviewing the collection of information. Send comments regarding this burden estimate or any other aspect of this collection of information, including suggestions for reducing this burden, to Washington Headquarters Services, Directorate for Information Operations and Reports, 1215 Jefferson Davis Highway, Suite 1204, Arlington, VA 22202-4302, and to the Office of Management and Budget, Paperwork Reduction Project (0704-0188), Washington, DC 20503.

1. AGENCY USE ONLY (Leave blank)	2. REPORT DATE February 1996	3. REPORT TYPE AND DATES COVERED Final, June 92 – June 95

4. TITLE AND SUBTITLE
Fatigue Crack Growth Mechanisms in Titanium Metal Matrix Composites

5. FUNDING NUMBERS
AFOSR-92-F49620

6. AUTHOR(S)
Hamouda Ghonem

7. PERFORMING ORGANIZATION NAME(S) AND ADDRESS(ES)

Mechanics of Materials Laboratory
Department of Mechanical Engineering
University of Rhode Island
92 Upper College Rd., Kingston, RI 02881

AFOSR-TR-96

0241

9. SPONSORING / MONITORING AGENCY NAME(S) AND ADDRESS(ES)
USAF Office of Scientific Research
Bolling Air Force Base
Washington, DC 20332-6448

NA F4960C

10. SPONSORING / MONITORING AGENCY REPORT NUMBER
92-J-0291

11. SUPPLEMENTARY NOTES

Dr. W. Jones, Program Manager

12a. DISTRIBUTION / AVAILABILITY STATEMENT

Approved for public release
Distribution is unlimited

19960523 199

13. ABSTRACT (Maximum 200 words)

This report details studies carried out to identify the high temperature fatigue crack growth damage mechanisms in fiber-reinforced titanium metal matrix composites. The report consists of eight separate sections. In the first section, the fatigue and fatigue crack growth characteristics in neat laminates made of Timetal 21S were studied in relation to both temperature and loading frequency effects. The second section deals with the evolution of the thermal residual stresses in the composite when cooling from consolidation temperature or subjecting the composite to thermal cycles. A new mechanical simulation method capable of measuring the induced residual stress on real time basis has been developed in this study. The third section extends this issue to the time-dependent internal stress and strain states of MMCs under the thermomechanical loading conditions. Here, a new micromechanical model employing the four-phase concentric cylinder configuration has been proposed. Based on this model, the time-dependent behavior of continuous fiber reinforced metal matrix composites has been evaluated. These results are presented in the fourth section. The fifth, sixth and seventh sections of this report describe the influence of temperature and loading frequency on the crack growth process and suggest a fatigue-creep interactive mechanism acting at the crack tip during high temperature loadings. The last section of the report deals with the determination of the stress evolution in bridging fibers during the fatigue crack growth in SM1240/Timetal-21S composite using the finite element method. Several parameters affecting this evolution were considered; namely, the process-induced residual stress, the creep characteristics of the matrix layer surrounding the fiber, the test temperature and the loading frequency.

14. SUBJECT TERMS
crack growth, residual stress, crack bridging, fiber, viscoplasticity, composite, interface

**15. NUMBER OF PAGES**
217

16. PRICE CODE

17. SECURITY CLASSIFICATION OF REPORT unclassified	18. SECURITY CLASSIFICATION OF THIS PAGE unclassified	19. SECURITY CLASSIFICATION OF ABSTRACT unclassified	20. LIMITATION OF ABSTRACT UL

DISCLAIMER NOTICE

UNCLASSIFIED

Technical Report
distributed by

**DEFENSE
TECHNICAL
INFORMATION
CENTER**

DTIC/ Acquiring Information—
Imparting Knowledge

Cameron Station
Alexandria, Virginia 22304-6145

UNCLASSIFIED
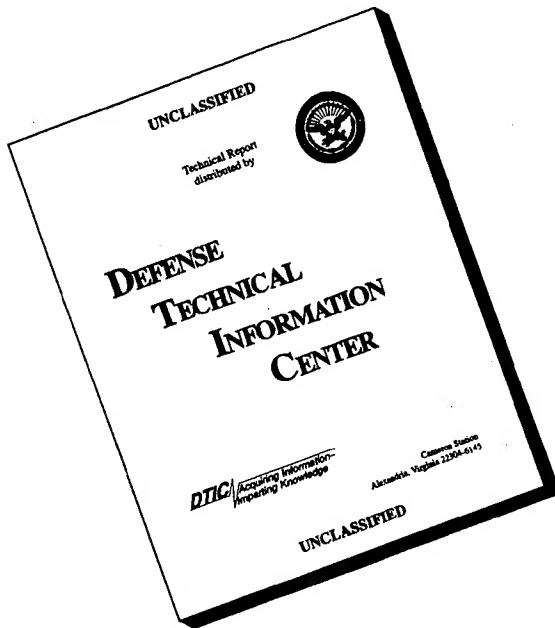
THIS DOCUMENT IS BEST
QUALITY AVAILABLE. THE
COPY FURNISHED TO DTIC
CONTAINED A SIGNIFICANT
NUMBER OF PAGES WHICH DO
NOT REPRODUCE LEGIBLY.

Fatigue Crack Growth Mechanisms in Titanium Metal Matrix Composites

Final Report
February 1996

By

Hamouda Ghonem

Department of Mechanical Engineering
University of Rhode Island
Kingston, Rhode Island

Prepared for

Department of Air Force
Air Force Office of Scientific Research
Bolling Air Force Base, DC

SUMMARY

In the period 1993-1995, a joint research program led by the University of Rhode Island and involving United Technologies Research Center, Pratt & Whitney and the Materials Laboratory of WPAFB, was carried out to identify the high temperature fatigue crack growth damage mechanisms in fiber-reinforced titanium metal matrix composites. To achieve this objective, 24 composite and fiberless plates each measuring 900 mm x 100 mm x 1 mm were consolidated using the fiber-foil-fiber vacuum hot-pressing technique. A total of 32 different crack growth tests were carried out at the Mechanics of Materials Laboratory, URI. These tests involved both high and low frequency loadings with and without hold time durations imposed at the maximum load level. Tests were performed in both air and vacuum at three different temperatures; room temperature, $500\,^{\circ}C$ and $650\,^{\circ}C$. Results of these tests provided basis for a series of experimental, numerical and analytical studies of the crack growth behavior in fiber reinforced Ti-MMC's. These studies are presented in this report in the form of eight separate sections. In the first section, the fatigue and fatigue crack growth characteristics in neat laminates made of Timetal 21S were studied in relation to both temperature and loading frequency effects. The second section deals with the evolution of the thermal residual stresses in the composite when cooling from consolidation temperature or subjecting the composite to thermal cycles. A new mechanical simulation method capable of measuring the induced residual stress on real; time basis has been developed in this study. The third section extends this issue to the time-dependent internal stress and strain states of MMCs under the thermomechanical loading conditions. Here, a new micromechanical model employing the four-phase concentric cylinder configuration has been proposed. Based on this model, the time-dependent behavior of continuous fiber reinforced metal matrix composites has been evaluated. These results are presented in the fourth section. The fifth, sixth and seventh sections of this report describe the influence of temperature and loading frequency on the crack growth process and suggest a fatigue-creep interactive mechanism acting at the crack tip during high temperature loadings. The last section of the report deals with the determination of the stress evolution in bridging fibers during the fatigue crack growth in SM1240/Timetal-21S composite using the finite element method. Several parameters affecting this evolution were considered; namely, the process-induced residual stress, the creep characteristics of the matrix layer surrounding the fiber, the test temperature and the loading frequency.

ACKNOWLEDGMENT

LIST OF CONTENTS

LIST OF TABLES

LIST OF FIGURES

SECTION 1

EFFECTS OF TEMPERATURE AND FREQUENCY ON FATIGUE CRACK GROWTH IN TIMETAL®21S MONOLITHIC LAMINATE

ABSTRACT

This section describes the high temperature fatigue crack growth behavior in the titanium β21S monolithic laminates. Effects of laminate consolidation procedure as well as the test specimen geometry on the reliability of the experimental crack growth data were first investigated. The influence of temperature and both high and low frequency loadings on the crack growth rate in this laminate material were then determined. In addition to room temperature three other temperature levels were used in this study: 482°C, 650°C and 760°C. The test frequencies encompassed the range 10 to 8×10^{-3} Hz. Results of this study demonstrate that temperature effects could be interpreted in terms of the yield strength and elastic modulus variations as function of the testing temperature. Furthermore, it was determined that crack growth rate in these laminates is influenced by viscoplastic related effects at frequencies as low as 1 Hz. This was supported by an analytical solution determining the transition time required for the crack tip to experience extensive creep behavior. Fractographic analysis carried out on fracture surfaces showed that the dominant fracture mechanism is transgranular cleavage with the appearance of intergranular facets in tests corresponding to 760°C at 10 Hz and 650°C at 5×10^{-2} Hz.

1.1 INTRODUCTION

With rapid advances in titanium alloys, extending their operating temperature to 593°C [1,2], fiber-reinforced titanium-based metal matrix composites have emerged as a class of composites with a potential for use in advanced high temperature applications. The target operation temperature range of 650-800°C in these applications would overlap that of superalloys.

Four basic titanium alloys are available for metal matrix composite applications [3,4]. These are: the α alloys, the α-β alloys, the metastable β alloys and the stable β alloys. In these types of alloys the α class is avoided as a matrix material due to its low alloy content and the inherent low strength. On the other hand, the stable β materials suffer generally from problems related to both processing [5] and the fabrication into the required thin-gage foils [6]. The $\alpha+\beta$ and metastable β alloys thus remain as the only candidates for use in matrix development; they can be fabricated with relative ease and can be aged to high strengths. One of the approaches that has been investigated in conditioning the metastable β alloys toward titanium-based MMC applications is through alloying with slower diffusing elements in order to reduce the reaction zone width at the consolidation temperature, thus limiting the complications ensuing from matrix-to-filament load transfer which takes place across the reaction zone. In this regard, it was proposed by Schmitz et al [7] that the optimum titanium

matrix, for a boron type filament, would be attained through the addition of enough diboride modifier, such as, vanadium or chromium, to reduce boron transport to a minimum as well as by the addition of aluminum or molybdenum to reduce the reactivity of the titanium. These two modifier requirements have been achieved with the development of a new metastable β alloy Timetal®21S. This alloy, when combined with a fiber with a boron-rich surface, should yield a composite that could prove to be thermally and mechanically stable at operating temperatures of up to the 700°C range.

Since applications of high temperature MMC involve in many cases cyclic loading due to thermal and or mechanical service conditions. The understanding of high temperature fatigue crack growth in the matrix material therefore becomes an important factor since it defines the limits of the composite response and identifies the nature and parameters governing the damage evolution in the intended composite structure. The purpose of this section is to evaluate the high temperature fatigue crack growth behavior in Timetal®21S laminate. The first part of the paper describes the material characteristics and basic properties and the experimental procedure used in this study. This will be followed by a discussion of experimental results, in particular temperature and frequency effects and their significance in relation to the use of the Timetal®21S as a matrix material for fiber-reinforced composites.

1.2 MATERIAL DESCRIPTION

The basic material used here is the metastable Timetal®21S alloy supplied in the form of foils with a thickness of 112 μm. The chemical composition of this alloy in wt% is 0.1 Fe, 16.0 Mo, 3.0 Al, 0.9 Nb, 0.2 Si, 0.22 C, 0.12 O, 0.005 N with the balance being Ti. The microstructure of the heat treated alloy consists of distinctive β grains containing widmanstätten acicular α phase and continuous grain boundary α layer with the thickness of about 0.8 μm, shown in Fig. 1-1. The average grain size is about 80 μm. The room temperature tensile properties of these foils are: ultimate tensile stress σ_{UTS} = 1089 MPa, elastic modulus E = 98 GPa and elongation δ = 5.6%. Laminates were fabricated by consolidating eight foils using vacuum hot pressing employing pre-established critical processing parameters. This process produced monolithic laminate plates with dimensions 25.4 mm x 0.8 mm x 150 mm. Prior to consolidation, the foils surface oxide was removed using a combined vapor hone and a mechanical oxide removal technique. Typical microstructure of the consolidated laminates is shown in Fig. 1-2. It is observed that while no changes have occurred in the basic microstructure of the foil, the microstructure of the interfaces displays a decrease in grain size. This was interpreted here as being related to strain bands formed along the foils interfaces during consolidation. These bands could result in heterogeneous nucleation of grains which are restricted by the foil interface resulting in smaller grain size than those in the foil interior.

As will be discussed later, no damage or partial separation was encountered along these interfaces during the early parts of the crack growth process. All laminates were heat treated (621°C/8 hrs) in a dynamic vacuum furnace prior to machining the required test specimens.

Preliminary tensile tests were performed on heat treated specimens made of the optimized laminates in order to determine their basic mechanical properties at five different temperatures: 24°C, 204°C, 316°C, 482°C and 649°C. Tensile stress-strain curves were recorded and ultimate tensile strength, 0.2% yield strength and elastic modulus were measured.

Quartz rod axial extensometry was utilized to measure strain. Results of these measurements in the form of stress-strain curves are shown in Fig. 1-3, while the different related properties are listed in Table 1.1.

Table 1.1   Mechanical Properties of Timetal®21S

Temperature (°C)	σ_{UTS} (MPa)	0.2% Yield Stress (MPa)	E (GPa)	Strain at Failure (%)
24	1089	1043	98.2	>3.9
204	877	779	90.3	8.7
316	843	696	84.8	6.8
482	684	589	76.0	>10.1
649	289	245	47.6	50-55

1.3 EXPERIMENTAL PROCEDURE

Three specimen configurations were investigated in order to identify the effect of geometry on crack growth behavior. These geometries include Compact Tension (width=25.4 mm, thickness = 0.87 mm), Single Edge Notch (SEN) and Middle Cracked Tension (MT) specimens. The latter two geometries had a gage section of 30 mm. All specimens were precracked at room temperature using a stress intensity factor shedding technique. In the case of the MT configuration, a small cut was introduced on both sides of the center hole in order to direct the initial precracks. These cuts were made using a silicon-carbide coated chromel wire with a diameter of 76 μm.

All tests were carried out on an automated servo-hydraulic test frame. Test specimens were gripped using a hydraulic flat grip with self aligning capabilities and heated with an open furnace utilizing infrared radiation lamps. The testing temperatures employed here were 23°C, 482°C, 650°C and 760°C. The variation of the temperature along the gage length during all tests was ± 5°C. Crack length increments were measured continuously using a direct current potential drop method based on optically derived calibration curves. All fatigue crack growth tests, summarized in Table 1.2, were carried out under load range control with loading frequencies of 1, 10, 5×10^{-2} and 8×10^{-3} Hz applied at a stress ratio of 0.1.

It was not possible to obtain crack opening displacement during either room or elevated temperature testings and therefore crack closure data are lacking here. Fracture specimens were examined using optical and scanning electron microscopy in order to identify fracture features and determine related cracking mechanisms as functions of both temperature and loading frequency.

1.4 RESULTS AND DISCUSSION

This section will focus on analyses of test results pertaining to effects of temperature

and loading frequency on crack growth behavior in the laminate understudy. This will be preceded by a description of efforts to determine the reliability of data obtained from specimens made of the laminates under study.

Since monolithic laminate material is a product of a consolidation process which involves the optimization of parameters such as temperature, pressure and environment, variations in any of these parameters could produce changes in the microstructure uniformity of the test specimens which in turn could influence the crack growth behavior in these specimens. Therefore, prior to carrying out any major crack growth characterization, two aspects of the laminate material reliability have been investigated: the degree of data scatter and the influence of specimen geometry. Results relating to each of these aspects and their significance in relation to the laminate performance will be discussed here.

Table 1.2 Test Matrix*

Test Case	Specimen Configuration	Temperature (°C)	Frequency (Hz)
1	MT	760	10
2	SEN	650	8×10^{-3}
3	SEN	650	5×10^{-2}
4	SEN	650	1
5	SEN	650	10
6	MT	482	10
7	SEN	23	1
8	CT	23	1
9	MT	23	1
10	SEN	23	1
11	SEN	23	10
12	SEN	23	10
13	SEN	23	10

* *All tests were carried out in laboratory air environment.*

The degree of crack growth data scatter has been investigated by carrying out several identical crack growth tests using different SEN specimens at room temperature under the same loading frequency of 10 Hz. This high level of frequency was selected in order not to introduce time-dependent related effects in the experimental outcome. Results in the form of da/dN versus ΔK are compared in Fig. 1-4. While the size of this data set is small and does not permit performing a quantitative statistical analysis, qualitative estimate of the scatter in these data in relation to that observed in other high temperature titanium alloys [8,9], indicates

that the crack growth response of a single experiment could be taken as representative of the laminate response under the particular test conditions.

The second reliability test carried out here was related to the effect of the specimen geometry and its inherent bending characteristics on the crack growth process of the laminate. Three geometries have been utilized: CT, SEN and MT configurations. Crack growth increments in these specimens were measured at room temperature under, again, a high loading frequency of 10 Hz. By utilizing the applicable ΔK expression for each of these specimen configurations, the da/dN versus ΔK results for test cases 7, 8 and 9 in Table 1.2 are plotted in Fig. 1-5. They show that the crack growth response is identical in all of the specimen geometries in the range of ΔK up to 30 MPa$\sqrt{m}$, which is the crack growth region of concern in this study. On the basis of these results, the SEN and MT configuration, due to the simplicity of their preparations and precracking procedures, have been adopted in the rest of this study.

The influence of temperature on crack growth was explored by carrying out tests labeled as cases 1, 5, 6 and 10 in Table 1.2, which were performed at temperatures of 760°C, 650°C, 482°C and 23°C, respectively, under a loading frequency of 10 Hz. Results of these tests which are plotted in Fig. 1-6(a), show that the increase in the test temperature from 23°C to 482°C has not produced any noticeable variations in the crack growth rate. The increase of the test temperature to 650°C and 760°C have however produced an increase in the crack growth rate along the entire range of ΔK and in particular in the low ΔK region. This difference could be interpreted in terms of time-dependent oxidation and or creep related effects. It could also result from variations in mechanical properties of the laminate due to temperature changes. In order to isolate these effects, the values of the stress intensity factor range, ΔK, were modified by accounting for the temperature induced changes in both the yield strength, σ_y, and elastic modulus, E. The normalized values of ΔK calculated as $(\Delta K^2/\sigma_y E)$ is plotted versus da/dN in Fig. 1-6(b). It shows that the crack growth curves corresponding to the three temperature levels: 23°C, 482°C and 650°C are almost identical. Since the loading frequency in these three cases was confined to the high frequency level of 10 Hz, thus ruling out the existence of creep effects, one would assume that crack tip oxidation is a major damage mechanism at these temperature levels. The absence of crack growth enhancement as function of temperature, however, could therefore be viewed as a measure of the material high resistance to oxidation effects over this temperature range. This conclusion, in fact, is supported by results obtained by Khobaib [10] who analyzed the weight gain during the thermal exposure of Timetal®21S laminates at different temperature levels in a 10 torr atmosphere. His work showed that little environment effects occurred in these laminates up to 650°C.

The exclusion of the 760°C test data from comparisons in Fig. 1-6(b) is due to the fact that the validity of this test was limited to the ΔK range 4-7 MPa$\sqrt{m}$. Beyond this ΔK level the corresponding test specimen experienced extensive delamination. This phenomenon of delamination was apparent in all the elevated temperature test specimens at ΔK above 25 MP$\sqrt{m}$. This ΔK value was found to increase with decreasing testing temperature and increasing loading frequency. The existence of delamination is speculated here to be a result of extensive viscoplastic flow taking place at high ΔK, which causes the material ligament ahead of the crack tip to experience bending effects during the rising part of the loading cycle.

5

This bending, which is exaggerated in the case of the SEN geometry, will consequently result in compressive stresses acting in the normal-to-loading direction. These stresses could cause delamination along the foils interfaces since they are expected to be weak boundaries of the laminate structure. This speculative view relies on the fact that the laminate material undergoes a transition to large scale yielding at high ΔK values in less than 10 seconds of thermal exposure at 650°C; this will be discussed later in this section. It should be mentioned here that delamination was not observed in tests carried out at room temperature.

While the results shown in Fig. 1-6(b) demonstrates the absence of extrinsic temperature effects on crack growth behavior, life to failure of this laminate material was found to be temperature dependent. This was evident from load versus life curves obtained at different temperature levels. These curves are plotted in Fig. 1-7 in the form of maximum stress normalized by ultimate tensile stress ($\sigma_{max}/\sigma_{UST}$) versus number of cycles to failure. They show that a decrease of life occurs as temperature increases from 482°C to 650°C. This was interpreted as due to the effect of the decrease in yield strength on the crack initiation life and increasing environmental effects [11,12]. Numerous surface crack initiation sites were found in the 650°C test specimen while no surface cracks were observed in the 482°C test.

Fractographic analysis of the high frequency fractured specimens showed that the cracking mechanisms in those specimens tested in the range of 23 °C to 650 °C are transgranular with cleavage-like fracture covering the fracture surfaces in regions extending from $\Delta K = 4$ to 20 MPa√m. Unlike other titanium alloys [7], no transition in fracture mode was found in this β21S monolithic laminate and the commonly observed striations were absent even at high ΔK values. Sheared facets were found to be more defined in the 650°C case than those observed in the room temperature tests, compare Figs. 8(a) and 8(b). At 760°C, however, the fracture mode becomes intergranular with distinct ledges on grain boundary facets, see Fig. 1-8(c).

The second aspect studied here was the influence of loading frequency on crack growth behavior. Generally, the change in the crack growth rate due to variations in time durations of the applied loading cycle is used as a measure of the crack tip material response to time dependent parameters which consist of creep and /or oxidation related effects [13-15]. This is particularly important in the low ΔK region where stress-controlled crack growth rate is generally small thus permitting the time dependent effects to be observed and evaluated. Two different frequencies were employed at the temperature of 650°C, 5×10^{-2} and 8×10^{-3} Hz. Crack growth rates due to these frequencies, in addition to those corresponding to 1 and 10 Hz used as references, are plotted in Fig. 1-9. Similar to most high temperature alloys, these results show that a decrease in the loading frequency leads to crack growth rate acceleration. In order to identify the nature of this acceleration, the following form of the Paris-type equation has been utilized in an analysis similar to that developed by Foerch et al [8] in their work on the Ti-1100 alloy:

$$\frac{da}{dN} = C(650°, freq, envir) \Delta K^{m(650°, freq, envir)} \tag{1}$$

In the case of cycle dependent crack growth processes which involve damage criteria related to crack opening displacement or strain accumulation, the exponent m could vary between 2 and 4, respectively. The steady state regions of the crack growth curves

6

corresponding to 650°C have been fitted into the form of the above equation. The exponents of the resulting equations were then plotted versus the loading frequency as shown in Fig. 1-10. They indicate that at loading frequencies above 0.1 Hz the cracking mechanism is a cyclic dependent, while below this frequency the damage is a mixed cycle- and time-dependent process. This results in an exponent m which varies inversely as a function of frequency. At the frequency level of 10^{-3} Hz the crack tip damage process becomes fully time dependent. This contention is further supported by results obtained in Fig. 1-11, where the crack growth rate at 650°C is plotted versus cycle duration for ΔK values of 5, 7, 9, 15 and 20 MPa$\sqrt{m}$. Here, on the basis of similar analyses made by other workers in their studies of crack growth in high temperature alloys [13-16], the slopes of these ΔK versus time lines are considered a measure of the time dependent contributions to the crack tip damage process. If the dotted curve in Fig. 1-11 is taken as a boundary at which transition to time-dependent behavior occurs (the slopes of curves approach to the unity), it could be seen that as ΔK increases the transition frequency increases; for ΔK of 20 MPa$\sqrt{m}$, the transition frequency is about 1 Hz. An attempt was then made to probe the nature of the time dependent effects by estimating the time required for the crack tip to experience extensive creep. This was achieved by employing an approach based on Riedel-Rice analysis for creeping materials [17]. In this approach, the time necessary for transition from small scale yielding to large scale secondary creep is estimated as function of the applied load and ΔK. Details of this calculation is given in an appendix at the end of this section. The results in the form of time required for extensive creep versus ΔK for the applied load level used in this study is shown in Fig. 1-12. It clearly shows that the crack tip undergoes large scale yielding in less than 10 seconds of thermal exposure at 650°C and ΔK of 17 MPa$\sqrt{m}$.

The influence of creep is in fact evident when viewing the fracture surface of specimens corresponding to test case 3, 650°C at 5×10^{-2} Hz, which shows distinctive intergranular failure with multiple grain boundary triple-point cracks (see Fig. 1-13). However, the intergranular fracture associated with the specimen tested at 760°C and 10 Hz is assumed here to be due to environmental degradation since the testing temperature is high enough to cause severe oxidation [10], while cycle duration is not long enough to produce creep flow effects. This conclusion is supported by comparing Figs. 8(c) and 11. They show that intergranular features associated with the 760°C, 10 Hz test condition are more brittle in appearance than those associated with the 650°C, 5×10^{-2} Hz test condition.

1.5 SUMMARY AND CONCLUSIONS

In this study, an experimental program has been carried out to characterize the high temperature fatigue crack growth behavior of the Timetal®21S monolithic laminate. In this, the influence of consolidation and specimen geometry on the reliability of crack growth data in this laminate material have been examined. It was concluded that the crack growth rate versus ΔK relationship at room temperature in laboratory air environment is repeatable and to a great extent insensitive to specimen geometry.

Effects of increase in testing temperature on the acceleration of crack growth rate was studied for temperatures 23°C, 482°C, 650°C and 760°C at the high frequency loadings of 1

7

and 10 Hz. The observed increase in the crack growth rate in this temperature range was interpreted in terms of variations in basic material properties, particularly yield strength and elastic modulus as function of testing temperature. Laminate delamination was shown to exist when exceeding certain ΔK levels that decrease as the temperature level increases and loading frequency decreases. It is speculated that the delamination in these laminates is a product of high viscoplastic flow acting in the specimen ligament in front of the crack tip. The bending of this ligament, particularly in the case of the edge notch specimen configuration, leads to normal-to-load direction compressive stresses which would result in the delamination of the test specimens.

Furthermore, the role of low loading frequency was investigated at the temperature level of 650°C. The increase in growth rate as frequency decreases was interpreted in terms of increasing viscoplastic effects as cycle duration increases. This was supported by an analytical analysis involving the determination of the time required for the crack tip to experience large scale yielding. It was concluded that the time-dependency of fatigue crack growth could be due to the extensive creep deformation. The fact that the oxidation effects may be limited and creep processes can be dominant in Timetal®21S laminate may make this material attractive for the use as a matrix in high temperature composites in selected applications.

1.6 APPENDIX

The transition time from small scale yielding to large scale creep can be estimated following Riedel-Rice approach [17]. In this approach, an elastic-secondary creeping material in which the strain rate tensor, $\dot{\varepsilon}_{ij}$, in the crack tip region is assumed to be expressed as

$$\dot{\varepsilon}_{ij} = \frac{1+\nu}{E} S_{ij} + \frac{1-2\nu}{3E} \sigma_{ij}\delta_{ij} + \frac{3}{2}B\bar{\sigma}^{n-1}S_{ij} \tag{2}$$

where the S_{ij} is the deviatoric stress tensor, $\bar{\sigma}$ is the effective stress, δ_{ij} is the Kronecker delta, E is the elastic modulus, ν is the Poisson's ratio, B is temperature-dependent coefficient and n is the Norton's exponent. The asymptotic stress fields in this case can be written as

$$\sigma_{ij} = \left(\frac{C(t)}{B I_n r}\right)^{\frac{1}{n+1}} \tilde{\sigma}_{ij}(\theta) \tag{3}$$

where $\sigma_{ij}(\theta)$ is the angular function, I_n is a dimensionless factor which is related to n and stress states, r is the distance measured from the crack tip, and the time-dependent loading parameter $C(t)$ is defined as

$$C(t) = \lim_{\Gamma_\epsilon \to 0} \int_{\Gamma_\epsilon} \frac{n}{n+1}\sigma_{ij}\dot{\varepsilon}_{ij}dy - \sigma_{ij}n_j\frac{\partial\dot{u}_i}{\partial x}ds \tag{4}$$

where u_i is a component of the displacement vector. The contour Γ_ϵ is a vanishingly small loop enclosing the crack tip and is traversed in a counter-clockwise direction.

For short times after application of the load, the near-tip stress field is a function of the

8

independent variables r, θ and t and the parameters K, E, B, ν and n. The Mode I stress intensity factor K is used for the load parameter in small-scale yielding. In this condition, the relationship between C(t) and K can be established as

$$C(t) = \frac{(1-v^2)K^2}{(n+1)Et}$$ (5)

thus, eq.(3) becomes

$$\sigma_{ij} = \left(\frac{(1-v^2)K^2}{(n+1)EBI_n rt}\right)^{\frac{1}{n+1}} \tilde{\sigma}_{ij}(\theta)$$ (6)

As $t \to \infty$, the secondary creep extends throughout the body, and $C(t) \to C^*$ as $t \to \infty$, where C^* is the path-independent integral defined as

$$C^* = \int_\Gamma W\,dy - \sigma_{ij}n_j\frac{\partial \dot{u}_i}{\partial x}ds$$ (7)

in which

$$W = \int_0^{\dot{\varepsilon}_{ij}} \sigma_{kp}d\dot{\varepsilon}_{kp}$$

is the strain energy rate density and the contour Γ is an arbitrary loop enclosing the crack tip and no other defect. Under this condition, the near-tip stress fields become

$$\sigma_{ij} = \left(\frac{C^*}{BI_n r}\right)^{\frac{1}{n+1}} \tilde{\sigma}_{ij}(\theta)$$ (8)

The characteristic time for transition from small-scale yielding to extensive creep can be estimated by equating the near-tip fields for short times (eq.(3)) and long times (eq.(8)), and is given as

$$t_T = \frac{(1-v^2)K^2}{(n+1)EC^*}$$ (9)

where the values of n and B at 650°C are estimated as 5.72 and 2.75 x 10^{-18}, respectively, see Ref.[10]. C^* can now be calculated using the following expression [18]:

$$C^* = h_1(W-a)B\left(\frac{a}{W}\right)\left(\frac{\sigma_{net}}{1.072\eta}\right)^{n+1}$$ (10)

where σ_{net} is the net section stress, and function $h_1(W-a)$ can be determined numerically from the table made by Kumar et al [19], while $\eta = (1 + \alpha^2)^{\frac{1}{2}} - \alpha$ and $\alpha = a/(W-a)$.

The transition time t_T versus ΔK for the applied load level is illustrated in Fig. 1-12. It clearly shows that the transition from small scale yielding which is controlled by K to large scale creep which is determined by C^* would occur as short as about 10 seconds when ΔK level exceeds 15 MPa√m. This transition time is smaller than low frequency cyclic durations

9

in most cases, which implies that severe creep deformation will be expected to occur when this monolithic laminate is subjected to the low frequency and high ΔK loadings.

1.7 REFERENCES

1   E. W. Collings, the Physical Metallurgy of Titanium Alloys, American Society for Metals, Metals Park, OH, 1984

2   W. Brentnall and I. Toth, High Temperature Titanium Composites, TWR, Inc., Cleveland, 1974

3   P. R. Smith and F. H. Froes, Developments in Titanium Metal Matrix Composites, Journal of Metals, March, Vol. 36, (1984) pp.19-26

4   Titanium: A Technical Guide, ed. by M. J. Donachie, Jr., ASM International, Metals Park, OH 44073, 1989

5   I. Weiss and F. H. Froes, "Grain Size Control in the Metastable Beta Titanium Alloy Ti-10V-2Fe-3Al", in Proceedings on Fifth International Titanium Conference, Munich, Germany, September, 1984

6   P. R. Smith and F. H. Froes and T. Cammet, "Correlation of Fracture Characteristics and Mechanical Properties for Titanium Composites", in Failure Modes in Composites VI, J. A. Cornie and F. W. Crossmann (eds.), the Metallurgical Society of AIME, Warrendale, PA, 1977

7   G. K. Schmitz, M. J. Klein, M. L. Reid and A. G. Metcalfe, "Compatibility Studies for Variable Titanium Matrix Composites", AFML-TR-70-237, September, 1970

8   H. Ghonem and R. Foerch, "Environmental Effects on Elevated Temperature Fatigue Crack Growth in A Near-α Ti-1100 Alloy", Materials Science and Engineering, Vol. 138A, (1991) pp.69-81

9   R. Foerch, A. Madsen and H. Ghonem, "Environmental Influence on the Fatigue Crack Growth Performance of Ti-1100", in 7th World Conference on Titanium, San Diego, CA, June, 1992

10   M. Khobaib and N. Ashbaugh, "Mechanical Behavior of β21S", Technique Report, University of Dayton Research Institute, Dayton, Ohio, 1991

11   W. S. Johnson, "Fatigue Testing and Damage Development in Continuous Fiber Reinforced Metal Matrix Composites", in Metal Matrix Composites: Testing Analysis and Failure Modes, ASTM STP 1032, W. S. Johnson (ed.), American Society of

Testing and Materials, PA, (1989) pp.194-221

12   T. P. Gabb, J. Gayda and R. A. MacKay, "Isothermal and Nonisothermal Fatigue Behavior of A Metal Matrix Composite", Journal of Composite Materials, Vol. 24, (1990) pp.667-686

13   T. Weerasooriya and S. Venkataraman, "Frequency and Environment Effect on Crack Growth in Inconel 718," in Effects of Load and Thermal Histories, P. K. Liaw and T. Nicholas (eds.), the Metallurgical Society of AIME, Warrendale, PA, (1987) pp.101-108

14   T. Weerasooriya, "Effect of Frequency on Fatigue Crack Growth Rate of Inconel 718 at High Temperature", in Fracture Mechanics: Nineteenth Symposium, ASTM STP 969, T. A. Cruse (ed.), American Society for Testing and Materials, Philadelphia, PA, (1988) pp.907-923

15   H. Ghonem and D. Zheng, "Depth of Intergranular Oxygen Diffusion during Environment-Dependent Fatigue Crack Growth in Alloy 718", Materials Science and Engineering, Vol.150, (1992) pp.151-160

16   A. Pineau, "Intergranular Creep-Fatigue Crack Growth in Ni-Base Alloys", in Flow and Fracture at Elevated Temperature, R. Raj (ed.), American Society for Metals, (1985) pp.317-348

17   H. Riedel and J. R. Rice, "Tensile Cracks in Creeping Solids", in Fracture Mechanics: Twelfth Conference, ASTM STP 700, American Society for Testing and Materials, Philadelphia, PA, (1980) pp.112-130

18   C. F. Shih and J. W. Hutchinson, "Fully Plastic and Large Scale Yielding Estimates for Plane Stress Crack Problems", Journal of Engineering Materials and Technology, Vol. 98, (1976) pp.289-295

19   V. Kumar, M. D. german and C. F Shih, "An Engineering Approach for Elastic-Plastic Fracture Analysis", EPRI NP-1931, Project 1287-1, Topical report, July, 1981

Fig. 1-1   Microstructure of Timetal®21S monolithic laminate.
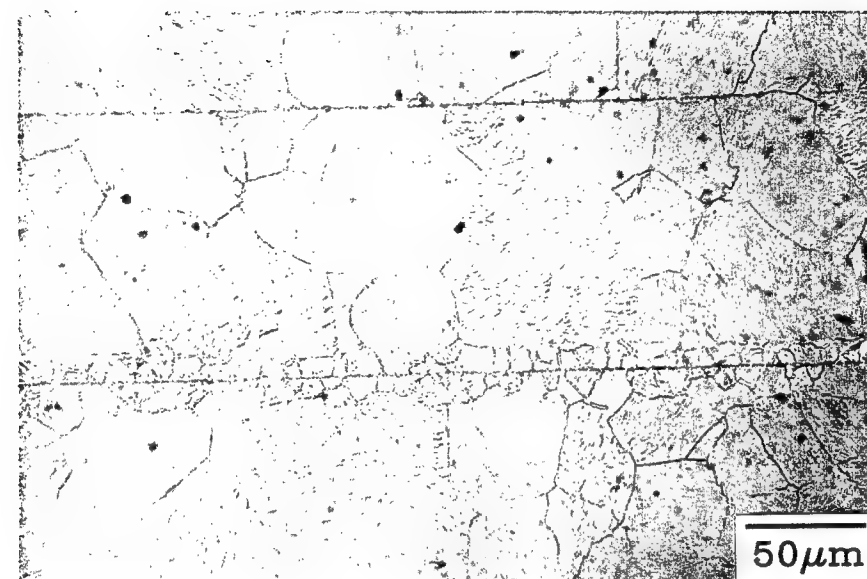
Fig. 1-2   Optical micrograph showing interface region in Timetal®21S monolithic laminate.
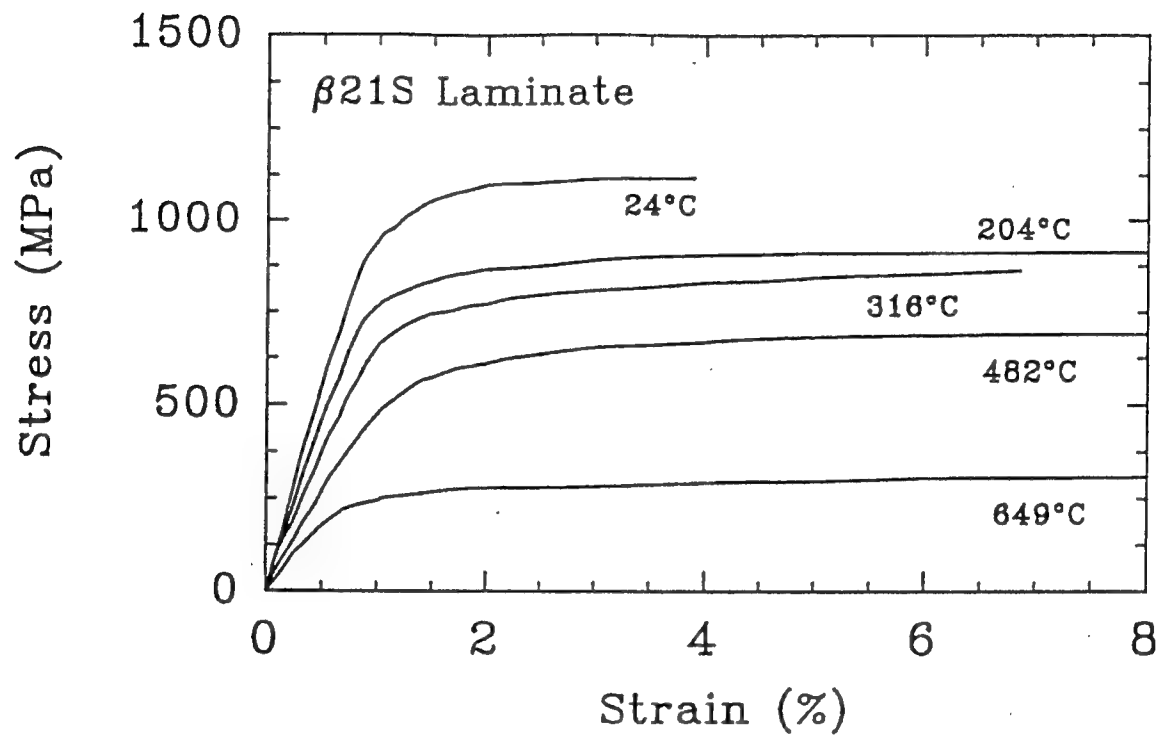
Fig. 1-3   Tensile stress-strain curve of Timetal®21S monolithic laminate at different temperatures.

14
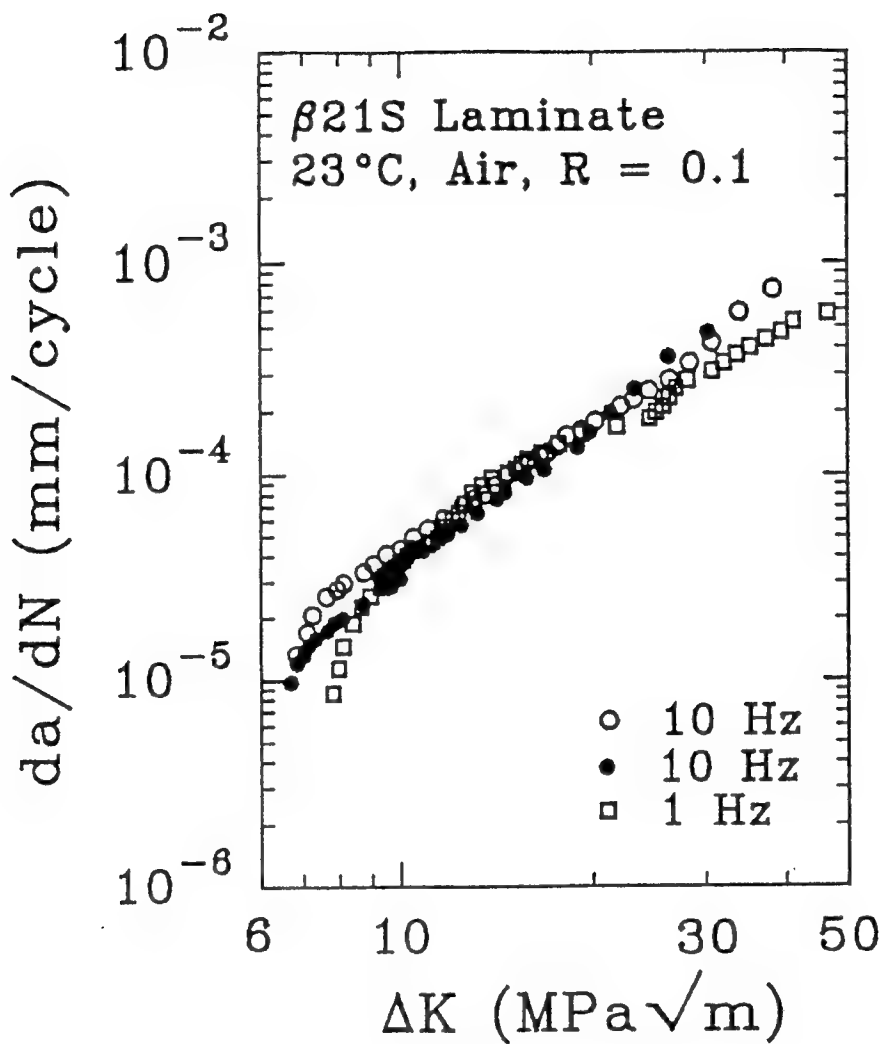
Fig. 1-4   Degree of data scatter of several identical fatigue crack growth tests.
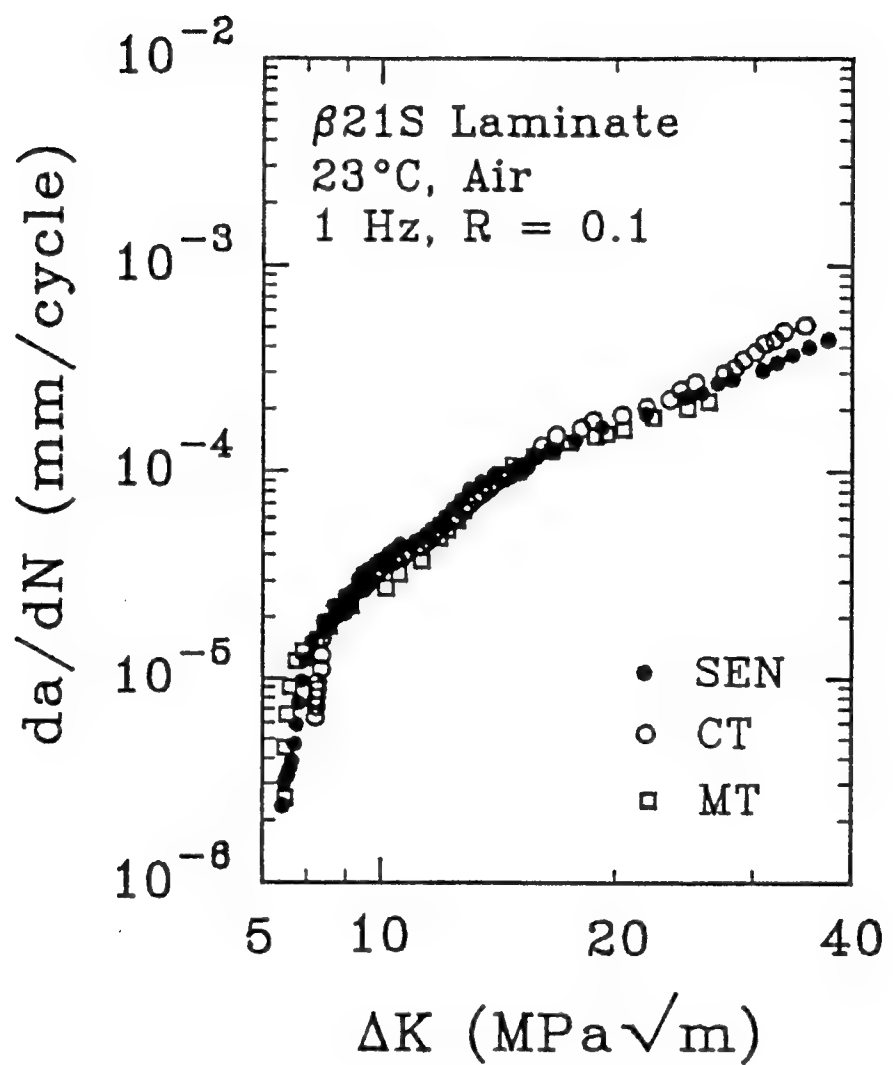
Fig. 1-5   Effects of specimen geometry on fatigue crack growth rates.
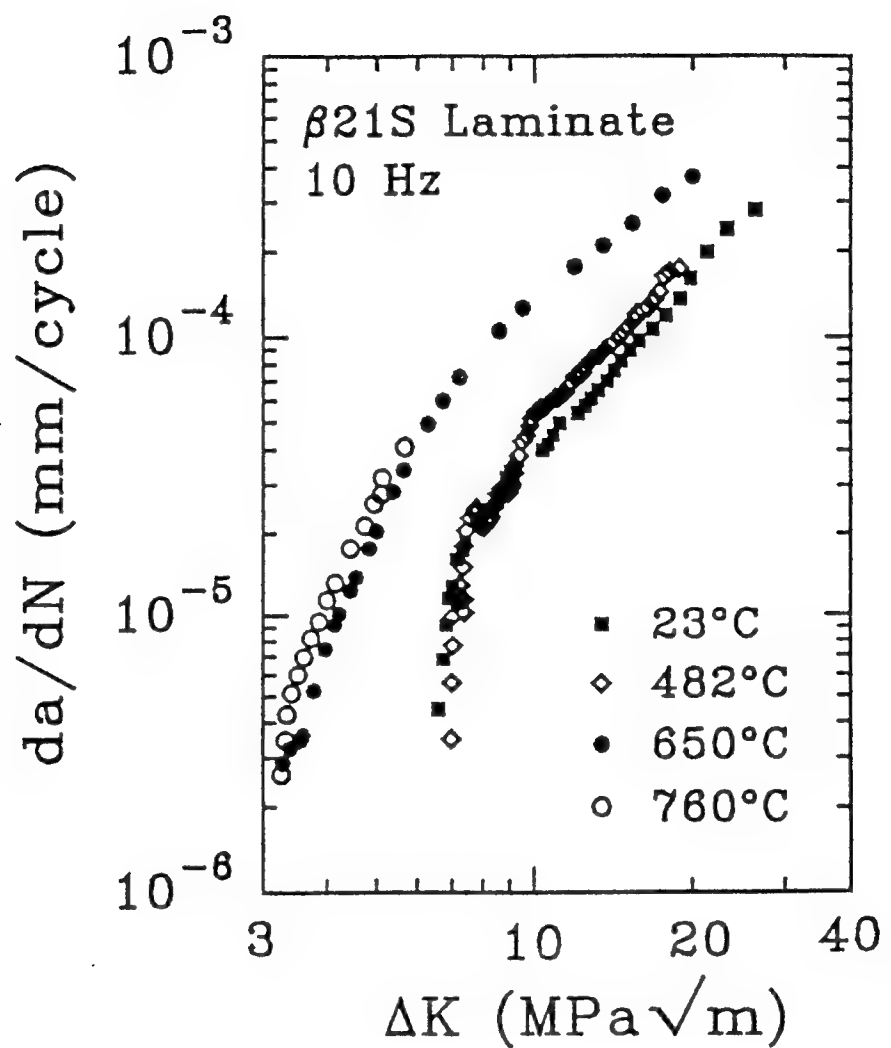
Fig. 1-6(a)   Temperature effects on fatigue crack growth rates.
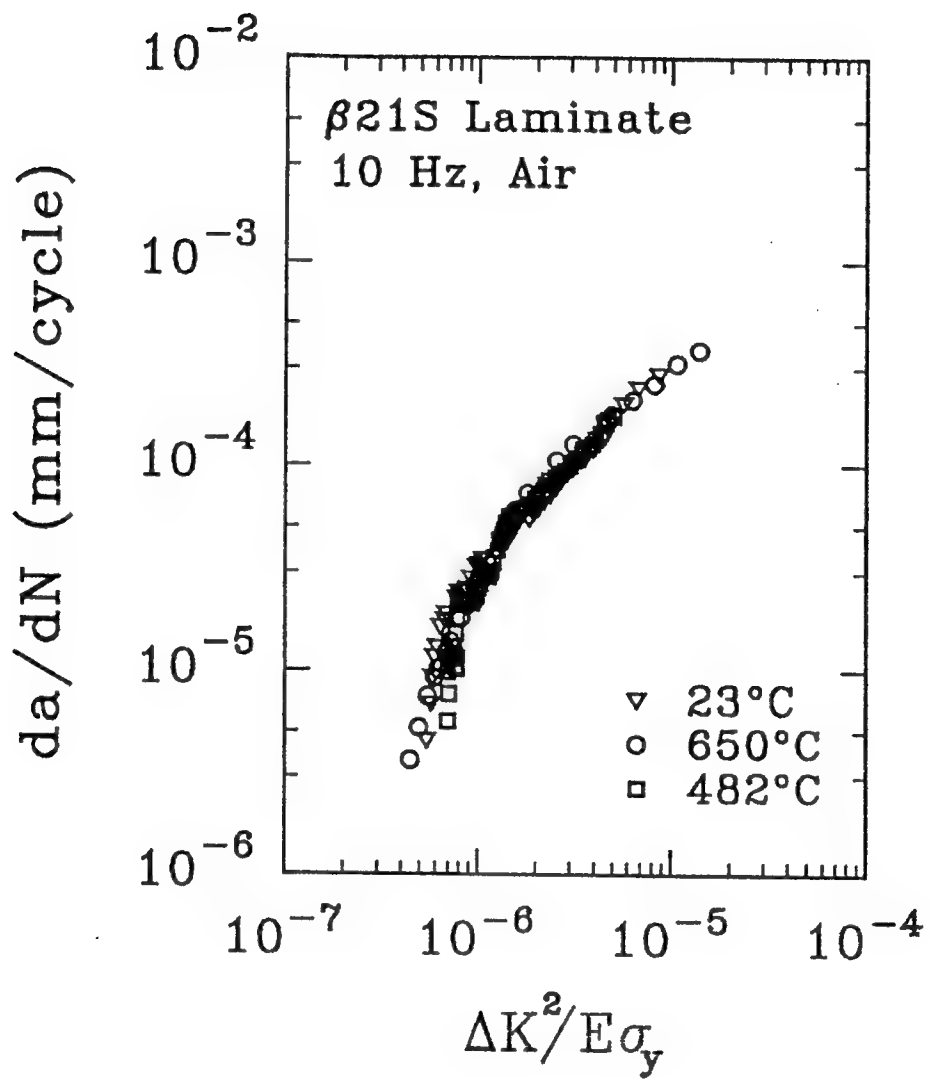
Fig. 1-6(b)   Effects of variations in yield strength and elastic modulus due to test temperature
               on fatigue crack growth rate data.
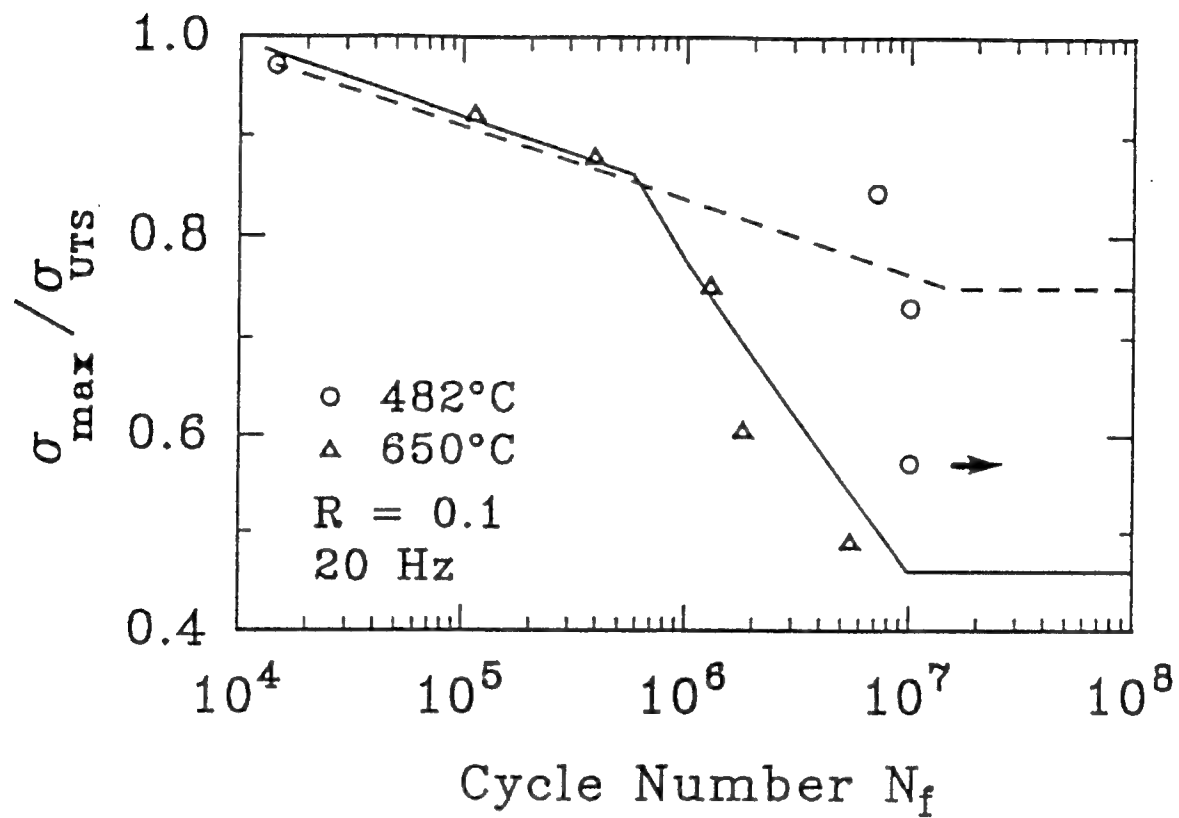
Fig. 1-7   Isothermal fatigue life of Timetal®21S monolithic laminate at 482°C and 650°C.
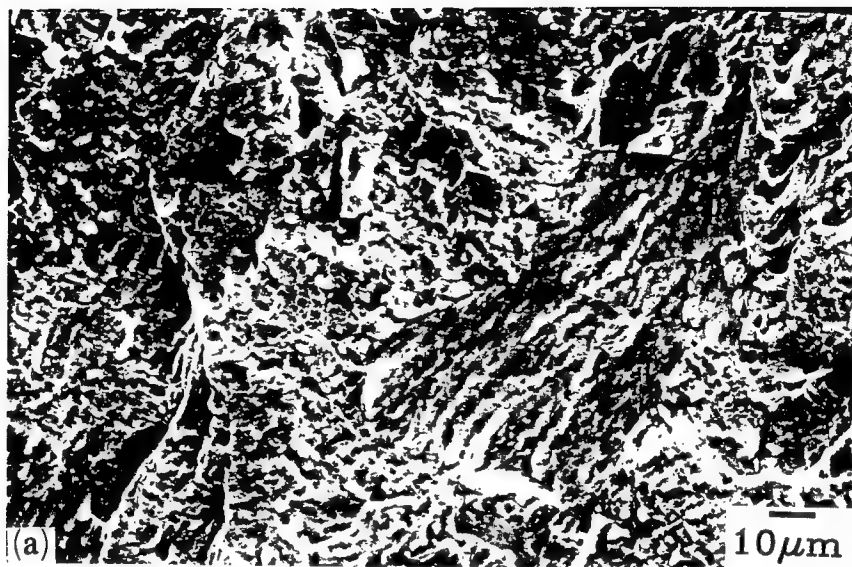
Fig. 1-8(a)   Typical fracture surface features of Timetal®21S monolithic laminate at
                     23°C, 10 Hz.

20
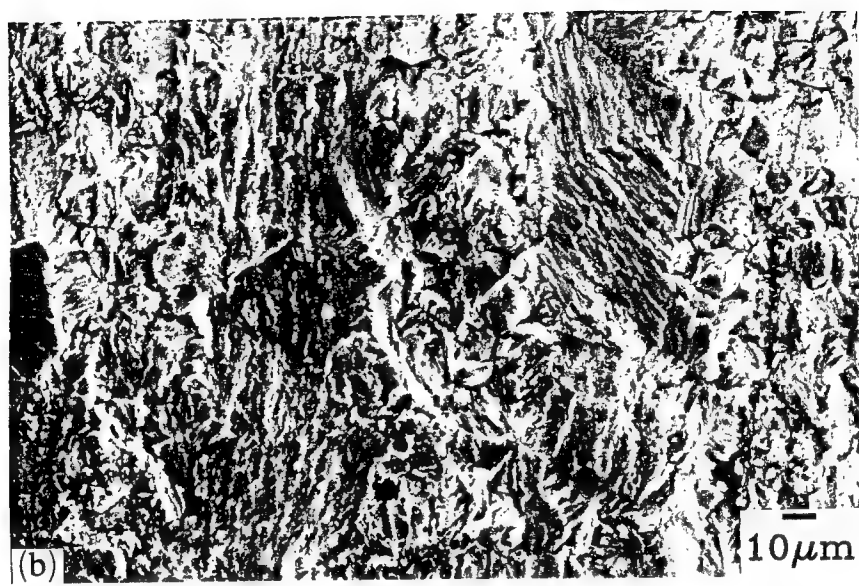
Fig. 1-8(b)   Typical fracture surface features of Timetal®21S monolithic laminate at 650°C, 10 Hz.
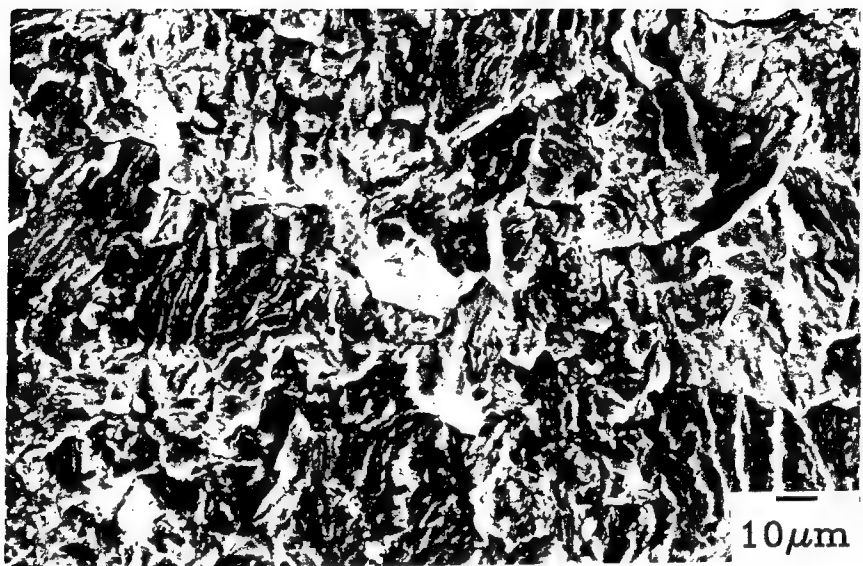
Fig. 1-8(c)   Typical fracture surface features of Timetal®21S monolithic laminate at
                      760°C, 10 Hz.
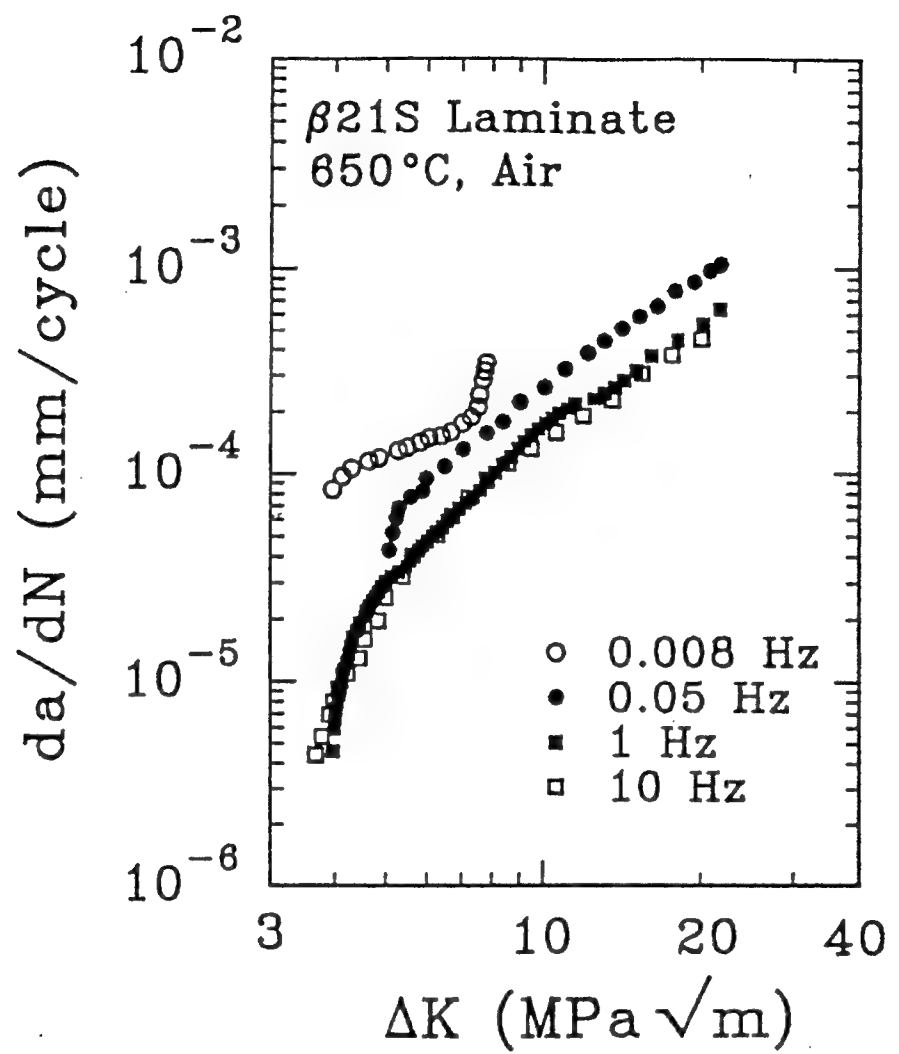
Fig. 1-9   Effects of loading frequency on fatigue crack growth rates in Timetal®21S monolithic laminate at 650°C.
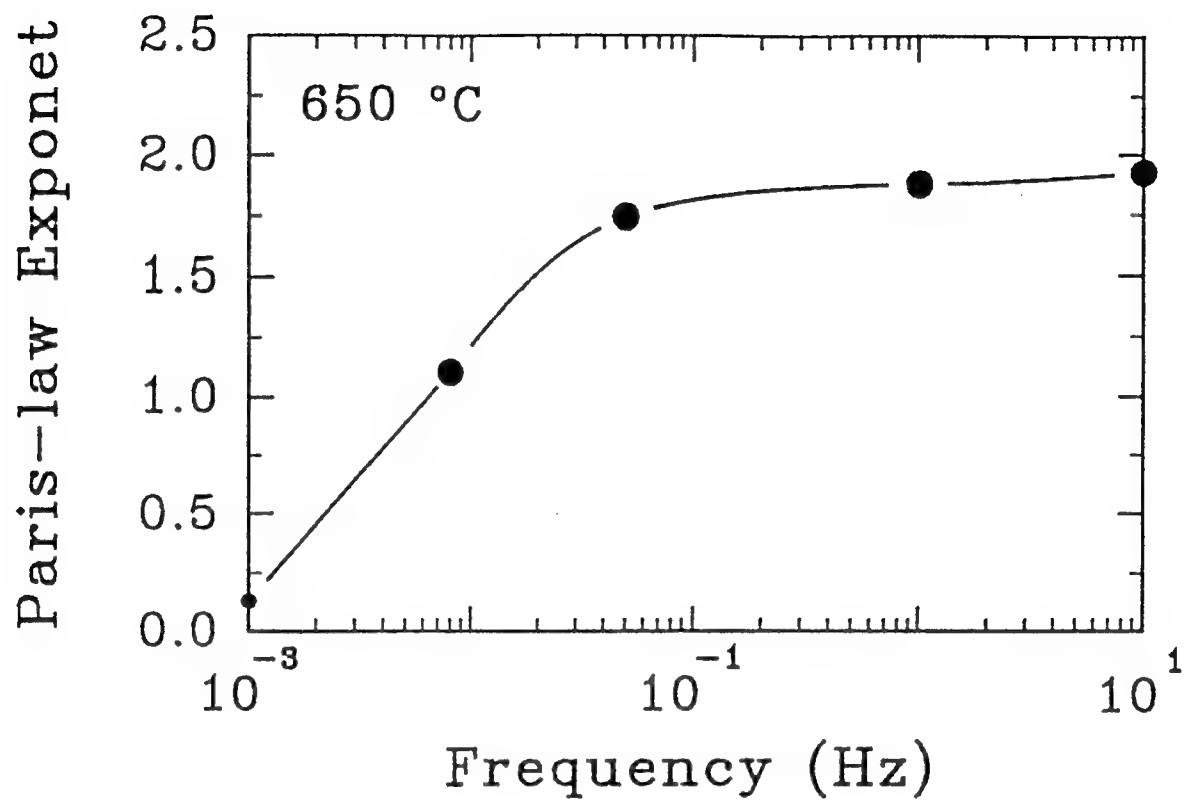
Fig. 1-10   Relationship between Paris law exponent and loading frequency.
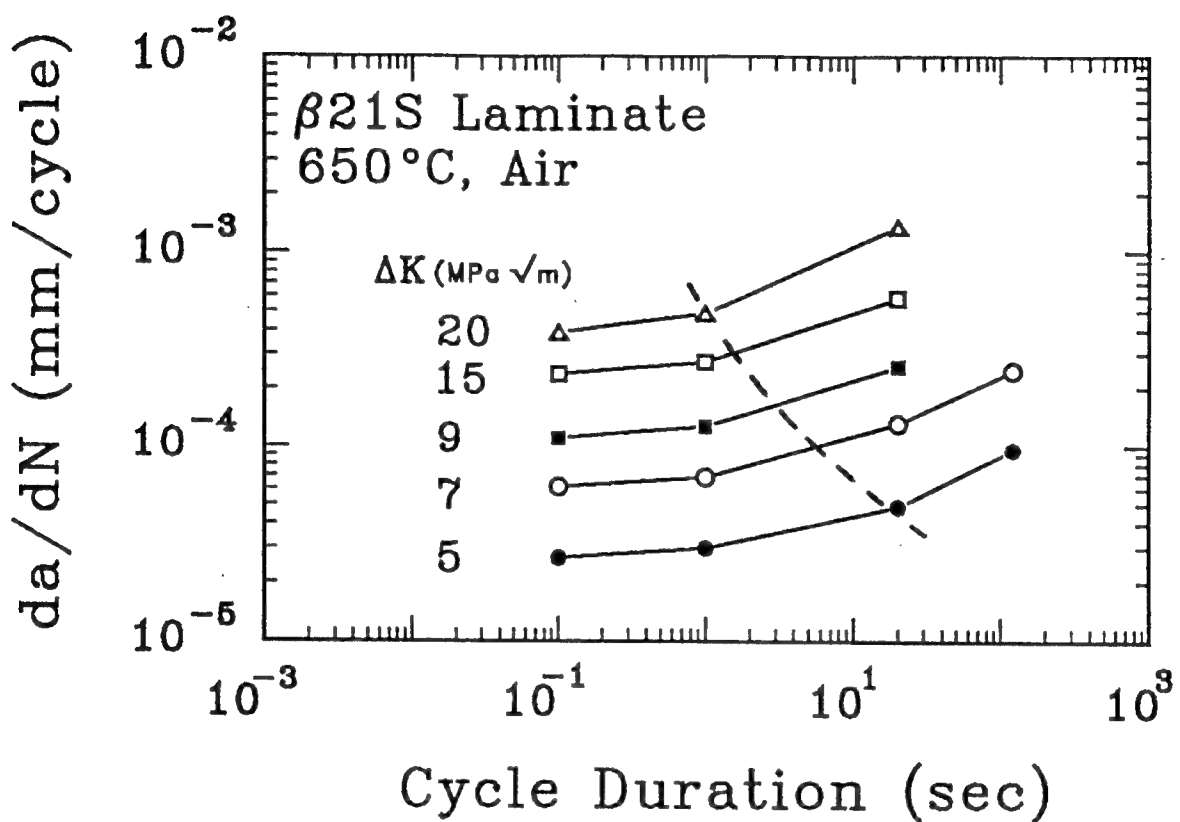
Fig. 1-11   Relationship between crack growth rate and loading cycle duration as function of ΔK.
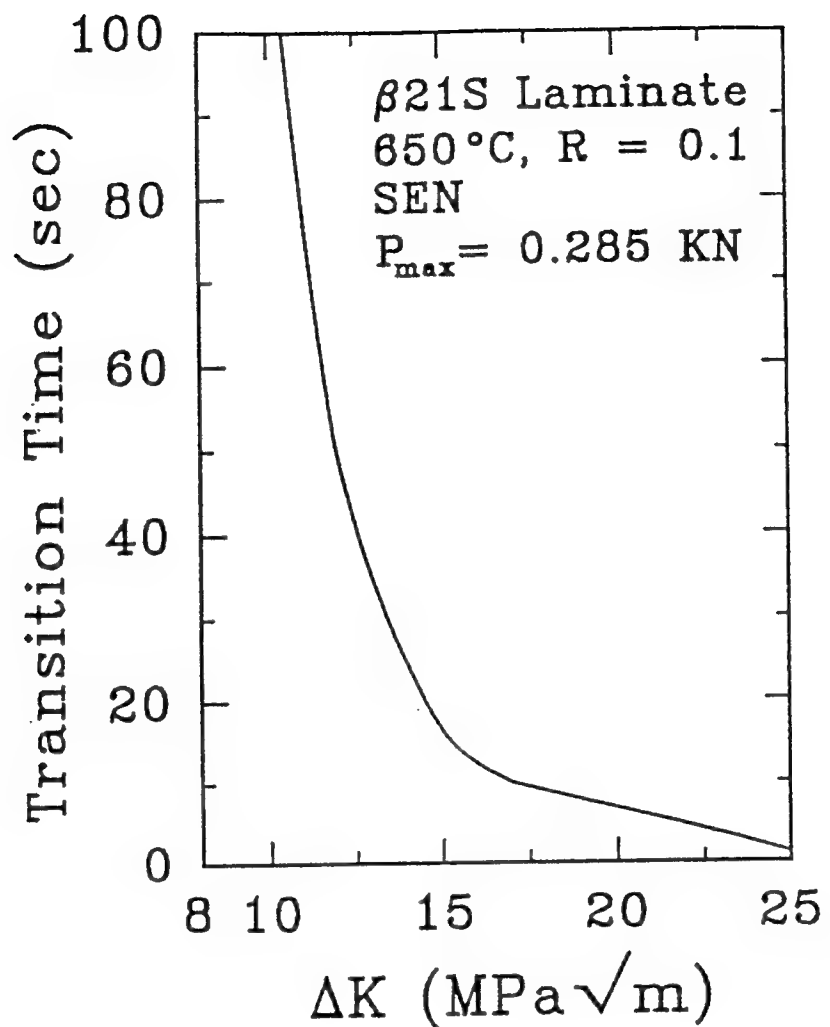
Fig. 1-12   Transition time from small scale yielding to secondary creep as a function of ΔK level at 650°C.

Fig. 1-13   Typical fracture surface features of Timetal®21S monolithic laminate at 650°C, 0.05 Hz.

SECTION 2

THERMAL RESIDUAL STRESS IN TITANIUM METAL MATRIX COMPOSITES

ABSTRACT

A new experimental approach designed to determine the axial thermal residual stress in the matrix of the continuously reinforced metal matrix composite is described in this section. This approach is based on the stress-strain expression in terms of the fiber thermal and mechanical properties as well as the volume fractions of the composite constituents. This expression is then incorporated into an experimental procedure in which a composite specimen is simulated by a fiberless titanium laminate plate gripped under load control across the frame of a hydraulic material testing system. The strain developed in the laminate specimen during heating or cooling is governed by the strain compatibility requirement imposed by the fiber phase which is represented by the testing frame. This restricted matrix strain is converted through a feedback logic into a matrix residual stress that could be followed on real time basis. The magnitude of the thermal residual stress measured at room temperature for SCS-6/Ti-15-3 composite after the cool-down from consolidation temperature has been compared with that obtained by the X-ray diffraction technique. The proposed technique was then applied to SCS-6/Timetal®21S composite yielding measurements of the matrix thermal residual stress as a function of several testing variables such as temperature, heating/cooling rate, thermal cycle upper limit and number of thermal cycles. Important features of the matrix axial thermal residual stress have been analyzed. The major conclusion of this analysis is that the development of the thermal residual stress is a cooling rate dependent while the relaxation of this stress depends on the magnitude of the viscoplastic strain generated in the matrix material at a particular testing condition.

2.1 INTRODUCTION

Fiber reinforced metal matrix composites (FRMMCs) generally consist of materials with different coefficients of thermal expansion (CTE) between the matrix and the reinforcing phase. Because of this difference, upon consolidation at high temperature, which may exceed 1000°C in the case of Ti-base MMC fabrication, and during cool-down from this strain-free temperature to room temperature, appreciable locked-in residual thermal stresses are formed in both the matrix and the reinforcing phase. These residual stresses can be detrimental as well as beneficial. The detrimental aspects are associated with a variety of damage types produced in the matrix material. For example, in the case of SCS-6/Ti-24Al-11Nb (at%) composite, the thermally induced effective residual stress exceeds the matrix yield stress at

temperatures below 500°C and as such the matrix undergoes plastic deformation [1]. While in the case of SCS-6/Ti-24Al-11Nb [2] and SCS-6/Ti-15-3 [3] compostes the residual hoop stresses are reported to be large enough to generate radial cracks at the fiber/matrix interface during cooling from the consolidation temperature. For the SCS-6/Ti-25-10-3-1Mo composite during cool-down from 927°C, multiple circumferential cracks were observed in matrix near fiber/matrix interfacial region [4]. From the beneficial viewpoint, the compressive radial stress at the interface acts to clamp the matrix around the fiber. This clamping effect plays a significant role in the fiber/matrix load transfer process. This is particularly important for the situation where debonding and slippage occurred between the matrix and fibers. In fact, for some composite systems, such as SCS-6/Ti-15-3, where the fiber/matrix chemical bonding is weak [5,6], the compressive residual radial stress friction provides the frictional force which is the critical means of achieving load transfer. For the axial residual stress, it is generally believed that this kind of residual stress superimpose directly on the applied stress in both the fiber and matrix material. However, recent studies showed that the axial residual stress has definite influences on debonding and fiber bridging processes [7-11]. For a bonded interface, the applied axial stress on the fiber required to debond the interface is modified by the presence of the residual axial stress. When the interfacial shear stresses induced by the residual axial stress and by the applied axial stress are in the same direction, the existence of the axial residual stress facilitates debonding process. When they are in opposite directions, interfacial debonding is inhibited by the axial residual stress. While for a partially debonded interface the axial residual stress influences the boundary condition at the end of debonding which, in turn, modifies the stress distribution in the debonded region [7,8]. In this region, the axial residual stress also influences the opening of matrix cracks [9,12], which will decrease or increase the bridging traction in the fiber thus modifies the driving force at crack tip. In this sense, axial residual stress can also affect the damage mode of the composite and plays a role as important as the radial residual stress.

Thus, the study of the residual stress distribution and its evolution in composite systems is important in the understanding of its role in the load transfer efficiency within the composite as well as in its influence on the damage mode and the damage location in relation to the composite constituents. These aspects are crucial in the process development and the structural design of composites. Many investigations have been made to calculate and/or measure these thermal residual stresses, see [1,4,13-22]. On the experimental side, the two frequently used nondestructive techniques for measuring residual stresses in composites are the X-ray diffraction method [15,23-25] and the neutron powder diffraction method [1,18,20,26,27]. The X-ray techniques have a wider application since the equipment is easier to access and well developed. However, the shallow beam penetration (a few microns) precludes clear volume sampling and thus X-ray measurement can only provide a near-surface residual stress field. While neutron diffraction techniques require a radiation source that is only available in a small number of laboratories, they offer unique advantages in determining the residual stresses within the cross section of the specimen owing to the deep penetration of the neutron beam; about 1000 times deeper than that of X-rays [18,20]. This deeper penetration provides an excellent volume sample thus providing a relative true bulk measurement of residual strains independent from surface-related effects. Furthermore, deeper

penetration produces the ability to simultaneously measure the residual strains parallel and perpendicular to the fiber in both fiber and matrix. The important common feature between X-ray and neutron diffraction techniques is the time required for each point of stress measurement. For X-rays, the sampling time at each measurement varies from 5 to 40 minutes [28,29] while for neutrons it requires about 2 hours [28,30]. This time requirement while acceptable for measurements at room temperature, represents a problem for those to be obtained at elevated temperature conditions or during cooling from consolidation temperature. This is due to the fact that a rapid stress relaxation could take place when attempts are made to hold the temperature for long durations while diffraction count is being made. This basic difficulty in tracing the evolution of residual stresses without introducing time dependent alteration in their magnitudes is the motivation to develop a real-time mechanical simulation technique which will be described in this section. This technique is a one-dimensional approach which focuses on the determination of the axial thermal stress in the matrix material during temperature variation in processes such as cool-down from fabrication temperature to room temperature or thermal cycling with or without externally applied load. As mentioned above, the axial thermal residual stress plays an important role in influencing the damage process of continuous fiber composites. Thus, the comprehensive knowledge of the axial thermal stress evolution will be expected to shed light on the understanding of the damage mechanisms and the corresponding mechanical behavior of the composite systems. Although the proposed technique can not provide direct estimation of the hoop and radial stresses, it could, however, since uniqueness exists between axial, hoop and radial stresses in the matrix and fiber components of the FRMMC, when combined with a numerical method tuned by the data from this technique, provide enough information to establish the required three-dimensional stress state. The theory and the concepts of this mechanical simulation method will be presented in the next two sections. This will be followed by a description of material and experimental procedure as well as a discussion of experimental results.

2.2 THEORY

In this section, the equations required to estimate the matrix thermal stresses on the basis of the knowledge of the total matrix strain and the thermal characteristics of the fiber will be derived. A simplification will then be made so that the three-dimensional analysis reduces to the case where the axial component of the stress vector is determined through a one-dimensional equation. This equation is related to the total matrix strain and the CTE of the fiber and, as will be discussed later, is the key for the mechanical simulation method proposed in this section.

For a unidirectional fiber reinforced metal matrix composite under the axial loading conditions, the composite is assumed to undergo axisymmetric deformation. Based on a representative unit cell analysis the stresses in the composite constituents are described by the following equilibrium equations:

$$\sigma_r^c = \frac{r_f}{2r_m}\sigma_r^f + \frac{r}{2r_m}\sigma_r^m$$

$$\sigma_r^c = V_f \sigma_\theta^f + V_m \sigma_\theta^m \tag{1}$$

$$\sigma_z^c = V_f \sigma_z^f + V_m \sigma_z^m$$

where the superscripts c, f and m represent composite, fiber and matrix, respectively, and the subscripts r, θ and z represent radial, hoop and axial directions, respectively. V_f is the volume fractions of the fiber and V_m is the volume fraction of the matrix. r_f is the radius of the fiber, r_m is a radius of the representative unit cell. By defining the overall composite stress vector $\tilde{\sigma}^c$, the fiber stress vector $\tilde{\sigma}^f$ and the matrix stress vector $\tilde{\sigma}^m$, eq. (1) can then be written as the following matrix form:

$$\tilde{\sigma}^c = A_f \tilde{\sigma}^f + A_m \tilde{\sigma}^m \tag{2}$$

In the axisymmetric deformation condition, the strains within the constituent of the composite must satisfy the following compatibility relationships

$$\varepsilon_r^c = V_f \varepsilon_r^f + V_m \varepsilon_r^m$$

$$\varepsilon_\theta^c = \varepsilon_\theta^f = \varepsilon_\theta^m \tag{3}$$

$$\varepsilon_z^c = \varepsilon_z^f = \varepsilon_z^m$$

here, the superscripts and the subscripts have the same meanings as in eq. (1). If ε_θ^c and ε_z^c are expressed as $\varepsilon_\theta^c = (\varepsilon_\theta^f + \varepsilon_\theta^m) / 2$ and $\varepsilon_z^c = (\varepsilon_z^f + \varepsilon_z^m) / 2$, respectively, and defining the overall strain vectors $\tilde{\varepsilon}^c$, the fiber strain vector $\tilde{\varepsilon}^f$ and the matrix strain vector $\tilde{\varepsilon}^m$ then eq. (3) can be written in the following form:

$$\tilde{\varepsilon}^c = B_f \tilde{\varepsilon}^f + B_m \tilde{\varepsilon}^m \tag{4}$$

In the matrix, the total strain, $\tilde{\varepsilon}^m$, can be considered as the sum of the mechanical strain, $\tilde{\varepsilon}^{m,me}$, and the thermal strain, $\tilde{\varepsilon}^{m,th}$ of the matrix, i.e.

$$\tilde{\varepsilon}^m = \tilde{\varepsilon}^{m,me} + \tilde{\varepsilon}^{m,th} \tag{5}$$

the matrix thermal strain, $\tilde{\varepsilon}^{m,th}$, can be calculated as

$$\tilde{\varepsilon}^{m,th} = \int_{T_0}^{T} \tilde{\alpha}^m(T')dT' \tag{6}$$

where T_0 is the reference temperature, T is the temperature, $\tilde{\alpha}^m(T)$ is the CTE vector of the matrix; $\tilde{\alpha}^m(T) = (\alpha_r^m(T), \alpha_\theta^m(T), \alpha_z^m(T))^T$. The mechanical strain, $\tilde{\varepsilon}^{m,me}$, consists of an elastic component, $\tilde{\varepsilon}^{m,e}$, and an inelastic component, $\tilde{\varepsilon}^{m,in}$, summed as follows:

$$\tilde{\varepsilon}^{m,me} = \tilde{\varepsilon}^{m,e} + \tilde{\varepsilon}^{m,in} \tag{7}$$

the elastic component, $\tilde{\varepsilon}^{m,e}$, can be obtained from the the following relationship:

$$\tilde{\varepsilon}^{m,e} = S_m \tilde{\sigma}^m \tag{8}$$

where S_m is the compliance matrix of the matrix material. The inelastic component, $\tilde{\varepsilon}^{m,in}$, generally consists of a time-independent plastic part, $\tilde{\varepsilon}^{m,p}$, and a time-dependent viscous flow part, $\tilde{\varepsilon}^{m,vis}(t)$:

$$\tilde{\varepsilon}^{m,in} = \tilde{\varepsilon}^{m,p} + \tilde{\varepsilon}^{m,vis}(t) \tag{9}$$

$\tilde{\varepsilon}^{m,vis}(t)$, is, generally, composed of an anelastic recoverable component, $\tilde{\varepsilon}^{m,visa}(t)$, and a viscoplastic component, $\tilde{\varepsilon}^{m,visp}(t)$:

$$\tilde{\varepsilon}^{m,vis}(t) = \tilde{\varepsilon}^{m,visa}(t) + \tilde{\varepsilon}^{m,visp}(t) \tag{10}$$

Thus, the total strain of the matrix could be written in the terms of its individual components as:

$$\tilde{\varepsilon}^m = \tilde{\varepsilon}^{m,e} + \tilde{\varepsilon}^{m,p} + \tilde{\varepsilon}^{m,visa}(t) + \tilde{\varepsilon}^{m,visp}(t) + \tilde{\varepsilon}^{m,th} \tag{11}$$

Turning attention to the fiber, it is assumed to be made of a noncreeping material and undergoes elastic deformation only. This assumption is suitable to most of SiC/Ti MMC composites at operating temperatures below 1000°C. In this case, the mechanical strain of the fiber, $\tilde{\varepsilon}^{f,me}$, equals the elastic strain of the fiber, $\tilde{\varepsilon}^{f,e}$, thus, the total strain of the fiber, $\tilde{\varepsilon}^f$, can be expressed as a sum of elastic and thermal components as follows:

$$\tilde{\varepsilon}^f = \tilde{\varepsilon}^{f,e} + \tilde{\varepsilon}^{f,th} \tag{12}$$

where the elastic strain, $\tilde{\varepsilon}^{f,e}$, and the thermal strain, $\tilde{\varepsilon}^{f,th}$, can be evaluated as follows:

$$\tilde{\varepsilon}^{f,e} = S_f \tilde{\sigma}^f \tag{13}$$

and

$$\tilde{\varepsilon}^{f,th} = \int_{T_0}^{T} \tilde{\alpha}^f(T') \, dT' \tag{14}$$

where S_f is the compliance matrix of the fiber, $\tilde{\sigma}^f$ is the fiber stress and $\tilde{\alpha}^f(T)$ is the CTE vector of the fiber; $\tilde{\alpha}^f(T) = (\alpha_r^f(T), \alpha_\theta^f(T), \alpha_z^f(T))^T$. Now, by combining eqs. (4), (12)-(14), $\tilde{\sigma}^f$, can be expressed as

$$\tilde{\sigma}^f = C_f \left[B_f^{-1} \left(\tilde{\varepsilon}^c - B_m \tilde{\varepsilon}^m \right) - \int_{T_0}^{T} \tilde{\alpha}^f(T') \, dT' \right] \tag{15}$$

where C_f is the stiffness matrix of the fiber. Furthermore, substituting (15) in (2), the matrix stress, $\tilde{\sigma}^m$, is obtained as

$$\tilde{\sigma}^m = A_m^{-1} \left\{ \tilde{\sigma}^c - A_f C_f \left[\tilde{\varepsilon}^f - \int_{T_0}^{T} \tilde{\alpha}^f(T') \, dT' \right] \right\} \tag{16}$$

For thermal loadings where no external mechanical load is applied, i.e. $\tilde{\sigma}^c = 0$, eq. (14) can be reduced to

32

$$\tilde{\sigma}^m = H \left[\int_{T_0}^{T} \tilde{\alpha}^f(T')dT' - \tilde{\varepsilon}^f \right] \qquad (17)$$

where $H = A_m^{-1} A_f C_f$.

Eq. (17) indicates that the matrix stress state at certain temperature can be determined as long as the fiber strain state at same temperature is known. It should be noticed that the matrix stress state obtained from eq. (17) corresponds to the situation where the matrix could undergo any combinations of elastic, plastic and viscous deformation. While in the usual diffraction methods (X-ray or neutron diffractions), the stress analysis basically relies on the Hook's law which only corresponds to the elastic deformation [27,31]. If, for the first approximation, the Poisson effect of the fiber is neglected, eq. (17) could then be decoupled and the z-component of the matrix stress vector, $\tilde{\sigma}^m$, can be written as

$$\sigma_z^m = \frac{V_f E_f}{V_m} \left(\int_{T_0}^{T} \alpha_z^f(T')dT' - \varepsilon_z^m \right) \qquad (18)$$

The mechanical simulation method developed in this study to examine the evolution of the thermal axial stress in matrix is based on the use of eq. (18).

2.3 MECHANICAL SIMULATION METHOD

It is known that as the temperature of a portion of composite material changes, both fiber and matrix materials tend to deform according to their respective CTE. However, the existence of the significant CTE difference and the fiber/matrix bond require the strain compatibility between the two composite phases, consequently the stress and the strain will be developed in the matrix and the fibers in order to accommodate the thermal mismatch. In order to illustrate the concept of the proposed approach, the composite is idealized as a one dimensional two-bar model representing the fiber and the matrix constituents, as schematically detailed in Fig. 2-1. Also, during post-fabrication cool down and subsequent thermal cycling, the cooling/heating path is viewed as being piecewise discretized into steps consisting of an instantaneous temperature increment, ΔT, followed by a time increment, Δt, as illustrated in Fig. 2-2. For a particular time/temperature step, the elastic-plastic response and creep response are considered as a summation of the elastic-plastic response due to ΔT and the creep response occurring during Δt.

The stress-state of the composite is assumed to be stress-free at the consolidation temperature, T_c, as shown in Fig. 2-3(a). When the composite cools down an increment of ΔT from the consolidation temperature, the matrix and fiber will attempt to contract freely by a strain amount of $\Delta\varepsilon_z^{i,th}$ (i = f for fiber and i = m for matrix), as if no constraint or bond existed between the fiber and the matrix. In reality, however, constraint does exist (assuming a perfect fiber/matrix bonding) and the requirement for isostrain must be satisfied across the fiber/matrix interface. In response to this restriction, the matrix will act as if it is elongated from its constraint-free length with a tensile mechanical strain, $\Delta\varepsilon_z^{m,me}$, and the fiber will be

33

as if compressed from its constraint-free length, with a compressive mechanical strain, $\Delta\varepsilon_z^{f,me}$, see Fig. 2-3(b). Accompanying these strains, a residual tensile stress, $\Delta\sigma_z^m$, is induced in the matrix while a residual compressive stress, $\Delta\sigma_z^f$, is induced in the fiber, as illustrated in Fig. 2-3(c). The significance of $\Delta\sigma_z^m$ is in its ability to generate a tensile inelastic strain component in the matrix. It is assumed here that the fiber does not develop significant plastic or creep strain. Therefore, the net axial stress developed in the matrix, $\Delta\sigma_z^m$, is the sum of a tensile stress component generated by the restriction imposed on the thermal contraction of the matrix and the stress relaxation due to the restricted creep flow in the matrix. Similarly, the matrix total strain, $\Delta\varepsilon_z^m$, at the end of the first cool-down step is calculated as the sum of the thermal strain component (due to ΔT) and an inelastic strain component (due to Δt). At the end of the first cool-down step, a unique correlation can be established between the matrix total axial strain, $\Delta\varepsilon_z^m$, and the matrix axial stress, $\Delta\sigma_z^m$, via the thermal and elastic properties of the reinforced fiber. This relationship takes the form of eq. (18) which is rewritten as:

$$\Delta\sigma_z^m = \frac{V_f E_f}{V_m} \left(\int_{T_c}^{T_c-\Delta T} \alpha_z^f(T')dT' - \Delta\varepsilon_z^m \right) \tag{19}$$

where T_c represents the consolidation temperature and all other parameters are as previously defined.

The concepts discussed above are identical for subsequent cool-down steps and hence the values of $\Delta\varepsilon_z^m$ and $\Delta\sigma_z^m$ at the end of each ΔT step can be determined. The thermal residual stress and strain evolution in the matrix phase of a composite during cool-down from consolidation and/or subsequent thermal cycling, can then be fully traced and described.

This notion can be exploited experimentally as follows: a fiberless (neat) titanium laminate specimen is gripped under load-control in a hydraulic testing frame with data acquisition and feedback capabilities. In this arrangement, the laminate specimen assumes the role of the composite matrix, while the actuator of the testing frame assumes the role of the composite fiber, as schematically illustrated in Fig. 2-4. The initial stress-free condition is then simulated by raising the temperature of the laminate specimen to the consolidation temperature with zero applied load, so that both the specimen (matrix) and the loading frame (fiber) are stress-free. A high-temperature strain extensometer attached to the specimen gage length is also set to zero strain level. On reducing the temperature from T_c for a finite temperature step ΔT, thermal strain is induced in the laminate specimen (at this moment, the system is still stress-free, since the test machine is at zero load-control). This thermal strain, $(\Delta\varepsilon_z^m)_1$, measured by the extensometer, is fed into eq. (19) in order to estimate the corresponding $(\Delta\sigma_z^m)_1$ which would exist in the matrix if it were constrained by the fiber/matrix bond. This calculated matrix stress is then applied to the specimen via the load frame (fiber). However, the strain in the specimen (as measured by the extensometer) will change to $(\Delta\varepsilon_z^m)_2$ in response to this applied stress, and the new matrix strain, being a combination of thermal and mechanical strains, is input back to eq. (19) and a new matrix stress is calculated and then applied to the specimen. This iterative process continues until the convergence occurs during the period Δt (Δt duration defines the cooling rate for this specific cool down process) as

illustrated in Fig 5. The converged values of $(\Delta\varepsilon^m_z)_n$ and $(\Delta\sigma^m_z)_n$ are therefore considered to be the thermal residual stress and strain states corresponding to the temperature T_c-ΔT and the certain cooling rate. It should be emphasized that the measured matrix strain, $(\Delta\varepsilon^m_z)_i$; i = 1, 2,.., n, includes any creep strain component that may develop due to the loading of the matrix. As this process is repeated for additional decrements in temperature, the matrix thermal residual stress and strain history as a function of temperature could be established.

2.4 MATERIAL AND EXPERIMENTAL PROCEDURE

Two metastable β titanium alloys were used as matrix materials, Timetal®21S and Ti-15-3. The chemical composition of β21S (in wt%) is: 0.1 Fe, 16.0 Mo, 3.06 Al, 2.9 Nb, 0.2 Si, 0.22 C, 0.12 O, 0.005 N with the balance being Ti. The microstructure of the heat treated alloy consists of distinctive β grains with an average size of 80 μm containing Widmanstätten acicular α phase and continuous grain boundary α material with the thickness of about 0.8 μm. Laminates were fabricated by consolidating eight foils using vacuum hot pressing employing pre-established critical processing parameters. The Ti-15-3 alloy has the following nominal composition (in wt%): 14-16 V, 2.5-3.5 Cr, 2.5-3.5 Al, 2.5-3.5 Sn, < 0.05 C, < 0.05 Ni, < 0.15 O and < 0.015 H with the balance being Ti. The Ti-15-3 matrix was also supplied in 8 ply monolithic laminate. The fiber mechanical and thermal properties simulated in this study were those of the SCS-6 fiber. The fiber volume fraction utilized here for both Ti-15-3 and Timetal®21S composites was assumed to be 35%.

Table 2.1 Test Conditions

Test Condition	Cooling/Heating Rate (°C)	Thermal Cyclic Range (°C)	Material
A	0.5	100-550	Timetal®21S
B	0.5	100-650	Timetal®21S
C	0.05	100-575	Timetal®21S
D	0.05	—	Ti-15-3

Four Timetal®21S and one Ti-15-3 laminate strips were used in this study. The dimension of the test specimens were 76.5mm x 7.25mm x 0.85mm with the gage length measuring 40mm. All tests were carried out using an automated servo-hydraulic test frame. Test specimens were gripped using a hydraulic flat grip with self aligning capabilities and heated with an open furnace utilizing infrared radiation lamps. In all tests, heating from room temperature to the consolidation level was achieved using a heating rate of 0.05°C/sec under

the stress-free condition. The consolidation temperature was taken as 871°C, and 900°C for the Timetal®21S and Ti-15-3 matrices, respectively. Tests after that were conducted using two different cooling/heating rates 0.5°C/sec and 0.05°C/sec. Several specimens of the Timetal®21S material were subjected to thermal reversals between 100°C and three different upper temperatures; 525°C, 575°C and 650°C. The variation of the temperature along the gage length during all tests was ± 3°C. All test conditions are listed in Table 2.1.

2.5 RESULTS, ANALYSIS AND DISCUSSION

As mentioned before, the focuse of this study is the evolution characteristics of the axial thermal residual stress in the Timetal®21S matrix material. However, for the absence of data in literature regarding the Timetal®21S material, the Ti-15-3 laminate was also used in order to compare the results using the proposed simulation technique with the limited Ti-15-3 data available in literature (e.g. see [32]).

The axial thermal residual stress profiles in Ti-15-3 and Timetal®21S matrix materials are shown in Figs. 6-8 for different cooling rates. These profiles were obtained by simulating the thermal response of composite systems in which the properties of SCS-6 fiber were used. Fig. 2-6 shows the stress profile corresponding to the Ti-15-3 during cool-down from consolidation temperature to room temperature with a cooling rate of 0.05°C/sec. From this figure, the stress level achieved at room temperature is 198 MPa. This result could be compared with that obtained by Cox et al [32] using the X-ray diffraction technique. Their work showed that the axial residual stress at room temperature in SCS-6/Ti-15-3 composite has the value of 130 ± 30. While the results of the two studies are close, the difference could be due to the fact that the work of Cox et al [32] may have been carried out on as received specimens that are generally cooled from the consolidation temperature using a natural cooling rate which is lower than any of the rates used in this study. In addition, while the X-ray diffraction provides surface stress measurements, the proposed technique provides an average bulk stress. It should be mentioned here that the calculated results by Mall et al [33] for the axial residual stress in the Ti-15-3 matrix is 81 MPa which is lower than the experimental result discussed above. The possible reason for this lower value is that the viscoplastic response of the matrix material which dominantes the final stress state is too complix to be described accuratly in constitutive laws used in the current numerical models.

Turning attention to the Timetal®21S matrix material, the axial thermal residual stresses, σ_z^m generated in the SCS-6/Timetal®21S composite system during the cool-down from the consolidation temperature to room temperature are shown in Figs. 7 and 8 for two different cooling rates: a fast cooling rate, 0.5°C/sec, and an equivalent to a natural cooling rate, 0.05°C/sec. For all those tests, neither surface cracks nor interior damage were found. These figures also show the residual stress during subsequent thermal cycles reversing between 100°C and two high temperature levels: 550°C and 575°C. The analysis will focus first on the thermal residual stress developed during the first cool-down. Here, it is observed that σ_z^m is cooling-rate dependent: the higher the cooling rate, the lower the thermal residual stress. This is valid for the entire cool-down range. Furthermore, the stress build-up as a function

36

of the decreasing temperate rate is also cool-rate dependent. It is also observed that two distinct stages exist during the cool-down duration. In the first stage, the built-up stress is small and rises with a small $d\sigma/dT$ value. This trend ends at a certain transition temperature and a new stage begins where both the magnitude of the thermal residual stress and $d\sigma/dT$ show higher values than those in the previous stage. The transition between these two stages in the case of the 0.5°C/sec testing occurred at about 750°C while in the case of 0.05°C/sec, this transition is delayed and occurred at about 600°C. It is important to notice here that the $d\sigma/dT$ in the second stage is higher in the 0.05°C/sec case than that of the 0.5°C/sec case.

Two important points should be mentioned here. The first is the fact that σ_z^m during the cool-down process of the two simulated composites used in this study has always been lower than the yield stress, σ_{ys}, of the matrix material. If one assumes that σ_r^m, σ_θ^m and σ_z^m are related as folows [1]: $|\sigma_r^m| \le \sigma_z^m$ and $|\sigma_\theta^m - \sigma_z^m| = \sigma_z^m / 2$, the corresponding equivalent stress, σ_{eq}, could then be calculated. In this case σ_{eq} is found to be always less than the yield stress levels [34,35] of the Ti-15-3 and Timetal®21S monolithic laminates. This indicates that no plastic deformation took place in the matrix material during the cool-down process. The second point to be addressed is that all specimens have been subjected to post test optical microscope analysis which showed that no surface microcracking has developed during the cool-down process in both material. Recognizing these two facts, an attempt will be made here to interpret the observations described above on the basis of the inelastic behavior of the matrix material and the deformation constraints imposed by the matrix/fiber strain compatibility requirement. First, we will deal with the existence of two distinctive stages in the σ-T relationship. At the onset of the cool-down process, the inelastic strain of the matrix material, $\varepsilon_z^{m,in}$, for a particular net stress level, σ_z^m, and during a time interval, t, can be described using the Bailey-Norton type equation which is written as

$$\varepsilon_z^{m,in} = B(\sigma_z^m)^n t^\alpha \qquad (20)$$

where n and α are material constants, and B takes the Arrhenius form:

$$B = A \exp\left(-\frac{Q}{RT}\right) \qquad (21)$$

A is a constant, R is the gas constant and T is the temperature in Kelvin. Q is the thermal activation energy of the stressed material, it is written as a function of the inelastic strain accumulated in the material $f(\varepsilon_z^{m,in})$ [36]:

$$Q = Q_0 - f(\varepsilon_z^{m,in}) \qquad (22)$$

where Q_0 is the thermal activation energy of the unstressed material. Since the magnitude of residual stress is small in the early stage of the cool-down, it could then be suggested that the development of the inelastic strain and the corresponding compressive stress component, which leads to the decrease in the net axial residual stress, is primarily governed by temperature through the parameter B. In the second stage of cool-down below the transition temperature, where B is small, the development of the inelastic strain becomes more sensitive to the magnitude of σ_z^m. In this stage therefore, at a certain temperature and for the same time

37

duration, the net inelastic strain in the 0.5 C°/sec test should be higher than that occurring in the 0.05C°/sec case. Consequently, the net residual stress corresponding to the former condition should, as experimentally observed, be lower than that of the later condition. Furthermore, the existence of a difference in the transition temperature between the two stages for the two different cooling rates could be explained on the basis that the function $f(\varepsilon_z^{m,in})$ in eq.(22) should have a higher value in the case of the lower cooling rate testing due to the higher accumulated inelastic strain. Therefore, the thermal activation energy, Q, in the case of the lower cooling rate would maintain a relatively lower value (thus higher creep strain) at lower temperature levels, which signifies a transition temperature lower than that corresponding to the high cooling rate testing.

The second part of the analysis focuses on the evolution of the axial residual stress profile during the thermal cycles following the first cool-down process. These profiles obtained for different temperature ranges and different heating/cooling rates are shown in Figs. 7 and 8. The general observation here is that at any temperature within the cycle range, thermal reversals tend to reduce the axial thermal residual stress. Furthermore, the stress relaxation towards the zero level seems to increase as both the upper limit of the cycle temperature range and the cooling/heating rate increase. It is also observed that the decrease in the axial thermal residual stress follows an almost linear path parallel to its increase during the cool-down part of the preceding cycle. On reaching a transitional temperature, this path deviates from linearity with an increasing negative $d\sigma/dT$ slope as temperature increases. This behavior could be interpreted in terms of the relative influence of temperature on the development of viscous flow in the matrix material. At low temperature levels the magnitude of viscous flow is negligible and the thermal elastic unloading of the stress dominates. As the temperature increases, the influence of viscous flow becomes important resulting in a higher compressive stress component which leads to a rapid decrease of the matrix residual stress. The temperature at which this acceleration in the stress reduction takes place was found to decrease as the number of thermal reversals increases, see doted lines in Fig. 2-7. This temperature was also observed to depend on the heating-rate. This may be due to the fact that lower heating rate permit sufficient time for the development of viscous flow which in turn leads to a drop in the stress level at temperatures lower than that required to achieve the same drop in the case of high heating rate.

The role of the matrix viscous flow can further be examined by exploring the relationship between the inelastic strain, $\varepsilon_z^{m,in}$ and the axial thermal residual stress, σ_z^m. Since no matrix plastic deformation is realized during the thermal history of all tests carried out on the SCS-6/Timetal®21S composite, the inelastic strain $\varepsilon_z^{m,in}$ could be written as

$$\varepsilon_z^{m,in} = \varepsilon_z^{m,visa}(t) + \varepsilon_z^{m,visp}(t)$$

$$= \varepsilon_z^m - \int_{T_0}^T \alpha_z^m(T')dT' - \varepsilon_z^{m,e}$$

(23)

All terms being identified previously. ε_z^m could be replaced using eq.(18) and the relationship between $\varepsilon_z^{m,in}$ and σ_z^m is established as:

38

$$\varepsilon_z^{m,in} = \int_{T_o}^{T} \left(\alpha_z^f(T') - \alpha_z^m(T') \right) dT' - \frac{V_m}{V_f E_f} \sigma_z^m - \varepsilon_z^{m,e} \tag{24}$$

This relationship between $\varepsilon_z^{m,in}$ and σ_z^m for the test condition A is plotted in Fig. 2-9. It is seen here that for the same temperature level and at a particular thermal cycle, the value of $d\sigma/d\varepsilon$ increases as the temperature range of the thermal reversal increases. The increase in the slope $d\sigma/d\varepsilon$ means that the viscoplastic part of the inelastic strain in this particular cycle has increased thus permitting, opposite to the role of anelastic recoverable strain, unrecoverable drop in the residual stress level. Higher upper temperature limit of the thermal cycle and lower cooling/heating rates are favorable conditions for the promotion of viscoplastic strain.

Additionally, the ability to accumulate inelastic strains during thermal cycles could be determined by defining a strain hardening parameter, κ, as:

$$\kappa = \frac{d\sigma_z^m}{d\varepsilon_z^{m,in}} \tag{25}$$

This parameter was measured along isothermal lines (slanted lines in Fig. 2-9) for different temperature levels. The strain hardening parameter, κ, in terms of number of thermal cycles is shown in Fig. 2-10. It is apparent that κ decreases as number of cycles increases. This softening characteristic is proportional to both the increase in the upper temperature limit of the thermal cycle and the decrease in heating/cooling rates.

2.6 CONCLUSIONS

A new experimental approach designed to determine the axial thermal residual stress in the matrix of the continuously reinforced metal matrix composite is described in this section. Using this technique, the magnitude of the thermal residual stress measured at room temperature for SCS-6/Ti-15-3 composite after the cool-down from consolidation temperature has compared well with that obtained by the X-ray diffraction technique, taking anto consideration the difference in the fundamental nature between the two techniques. The proposed technique was then applied to SCS-6/Timetal®21S composite yielding measurements of the matrix thermal residual stress as a function of several testing variables such as temperature, heating/cooling rate, thermal cycle upper limit and number of thermal cycles. Important features of the matrix axial thermal residual stress can be summarized as follows:

1. The level of the axial thermal residual stress in both the SCS-6/Timetal®21S and SCS-6/Ti-15-3 composites is always lower than the yield stress of the corresponding matrix material.

2. The level of the thermal residual stress at room temperature is proportional to the cooling rate.

3.   At any temperature level, the axial thermal residual stress decreases as the number of thermal cycles increases. The magnitude of this decrease is proportional to the upper limit of the thermal cycle and inversely proportional to the cooling rate.

4.   The relaxation of the thermal residual stress during a thermal cycle is governed by the amount of nonrecoverable viscous flow developed in the matrix during this cycle.

5.   An important feature of the proposed technique is its ability to be extended to the study of thermomechanical responses of MMCs. In this case the experimental procedure would be executed with the inclusion of an externally applied load into the feedback governing equation. This technique is currently being utilized by the authors to study cases where the external load is constant (creep case) or time dependent (thermal mechanical fatigue cases).

2.7 REFERENCES

[1]   A. Saigal, D. S. Kupperman and S. Majumdar, Residual Strain in Titanium Matrix High-Temperature Composites. Materials Science and Engineering, Vol. 150A, 1992, pp.59-66

[2]   P. K. Brindley, S. L. Draper, J. I. Eldridge, M. V. Nathal and S. M. Arnold, The Effect of Temperature on the Deformation and Fracture of SiC/Ti-24Al-11Nb. Metallurgical Transactions, Vol. 23A, 1992, pp. 2527-2540

[3]   R. A. MacKay, Scipta Metall. et Mater. 24, 1990, pp.167-172

[4]   M. Sohi, J. Adams and R. Mahapatra, Transverse Constitutive Response of Titanium-Aluminum, Metal-Matrix Composites. In Constitutive Law for Engineering Materials, Eds. by C. D. Desai et al, ASME Press, New York, 1991, pp.617-626

[5]   W. S. Johnson, S. J. Lubowinski, A. L. Highsmith, W. D. Brewer and C. A. Hoogstraten, Mechanical Characterization of SCS_6/Ti-15-3 Metal Matrix Composites at Room Temperature, NASP TM-1014, 1988

[6]   W. S. Johnson, Mechanisms Controlling Fatigue Damage Development in Continuous Fiber Reinforced Metal Matrix Composites. In Advances in Fracture Research, eds. by K. Salama, K. Ravi-Chandar, D. M. R. Taplin and P. R. Rao, Vol. 2, Pergamon Press, New York, 1989, pp.897-905

[7]   C. -H. Hsueh, Interfacial Debonding and Fiber Pull-Out Stresses of Fiber-Reinforced Composites, III: With Residual Radial and Axial Stresses, Materials Science and Engineering, Vol. A145, 1991, pp.135-142

[8]   R. J. Kerans, Theoretical Analysis of the Fiber Pullout and Pushout Tests, J. Am. Ceram. Soc., Vol. 74, 1991, pp.1585-1596

[9]   Davidson, D. L., The Micromechanics of Fatigue Crack Growth at 25°C in Ti-6Al-4V Reinforced with SCS-6 Fibers, Metallurgical Transactions, Vol. 23A, 1992, pp.865-879

[10]   D. B. Marshall and B. N. Cox, A J-Integral Method for Calculating Steady-State Matrix Cracking Stresses in Composites, Mechanics of Materials, Vol. 7, 1988, pp.127-133

[11]   L. S. Sigl and A. G. Evans, Effects of Residual Stress and Frictional Sliding on Cracking and Pull-out in Brittle Matrix Composites, Mechanics of Materials, Vol. 8, 1989, pp.1-12

[12]   D. B. Marshall and A. G. Evans, Failure Mechanisms in Ceramic-Fiber/Ceramic-Matrix Composite, Journal of the American Ceramic Society, Vol. 68, 1985, pp.225-231

[13]   S. M. Arnold and T. E. Wilt, Influence of Engineered Interfaces on Residual Stresses and Mechanical Response in Metal Matrix Composites, NASA TM-105438, March, 1992

[14]   Y. Mikata and M. Taya, Stress Field in a Coated Continuous Fiber Composite Subjected to Thermo-Mechanical Loadings, Journal of Composite Materials, Vol. 19, 1985, pp.554-578

[15]   B. N. Cox, M. R. James, D. B. Marshall and R. C. Addison, Jr., Determination of Residual Stresses in Thin Sheet Titanium Aluminide Composites, Metallurgical Transactions, Vol. 21A, 1990b, pp.2701-2707

[16]   S. S. Hecker, C. H. Hamilton and L. J. Ebert, Elastoplastic Analysis of Residual Stresses and Axial Loading in Composite Cylinders, Journal of Materials, Vol. 5, No. 4, 1970, pp.868-900

[17]   E. E. Gdoutos, D. Karalekas and I. M. Daniel, Thermal Stress Analysis of a Silicon Carbide/Aluminum Composite, Experimental Mechanics, Vol. 31, 1991, pp.202-208

[18]   A. D. Krawitz, D. G. Reichel and R. L. Hitterman, Residual Stress and Stress Distribution in a WC-Ni Composite, Materials Science and Engineering, Vol. A119, 1989, pp.127-134

[19]   M. Uemura, H. Iyama and Y. Yamaguchi, Thermal Residual Stresses in Filament-Wound Carbon-Fiber-Reinforced Composite, Journal of Thermal Stresses, Vol. 2, 1979, pp.393-412

[20]   S. Majumdar, J. P. Singh, D. Kupperman and A. D. Krawits, Application of Neutron Diffraction to Measure Residual Strains in Various Engineering Composite Materials, Journal of Engineering Materials and technology, Vol. 113, 1991, pp.51-59

[21]   K. Jayaraman and K. L. Reifsnider, Residual Stresses in a Composite with Continuously Varying Young's Modulus in the Fiber/Matrix Interphase, Journal of Composite Materials, Vol. 26, 1992, pp.770-791

[22]   D. A. Koss and S. M. Copley, Thermally Induced Residual Stresses in Eutectic Composites, Metallurgical transactions, Vol. 2, 1971, pp.1557-1560

[23]   H. M. Ledbetter and M. W. Austin, Thermal Stress in a Silicon-Carbide/Aluminum Composite, in Residual Stresses in Science and Technology, eds. by E. Macherauch and V. Hauk, Vol. 1, Deutsche Gesellschaft für Metallkunde Informationsgesellschaft, Verla, Germany, 1987, pp. 517-521

[24]   Y. Ikeuchi, Measurements of Thermal Stress Behavior on Tungsten Fiber-Copper Composites, in Residual Stresses in Science and Technology, eds. by E. Macherauch and V. Hauk, Vol. 1, Deutsche Gesellschaft für Metallkunde Informationsgesellschaft, Verla, Germany, 1987, pp. 523-530

[25]   W. Grellner and K. A. Schwetz, Investigations of Residual Stresses in Ceramic Components, in Residual Stresses in Science and Technology, eds. by E. Macherauch and V. Hauk, Vol. 1, Deutsche Gesellschaft für Metallkunde Informationsgesellschaft, Verla, Germany, 1987, pp. 531-537

[26]   S. Majumdar, D. Kupperman and J. Singh, Determinations of residual Thermal Stresses in a $SiC-Al_2O_3$ Composite Using Neutron Diffraction, 1988, Journal of the American Ceramic Society, Vol. 71, pp.858-863

[27]   A. J. Allen, M. Bourke, M. T. Hutchings, A. D. Krawitz and C. G. Windsor, Neutron Diffraction Measurement of Internal Stress in Bulk Materials: Metal-Matrix Composites, in Residual Stresses in Science and Technology, eds. by E. Macherauch and V. Hauk, Vol. 1, Deutsche Gesellschaft für Metallkunde Informationsgesellschaft, Verla, Germany, 1987, pp.151-157

[28]   V. Hauk, Measuring Techniques of Residual Stresses — Present Situation and Future Aimes, in Residual Stresses in Science and Technology, eds. by E. Macherauch and V. Hauk, Vol. 1, Deutsche Gesellschaft für Metallkunde Informationsgesellschaft, Verla, Germany, 1987, pp.231-242

[29]   N. E. Dowling, R. W. Hendricks and K. Ranganthan, X-Ray Residual Stress Measurements in Notched Test Specimens, Journal of Testing and Evaluation, Vol. 16,

1988, pp.456-460

[30]   A. Saigal, private communication, 1992

[31]   M. R. James and J. B. Cohen, The Measurement of Residual Stresses by X-Ray Diffraction Techniques, Treatise on Materials Science and Technology, ed. by H. Herman, Vol. 19, 1-62

[32]   B. N. Cox, M. S. Dadkhah, M. R. James, D. B. Marshall, W. L. Morris and M. Shaw, On Determining Temperature Dependent Interfacial Shear Properties and Bulk Residual Stresses in Fiberous Composites, Acta Metall. Mater. Vol 38, No 12, 1990a, pp. 2425-2433

[33]   S. Mall and P. G. Ermer, Thermal Fatigue behavior of a Unidirectional SCS6/Ti-15-3 Metal Matrix Composite. Journal of Composite Materials, Vol. 25, 1991, pp. 1668-1686

[34]   H. W. Rosenberg, Ti-15-3 Property Data, in Beta Titanium Alloys in the 80's, eds. by R. R. Boyer and H. W. Rosenberg, The Metallurgical Society of AIME, Warrendal, PA, 1984, pp.409-432

[35]   H. Ghonem, Y. Wen, D. Zheng, M. Thompson and G. Linsey, Effects of Temperature and Frequency on Fatigue Crack Growth in Timetal®21S Monolithic Laminate, to be published in Materials Science and Engineering, 1992

[36]   H. Ghonem and D. Zheng, The Depth of Intergranular Oxygen Diffusion during Environment-Dependent Fatigue Crack Growth in Alloy 718, Materials Science and Engineering, Vol. 150A, 1992, pp.151-160
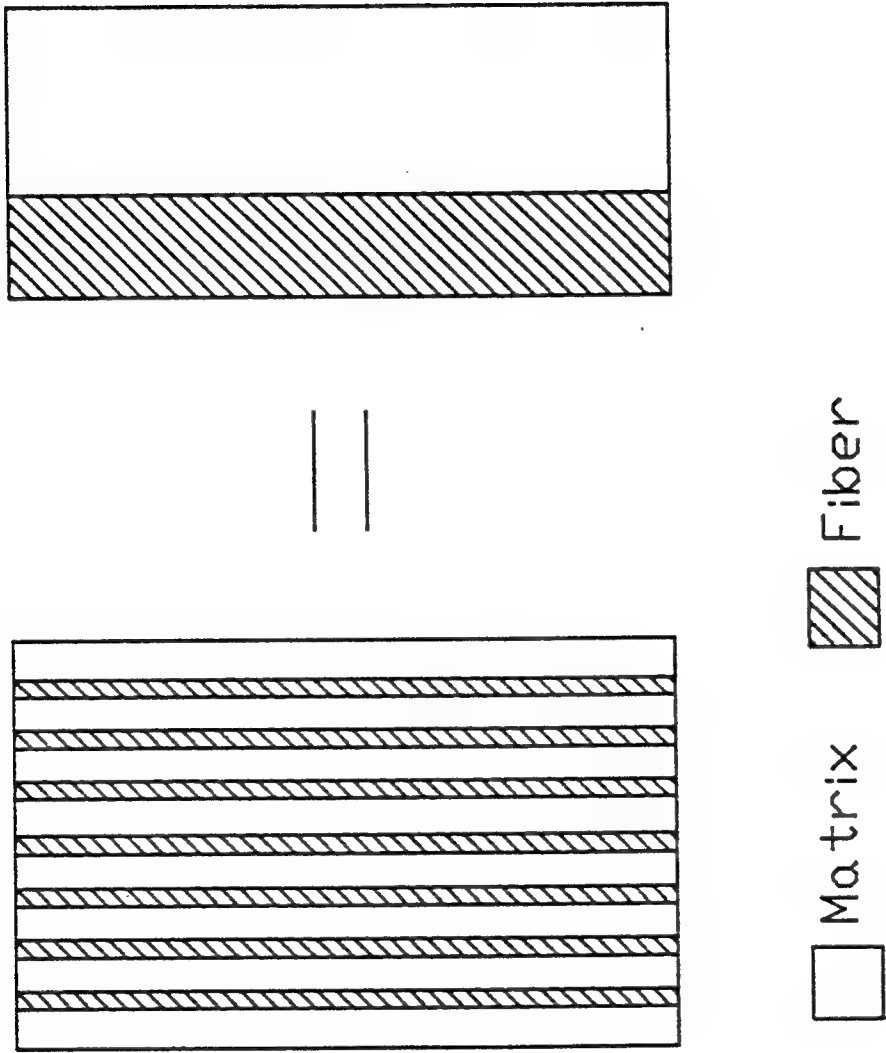
Fiber

Matrix

Fig. 2-1   Schematic of simplifying the composite major constituents, fiber and matrix, into two bar composite model.
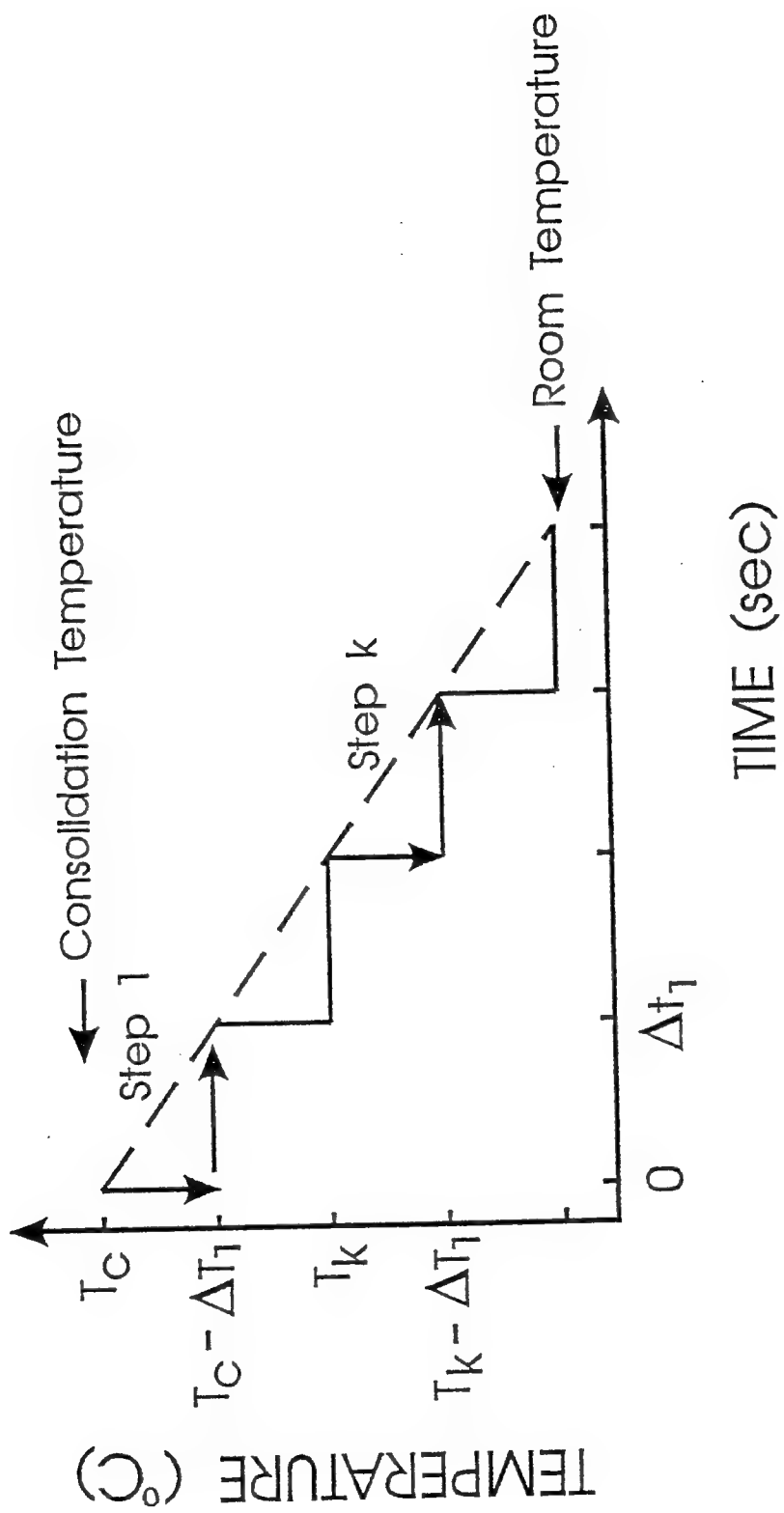
Fig. 2-2   Discretization of the cooling path from consolidation temperature to room temperature (no externally applied mechanical load).

45
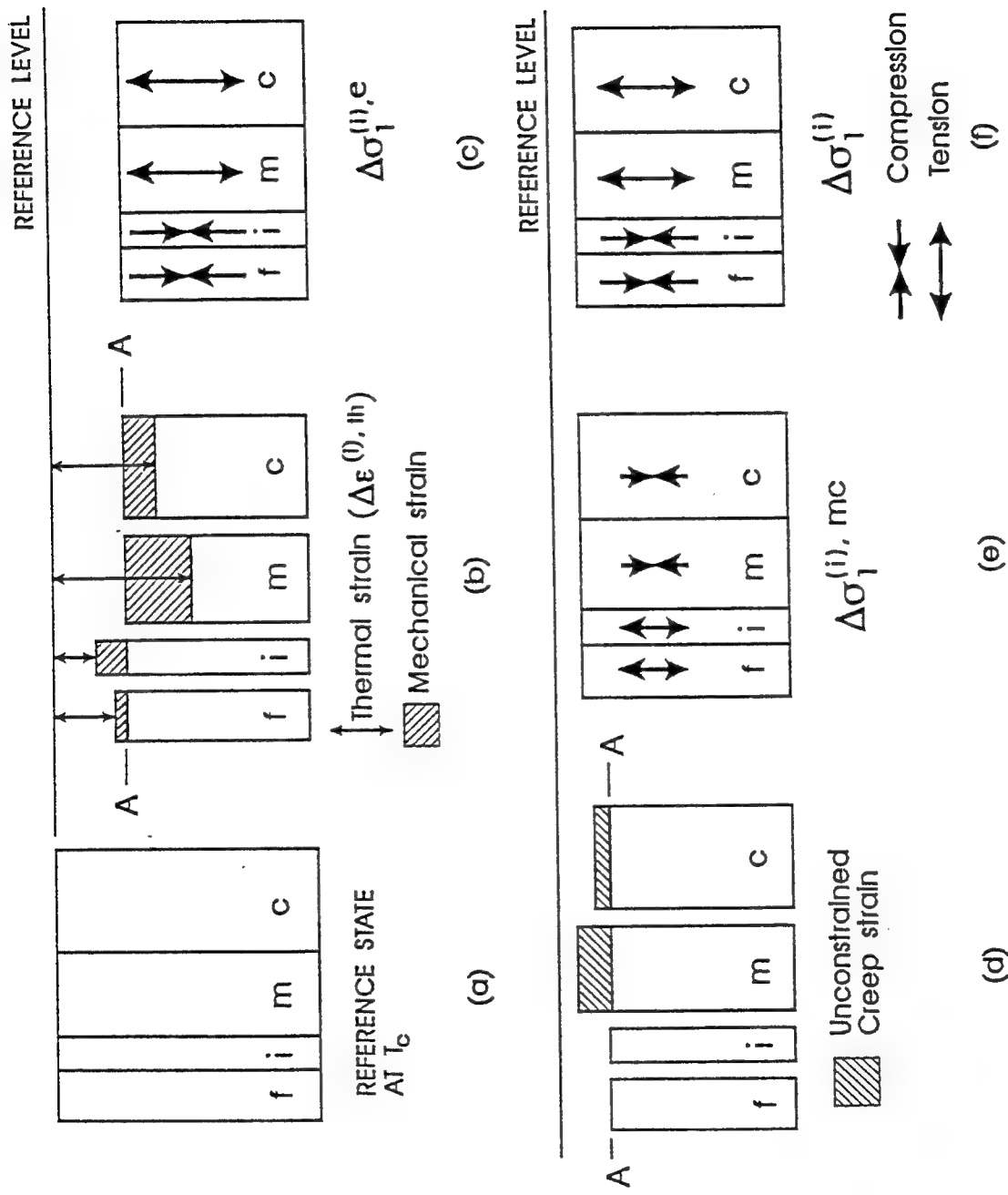
Fig. 2-3 Two bar model showing fiber and matrix responses during the first cool down step.

46

(a।) (b) (c)
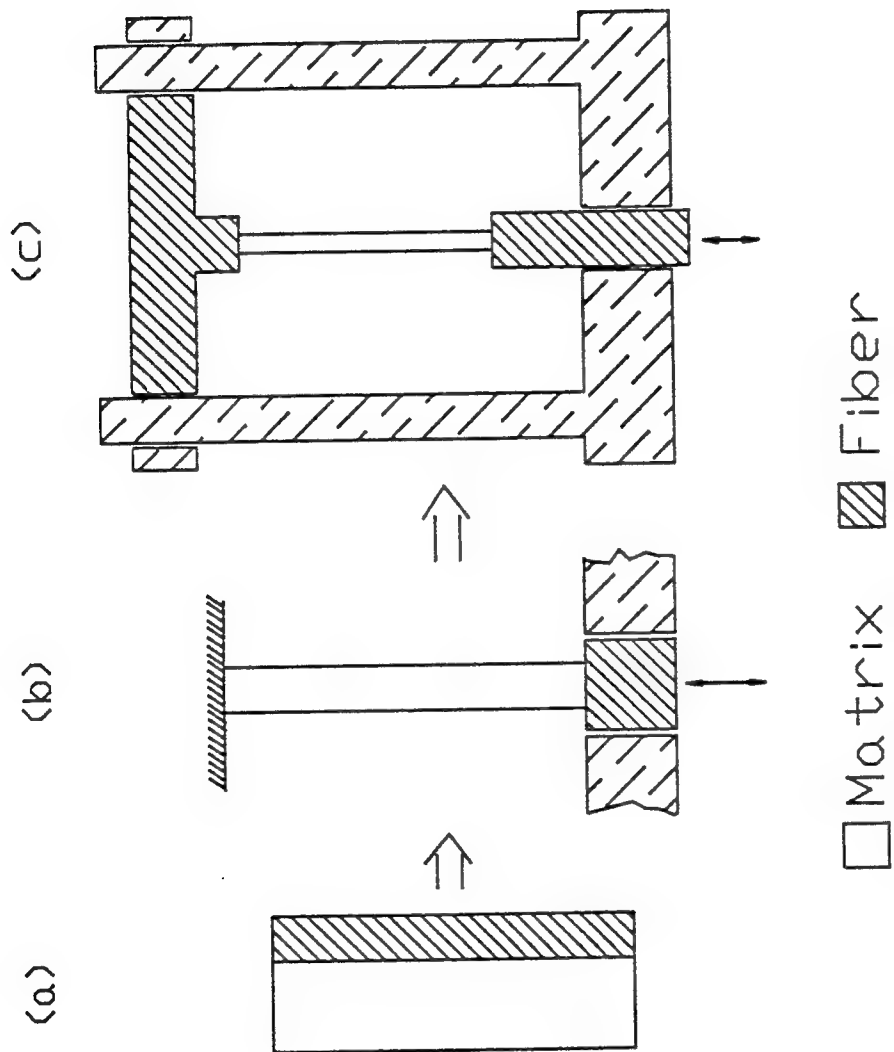
☐ Matrix ▨ Fiber

Fig. 2-4 Schematic of the idealization of fiber and matrix components in relation to a neat laminate (matrix material) loaded in a testing frame: (a) two bar composite model; (b) equivalent composite specimen where the matrix is restricted by a higher stiffness boundary; (c) equivalent composite system where a fiberless laminate specimen acts as a matrix while the restriction between matrix and fibers is imposed through adjustable loading system.

47
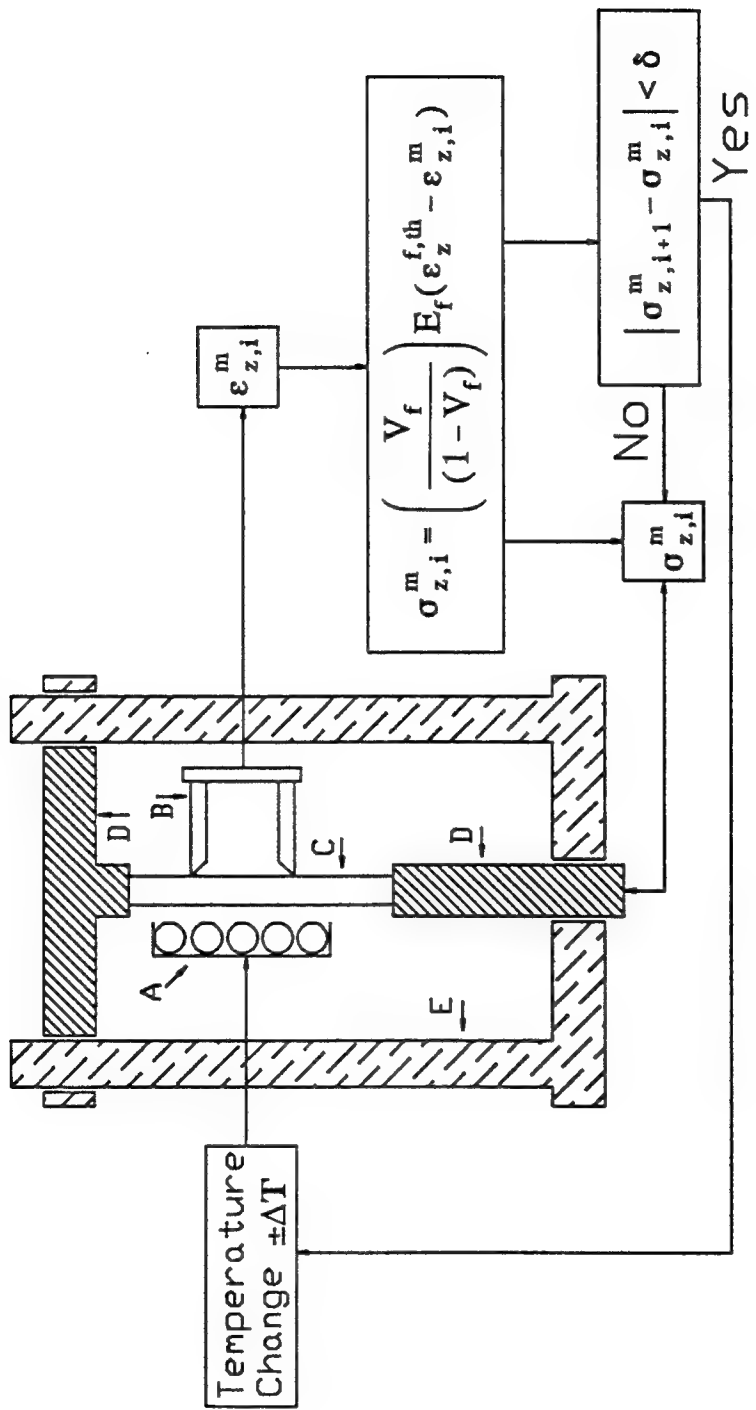
Fig. 2-5   Schematic of the simulation logic applied in the present study to estimate residual stress in the matrix component of a unidirectional reinforced metal matrix composite.   A: heating unit;   B: extensometer;   C: fiberless laminate specimen;   D: loading system;   D: testing frame.

48
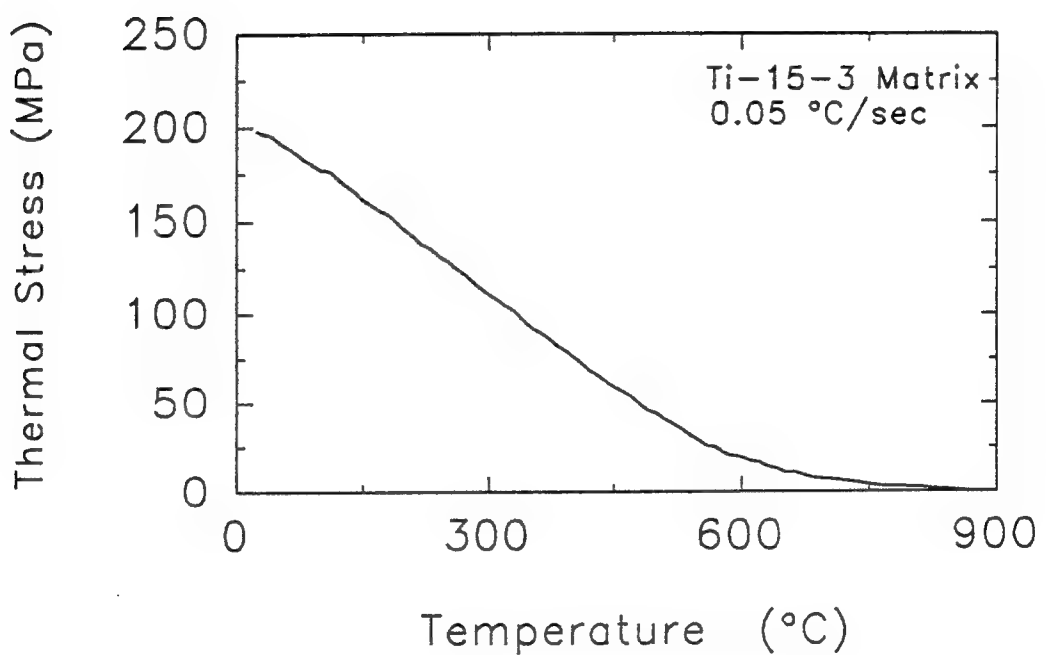
Fig. 2-6 Evolution of the thermal residual stress in Ti-15-3 matrix during cool-down from consolidation temperature using a cooling rate of 0.5°C/sec.
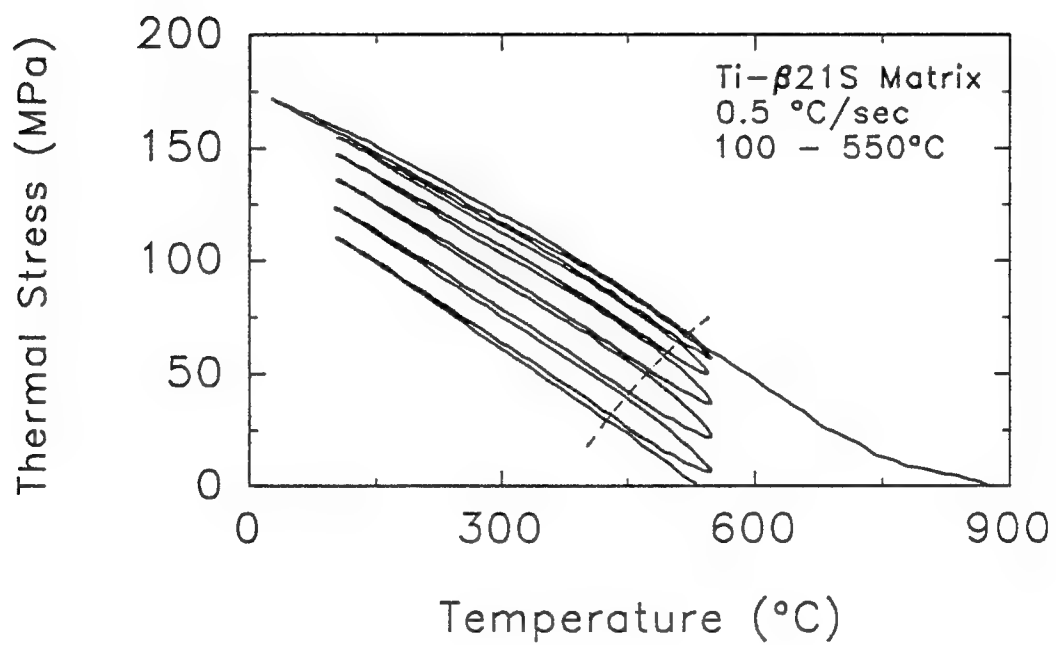
Fig. 2-7   Evolution of the thermal residual stress in Timetal®21S matrix during cool-down from consolidation temperature and subsequent thermal cycling between 100°C and 550°C using a cooling rate of 0.5°C/sec.
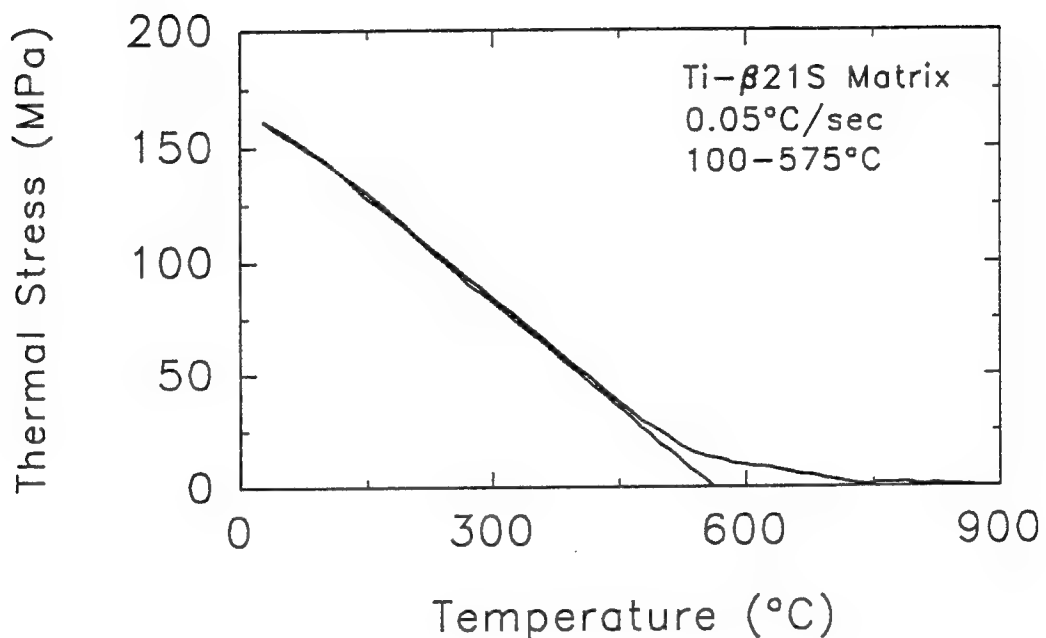
Fig. 2-8   Evolution of the thermal residual stress in Timetal®21S matrix during cool-
down from consolidation temperature and reheating to 575°C using a cooling
rate of 0.05°C/sec.
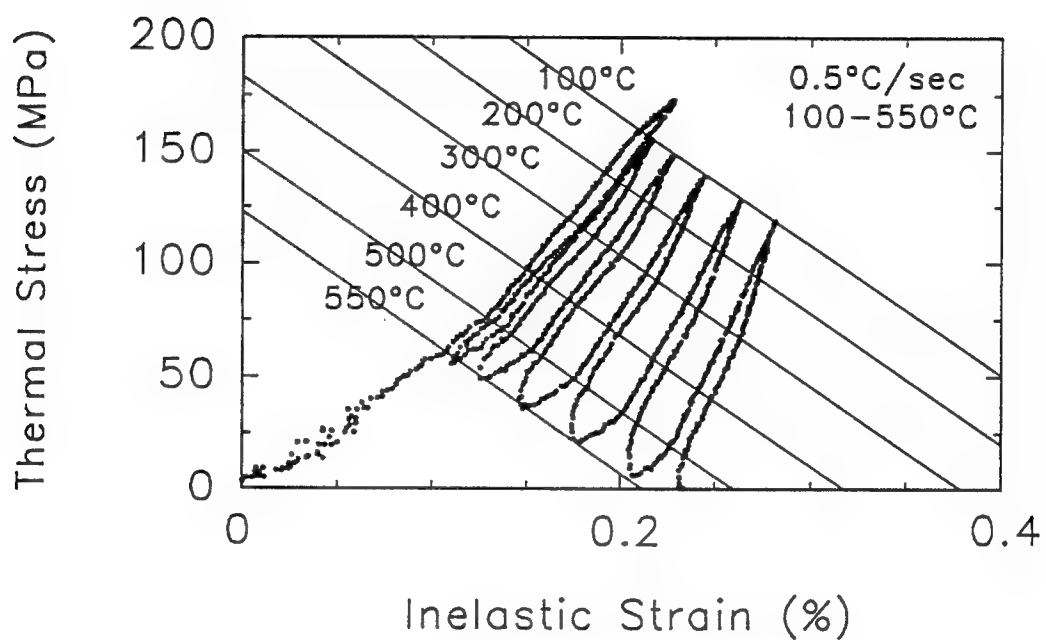
Fig. 2-9   Relationship between thermal residual stress in the matrix of SCS-6/Timetal®21S composite and corresponding inelastic strain as function of testing temperature.
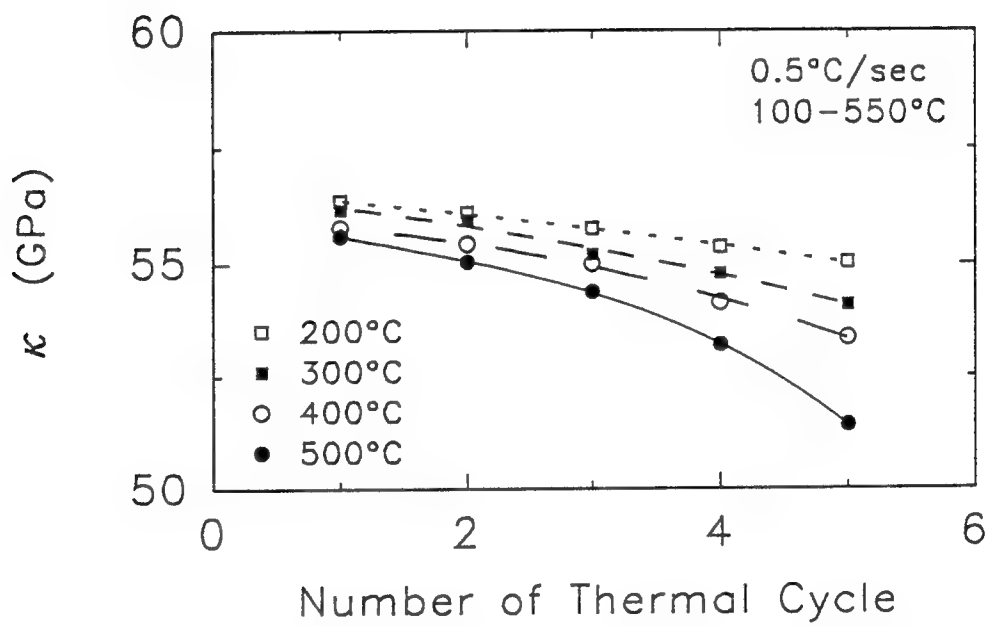
Fig. 2-10   Relationship between the strain hardening parameter of the matrix material of SCS-6/Timetal®21S and the number of thermal cycles.

SECTION 3

MICROMECHANICAL MODELLING OF TIME-DEPENDENT BEHAVIOR OF CONTINUOUS-FIBER-REINFORCED METAL MATRIX COMPOSITES

ABSTRACT

A new time-dependent model has been developed in order to predict the response of metal matrix composites subjected to thermal loadings. In this model, elastic, plastic and creep behavior have been considered. The model consists of a fiber and an interphase zone which behave elastically while the matrix and the surrounding composite media exhibit creep deformation. The cooling/heating path is discretized into load steps where elastic-plastic behavior is assumed to occur spontaneously over a temperature increment while creep behavior occurred over the following time increment. The plastic characteristics follows the deformation theory of plasticity. In the transient and steady-state stages of creep, the constraint-free creep deformation of the matrix and the composite media are calculated using the Bailey-Norton law with an Arrhenius-type expression for time-dependent creep coefficient. The "stiffness" method with a modified load vector is employed in calculating the constrained deformation in the composite. The accumulated creep strain history is predicted using the "strain hardening" formulation. The model can be easily extended to include external loading and employed to study the evolution of the stress and strain states in the constituents of the composite during isothermal and thermo-mechanical loadings.

3.1 INTRODUCTION

In Titanium-based metal matrix composites, the metallic matrix properties of ductility and toughness are combined with reinforcement properties of high strength and high modulus to yield increased strength-to-weight ratio and higher stiffness materials. These metal matrix composites (MMCs) are being developed as high performance materials capable of withstanding high temperatures and operating loads typical for advanced aerospace applications.

Continuous-fiber-reinforced MMCs are consolidated at high temperature which induce high thermal residual stresses during post-fabrication cool down. This is a consequence of mismatches of the coefficients of thermal expansions (CTEs) of the matrix and the fibers. These thermal residual stresses may initiate fiber/matrix debonding and radial cracking in the matrix and hence, dictate the subsequent behavior of the composites when subjected to thermo-mechanical loading. It was found that post-fabrication procedures such as thermal cycling can alter the residual stress states in titanium composites [1]. Consequently, determination of thermal residual stress and strain fields in a continuous-fiber-reinforced MMC is an essential step in characterizing the performance of the composite system.

Various analytical models have been developed and applied to study the thermal stress behavior of continuous-fiber-reinforced composites. Besides the plane-stress lamina model (e.g.

54

[2,3]), the concentric cylinder model has been well studied (e.g. [4-7]). Uemura [5] developed a two-phase model which consists of inner and outer cylinder to simulate the fiber and the matrix phase, respectively. In this model, the fiber-matrix interface has been treated as a perfect mathematical surface. Experimental work, however, indicated that the interphase formation accompanying the development of reaction zones in metal matrix composites is inevitable (e.g. [8,9]). Incorporation of interphase behavior into the micromechanical analyses of composite systems is therefore critical in realistic modelling of the mechanical behavior of the composites [7,10]. Based on this consideration, several researchers have proposed the three-phase model (fiber/interphase/matrix) to account for interphase effects (e.g. [7,10-12]). In reality, the "matrix cylinder" is surrounded by the composite media instead of a free surface, thus it is reasonable to impose a layer of homogeneous material with the composite properties surrounding the matrix layer in order to retain realistic boundary conditions (e.g. [13,14]). Following these ideas, Mikata [6] proposed a four-phase model (fiber/interphase(coating)/matrix/surrounding composite media) for elastic analysis of stress field in the composites.

As mentioned above, Titanium-based metal matrix composites are primarily developed for high temperature applications. At such extreme thermal and mechanical service conditions, the composite will experience time dependent deformation. Accurate representation of this nonlinear material behavior is essential in realistic determination of the stress and strain response of the composite. Experimental creep study on SCS-6/Ti-6Al-4V composite indicated that titanium-based composite exhibits creep behavior similar to that of the monolithic matrix (even though the longitudinal creep has been suppressed considerably by fiber reinforcement). This fact implies that creep behavior of the matrix alloy and the corresponding composite must be incorporated into the model formulation. However, fewer work has been done to model the creep behavior of fiber-reinforced metal matrix composites. Min [15] developed a plane-stress continuum model to analyze the primary creep deformation of a unidirectional metal matrix composite. Gayda [16] employed a cylindrical two-phase model to study the time-dependent behavior of TMCs in which the creep behavior of the matrix was considered by a relaxation curve obtained from an empirical fit of stress relaxation data for the matrix alloy. Since the composite media and the reaction zone were not included in these models, the models could not consider influences of the existence of these two phases on the overall creep behavior of the composite.

The objective of this section is to develop a micromechanical approach to analyze the elastic-plastic and creep behavior of a unidirectional continuous-fiber-reinforced metal matrix composite. This approach emphasizes the time-dependent stress analysis which is critical to high temperature applications. The four-phase cylinder model adopted in the present approach makes it possible to trace the evolution of the stress states for each constituent in the composite during cyclic thermal loadings. The concept of the model including mathematical formulations of the elastic, plastic and creep analyses are presented in the next section of the paper. This is followed by narration of a typical elastic-plastic-creep calculation routine. The last part of the paper includes conclusions and summary.

3.2 CONCEPTS OF THE MICROMECHANICAL APPROACH

The four-phase configuration adopted in this approach is illustrated in Fig. 3-1(a) where the fibers in the composite are assumed to be arranged in a hexagonal array. A hexagonal unit is substituted for the concentric fiber, reaction zone and matrix cylinders with radii r_4, r_3, and r_2,

respectively, while the equivalent composite media is represented by the outermost cylinder with radius r_1, as shown in Fig. 3-1(b). The fiber and the reaction zone are assumed to behave elastically at all loading conditions while the matrix and the surrounding equivalent composite media may undergo any combination of elastic, plastic and creep deformation depending on the nature of the applied load. All the constituent phases are assumed to be isotropic. In addition, the model is subjected to axisymmetric thermal loading with a uniform temperature distribution across all layers.

During post-fabrication cool down and subsequent thermal cycling, the cooling/heating path is piecewise discretized into load steps, each of which consists of a temperature increment, ΔT, followed by a time increment, Δt, as shown in Fig. 3-2. For a particular load step, the elastic-plastic and creep response is a summation of the elastic-plastic response due to ΔT and the creep response over the range of Δt.

In order to illustrate the fundamental concepts of the approach proposed here, a one-dimensional four-bar model is utilized as schematically detailed in Fig. 3-3. The assumed stress-free state of the composite at consolidation temperature, T_c, is shown in Fig. 3-3(a) while Fig. 3-3(b) represents the relative amount of thermal strain increments (shrinkage), $\Delta \varepsilon_1^{(i),th}$, in each layer if subjected to a uniform finite temperature drop, $-\Delta T_1$ corresponding to the first load step. Superscript $i = 1, 2, 3, 4$ denotes the outermost composite media, the matrix, the reaction zone and the fiber, respectively. Assuming that all layers are perfectly bonded at interfaces, the deformation compatibility requires that an isostrain condition exists in all layers giving rise to elastic stress increments, $\Delta \sigma_1^{(i),e}$ as illustrated in Fig. 3-3(c). These uniaxial stresses are compressive in the fiber and reaction zone thus making the layers as if compressed from their initial strain-free position to the common level A-A. However, the matrix layer and the composite media are elongated from their initial strain-free position to the same level A-A resulting in tensile stresses. The magnitude of the stresses depend on the values of CTE and elastic modulus of each layer. The difference between the strain level due to free thermal contraction for each layer and the strain at the constrained level A-A is termed the mechanical strain. The mechanical strain increments corresponding to each of the model layers, $\Delta \varepsilon_1^{(i),me}$ are represented as shaded areas in Fig. 3-3(b) with positive values lying below and negative values above the level A-A.

If the effective stress in the matrix exceeded the yield limit of the matrix material at a particular temperature level, plastic deformation in the matrix is calculated using the deformation theory of plasticity [17]. Stresses in all layers are redistributed such that equilibrium and compatibility conditions are satisfied. The new stress and strain increments in all layers due to matrix plasticity are denoted as $\Delta \sigma^{(i),mp}$ and $\Delta \varepsilon^{(i),mp}$, respectively.

The important feature of the present model is the incorporation of the creep behavior of the matrix and the surrounding equivalent composite media into the stress analysis. This concept can also be explained by the four-bar representation shown in Fig. 3-3. The stresses induced in the matrix and the composite media due to temperature change, ΔT_1 will produce a relative constraint-free creep strain increment, $\Delta \varepsilon_1^{(i),cr}$ in the respective layer over the proceeding time duration, Δt_1 (see Fig. 3-3(d)). The existence of non-creeping phases (the reaction zone and the fiber) and perfect bonding at layer interfaces will restrain the creep deformation in both the matrix and the equivalent composite media, resulting in stress redistribution in all layers. These creep-related stress increments are denoted as $\sigma_1^{(i),mc}$ (see Fig.3-3(e)). The net stress developed for the first load step is taken as the summation of the stress increments, $\Delta \sigma^{(i),e}$ or $\Delta \sigma^{(i),mp}$, generated by restriction imposed on free thermal contraction of each layer, and the stress increments, $\Delta \sigma^{(i),mc}$, induced by constrained creep deformation of the matrix and the equivalent composite media. Since the creep

56

stress increments in the matrix and equivalent composite media are compressive, the net stress increments in these layers are always less than that calculated for the elastic-plastic case.

The concepts discussed above are identical for subsequent load steps. For the kth load step, elastic calculation is first performed to obtain the elastic stress increments, $\Delta\sigma_k^{(i),e}$, corresponding to the current temperature change, ΔT_k. The elastic stress increments are then added to the total stress level in the matrix up to the last load step and the value is compared with the yield limit at the current temperature. If the yield criterion is satisfied, the plasticity analysis is executed and the stresses in all phases are redistributed resulting in the stress increments, $\Delta\sigma_k^{(i),mp}$. The total stresses acting in the matrix and the equivalent composite media may cause constraint-free creep deformation during the time duration, Δt_k. However, restriction imposed on the creep deformation by the elastic reaction zone and fiber, and perfect bonding at layer interfaces result in stress increments, $\Delta\sigma^{(i),mc}$ in all layers. At the end of the kth load step, the total stress is the sum of the accumulated stresses from all previous load steps, stress increment due to temperature change and stress increment due to creep flow restriction imposed in the current load step, i.e.

$$\sigma_k^{(i)} = \sigma_{k-1}^{(i)} + \Delta\sigma_k^{(i),mp} + \Delta\sigma_k^{(i),mc} \tag{1}$$

The simultaneous evolution of the corresponding radial and hoop stress components in the complex stress state of MMC are analogous to the axial component described above. However, the relative magnitudes of these transverse stresses are also influenced by the Poisson's ratio effects in all the phases.

3.3 FORMULATIONS

A cylindrical coordinate system with the radial, hoop, and axial coordinates denoted as r, θ, and z, respectively is shown in Fig. 3-1(a). Due to the axisymmetry of the model, the shear stress and shear strain components are zero. Neglecting body forces, the equilibrium equations for the ith layer can be written as:

$$\frac{\partial\sigma_{rr}^{(i)}}{\partial r} + \frac{\sigma_{rr}^{(i)} - \sigma_{\theta\theta}^{(i)}}{r} = 0 \quad , \quad \frac{\partial\sigma_{zz}^{(i)}}{\partial z} = 0 \tag{2}$$

It is assumed that the total strain in i^{th} layer can be decomposed into elastic, $\varepsilon^{(i),e}$, thermal, $\varepsilon^{(i),th}$, plastic, $\varepsilon^{(i),p}$, and creep, $\varepsilon^{(i),cr}$, components such that

$$\varepsilon_{rr}^{(i)} = \varepsilon_{rr}^{(i),e} + \varepsilon_{rr}^{(i),th} + \varepsilon_{rr}^{(i),p} + \varepsilon_{rr}^{(i),cr}$$

$$\varepsilon_{\theta\theta}^{(i)} = \varepsilon_{\theta\theta}^{(i),e} + \varepsilon_{\theta\theta}^{(i),th} + \varepsilon_{\theta\theta}^{(i),p} + \varepsilon_{\theta\theta}^{(i),cr} \tag{3}$$

$$\varepsilon_{zz}^{(i)} = \varepsilon_{zz}^{(i),e} + \varepsilon_{zz}^{(i),th} + \varepsilon_{zz}^{(i),p} + \varepsilon_{zz}^{(i),cr}$$

The constitutive relations for isotropic material behavior in generalized plane strain conditions can be written as:

$$\sigma_{rr}^{(i)} = K^{(i)} \left[(1-v^{(i)})(\varepsilon_{rr}^{(i)} - \varepsilon_{rr}^{(i),p} - \varepsilon_{rr}^{(i),cr}) + v^{(i)}(\varepsilon_{\theta\theta}^{(i)} - \varepsilon_{\theta\theta}^{(i),p} - \varepsilon_{\theta\theta}^{(i),cr}) \right.$$

$$\left. + v^{(i)}(\varepsilon_{zz}^{(i)} - \varepsilon_{zz}^{(i),p} - \varepsilon_{z,z}^{(i),cr}) - (1+v^{(i)})\varepsilon^{(i),th} \right]$$

$$\sigma_{\theta\theta}^{(i)} = K^{(i)} \left[(1-v^{(i)})(\varepsilon_{\theta\theta}^{(i)} - \varepsilon_{\theta\theta}^{(i),p} - \varepsilon_{\theta\theta}^{(i),cr}) + v^{(i)}(\varepsilon_{zz}^{(i)} - \varepsilon_{zz}^{(i),p} - \varepsilon_{zz}^{(i),cr}) \right. \tag{4}$$

$$\left. + v^{(i)}(\varepsilon_{rr}^{(i)} - \varepsilon_{rr}^{(i),p} - \varepsilon_{r,r}^{(i),cr}) - (1+v^{(i)})\varepsilon^{(i),th} \right]$$

$$\sigma_{zz}^{(i)} = K^{(i)} \left[(1-v^{(i)})(\varepsilon_{zz}^{(i)} - \varepsilon_{zz}^{(i),p} - \varepsilon_{zz}^{(i),cr}) + v^{(i)}(\varepsilon_{rr}^{(i)} - \varepsilon_{rr}^{(i),p} - \varepsilon_{rr}^{(i),cr}) \right.$$

$$\left. + v^{(i)}(\varepsilon_{\theta\theta}^{(i)} - \varepsilon_{\theta\theta}^{(i),p} - \varepsilon_{\theta\theta}^{(i),cr}) - (1+v^{(i)})\varepsilon^{(i),th} \right]$$

where the constant $K^{(i)}$ is defined as:

$$K^{(i)} = \frac{E^{(i)}}{(1+v^{(i)})(1-2v^{(i)})} \tag{5}$$

and $E^{(i)}$ is the elastic modulus, $v^{(i)}$ is the Poisson's ratio, $\varepsilon_{rr}^{(i),p}$, $\varepsilon_{\theta\theta}^{(i),p}$ and $\varepsilon_{zz}^{(i),p}$ are the radial, hoop and axial components, respectively of the plastic strain, while $\varepsilon_{rr}^{(i),cr}$, $\varepsilon_{\theta\theta}^{(i),cr}$ and $\varepsilon_{zz}^{(i),cr}$ are the radial, hoop and axial components, respectively of the creep strain of the constituent phases. The thermal strain, $\varepsilon^{(i),th}$, is defined as:

$$\varepsilon^{(i),th} = \int_{T_0}^{T} \alpha^{(i)} dT \tag{6}$$

where $\alpha^{(i)}$ is the CTE of ith layer, T_0 is the reference temperature and T is the current temperature.

Due to the axial symmetry of the model configuration, the radial and axial displacements in each layer can be expressed as functions of r and z, respectively while the hoop displacement component is zero, i.e.

$$u_r^{(i)} = u^{(i)}(r) \quad , \quad u_\theta^{(i)} = 0 \quad , \quad u_z^{(i)} = w^{(i)}(z) \tag{7}$$

The non-zero strain-displacement relations could then be obtained using the displacement field which, when used in the constitutive relations, eqs. (4), would result in the governing equations for elastic-plastic-creep behavior of MMC as follows:

$$r^2 \frac{d^2 u^{(i)}}{dr^2} + r \frac{d u^{(i)}}{dr} - u^{(i)} = \Phi^{(i)}(r) \quad , \quad \frac{d^2 w^{(i)}}{dz^2} = 0 \tag{8}$$

where $\Phi^{(i)}(r)$ is defined as:

$$\phi^{(i)}(r) = r\left[\frac{1-2v^{(i)}}{1-v^{(i)}}\left(\varepsilon^{(i),P_{rr}} + \varepsilon^{(i),cr_{rr}}\right) + r\frac{d}{dr}\left(\varepsilon^{(i),P_{rr}} + \varepsilon^{(i),cr_{rr}}\right)\right.$$

$$-\frac{1-2v^{(i)}}{1-v^{(i)}}\left(\varepsilon^{(i),P_{\theta\theta}} + \varepsilon^{(i),cr_{\theta\theta}}\right) + r\frac{v^{(i)}}{1-v^{(i)}}\frac{d}{dr}\left(\varepsilon^{(i),P_{\theta\theta}} + \varepsilon^{(i),cr_{\theta\theta}}\right) \tag{9}$$

$$\left. + r\frac{v^{(i)}}{1-v^{(i)}}\frac{d}{dr}\left(\varepsilon^{(i),P_{zz}} + \varepsilon^{(i),cr_{zz}}\right)\right]$$

It is noted that $\Phi^{(i)}(r)$ consists of plastic strain terms pertaining to the matrix and creep strain terms pertaining to both the matrix and the outermost composite media. Consequently, for a purely elastic loading, the function, $\Phi^{(i)}(r)$ is reduced to zero. The form of $\Phi^{(i)}(r)$ used in this analysis will be discussed in detail in the creep analysis part of this section.

The boundary conditions for the present study under the assumption that no external applied loading exist, are specified as follows:

(a) The continuity requires that both radial displacements and stresses at all layer interfaces be continuous.

(b) Since there is no external radial load at the outermost surface, therefore:

$$\text{at } r = r_1 \text{ , } \sigma_{rr}^{(1)} = 0 \tag{10}$$

(c) In the absence of external axial load, the axial forces in each layer due to thermal loading are equilibrated in the average sense, i.e.

$$\int_0^{r_4}\sigma_{zz}^{(4)}r\,dr + \int_{r_4}^{r_3}\sigma_{zz}^{(3)}r\,dr + \int_{r_3}^{r_2}\sigma_{zz}^{(2)}r\,dr + \int_{r_2}^{r_1}\sigma_{zz}^{(1)}r\,dr = 0 \tag{11}$$

In addition, under the assumption of perfect bonding at layer interfaces, the isostrain condition is applied to the total strains for all layers.

3.3.1 Elastic-Plastic Analysis

As discussed above, the cooling and heating paths are discretized into load steps each of which consists of a temperature increment, ΔT followed by a time increment, Δt. The analysis begins with a purely elastic formulation due to the temperature increment, so that the function $\Phi^{(i)}(r)$ diminishes and eq. (8) is reduced to

$$r^2\frac{d^2u^{(i)}}{dr^2} + r\frac{du^{(i)}}{dr} - u^{(i)} = 0 \quad , \quad \frac{d^2w^{(i)}}{dz^2} = 0 \tag{12}$$

The above homogeneous equations have the following general solutions for the radial and axial displacement, respectively,

$$u^{(i)} = A_i r + \frac{B_i}{r} \quad , \quad w^{(i)} = L_i z + P_i \tag{13}$$

59

where A_i, B_i, L_i and P_i are unknown constants.

Since the displacement is finite at the center of the fiber, where $r = 0$, i.e. $|u^{(4)}(0)| < \infty$, thus $B_4 = 0$. It is also noted that P_i in the above equations account for rigid body motion in axial direction, thus P_i can be set to zero without loss of generality. In addition, application of the boundary conditions for axial displacement components results in

$$L_1 = L_2 = L_3 = L_4 = L \tag{14}$$

The elastic strain field can now be expressed as:

$$\varepsilon_{rr}^{(i),e} = A_i - \frac{B_i}{r^2} \quad , \quad \varepsilon_{\theta\theta}^{(i),e} = A_i + \frac{B_i}{r^2} \quad , \quad \varepsilon_{zz}^{(i),e} = L \tag{15}$$

and the corresponding stress field for the elastic case are given as:

$$\sigma_{rr}^{(i),e} = K^{(i)} \left[A_i - (1 - 2v^{(i)}) \frac{B_i}{r^2} + v^{(i)}L - (1 + v^{(i)})\varepsilon^{(i),th} \right]$$

$$\sigma_{\theta\theta}^{(i),e} = K^{(i)} \left[A_i + (1 - 2v^{(i)}) \frac{B_i}{r^2} + v^{(i)}L - (1 + v^{(i)})\varepsilon^{(i),th} \right] \tag{16}$$

$$\sigma_{zz}^{(i),e} = K^{(i)} \left[2v^{(i)}A_i + (1 - v^{(i)})L - (1 + v^{(i)})\varepsilon^{(i),th} \right]$$

The unknown constants in eqs. (13) ~ (16) are determined by the boundary conditions. Applying these conditions to eqs. (13) and (16) results in a set of eight simultaneous equations which should be solved for the determination of the constants $A_1 \sim A_4$, $B_1 \sim B_3$ and L. These equations can be arranged in the following matrix form:

$$\mathbf{Ac} = \mathbf{b} \tag{17}$$

where $\mathbf{A}$ is an 8 x 8 matrix termed the stiffness matrix consisting of model geometry and mechanical properties of all constituents of the composite, $\mathbf{b}$ is the thermal loading vector and $\mathbf{c}$ is the vector of unknown constants. Once the unknown vector $\mathbf{c}$ is solved from eq. (17), the elastic stress and strain states in the composite are then established.

The thermal stresses developed in the matrix during cool down may be high enough to initiate plastic yielding in the monolithic matrix material. Matrix plasticity is assumed to be a time-independent process and its effect can be treated separately from the time-dependent creep response of the matrix material. The governing equation for the elastic-plastic deformation of the composite is then given by eqs. (8) but without the creep strain terms in the loading function, $\Phi^{(i)}(r)$ given by eq. (9). One solution approach requires the knowledge of plastic strain distribution across the matrix layer. The assumption on this distribution will dictate the form and order of the displacement field in each layer due to the occurrence of matrix plasticity. This approach results in a similar stiffness equation, eq. (17) but with a new load vector, $\mathbf{f}$, for thermal and matrix plasticity effects.

An alternate solution approach which modifies the stiffness matrix instead of the load vector of eq. (17), to account for strain hardening of the matrix material is employed in the present analysis. This approach utilizes the deformation theory of plasticity in conjunction with the von Mises yield criterion and the isotropic hardening rule. Matrix yielding commences when the effective stress, $\bar{\sigma}$ is equal to the temperature-dependent yield limit of the matrix material, $\sigma_{ys}(T)$. Here, $\bar{\sigma}$ is defined as:

$$\bar{\sigma} = \frac{1}{\sqrt{2}}\left[(\sigma_{rr}-\sigma_{\theta\theta})^2+(\sigma_{\theta\theta}-\sigma_{zz})^2+(\sigma_{zz}-\sigma_{rr})^2\right]^{\frac{1}{2}} \tag{18}$$

The constitutive relations for total strain increment (elastic plus plastic) are employed based on the work of Hecker [4,17], and are given as:

$$d\varepsilon_{rr} = \frac{1}{H(T)}\left[d\sigma_{rr}-\eta(d\sigma_{\theta\theta}+d\sigma_{zz})\right]$$

$$d\varepsilon_{\theta\theta} = \frac{1}{H(T)}\left[d\sigma_{\theta\theta}-\eta(d\sigma_{rr}+d\sigma_{zz})\right] \tag{19}$$

$$d\varepsilon_{zz} = \frac{1}{H(T)}\left[d\sigma_{zz}-\eta(d\sigma_{rr}+d\sigma_{\theta\theta})\right]$$

where $H(T)$ is the plastic modulus of the uniaxial tensile stress-strain curve of the matrix and η is the effective Poisson's ratio which is defined for a small increment of effective total strain, $d\bar{\varepsilon}$, as:

$$\eta = 0.5 - (0.5-\nu)\frac{H(T)}{E(T)} \tag{20}$$

The effective total strain increment is defined as:

$$d\bar{\varepsilon} = \frac{\sqrt{2}}{2(1+\eta)}\left[(d\varepsilon_{rr}-d\varepsilon_{\theta\theta})^2+(d\varepsilon_{\theta\theta}-d\varepsilon_{zz})^2+(d\varepsilon_{zz}-d\varepsilon_{rr})^2\right]^{\frac{1}{2}} \tag{21}$$

It is assumed that the effective stress-strain curve of the matrix material in the region the yield limit can be represented by

$$\bar{\sigma} = k(T)\bar{\varepsilon}^{\frac{1}{n(T)}} \tag{22}$$

where $k(T)$ and $n(T)$ are material parameters varying with temperature T. The slope of the curve represented by this equation is equal to the plastic modulus, $H(T)$, i.e.

$$\frac{d\bar{\sigma}}{d\bar{\varepsilon}} = \frac{\bar{\sigma}}{n(T)\bar{\varepsilon}} = H(T) \tag{23}$$

If plastic deformation occurs in the matrix, the stresses in all the four layers must be redistributed such that equilibrium and compatibility conditions are always satisfied. The stiffness matrix in eq. (19) is modified by substituting the plastic modulus, $H(T)$ and the effective Poisson's ratio, η for the elastic modulus, $E(T)$ and Poisson's ratio, ν, respectively. Consequently, the stiffness equation which accounts for matrix plasticity can be written as:

$$\mathbf{Mc} = \mathbf{b} \tag{24}$$

It is noted that in elastic region $H(T)$ is equivalent to $E(T)$ and η reduces to ν, so that eq. (19) resembles the Hooke's law. Since the equilibrium equations, the compatibility equations and the boundary conditions are independent of the state of the material, therefore, the plasticity formulation is identical to the elastic case with the modified stiffness matrix, $\mathbf{M}$ in eq. (24). The resulting stress components, $\Delta\sigma_{ij}^{(i),mp}$ and strain components, $\Delta\varepsilon_{ij}^{(i),mp}$ due to matrix yielding are given by eqs. (16) and (15), respectively.

61

3.3.2 Creep Analysis

The effect of creep deformation in both the monolithic matrix and the surrounding effective composite media on the residual stress and strain fields in the composite is now considered. It is assumed that the creep behavior of both layers in the primary and secondary stages of creep can be represented by the Bailey-Norton law as:

$$\varepsilon^{cr} = B \, \sigma^m \, t^n \tag{25}$$

where ε^{cr} is the creep strain occurring in the material under uniaxial stress, σ, over a time duration t. The superscript i is omitted in the following derivation for convenience. Parameters B, m and n are material parameters. Based on the fit of experimental data, parameters B and m are generally taken to be functions of temperature while n is viewed as temperature-independent (e.g. [18,19]). Here, B is assumed to follow a general expression of Arrhenius-type:

$$B = b_0 \exp\left(-\frac{Q}{RT} \right) \tag{26}$$

where b_0 is a constant, Q is the activation energy for creep, R is the gas constant and T is temperature in Kelvin scale. Extension of uniaxial case to multiaxial case is made by introducing effective quantities such that

$$\bar{\varepsilon}^{cr} = B \, \bar{\sigma}^{m(T)} \, t^n \tag{27}$$

where $\bar{\sigma}$ is the effective stress defined in eq. (18).

The path-dependent creep process is incorporated into the model through the use of the flow rate which describes the creep strain components, $\dot{\varepsilon}_{ij}^{cr}$, in terms of the stress deviator tensor, S_{ij}, i.e.

$$\dot{\varepsilon}_{ij}^{cr} = \lambda S_{ij} \tag{28}$$

The use of the deviatoric stress components, S_{ij} in the above equation ensures that creep deformation is independent of the hydrostatic state of stress as have been observed experimentally. In this equation, the proportionality factor, λ, is defined as:

$$\lambda = \frac{3}{2\bar{\sigma}} \frac{d\bar{\varepsilon}^{cr}}{dt} = n \, B \, \bar{\sigma}^{m(T)} t^{n-1} \tag{29}$$

The strain history prediction in this analysis follows the "strain hardening" formulation in which the creep strain rate in a variable stress situation depends on the stress, strain and temperature. Eliminating time from eq.(29) with the aid of eq.(25), the flow rule can be rewritten as:

$$\dot{\varepsilon}_{ij}^{cr} = \frac{3}{2} n \, B^{\frac{1}{n}} \bar{\sigma}^{-\frac{m}{n}} \left(\bar{\varepsilon}^{cr} \right)^{\frac{n-1}{n}} \frac{S_{ij}}{\bar{\sigma}} = \frac{3 \, F}{2 \bar{\sigma}} S_{ij} \tag{30}$$

where F is a scalar defined as:

$$F = n \, B^{\frac{1}{n}} \bar{\sigma}^{-\frac{m}{n}} (\bar{\varepsilon}^{cr})^{\frac{n-1}{n}} \tag{31}$$

It can be shown using eqs. (27) and (29) that:

$$\bar{\varepsilon}^{cr} = \left(\frac{2}{3}\,\dot{\varepsilon}_{ij}^{cr}\,\dot{\varepsilon}_{ij}^{cr}\right)^{\frac{1}{2}} = F \qquad (32)$$

thus, the flow rule can now be expressed in differential form as:

$$d\varepsilon_{ij}^{cr} = \frac{3}{2}\frac{d\bar{\varepsilon}^{cr}}{\bar{\sigma}}S_{ij} \qquad (33)$$

This equation can be written explicitly for the three components of the constraint-free creep strain increments as:

$$\Delta\varepsilon_{rr}^{cr} = \frac{\Delta\bar{\varepsilon}^{cr}}{2\bar{\sigma}}(2\sigma_{rr}-\sigma_{\theta\theta}-\sigma_{zz})$$

$$\Delta\varepsilon_{\theta\theta}^{cr} = \frac{\Delta\bar{\varepsilon}^{cr}}{2\bar{\sigma}}(2\sigma_{\theta\theta}-\sigma_{rr}-\sigma_{zz}) \qquad (34)$$

$$\Delta\varepsilon_{zz}^{cr} = \frac{\Delta\bar{\varepsilon}^{cr}}{2\bar{\sigma}}(2\sigma_{zz}-\sigma_{rr}-\sigma_{\theta\theta})$$

where the effective creep strain increment, $\Delta\bar{\varepsilon}^{cr}$, occurring over the time increment, Δt is approximated from uniaxial creep behavior given by eq. (27) as:

$$\Delta\bar{\varepsilon}^{cr} = B\,\bar{\sigma}^{m(T)}\Delta t^{\,n} \qquad (35)$$

The axisymmetric creep strain components are represented by the effective value defined as:

$$\bar{\varepsilon}^{cr} = \frac{\sqrt{2}}{3}\left[\left(\varepsilon_{rr}^{cr}-\varepsilon_{\theta\theta}^{cr}\right)^2+\left(\varepsilon_{\theta\theta}^{cr}-\varepsilon_{zz}^{cr}\right)^2+\left(\varepsilon_{zz}^{cr}-\varepsilon_{rr}^{cr}\right)^2\right]^{\frac{1}{2}} \qquad (36)$$

Constraint-free creep deformation in the matrix and the composite media, as described above, is coupled with the existence of perfect bonding at layer interfaces and the relative inextensibility of the reaction zone and the fiber. Consideration of creep behavior of the composite, therefore, results in inhomogeneous Euler equation as described by eq. (8) but without the plastic strain terms in the loading function, $\Phi^{(i)}(r)$ of eq. (9). The solution for the displacement field is obtained by assuming that the radial variation of the constraint-free creep strain increments in the matrix and the outermost equivalent composite media can each be represented as a third order polynomial as follows:

$$\Delta\varepsilon_{rr}^{(i),cr} = a_1^{(i)}+a_2^{(i)}r+a_3^{(i)}r^2+a_4^{(i)}r^3$$

$$\Delta\varepsilon_{\theta\theta}^{(i),cr} = b_1^{(i)}+b_2^{(i)}r+b_3^{(i)}r^2+b_4^{(i)}r^3 \qquad (37)$$

$$\Delta\varepsilon_{zz}^{(i),cr} = c_1^{(i)}+c_2^{(i)}r+c_3^{(i)}r^2+c_4^{(i)}r^3$$

where the coefficients $a_1^{(i)}\sim a_4^{(i)}$, $b_1^{(i)}\sim b_4^{(i)}$, and $c_1^{(i)}\sim c_4^{(i)}$ (i = 1,2) are obtained from least-squared curve fit procedures. This assumption dictates the form and order of the particular solution for the displacement field in the creeping layers. Upon substitution of eqs. (37) into eq. (9), the governing differential equations for the deformation of the composite in the case of elastic-plastic-creep can

63

be written as:

$$r^2 \frac{d^2 u^{(i)}}{dr^2} + r \frac{d u^{(i)}}{dr} - u^{(i)} = \phi_1^{(i)} r + \phi_2^{(i)} r^2 + \phi_3^{(i)} r^3 + \phi_4^{(i)} r^4 \quad , \quad \frac{dw^{(i)}}{dz} = 0 \tag{38}$$

where the coefficients, $\phi_1^{(i)} \sim \phi_4^{(i)}$ consists of material constants for the ith layer. For the elastic fiber and interphase zone, these coefficients are zero. The solution of the above equations which corresponds to the displacement field with creep deformation in the matrix and the equivalent composite media are obtained as:

$$u^{(i),mc} = A_i r + \frac{B_i}{r} + \frac{\phi_1^{(i)}}{2} \ln r + \frac{\phi_2^{(i)}}{3} r^2 + \frac{\phi_3^{(i)}}{8} r^3 + \frac{\phi_4^{(i)}}{15} r^4 \quad , \quad w^{(i)} = Lz \tag{39}$$

The stress field in the composite for the elastic-plastic-creep case accumulate incrementally throughout the cooling process. The expressions for this stress field are obtained with the aid of the strain-displacement relations and the above displacement field as follows:

$$\sigma_{rr}^{(i),mc} = K^{(i)} \Bigg[A_i - (1 - 2v^{(i)}) \frac{B_i}{r^2} + v^{(i)} L - (1 + v^{(i)}) \varepsilon^{(i),th}$$

$$+ (1 - v^{(i)}) \frac{\phi_1^{(i)}}{2} + \frac{\phi_1^{(i)}}{2} \ln r + (2 - v^{(i)}) \frac{\phi_2^{(i)}}{3} r + (3 - 2v^{(i)}) \frac{\phi_3^{(i)}}{8} r^2$$

$$+ (4 - 3v^{(i)}) \frac{\phi_4^{(i)}}{15} r^3 - (1 - v^{(i)}) \varepsilon_{rr}^{(i),mc} - v^{(i)} \varepsilon_{\theta\theta}^{(i),mc} - v^{(i)} \varepsilon_{zz}^{(i),mc} \Bigg]$$

$$\sigma_{\theta\theta}^{(i),mc} = K^{(i)} \Bigg[A_i + (1 - 2v^{(i)}) \frac{B_i}{r^2} + v^{(i)} L - (1 + v^{(i)}) \varepsilon^{(i),th}$$

$$+ v^{(i)} \frac{\phi_1^{(i)}}{2} + \frac{\phi_1^{(i)}}{2} \ln r + (1 + v^{(i)}) \frac{\phi_2^{(i)}}{3} r + (1 + 2v^{(i)}) \frac{\phi_3^{(i)}}{8} r^2 \tag{40}$$

$$+ (1 + 3v^{(i)}) \frac{\phi_4^{(i)}}{15} r^3 - (1 - v^{(i)}) \varepsilon_{\theta\theta}^{(i),mc} - v^{(i)} \varepsilon_{rr}^{(i),mc} - v^{(i)} \varepsilon_{zz}^{(i),mc} \Bigg]$$

$$\sigma_{zz}^{(i),mc} = K^{(i)} \Bigg[2v^{(i)} A_i + (1 - v^{(i)}) L - (1 + v^{(i)}) \varepsilon^{(i),th} + v^{(i)} \frac{\phi_1^{(i)}}{2} + v^{(i)} \phi_1^{(i)} \ln r + v^{(i)} \phi_2^{(i)} r$$

$$+ v^{(i)} \frac{\phi_3^{(i)}}{2} r^2 + v^{(i)} \frac{\phi_4^{(i)}}{3} r^3 - (1 - v^{(i)}) \varepsilon_{zz}^{(i),mc} - v^{(i)} \varepsilon_{rr}^{(i),mc} - v^{(i)} \varepsilon_{\theta\theta}^{(i),mc} \Bigg]$$

Applying the same boundary conditions specified earlier results in a similar set of eight simultaneous equations as arranged in eq. (17), but with additional terms in the load vector, **d** resulting from creep contributions, i.e.

64

$$\mathbf{A} \, \mathbf{c} = \mathbf{d} \qquad\qquad (41)$$

This equation should be solved for the unknown constants, $A_1 \sim A_4$, $B_1 \sim B_4$ and L appearing in the vector **c**.

3.4 SOLUTION PROCEDURES

The algorithm for the determination of thermal stresses in MMC is shown in Fig. 3-4. It initially reads the model geometry, cooling rate and temperature dependent material data from a tabular input file. Starting with an initial stress and strain free states at consolidation temperature, the first load step is initiated which consists of a negative temperature increment followed by a time step. The stiffness equation, eq. (17) is solved for elastic stress increments induced over the temperature drop. A yield limit is determined for the present temperature and compared with the effective stress in the matrix. If the effective stress is less than the yield limit, the procedure proceeds to calculate creep strain increments for the matrix and the outermost equivalent composite media. Otherwise, plasticity calculations are executed in which the plastic modulus, H(T), and the effective Poisson's ratio, η, are determined using the current values of the effective stress and strain in eq. (23) and eq. (20), respectively. They are substituted for the elastic modulus, E(T), and the Poisson's ratio, ν, respectively in the stiffness matrix of eq. (17). These equations are then solved for the new stress and strain increments in all layers due to matrix plasticity and the latter is compared with the previous value. If the difference is less than a prescribed value, plasticity calculations are completed. Otherwise, new values for H(T) and η are established and plasticity calculations are repeated until convergence of the incremental effective strain is achieved.

The procedure then performs the creep analysis of the composite over the proceeding time increment. During the first Δt step, the constraint-free creep strain increments for the matrix and the composite media are initially calculated using eqs. (34) with the previously calculated stress acting in the respective layers. The distribution of each component of the creep strain increment across the matrix layer and the equivalent composite media are fitted to polynomials as described by eqs. (37). The creep effect is accommodated in the load vector, **d** of eq. (41) and the resulting stiffness equation, is solved for the constrained deformation of all layers due to creep. Since temperature decreases and time proceeds simultaneously during the consolidation stage of the composite, employing the average of the stress increments from elastic-plastic calculation and the creep calculation should provide a better estimate of the constrained creep deformation. This is utilized in the second estimation of the creep strain increments, and the resulting stress increments due to constrained creep deformation in the matrix and the equivalent composite media are used in the next iteration. Convergence of the iterative process is achieved when the difference between the incremental creep strain in the matrix from the last two successive iterations are within a small prescribed value.

The stress and strain increments from both the elastic-plastic and the creep calculations are then summed to represent the total thermal stress and strain at the beginning of the next load step.

For any subsequent load step, the elastic stress increments occurring over the current temperature increment is summed with the previously accumulated thermal stress until the last load step. This (effective) stress is then used to determine the occurrence of plastic flow in the matrix at the current temperature. The sum of the stress increments from the elastic-plastic calculations and the previously accumulated thermal stress is used to provide the first estimate of the constraint-free

creep strain increment in the matrix and the equivalent composite media. Equation (41) is again solved to provide the constrained creep deformation in these layers and the resulting stress increments in all layers due to creep. The average of the resulting stress increments due to creep and the stress increments from elastic-plastic calculations are summed with the previously accumulated stress for the next estimate of the constraint-free creep strain. The iteration process continues until convergence is achieved.

The accumulated stress and strain values at the current temperature are written to output files. The next load step is then incremented and the process continues until room temperature is reached.

The history of the accumulated creep strain in both the matrix and the equivalent composite media, as mentioned before is based on the strain hardening creep formulation in which the creep strain rate is assumed to be a function of stress, strain and temperature. This history is schematically illustrated in Fig. 3-5 in terms of effective stress and strain values for the first two load steps. During the initial load step from consolidation temperature, constraint-free creep strain increment, $\Delta\bar{\varepsilon}_1^{cr}$, occurring over time increment Δt_1, is estimated using eqs. 33- 35 and indicated as open circle (point 1) on the creep curve corresponding to load condition $(\bar{\sigma}_1,T_1)$. Physical constraints imposed by the existence of perfectly bonded interfaces and non-creeping phases modify the magnitude of $\Delta\bar{\varepsilon}_1^{cr}$ to a lower value $\Delta\bar{\varepsilon}_1^{mc}$ (point 2). This latter strain must fall on the creep curve corresponding to current stress and temperature levels. This would then lead to the determination of point 3. In the second load step, as the stress increases to $\bar{\sigma}_2$, the end response of the load step, following the strain hardening concept, is shifted horizontally to point 4 which marks the onset of the creep flow of the unconstrained matrix and equivalent composite material along the creep curve corresponding to load condition $(\bar{\sigma}_2,T_2)$. Tracing this curve for the duration Δt_2 would define point 5. Again, this point under constrained deformation condition would be modified to point 7 along the path 5-6-7. The strain magnitude generated between the points 4 and 7 thus represents the actual $\Delta\bar{\varepsilon}_2^{mc}$ occurring during the second load step. This path 4-7 must be shifted horizontally to have its starting position initiating at point 3. This would then generate the curve 3-8 for which point 8 marks the starting position for the third load step. The total creep strain accumulated in the matrix at the end of the second load step, $\bar{\varepsilon}_2^{mc}$, is then the sum of $\Delta\bar{\varepsilon}_1^{mc}$ and $\Delta\bar{\varepsilon}_2^{mc}$. This procedure is repeated for all load steps between consolidation temperature and end temperature level.

The composite may be subjected to thermal fatigue in order to reduce the magnitude of the thermal residual stress induced during post-fabrication cool down. Throughout these processes, creep deformation is expected to progress.

3.5 SUMMARY AND CONCLUSIONS

In this section, a new micromechanical stress analysis approach has been proposed which considers time-dependent behavior of a continuous-fiber-reinforced MMC during post-fabrication cool down and subsequent thermal fatigue. A four-phase concentric cylinder model consisting of an embedded fiber and an interphase zone which behave elastically, while the matrix and the equivalent composite media may experience plasticity and creep was employed in the formulation. All the constituent phases of the composite model are assumed to be isotropic. The conceptual uniaxial four-bar model has illustrated that the deformation behavior of the composite can be isolated into time-independent and time-dependent deformation and treated separately for mathematical convenience. The former considers elastic-plastic deformation occurring over discrete temperature

66

change, while the latter emphasizes creep response of the matrix and the equivalent composite media over the corresponding duration of time. Both effects are then combined at the end of each discrete load step. The tensile thermal stress induced in the matrix due to mismatches of the CTEs of the matrix and other constituents of the composite is lowered through the evolution of the compressive stress set-up in the matrix due to constrained creep deformation at elevated temperature. The occurrence of matrix plasticity is treated using the deformation theory of plasticity with total strain increment (elastic plus plastic) in conjunction with the von Mises yield criterion. Strain hardening characteristics of the matrix material are represented by the tangent modulus of the stress-strain curve beyond the initial yield point and the corresponding effective Poisson's ratio. Constraint-free creep deformation of the matrix and the equivalent composite media is estimated using the Bailey-Norton law in the transient and steady-state stages of creep. An Arrhenius-type expression is used for the time-dependent creep coefficient of the creep law. Constrained creep deformation in the composite is calculated using the "stiffness" method with modified load vector resulting in stress redistribution in all layers due to creep. The creep strain history prediction followed the strain hardening formulation which assumed the creep strain rate to be dependent on stress, strain and temperature. The model has been used in a parametric study and the results will be discussed in the next section.

The present micromechanical analysis can be extended to predict the variation of stress and strain states in the fiber, the interphase zone and the matrix when subjected to thermo-mechanical loadings. External radial pressure and axial stress can be accommodated through the boundary conditions in eqs. (10) and (11), respectively. In addition, non-uniform temperature distribution across a layer can be specified by the temperature gradient through the right-hand side of the governing equation (8). This will result in additional terms in the load vector, **b** and **d** of eq. (17) and (41), respectively. Extension of the model to n-layers can be made with additional boundary conditions on the continuity of the radial displacements and radial stresses specified at each new interface. An additional pair of unknown constants and hence additional two new equations in the stiffness equation, eq. (41) are associated with each new layer.

3.6 REFERENCES

1.   Saigal, A., Kupperman, D. S. and Majumdar, 1992. Mat. Sc. Engng.,:59-66.

2.   Min, B. K., 1981. J. The Mechanics and Physics of Solids, 29:327-352.

3.   Min, B. K. and Crossman, F. W., 1982. Composite Materials: Testing and Design (Sixth Conference), ASTM STP 787, ed. by Daniel, I. M., American Society for Testing and Materials, :371-392.

4.   Hecker, S. S., Hamilton, C. H. and Ebert, L. J., 1970. J. Materials, JMLSA, 5,No.4:868-900.

5.   Uemura, M., Iyama, H. and Yamaguchi, Y., 1979. J. Thermal Stresses, 2:393-412.

6.   Mikata, Y. and Taya, M., 1985. J. Composite Materials, 19:554-578.

7.   Jayaraman, K. and Reifsnider, K. L., 1992. J. Composite Materials, 26,No.6:771-791.

8.   Yang, J. M. and Jeng, S. M., 1989. <u>J. Metals</u>, Nov.:56-59.

9.   Gundel, D. B. and Wawner, F. E., 1991. <u>Scripta Metallurgica et Materialia</u>, 25:437-441.

10.   Theocaris, P., 1985. <u>Advances in Polymers Science</u>, ed. by Kausch, H. H. and Zachmann, H. G., Springer-Verlag, Berlin, 66:149-187.

11.   Nairn, J. A., 1985. <u>Polymer Composites</u>, 6:123-130.

12.   Jansson, S. and Leckie, F. A., 1992. <u>J. Composite Materials</u>, 26:1474-1486.

13.   Hashin, Z. and Rosen, B. W., 1964. <u>J. Applied Mechanics</u>, 31:223-232.

14.   Christensen, R. M. and Lo, K. H., 1979. <u>J. The Mechanics and Physics of Solids</u>, 27:315-330.

15.   Min, B. K. and Crossman, F. W., 1982. <u>J. Composite Materials</u>, 16:188-203.

16.   Gayda, J., Gabb, T. P. and Freed, A. D., 1990. <u>Fundamental Relationships Between Microstructure and Properties of Metal Matrix Composites</u>, ed. by Liaw, P.K. and Gungor, M.N., The Mineral, Metal and Materials Society, Warrendale, PA:497-513.

17.   Hecker, S. S., Hamilton, C. H. and Ebert, L. J., 1969. <u>Metallurgica</u>, 3:793-798.

18.   Kraus, H., 1980. <u>Creep Analysis</u>, John Wiley and Sons, Inc., NY.

19.   Lemaitre, J. and Chaboche, L., 1990. <u>Mechanics of Solid Materials</u> (English Translation), Cambridge University Press, NY.
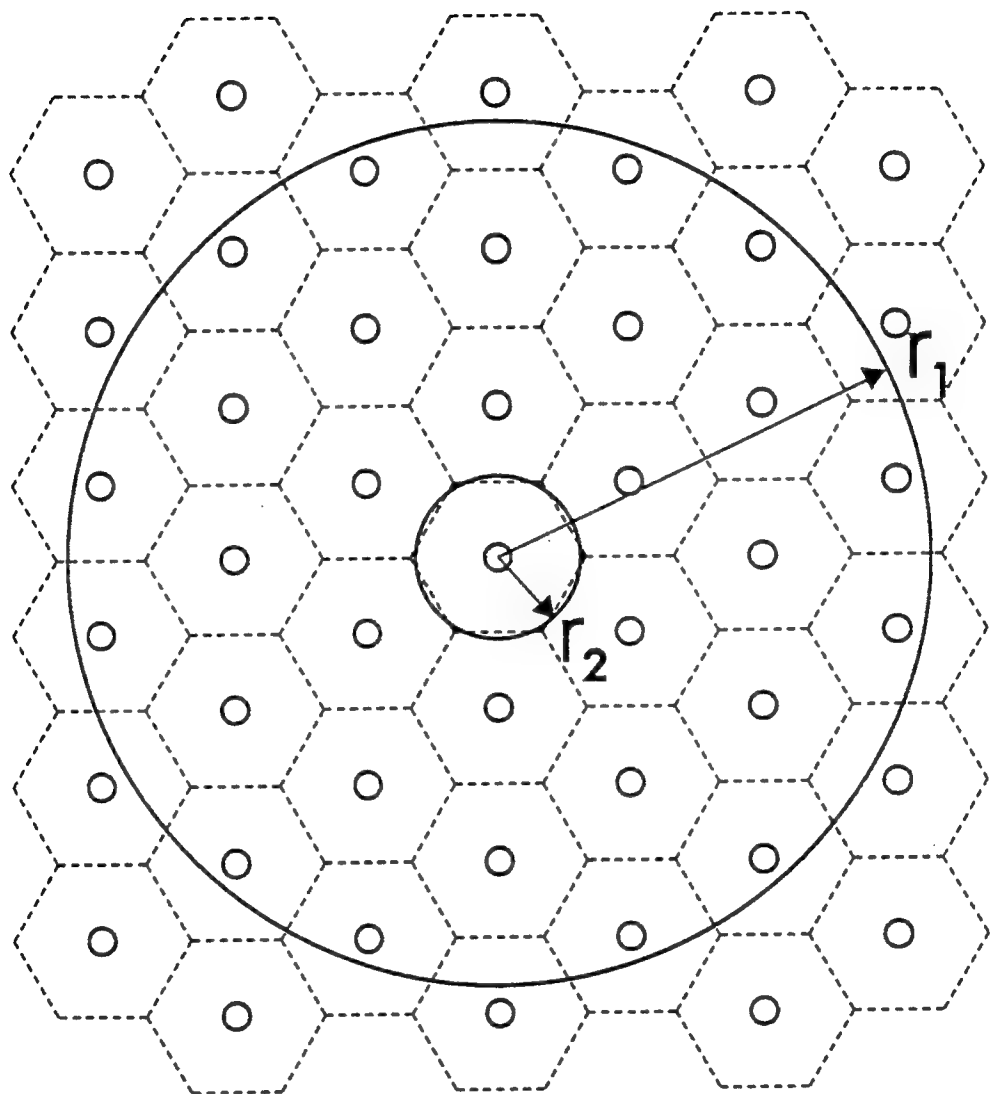
Fig. 3-1(a)   Selected configuration of a unit cell with surrounding composite material.
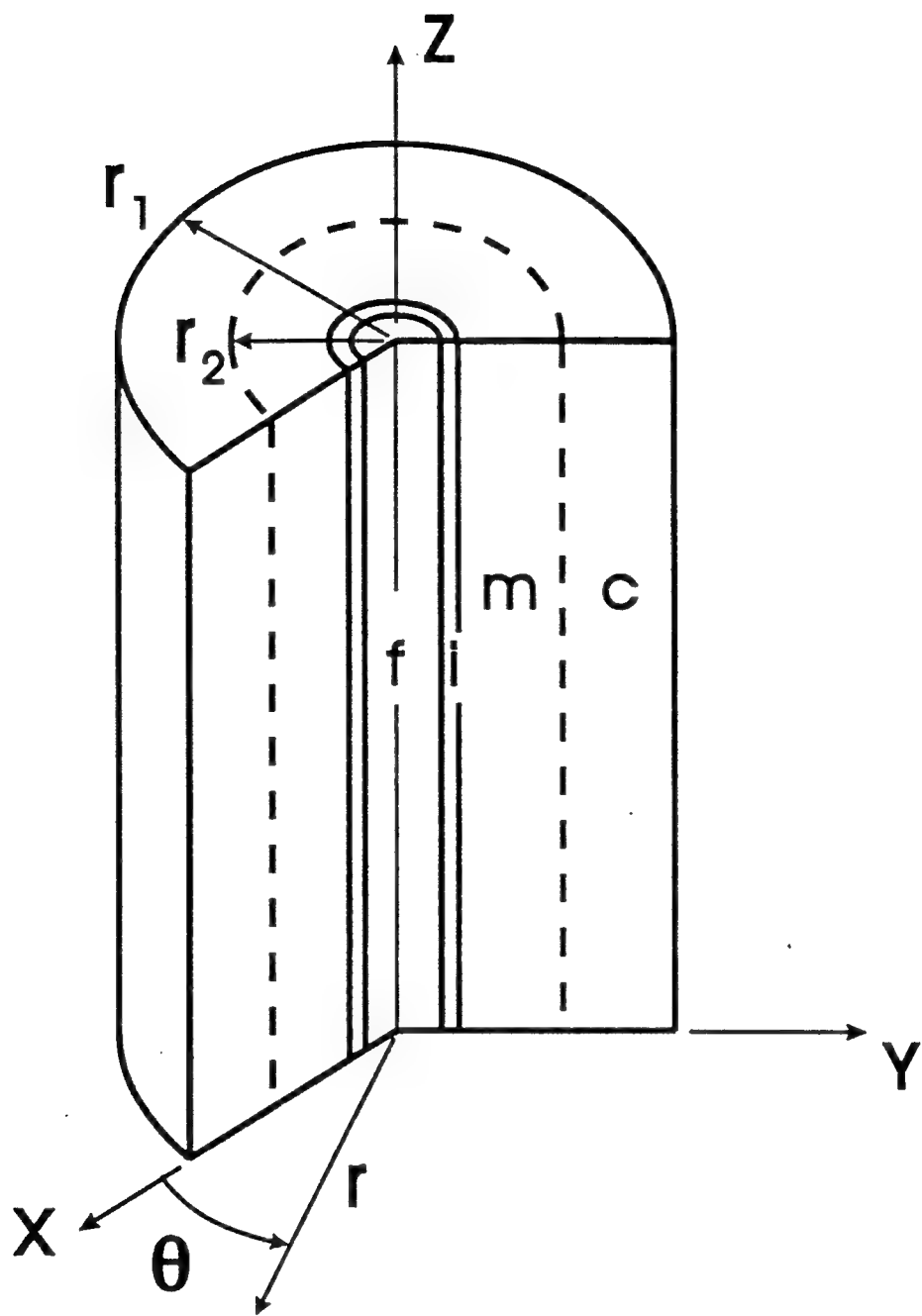
Fig. 3-1(b)   Cut-out section of the four-phase model.
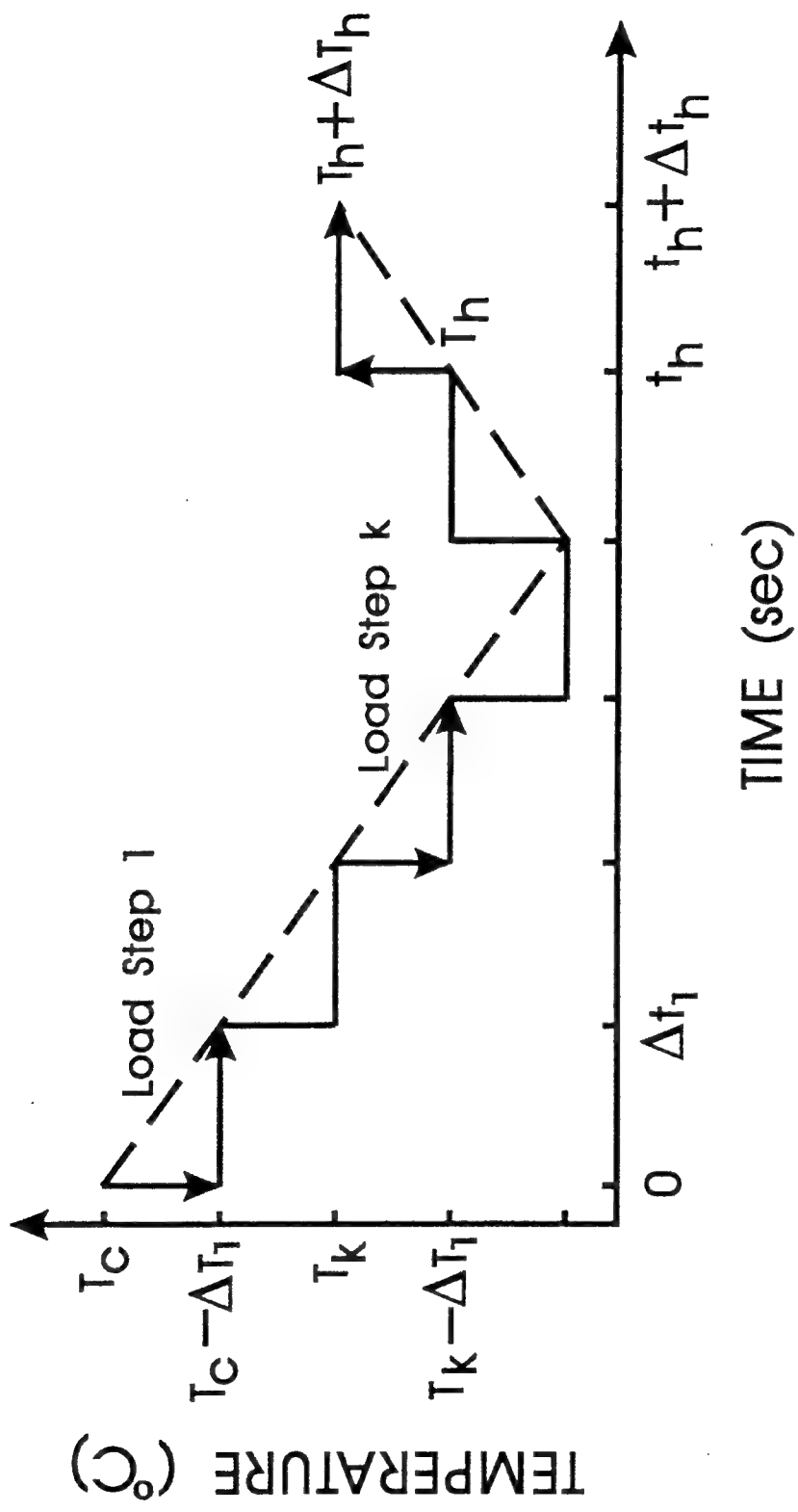
Fig. 3-2   Discretization of the cooling/heating path (no externally applied mechanical load).

71

REFERENCE LEVEL

$\Delta\sigma_1^{(ii),e}$

(c)

Thermal strain $(\Delta\varepsilon^{(i),th})$

Mechanical strain

(b)

A — A

REFERENCE STATE
AT T_c

(a)

REFERENCE LEVEL

$\Delta\sigma_1^{(ii)}$

Compression

Tension

(f)

$\Delta\sigma_1^{(ii)}, mc$

(e)

Unconstrained
Creep strain

(d)
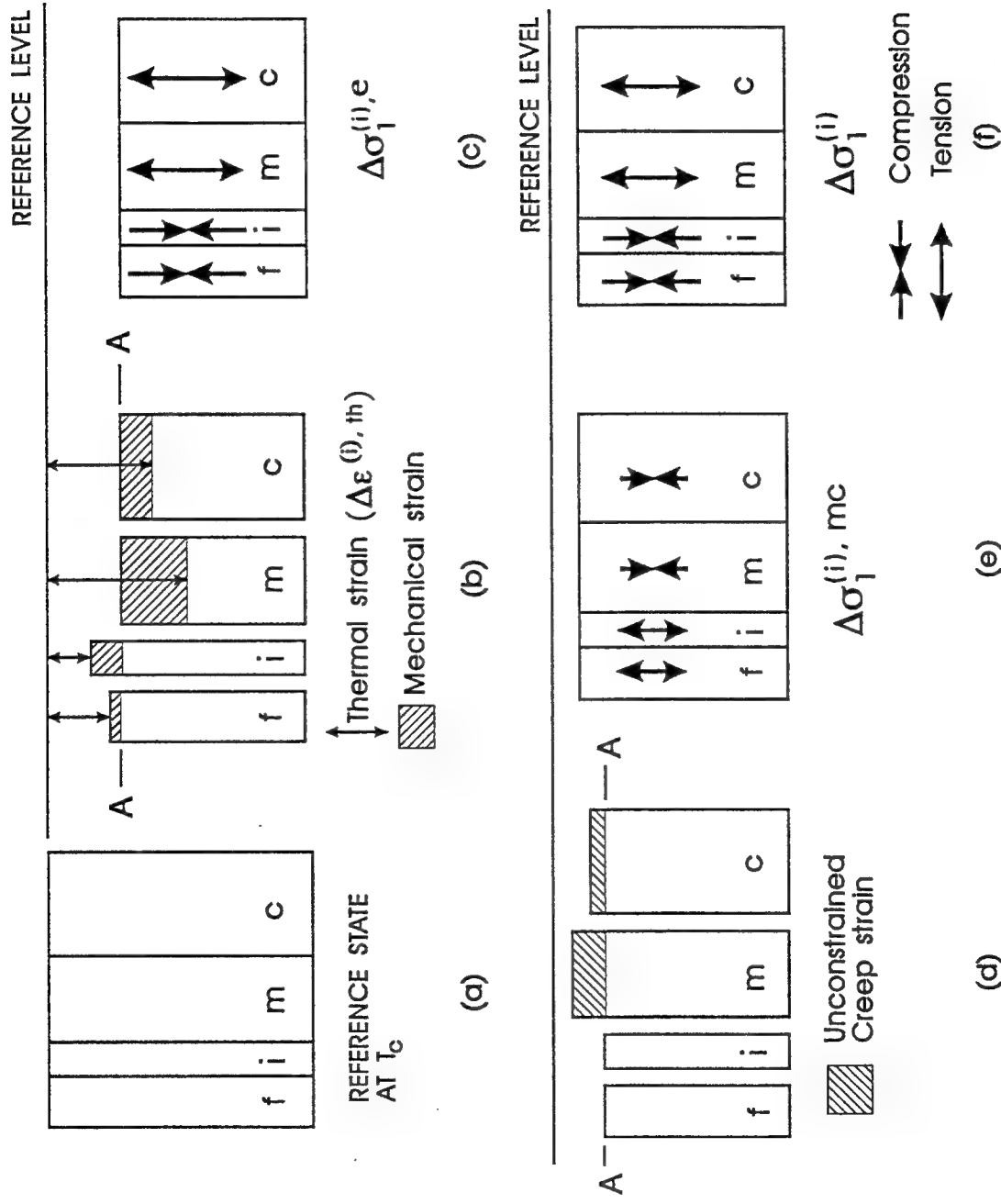
Fig. 3-3   (a) Reference state at consolidation. (b) Constraint-free thermal deformation. (c) Equilibrium conditions due to boundary constraints. (d) Constraint-free creep deformation. (e) Equilibrium conditions due to boundary constraints. (f) Final equilibrium conditions at the end of the first temperature-time step loading (sum of conditions at (c) and (e)).

72
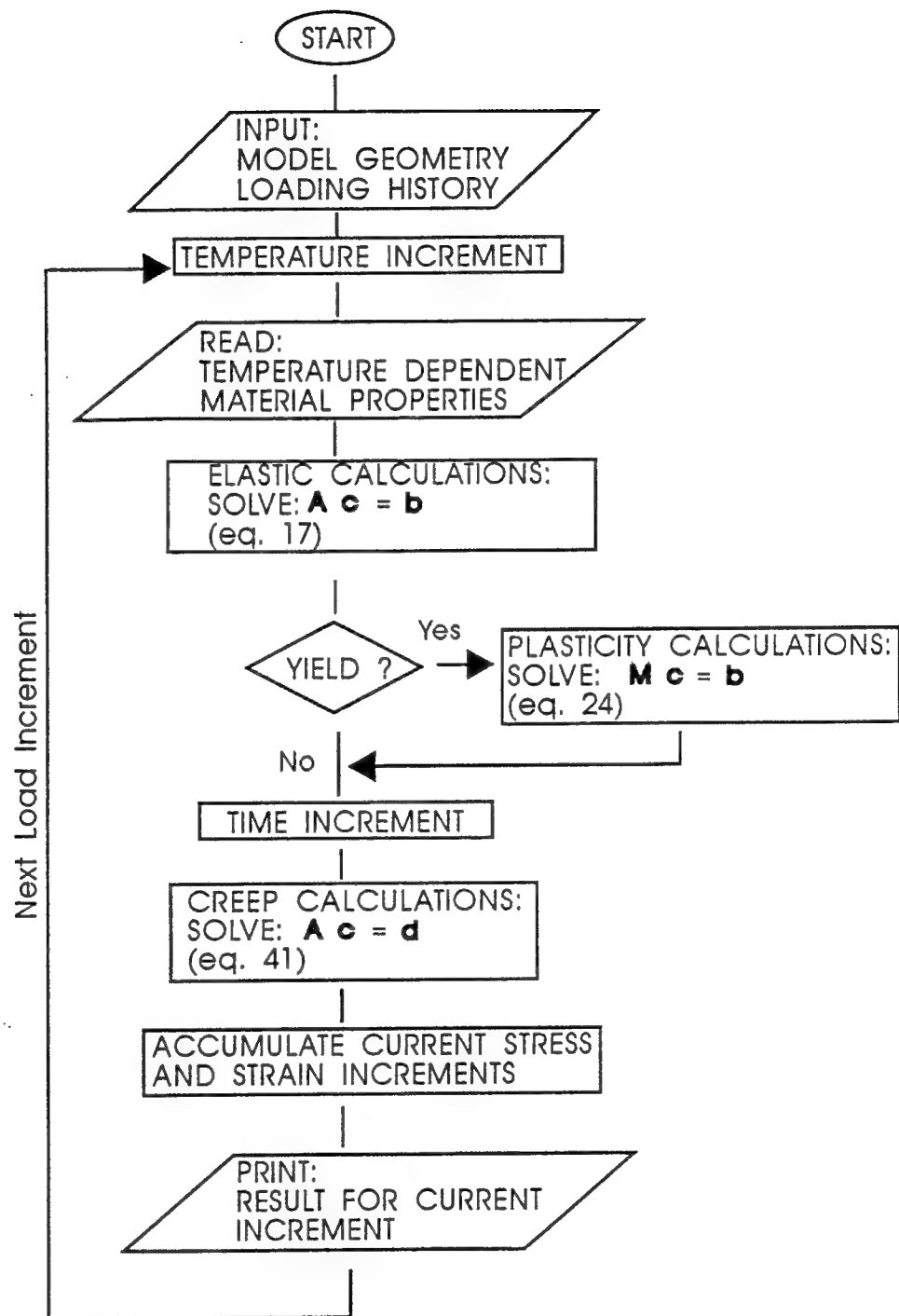
Fig. 3-4   Flow charts for elastic-plastic-creep algorithm.
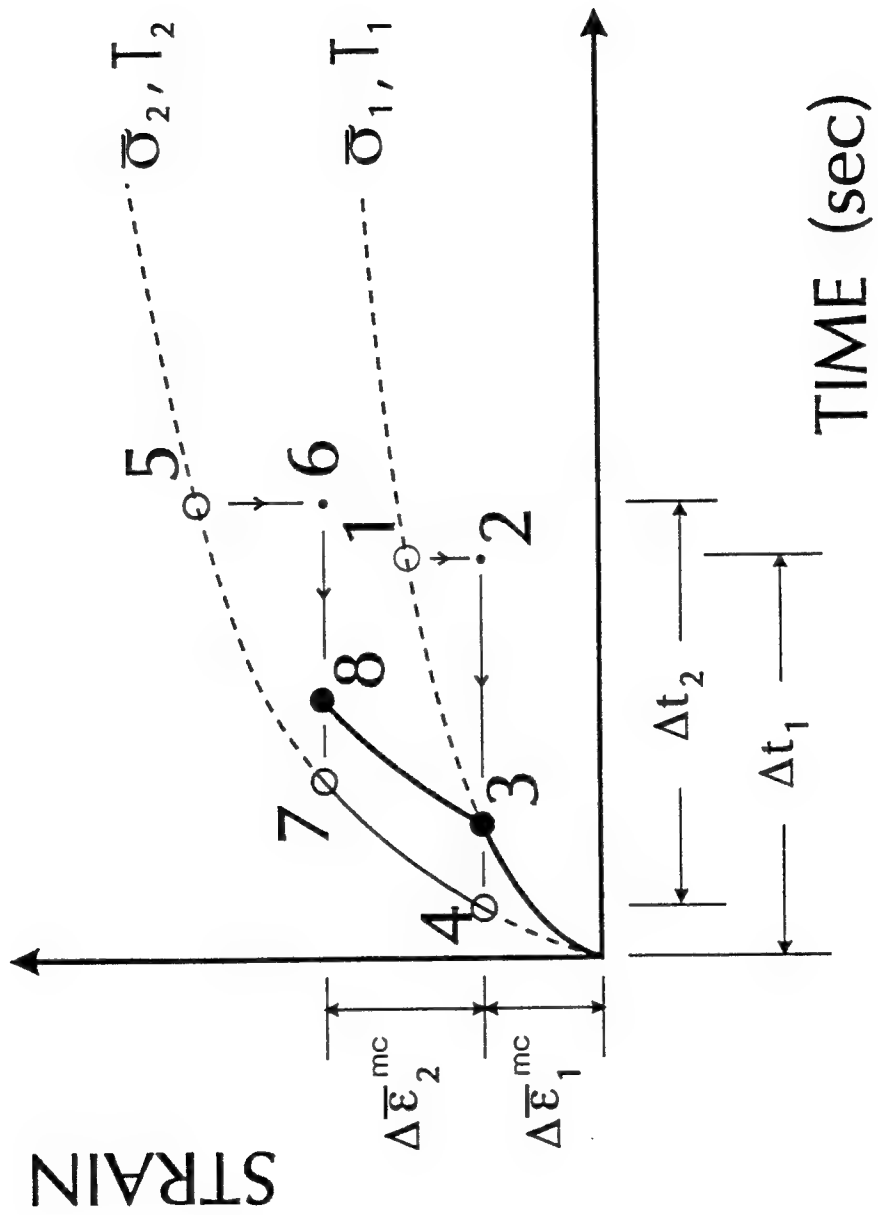
Fig. 3-5   Strain history prediction for the first two load steps from strain hardening method.

74

SECTION 4

PARAMETRIC STUDY OF THE TIME-DEPENDENT BEHAVIOR OF CONTINUOUS-FIBER REINFORCED METAL MATRIX COMPOSITES BASED ON MICROMECHANICAL MODEL

ABSTRACT

The micromechanical model developed in section 3 for the evaluation of the time-dependent stress-strain response of continuous-fiber-reinforced MMCs is applied to the SCS-6/Timetal®21S composite system. The influence of several parameters were examined; they include the thickness of the equivalent composite media, the type of fiber coating material, the thickness of the reaction zone, cooling rate from the consolidation temperature and the kinetics of the creep process during thermal cyclic loading. Results of this application show that the optimum ratio of the radii of composite media to that of the matrix layer should be larger than seven. At this ratio, sufficient fiber interactions is provided by the equivalent composite media. The analysis also indicates that the process-induced thermal stresses in the matrix can be relaxed due to creep during initial cool-down from fabrication. This stress reduction is enhanced at a slower cooling rate. Furthermore, the study of the role of different fiber coating materials shows that Copper coating is most effective in lowering the tensile stress components in the matrix when compared to Niobium, porous TiB_2 and Amorphous Carbon. The effectiveness increases with increasing thickness of the interfacial region. TiB_2 and Niobium coatings are favorable because they induce compressive radial stress in the brittle interfacial region and the matrix. The effect of thermal cycles subsequent to initial cool-down has been analyzed. It is found that the matrix thermal activation energy, Q, is history dependent and can be correlated with the level of the accumulated creep strain in the matrix layer. Furthermore, the residual thermal stresses in the matrix due to cool-down from consolidation can be fully relaxed by the thermal fatigue process.

4.1 INTRODUCTION

A micromechanical approach which takes into account the influence of time dependent effects on the evolution of thermal stresses in continuous fiber-reinforced metal matrix composites (MMCs) was developed in the previous section [1]. This approach which adopts the four-phase concentric cylinder model is able to provide information on the stress and strain states as well as their evolution in each constituent of the composite during the loading history.

A critical aspect of this approach is the inclusion of the creep deformation developed in the matrix and the effective composite media due to thermal variations. This inelastic deformation is described through the use of the Bailey-Norton's equation which accounts for the primary and secondary creep stages. A numerical scheme based on the "strain-hardening" creep formulation is employed to predict the accumulation of creep strain during the simultaneous variation of both stress and temperature in the composite.

75

In this section, the model is applied to SCS-6/Timetal®21S composite system under the thermal loading conditions which include cooling from processing temperature and subsequent thermal cycling. Through this application, an attempt has been made to identify the key parameters in the model and their physical significance. The minimum size of the equivalent composite media necessary to account for the effect of fibers interaction in the composite is investigated. MMCs with different fiber coating materials and various thickness are modelled to study their effects on the thermal stress level in the constituents of the composite. The significant influence of time-dependent behavior of MMCs during initial cool-down and subsequent thermal fatigue are also studied. In addition, effects of different cooling rates during consolidation on the residual thermal stress level in the composite are considered. The characteristics of the stress state in the fiber, the reaction zone and the matrix during consolidation and subsequent thermal cycles are presented. Finally, certain interesting features of the thermal stresses in the composites revealed from the application of the model to thermal fatigue conditions are discussed.

4.2 PARAMETRIC STUDY

The composite employed for the model here is the Titanium-based SCS-6/Timetal®21S composite system. The Silicon Carbide fiber reinforcement, SCS-6 is assumed to behave elastically for all loading conditions with temperature-independent elastic modulus and Poisson's ratio. The coefficient of thermal expansion (CTE) is taken as temperature-dependent [2-6]. The reaction zone formed between the fiber and the matrix with a thickness of 3 μm is assumed to have mechanical and thermal properties similar to those of the fiber coating material used. The elastic modulus, CTE, and yield limit of the metastable Timetal®21S monolithic matrix alloy were also considered to be temperature-dependent [7]. The properties of the equivalent composite media were obtained using the rule of mixture for fiber volume fraction of 35%. The volume fractions of the fiber, v_f, the reaction zone, v_{re}, and the matrix, v_m, are expressed as:

$$v_f = \left(\frac{r_4}{r_2}\right)^2 \quad , \quad v_{re} = \frac{r_3^2 - r_4^2}{r_2^2} \quad , \quad v_m = 1 - \left(\frac{r_3}{r_2}\right)^2 \tag{1}$$

where r_1, r_2, r_3 and r_4 are the radii of the equivalent composite media, the matrix, the reaction zone and the fiber, respectively. The mechanical properties of all the constituents of the composite are shown in Fig. 3-1(a)~(c).

Both the monolithic matrix and the composite exhibit creep behavior during consolidation. The creep properties of Timetal®21S monolithic matrix and the composite material are based on limited experimental data given in reference [7,8]. It is assumed that the creep curves can be represented by the Bailey-Norton's equation in the transient and the steady state stages of creep as:

$$\bar{\varepsilon}^{cr} = B \bar{\sigma}^{m(T)} t^n \tag{2}$$

where $\bar{\varepsilon}^{cr}$ and $\bar{\sigma}$ are the effective creep strain and the effective stress, respectively. The parameters B, m(T) and n are obtained from correlations with the experimental data. The coefficient, B can be expressed by an Arrhenius-type expression:

$$B - b_0 \exp\left(-\frac{Q}{RT}\right) \tag{3}$$

where b_0 is a constant, R is the gas constant, Q is the thermal activation energy and T is temperature in degrees Kelvin. The stress exponent, $m(T)$, which is treated as a function of temperature is described as a polynomial function in the form [9]:

$$m(T) - A_1 + A_2 T + A_3 T^2 + A_4 T^3 \tag{4}$$

where A_i, (i=1,2,3,4) are material constants.

Due to lack of creep data for the SCS-6/Timetal®21S composite, the creep response of the equivalent composite media under thermal loading conditions is estimated from the matrix creep data by accounting for the effect of fiber reinforcement in the following manner:

$$\varepsilon_{rr}^{(1),cr} - (1 - v_f)\, \varepsilon_{rr}^{(2),cr} \quad , \quad \varepsilon_{\theta\theta}^{(1),cr} - (1 - v_f)\, \varepsilon_{\theta\theta}^{(2),cr} \quad , \quad \varepsilon_{zz}^{(1),cr} - (1 - v_f)\, \varepsilon_{zz}^{(2),cr} \tag{5}$$

where $\varepsilon_{rr}^{(1),cr}$, $\varepsilon_{\theta\theta}^{(1),cr}$ and $\varepsilon_{zz}^{(1),cr}$ are the radial, hoop and axial component, respectively, of the unconstrained creep strain for the composite while $\varepsilon_{rr}^{(2),cr}$, $\varepsilon_{\theta\theta}^{(2),cr}$ and $\varepsilon_{zz}^{(2),cr}$ are the corresponding creep strain components for the matrix.

The first part of this section will deal with the thickness of the equivalent composite media surrounding the matrix, the reaction zone and the embedded fiber. The effect of the reaction zone thickness and different types of fiber coating materials on the stress states in the matrix and the reaction zone will be examined next. This will be followed by analysis related to the role of creep deformation and the response of the matrix activation energy to thermal loadings. In this section, the stress fields in the matrix and the reaction zone are calculated in the vicinity of the matrix/reaction zone interface.

4.2.1 Thickness of the Equivalent Composite Media

As described in the last section, the geometry of the model adopted in the present approach consists of a fiber surrounded by a reaction zone and the matrix layer, and embedded in an unbounded homogeneous media that has the properties of the composite. This model is the counterpart for multi-phase media of the self-consistent method for single phase media [10]. Theoretically, the equivalent composite media surrounding the matrix cylinder should be infinitely large, and generally the numerical techniques take this size fairly large to meet infinite requirement. The choice of a large equivalent composite media leads to a stable stress field solution at the expense of longer computational time and larger required computer memory. Fig. 4-2(a)~(c) show the relationship between the stress fields in the matrix layer and the size of the equivalent composite media in terms of the ratio of the radii of the matrix to the surrounding equivalent composite media. The stresses are normalized by $\sigma_0 = E^{(2)}\alpha^{(2)}\Delta T$, where $E^{(2)}$ and $\alpha^{(2)}$ are the Young's modulus and CTE, respectively of the matrix at room temperature, and ΔT is 840 °C. It indicates that the stress fields of the phases are stable until the ratio is less than seven, and this trend is not affected by the fiber volume fraction. The significance of this ratio of seven could be explained in terms of the minimum number of fibers that should be contained in the optimum thickness of the composite media for the model. In the real composite, the fibers are not regularly align in the matrix. The distribution of the center-to-center fiber spacing for

a typical SCS-6/Ti-15-3 composite with 35% fiber volume fraction can be obtained using the method of quantitative stereology [11] as illustrated in Fig. 4-3. The mean center-to-center fiber spacing for this composite is 230μm. Assuming that the fiber arrangement follows the hexagonal array with the fiber, the reaction zone and the matrix cylinders at the center of the arrangement, then other fibers are arranged in series of concentric hexagonal arrays about this center as depicted in Fig. 4-4. The minimum diameter of the equivalent composite media is also illustrated in the figure. It can be shown that for the hexagonal array architecture, the minimum size of the equivalent composite media consists of 40 fibers surrounding the embedded fiber which is being modelled (see Fig. 4-4). This provides sufficient effects of interaction of fibers in the composite.

4.2.2 Fiber Coating Material and Thickness of the Interfacial Region

Previous work [5,6,12] showed that the reaction zone in the composites is a susceptible site for generating cracks after fabrication. Microscopic radial cracks after fabrication are frequently observed in several titanium metal matrix composites. These cracks are caused by the high level of tensile hoop stress component induced in the reaction zone during consolidation [13]. The popular criteria for selecting coating material are currently based on the enhancement of wetting behavior of fiber and matrix and the minimization of interface reactions by reducing the rate of diffusion [14]. Besides being an effective diffusion barrier against chemical reaction leading to the formation of a brittle layer, a promising coating material should also minimize the local tensile residual thermal stresses in the composite especially at the interfacial region. In view of either preventing premature damage caused by residual thermal stresses in the composite, or load transfer mechanism provided by these stresses, the stress state in the reaction zone and the matrix as influenced by the thickness of the reaction zone and the mechanical properties of the fiber coating material have been investigated. Typical SiC fiber coating materials; Cu, Nb, Amorphous Carbon and TiB_2 with 50% porosity are employed here.

Fig. 4-5(a)~(f) show the variation of the radial, hoop and axial stress components induced in the matrix and the reaction zone during post fabrication cool-down with various thickness of the interfacial region for different fiber coating materials. The results do not reveal any general trend for the relationship between the thickness of the reaction zone, its mechanical properties and the thermal stress states in the constituents of the composite for all coating materials considered. The magnitude of the transverse (radial and hoop) stress components in the matrix decreases as the thickness of the interfacial region increases. While Cu-coating also decreases the axial thermal stress in the matrix, other coating materials considered cause an increase in the axial stress component with increasing thickness of the interfacial region. The radial stress component is compressive in the interfacial regions for all fiber coating materials considered. However TiB_2- and Cu-coating induce highly tensile hoop and axial stresses in the interfacial region. Since this region is usually brittle in nature and is sensitive to tensile loading, thus reducing the magnitude of the tensile stress components in this layer is of prime importance. This tensile hoop stress is responsible for generating radial cracks in the composite. The result indicates that Cu-coating induces the highest tensile hoop and axial stress level in the reaction zone which would facilitate the nucleation and propagation of radial cracks in this layer. On the other hand, a small compressive hoop and axial stress components result from the use of C-coated fibers, which potentially increase the ability of the layer to resist cracking. From the load

transfer point of view, both fiber coating materials, TiB_2 and Nb, are favorable because they induce high compressive radial stress components in the reaction zone and the matrix. The relative magnitudes of the CTEs and Young's moduli of the different coating materials considered, the SCS-6 fiber, and the Timetal®21S matrix are shown in Fig. 4-6(a)~(b). It is noted that C-coating with both CTE and Young modulus values much smaller than for the matrix generates lower level of residual thermal stress in the interfacial region. Although the radial stress component decreases substantially with increasing thickness of the interfacial layer, the thickness has small effect on other components of thermal stress in the layer (see Fig. 4-5(d)~(f)). The radial stress component which is beneficial based on the load transfer mechanism is preserved in the reaction zone and the matrix when employing fiber coating materials (Nb or TiB_2) with both CTE and Young's modulus values close to the values for the matrix.

Throughout consolidation, a compressive stress state is induced in the fiber because both the reaction zone and the matrix with higher CTEs but lower Young's moduli than the fiber shrink rapidly around the fiber.

The results of this study indicate that the selection of a suitable fiber coating material should be based on the application requirement of the composite.

4.2.3 Role of Creep Deformation in the Evolution of Thermal Stresses

During post-fabrication cool-down of the composite from consolidation temperature, the thermal stresses induced in the matrix may cause creep deformation at relatively high temperature. The deformation however, is constrained by the relative inextensibility of the elastic fiber and the reaction zone, and the bonding between each constituents of the composite. In the present study, the significant influence of time-dependent deformation behavior on the evolution of thermal stresses in MMCs during initial cool-down has been investigated. Fig. 4-7 shows the evolution of thermal stresses in the matrix throughout consolidation for purely elastic, elastic-plastic and elastic-plastic-creep cases. The elastic-plastic-creep calculations predicted that at high temperature following consolidation, the thermal stresses were relaxed extensively by creep. Consequently, no plasticity occurred in the composite since the effective stress level is always lower than the yield stress of the matrix throughout the initial cool-down. However, elastic-plastic calculations predicted that the matrix yielded at 720 °C and the stress is brought down to the yield value of the matrix. The final locked-in residual thermal stresses at room temperature are considerably lowered due to creep deformation.

The time-dependent characteristics have been studied through the effect of cooling rate during consolidation on the creep behavior and the residual thermal stress state of the composite. Several cooling rates ranging from 5×10^{-3} to 1.0 °C/sec are utilized in the model and the results are presented in terms of the reduction in effective stress accounted for creep effect in relation to elastic case as shown in Fig. 4-8. The amount of reduction in the effective stress increases exponentially as the cooling rate is lowered. A stress reduction of 9.97% was calculated for cooling rate of 0.5 °C/sec while an additional 10.72% occurred for a slower cooling rate of 0.005 °C/sec. At a slower cooling rate, the composite is exposed to high temperature creep for a longer duration of time, which enhance the accumulation of creep strain resulting in extensive stress relaxation in the matrix. This result indicates that the final locked-in residual thermal stress can be tailored by controlling the cooling rate during consolidation of the composite.

For a particular cooling rate, the maximum reduction in thermal stress always occurs in

the vicinity of the matrix/reaction zone interface where the elastic stress is maximum due to the largest difference in CTEs of adjacent layers. The magnitude of the stress relaxation in the matrix due to creep decreases non-linearly from 10% at the interface to 5.3% at the outer layer of the matrix. The results indicate that the matrix creep deformation has a significant effect on the evolution of the thermal stresses and the stress relaxation mechanism in MMCs.

4.2.4 Evolution of Thermal Stresses During Thermal Cycling

As discussed above, the time-dependent deformation plays a significant role in generating thermal stresses in MMCs. The determination of the key parameters which yield the correct stress state in the composite is of prime importance in the current mathematical modelling. During initial cool-down from consolidation temperature, the matrix experiences creep deformation which is governed by eq. (2) and (3). The matrix thermal activation energy, Q in eq. (3) can be treated as a constant for the evolution of thermal stresses in the matrix throughout this process, as indicated by a good agreement between the calculated and the experimental results, see Fig. 4-9. Previous experimental work by Ghonem and Zheng [15] showed that for loading conditions consisting of the initial cool-down followed by thermal cycling between 100 - 550 °C, the axial thermal stress in the matrix has been reduced to zero at the upper temperature level after the application of only five cycles, as shown in Fig. 4-10. This reduction in thermal stresses has been attributed to the influence of the creep deformation developed in the matrix material during thermal cycling. However, the attempt to predict the stress history during a loading process similar to that of [15] using the present model with Q being kept as a constant, has resulted in a stress cycle pattern with a negligible amount of stress reduction at the upper limit of the thermal cycle. The parameter Q, was then linked to the variation in temperature to obtain the best curve fitting to experimental data. The resulting Q was further correlated to the induced matrix stress and strain during the thermal cyclic process. This correlation could be expressed in terms of the inelastic strain energy density, W_{pc}, as:

$$Q = Q_0 - f(W_{pc}) \tag{6}$$

where Q_0 is the value of Q prior to thermal cycling and $f(W_{pc})$ is a monotonic increasing function of W_{pc}, in which W_{pc} is defined as:

$$W_{pc} = \int_{\bar{\varepsilon}_0^{cr}}^{\bar{\varepsilon}^{cr}} \bar{\sigma} \, d\bar{\varepsilon}^{cr} \tag{7}$$

$\bar{\sigma}$, $\bar{\varepsilon}^{cr}$ are the effective stress and the creep strain, respectively, and $\bar{\varepsilon}_0^{cr}$ is the initial creep strain.

This result indicates that the level of thermal activation energy, Q, in the matrix is affected by the simultaneous variation of stress, strain and temperature experienced by the composite throughout consolidation and thermal cycling. This observation, in fact, supports similar conclusion made by Ghonem and Zheng [16] in their experimental work on Alloy 718 at 650 °C and by Freed et al. [17], on the basis of thermodynamics analysis conducted on Copper and LiF-22mol percent CaF hypereutectic salt.

4.3 CONCLUSIONS

The model developed in the last section was employed in a parametric study using SCS-6/Timetal®21S composite system. The following conclusions are derived through the analysis of the results:

1- The geometry of the four-phase model requires that the radius of the surrounding composite media to be at least seven times larger than the radius of the matrix to ensures its role in providing realistic geometrical constraints through the surrounding fiber interactions with the model unit.

2- The residual thermal stress induced in the composite during consolidation can be reduced considerably by the creep deformation occurring in the matrix. A slow cooling rate allows longer duration of time for the composite to be exposed to high-temperature creep effects resulting in extensive stress relaxation. The matrix layer experiences significant creep effects at the matrix/reaction zone interface where the residual stress level is high.

3- Subjecting a composite system to reversing thermal cycles indicate that the matrix thermal activation energy, Q, should be correlated with the creep behavior through the level of accumulated creep strain in the matrix layer.

4- The properties and thickness of the reaction zone formed in MMCs influence the thermal stress behavior in the matrix layer. The effective residual stress decreases as the thickness of the reaction zone increases.

5- The choice of a fiber coating material that inhibit fiber/matrix reaction and reduce the residual thermal stress level in the composite, and a particular cooling rate following fabrication provide a potential mean of optimizing the mechanical performance of the composite system.

4.4 REFERENCES

1. Tamin, M. N., Zheng, D. and Ghonem, H., 1993. J. Composite Materials.

2. Schwenker, S. W., Evans, D. J. and Eylon, D., 1992. Longitudinal Creep Behavior and Damage in SCS-6/Ti-6Al-4V Metal Matrix Composites, Seventh World Conference on Titanium, San Diego, CA.

3. Dicarlo, J. A., 1986. J. Material Science, 21:217-224.

4. Saigal, A., Kupperman, D. S. and Majumdar, S., 1992. Mat. Sc. Engng., :59-66.

5. Arnold, S. M. and Wilt, T. E., 1992. NASA TM 105438.

6. Arnold, S. M., Arya, V. K. and Melis, M. E., 1990. <u>NASA TM103204</u>.

7. Khobaib, M. and Ashbaugh, N., 1991. Unpublished work.

8. Martin, P.L., Bingel, W. H. and Mahoney, M.W., 1992. <u>Titanium Matrix Components, Workshop Proceedings</u>, ed. by Smith, P. R. and Revelos, W.C., WL-TR-92-4035, :277-291.

9. Lemaitre, J. and Chabache, L., 1990. <u>Mechanics of Solids</u> (English Translation), Cambridge University Press, NY.

10. Christensen, R. M. and Lo, K. H., 1979. <u>J. The Mechanics and Physics of Solids</u>, 27:315-330.

11. Underwood, E. E., 1969. <u>Quantitative Stereology</u>, Addison-Wesley, Reading, Man.

12. Sohi, M., Adams, J. and Mahapatra, R., 1991. <u>Constitutive Laws of Engineering Materials</u>, ed. by Desai, C. D., Krempl, E., Frantziskonis, G. and Saadatmanesh, H., ASME Press NY, :617-626

13. Buesking, K. W., Young, J. L. and Reynolds, G. H., 1992. <u>Titanium Matrix Components, Workshop Proceedings</u>, ed. by Smith, P. R. and Revelos, W. C., WL-TR-92-4035, :42-64.

14. Maruyama, G. Barrera,E. and Rabenberg, L., 1991. <u>Characterization and Modification of Composite Interfaces, Metal Matrix Composites: Processing and Interfaces</u>, ed. by Everett, R. K. and Arsenault, R. L., Academic Press, Inc., NY, :181-216.

15. Ghonem, H. and Zheng, D., 1993. <u>Mat. Sc. Engng.</u>, (in press).

16. Ghonem, H. and Zheng, D., 1991. <u>Fatigue & Fracture of Engineering Materials and Structures</u>, 14:749-760.

17. Freed, A. D., Raj, S. V. and Walker, K. P., 1992. <u>J. Engng. Mat. and Tech.</u>, 114:46-50.2
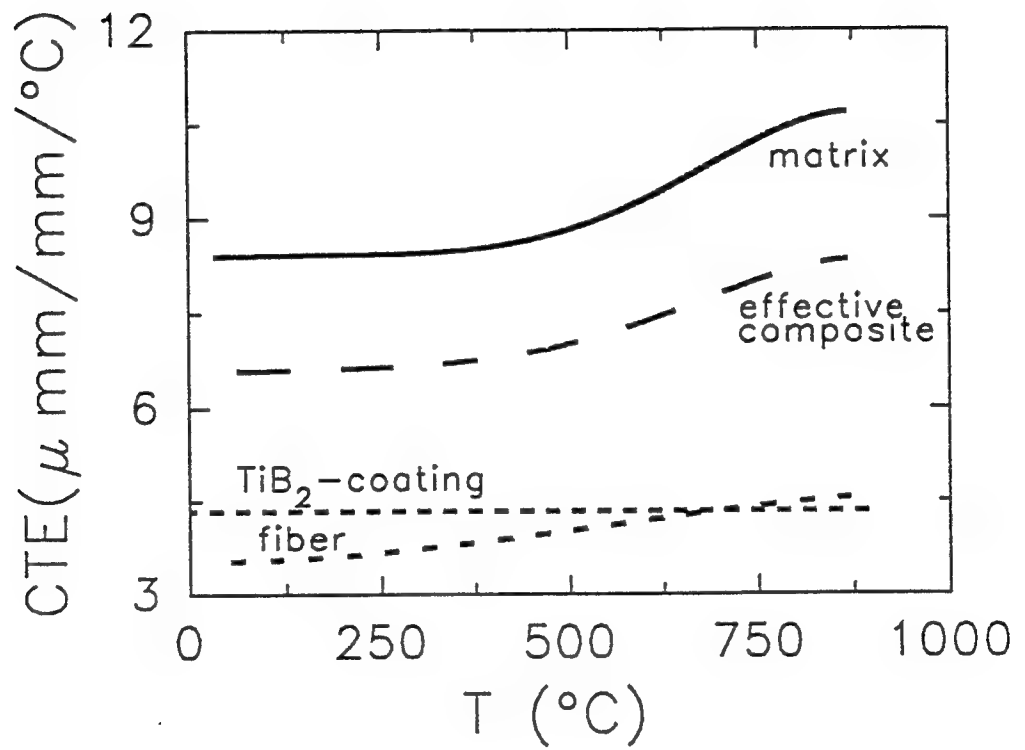
Fig. 4-1(a)   Physical properties of the constituents: CTE.
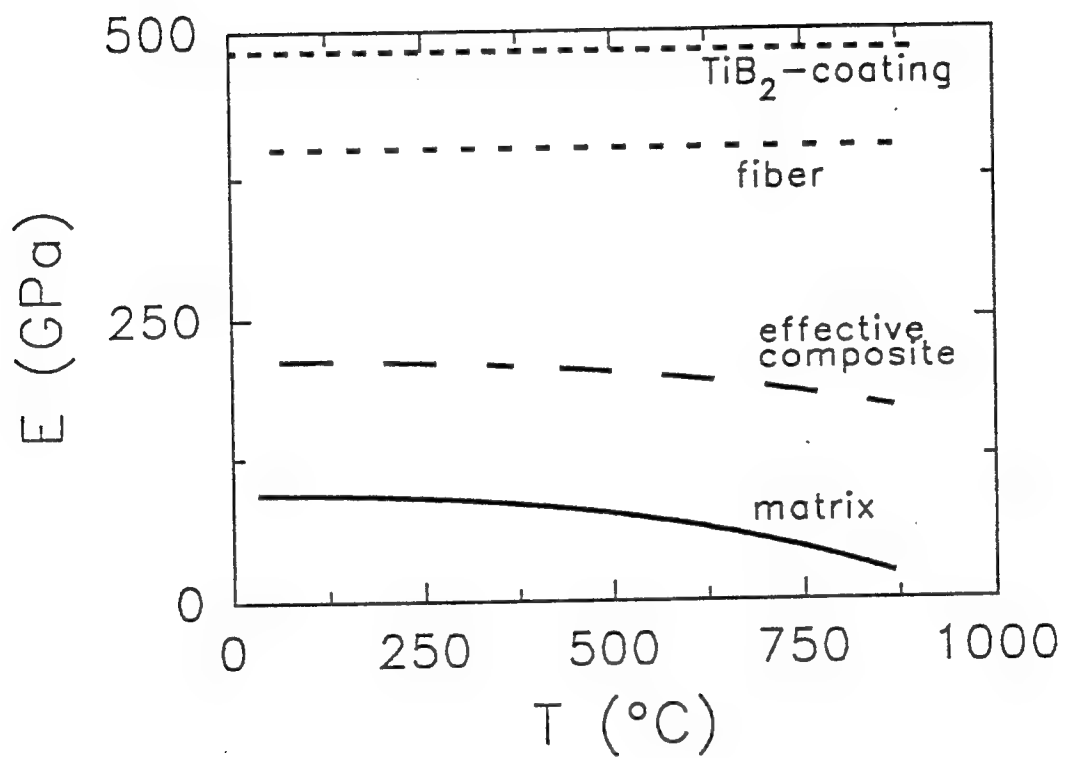
Fig. 4-1(b)   Physical properties of the constituents: Young's modulus.
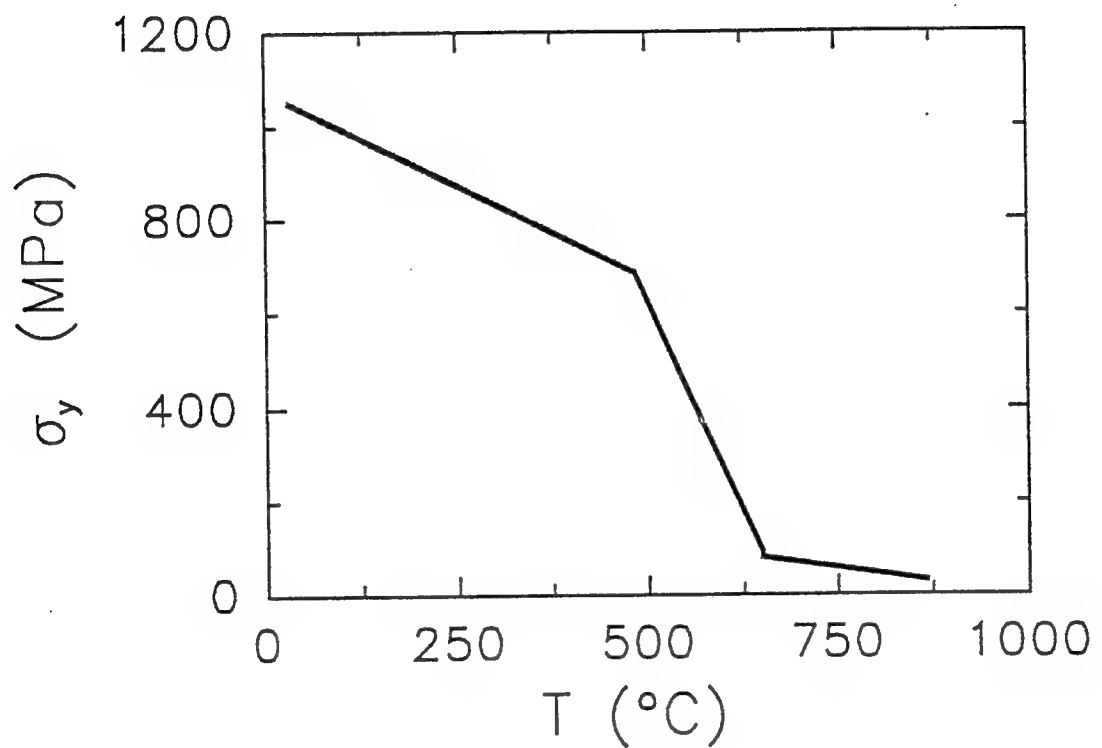
Fig. 4-1(c)   Physical properties of the constituents:Yield strength of Timetal®21S.
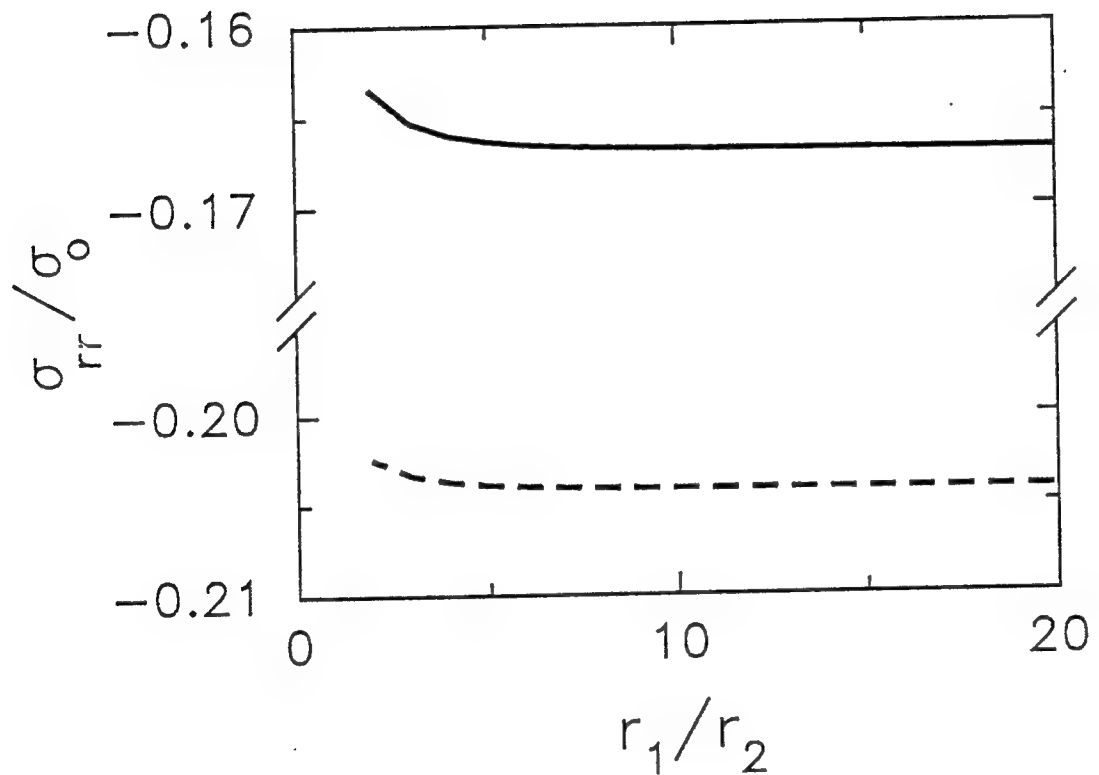
Fig. 4-2(a)   Variation of stress field in the matrix layer with size of the equivalent composite: Radial Component.   ——— $v_f = 35\ \%$,   - - - - $v_f = 20\ \%$.
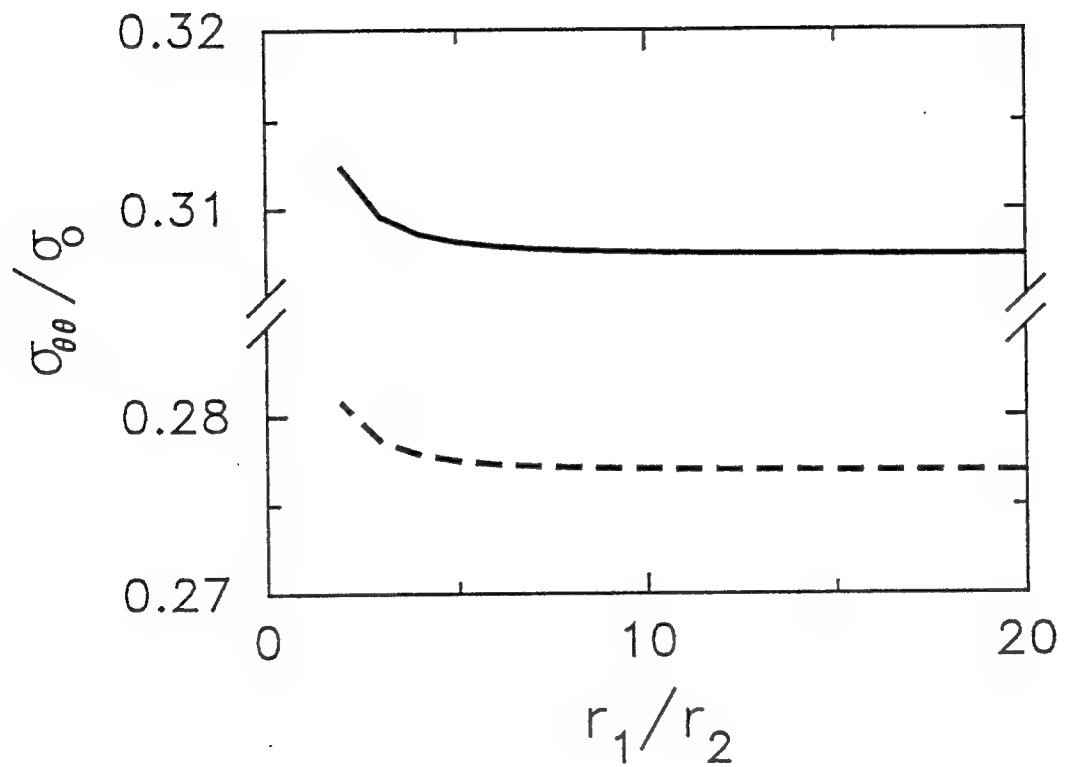
Fig. 4-2(b)   Variation of stress field in the matrix layer with size of the equivalent composite: Hoop component.   ——— $v_f = 35\%$,   – – – – $v_f = 20\%$.
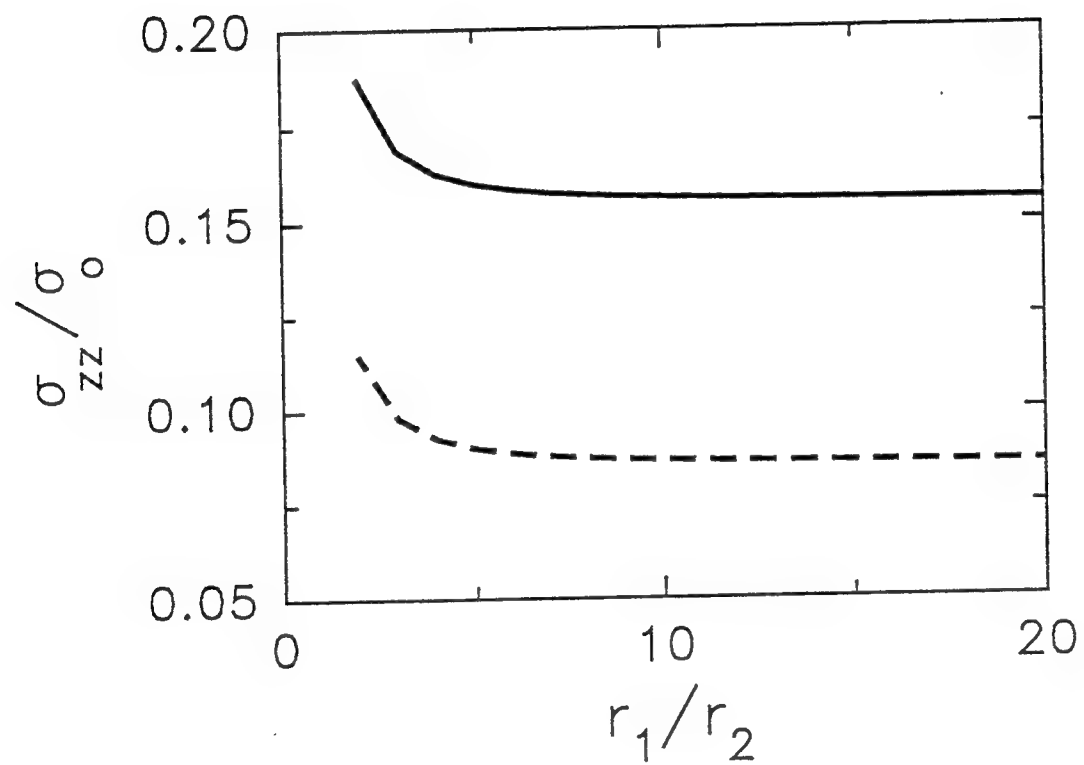
Fig. 4-2(c)   Variation of stress field in the matrix layer with size of the equivalent composite: Axial component.   ——— $v_f = 35\ \%$,   – – – – $v_f = 20\ \%$.
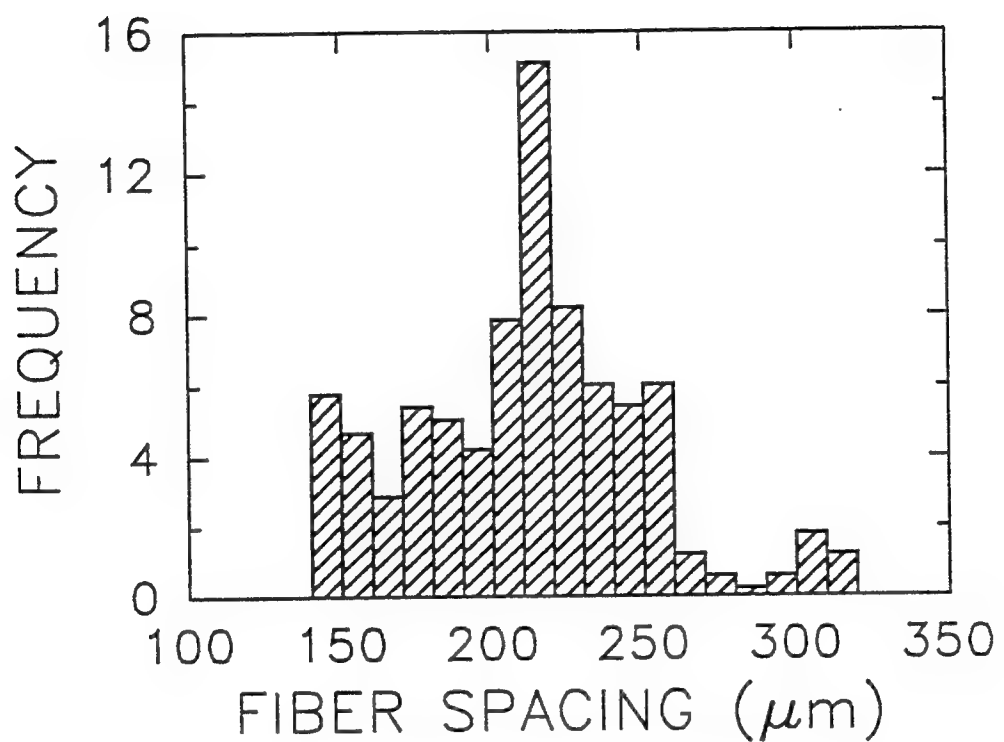
Fig. 4-3   Frequency distribution of center-to-center spacings between fibers in Ti-15-3 composite with 35% fiber volume fraction.
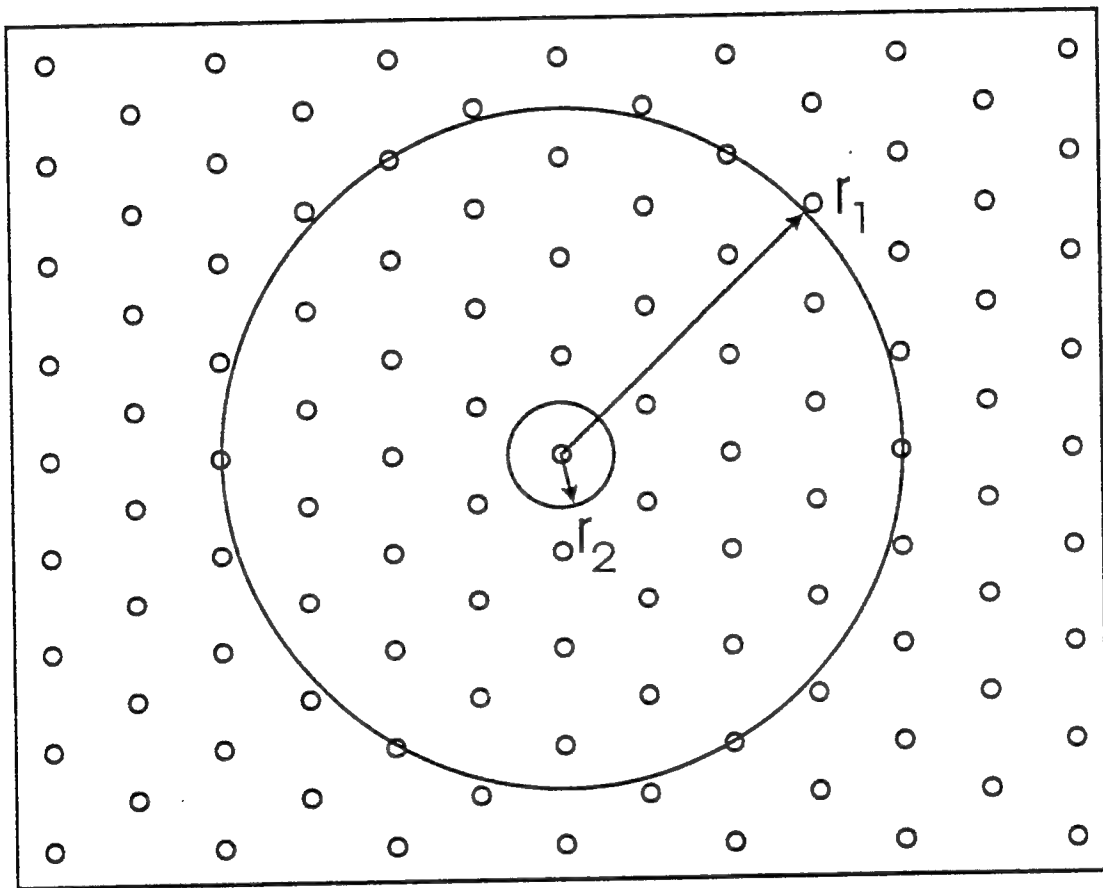
Fig. 4-4   Idealized array of fibers in MMC with 35 % fiber volume fraction.
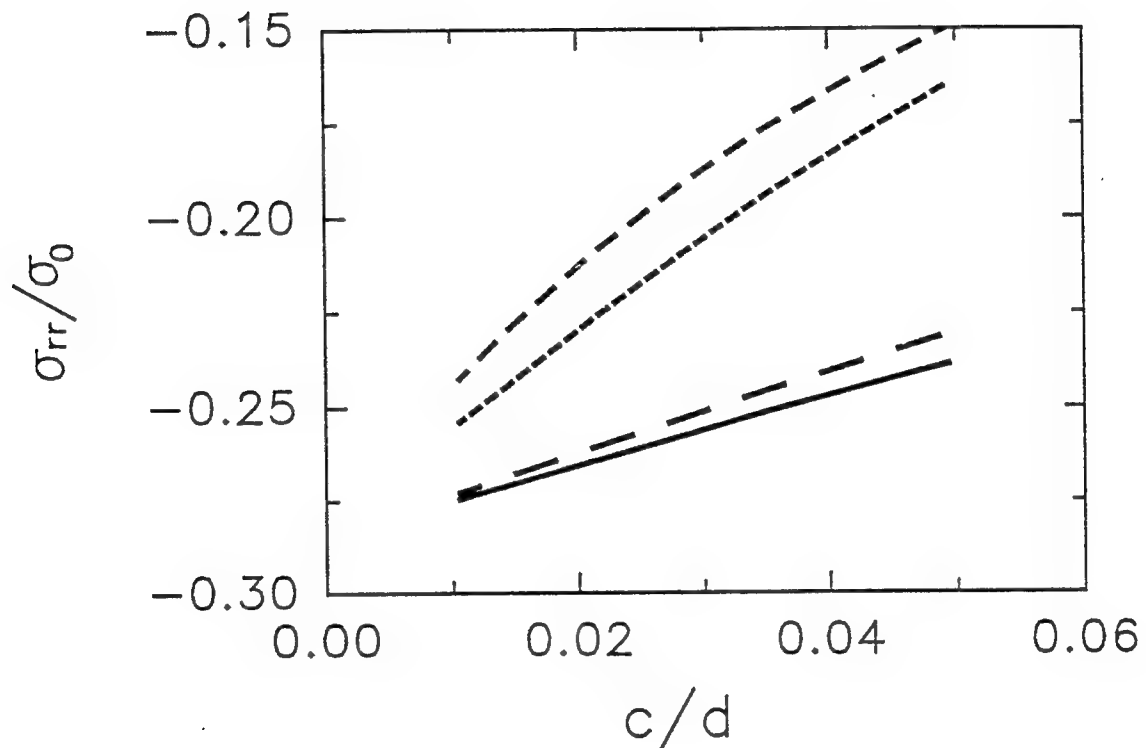
Fig. 4-5(a)   Variation of radial stress field in the matrix with thickness of fiber coating for different coating materials: ——— TiB_2, — — Nb, – – – – C, – – – – – Cu.
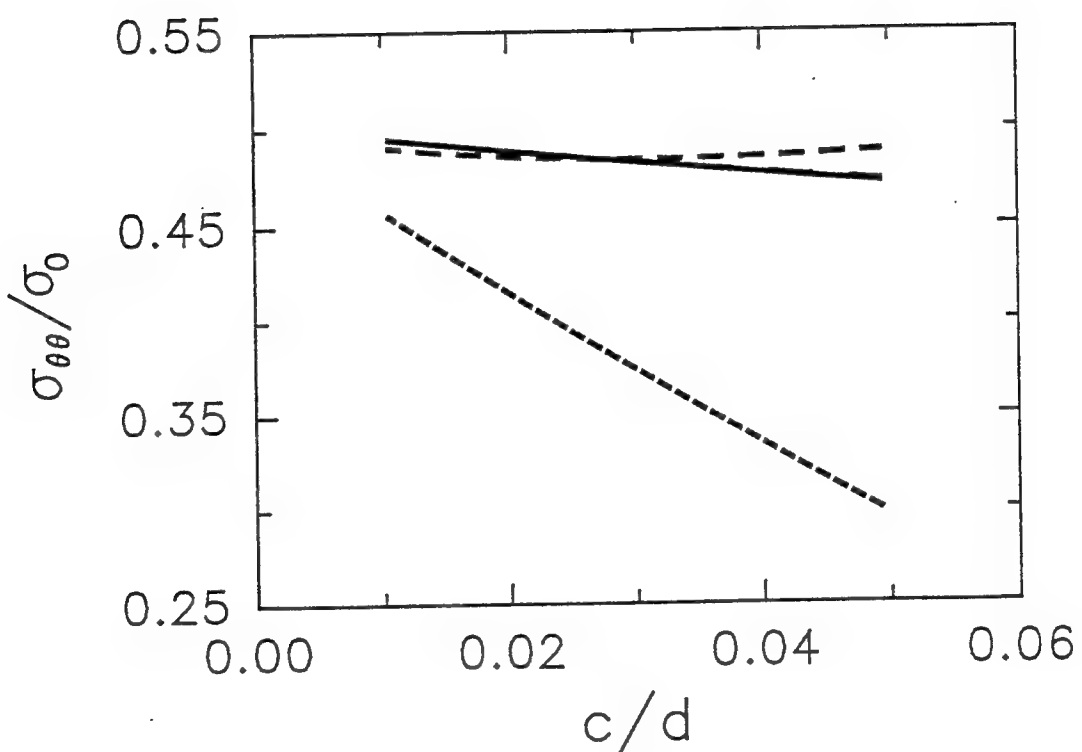
Fig. 4-5(b) Variation of hoop stress field in the matrix with thickness of fiber coating for different coating materials: ——— TiB_2, —— —— Nb, — — — C, — — — — — — Cu.
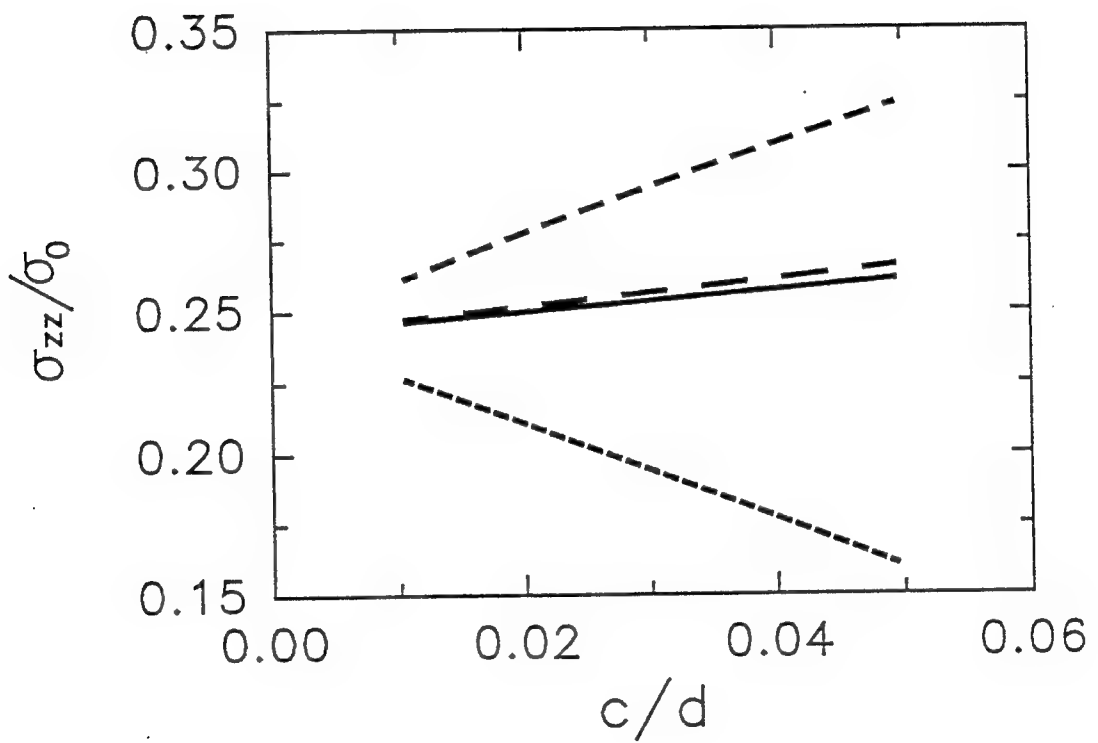
Fig. 4-5(c) Variation of axial stress field in the matrix with thickness of fiber coating for different coating materials: ——————TiB$_2$, —— —— Nb, — — — —C, — — — — — Cu.
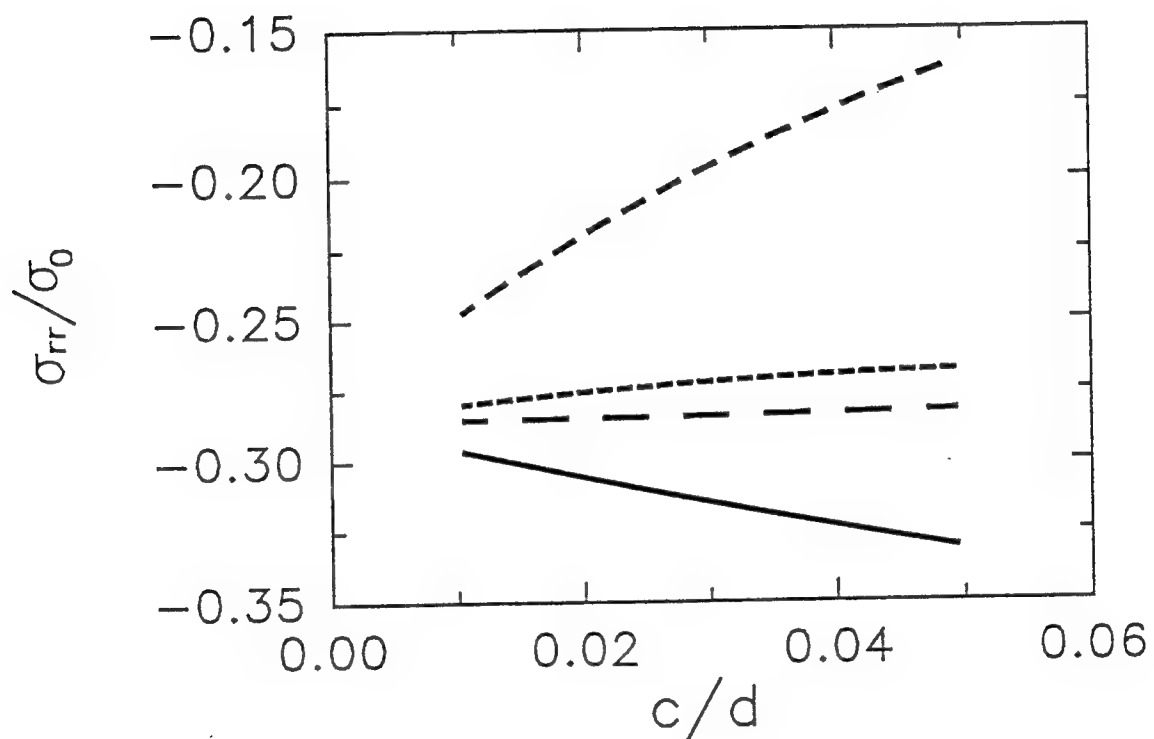
Fig. 4-5(d)   Variation of radial stress field in the interfacial region with thickness of fiber coating for different coating materials: ———— TiB_2, —— —— Nb, — — — — C, — — — — — —Cu.
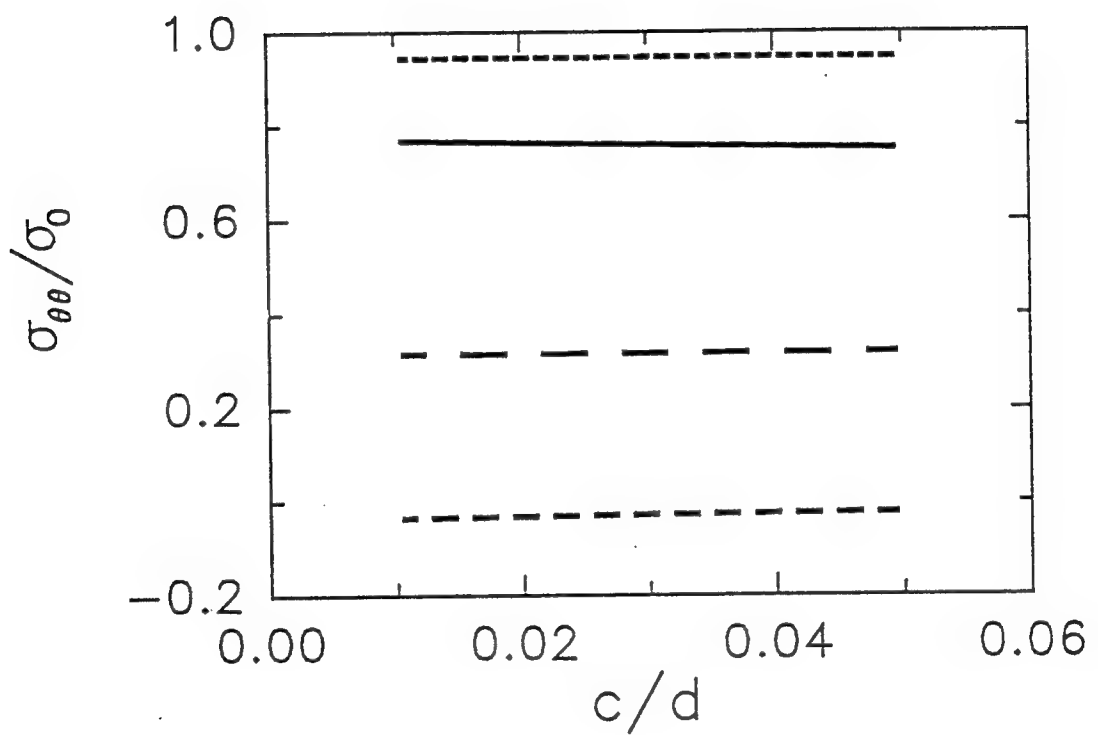
Fig. 4-5(e)   Variation of hoop stress field in the interfacial region with thickness of fiber coating for different coating materials: ———— TiB_2,   —— —— Nb, ————C,   ————— Cu.
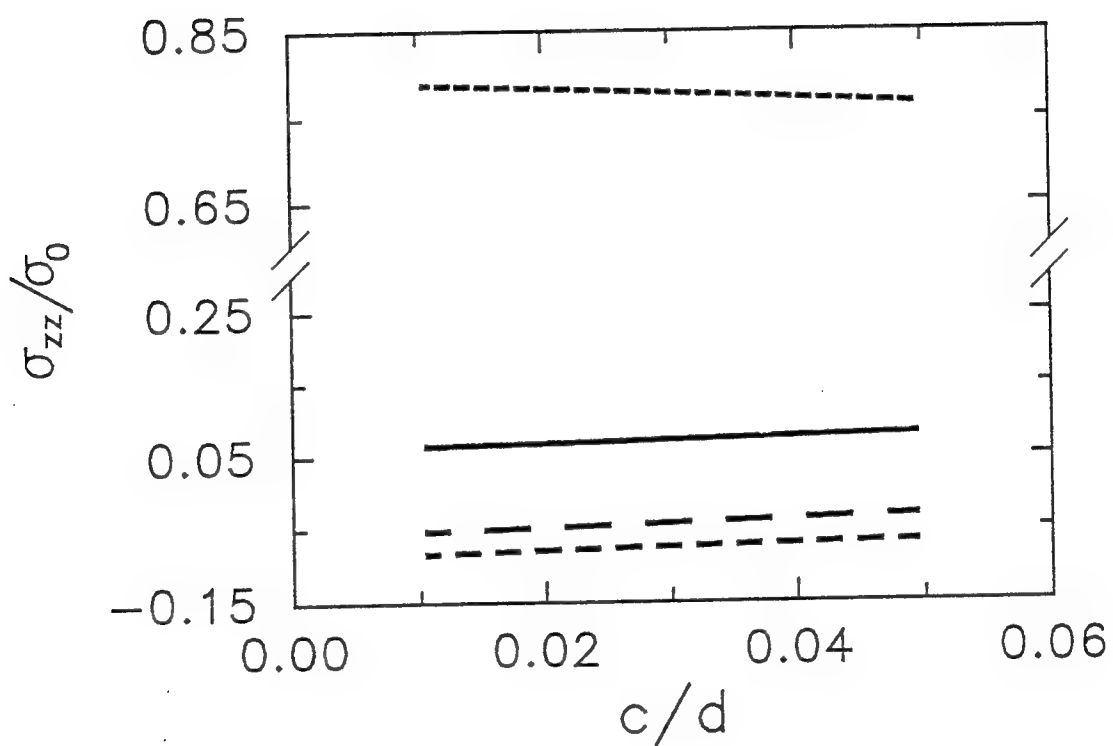
Fig. 4-5(f)   Variation of axial stress field in the interfacial region with thickness of fiber coating for different coating materials: ———— TiB$_2$,   —— —— Nb, — — — — —C,   — — — — — Cu.
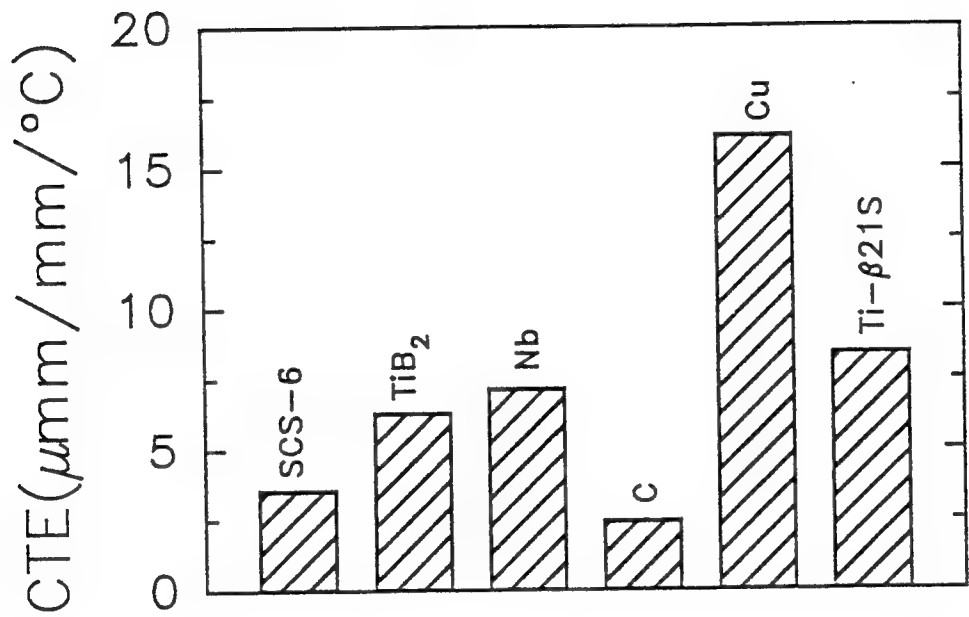
Fig. 4-6(a)   Physical properties of the composite constituents at room temperature: CTE.
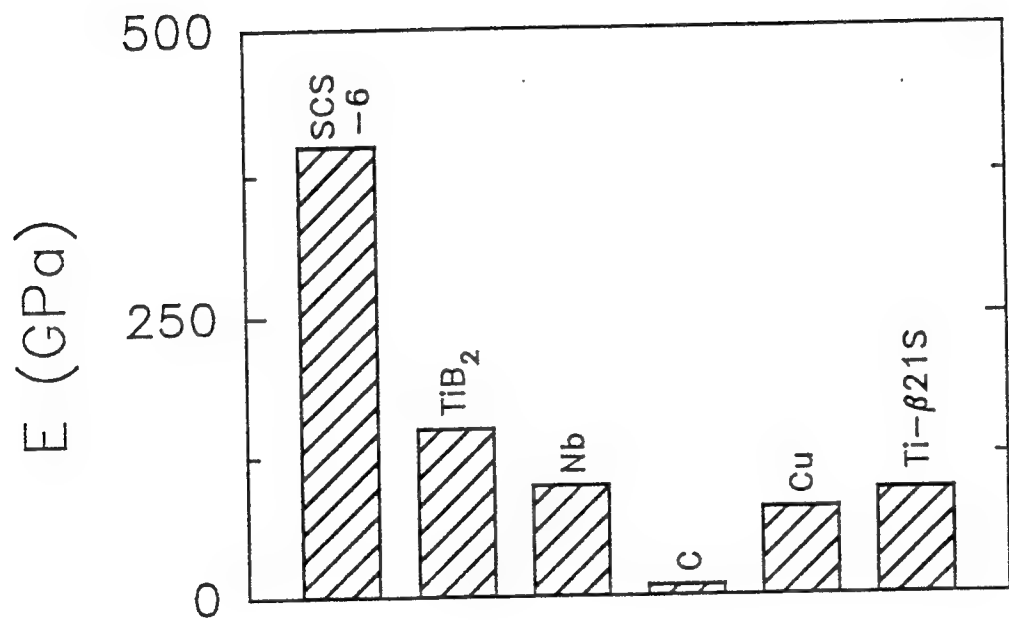
Fig. 4-6(b)   Physical properties of the composite constituents at room temperature: Young's
modulus.
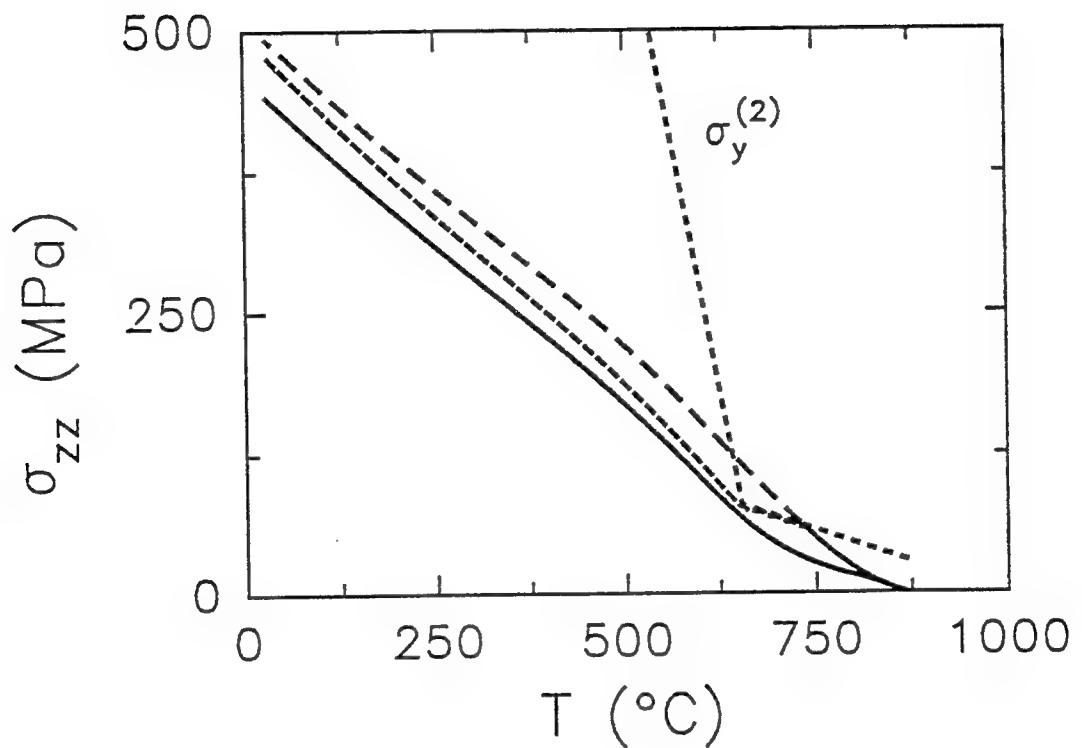
Fig. 4-7   Evolution of axial thermal stress in the matrix during initial cool-down at 0.5 °C/sec.: ———— elastic-plastic-creep, – – – – – – elastic-plastic, — — — elastic. $\sigma_y^{(2)}$ is the matrix yield strength.
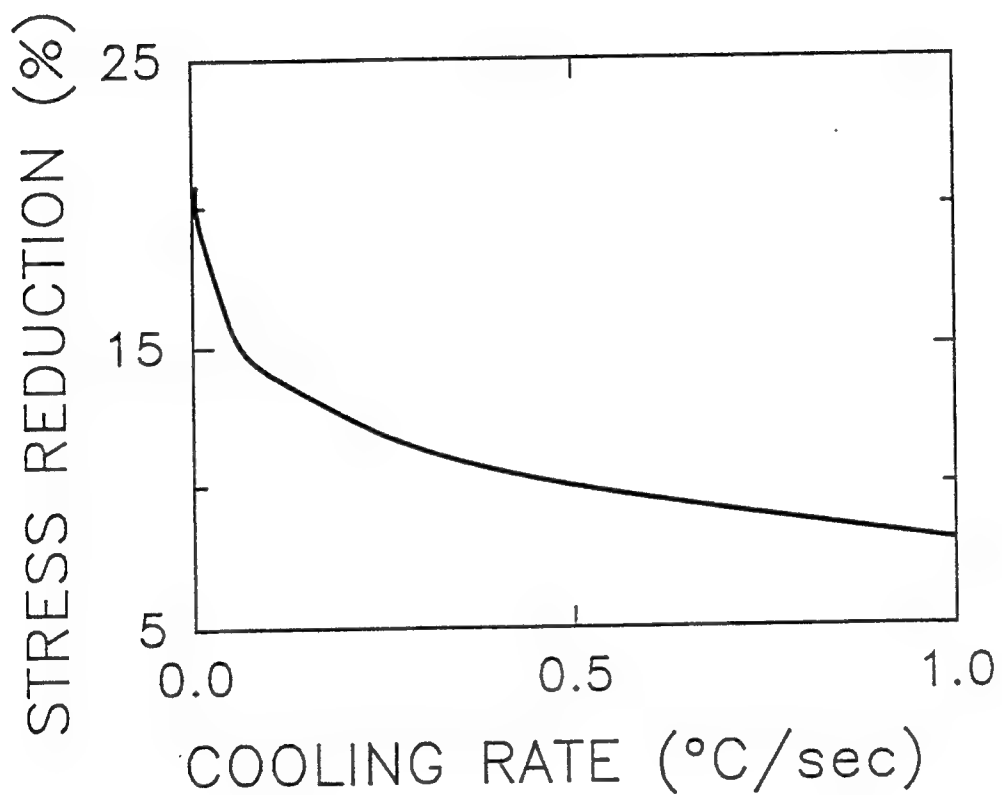
Fig. 4-8   Amount of stress reduction due to creep in the matrix at various cooling rates.
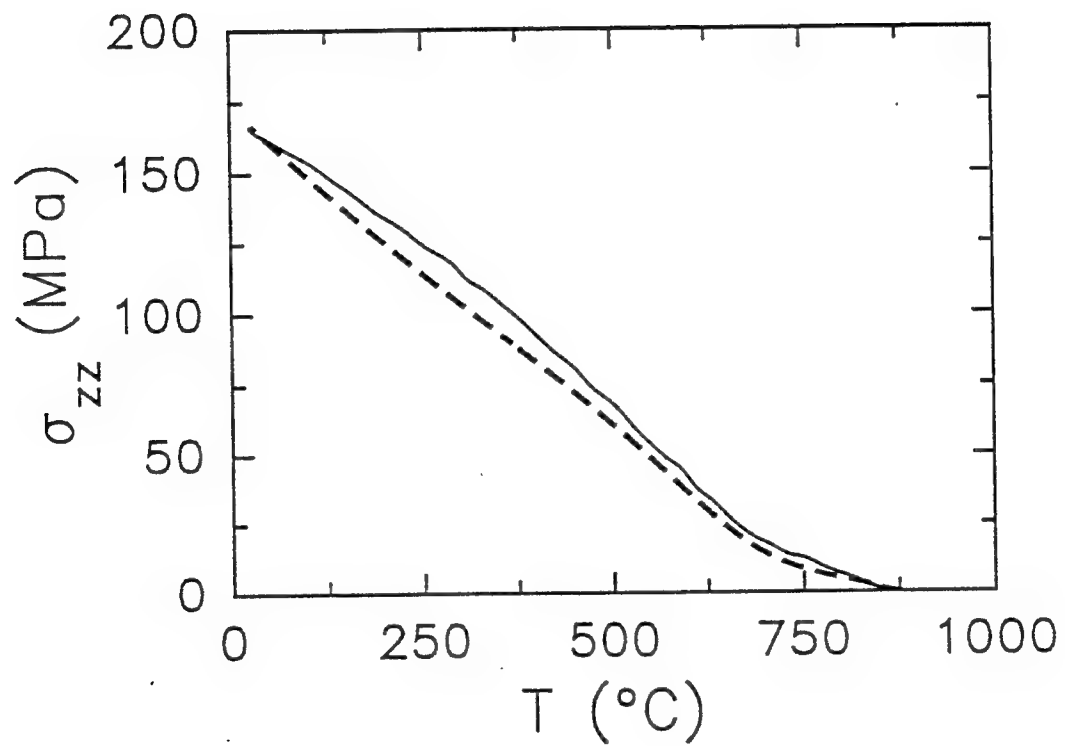
Fig. 4-9   Evolution of axial thermal stress during initial cool-down at 0.5 °C/sec.:
——————— experiment [Ref. 15],   — — — — present result.
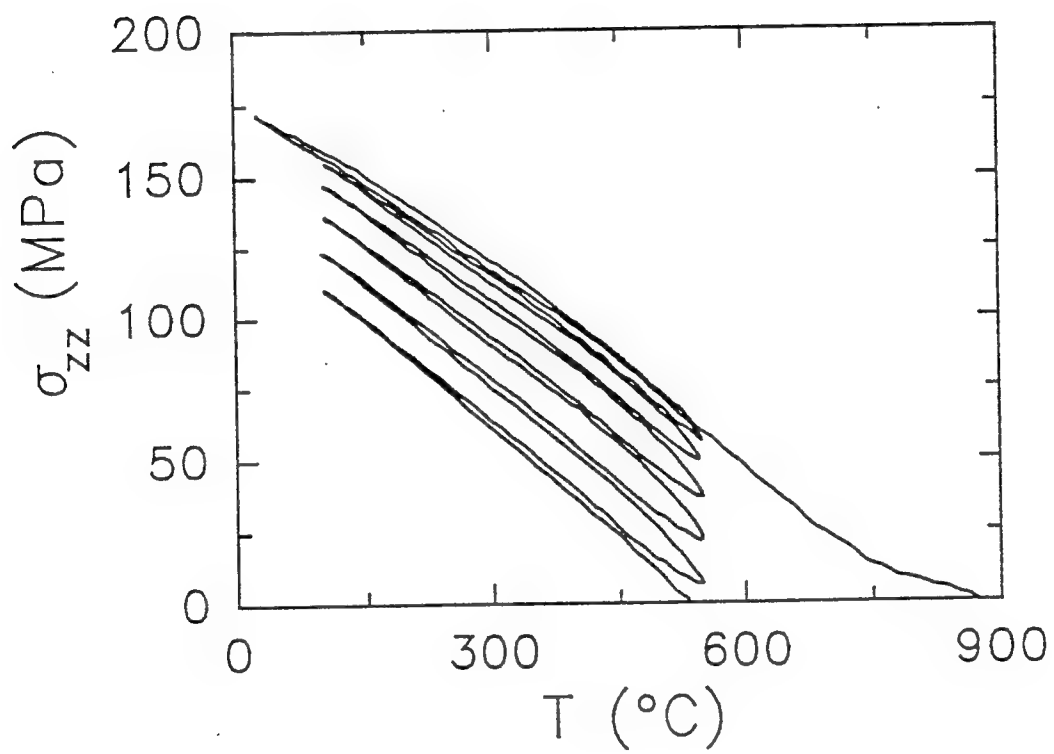
Fig. 4-10   Evolution of axial thermal stress in the matrix during initial cool-down and thermal cycle between 100 - 550 °C at 0.5 °C/sec.

SECTION 5

FATIGUE CRACK GROWTH OF SM-1240/TIMETAL-21S METAL MATRIX COMPOSITE AT ELEVATED TEMPERATURES [5]

ABSTRACT

A series of high temperature fatigue crack growth experiments was conducted on a continuous fiber reinforced SM1240/Timetal-21S composite using three different temperatures; room temperature (24°C), 500°C and 650°C and three loading frequencies; 10 Hz , 0.1 Hz and 0.02 Hz. In all the tests, the cracking process concentrated along a single mode I crack for which the principal damage mechanism was crack bridging and fiber/matrix debonding. The matrix transgranular fracture mode was not significantly influenced by temperature or loading frequency. The fiber debonding length in the crack bridging region was estimated based on the knowledge of the fiber pull-out lengths measured along the fracture surfaces of the test specimens. The average pull-out length was correlated with both temperature and loading frequency. Furthermore, the increase in the temperature was found to lead to a decrease in the crack growth rate. The mechanism responsible for this behavior is discussed in relation to the interaction of number of temperature-dependent factors acting along the bridged fiber/matrix debonded zone. These factors include the frictional stress, the radial stress, and the debonding length of the fiber/matrix interface. In addition, the crack growth speed was found to depend proportionally on the loading frequency. This relationship, particularly at low frequencies, is interpreted in terms of the development of a crack tip closure induced by the relaxation of the compressive residual stresses developed in the matrix phase in regions ahead of the crack tip during the time-dependent loading process.

5.1 INTRODUCTION

The development of continuous fiber reinforced titanium composites is particularly critical for the use in high temperature structural components which are stressed in one dimension only. A key issue in the potential success of these materials is the understanding of their high-temperature damage tolerance characteristics with respect to time-dependent related effects including inelastic deformation and environment attack. Few studies have, however, been made in the area of high temperature damage and, in particular, the high temperature fatigue crack growth behavior of continuous-fiber reinforced metal matrix

---

composites. The current literature shows that the optimum combination of matrix toughness and interfacial strength is achieved when the crack bridging becomes the principal damage mechanism in the metal matrix composites [1-3]. The crack bridging was found to occur in titanium matrix composites under conditions of practical interest, and work at ambient temperature showed that bridged fibers can provide shielding effects which decrease the crack tip driving force thus enhancing the composite resistance to crack propagation [2-5]. In the crack bridging mechanism, the crack growth rate is governed by a process in which the increase in the crack length is accompanied by an increase in the number of fibers bridging the crack. This would continue up to a "steady state" condition produced by the competition between creating more bridged fibers as the crack length increases and the fracture of these fibers as more stress is transferred to them by the increased crack-opening displacements. Here, however, it appears to be difficult to define the conditions at which stable/unstable crack growth transition occurs [2]. Although the subject of the crack bridging is very important and attracting increased attention, a full understanding of related phenomena in metal matrix composites, such as defining a failure criterion for bridged fibers, remains an open issue [1]. This situation is further complicated in cases involving elevated temperatures where fewer studies have been attempted. Bain, et al., worked on SCS-6/Ti-6Al-4V at 318 °C for frequencies of 20 Hz, 0.33 Hz and 0.033 Hz [6]. Their results showed that while there was no considerable difference in the fatigue crack growth rates for the first two frequencies, the fatigue crack growth rate for the 0.033 Hz testing increased by a factor of 40. This increase was attributed to environmental damage affecting the Ti-6Al-4V matrix material. They, however, did not observe changes in the fracture surface features of specimens tested at the three different frequencies. No crack bridging was reported in their work, and for all their tests the fatigue crack growth rate increased in proportion to the increase in crack length. Ibbotson, et al., studied the fatigue response of single edge notched (SEN) specimens made of a SiC/Ti-6Al-4V composite. Tests were carried out at both ambient temperature and 550 °C for two different loading frequencies: 10 Hz and 0.5 Hz [5]. They observed that in most cases the crack growth rates initially decreased with increasing crack length. The crack growth rates were, however, found to increase at 550 °C but only at low frequency when compared with those obtained at ambient temperature. Here, none of these studies has identified the mechanisms governing the high temperature crack growth process in titanium metal matrix composites.

In order to fully understand the high temperature fatigue resistance of titanium composites, it is necessary to explore the possible damage mechanisms related to the elevated temperature crack growth behavior of this kind of composites. This is the basic motivation behind the work performed in the present study which focuses on the high temperature bridged fatigue crack growth behavior of SM1240/Timetal-21S composite. In this work, the crack growth response at various temperatures and loading frequencies was obtained. Attempts were made, utilizing load conditions promoting the crack bridging, to identify the role of time-dependent effects on the crack bridging and related failure mechanisms.

5.2 MATERIAL AND EXPERIMENTAL PROCEDURE

The material used in this study is a SM1240/Timetal-21S composite. The matrix material is the Timetal-21S which is a metastable β titanium alloy. The composition of this alloy (in wt%) is 0.1 Fe, 16.0 Mo, 3.06 Al, 2.9 Nb, 0.2 Si, 0.22 C, 0.12 O, 0.005 N with the balance being Ti [7]. The SM1240 fiber consists of 10 μm diameter tungsten-cored SiC monofilament with dual vapor-deposited coatings of carbon and boron-rich titanium diboride at the surface. The thickness of each of these layers is about 1 μm with the total fiber diameter being 100 μm. The composite material is made of seven matrix foils (each is 112 μm in thickness) with continuous SM1240 fibers having approximately a volume fraction of 35% and oriented along the 0° direction. The mechanical properties of the matrix material as well as those of the fiber are listed in Table 5.1.

Table 5.1: Mechanical Properties of the SM1240 Fiber and the Timetal 21S Matrix

Property	[ref.]	24(°C)	500(°C)	650(°C)
E_m (GPa)	[7]	98.2	72.4	47.6
ν_m	[8]	0.35	0.35	0.35
$\sigma_{Y,m}$ (MPa)	[7]	1043	552	245
$\sigma_{U,m}$ (MPa)	[7]	1089	641	289
$\epsilon_{F,m}$ (%)	[7]	>3.9	>10.5	50-55
E_f (GPa)	[9]	390	390	390
ν_f	[10]	0.3	0.3	0.3
$\sigma_{U,f}$ (MPa)	[9]	3340	3340	3340
$\epsilon_{F,f}$ (%)	[11]	1	1	1

The composite was consolidated using the vacuum hot-pressing process employing pre-established critical processing parameters. All consolidated composite plates, measuring 900 mm x 100 mm x 1 mm, had received a stabilization heat treatment (621 °C/8 hours) in a dynamic vacuum furnace. Fig. 5.1(a) is a chemically etched cross-section of the as-fabricated composite showing a hexagonal fiber arrangement and traces of the foil-to-foil interfaces. The average center-to-center fiber spacing is approximately 150 μm. Typical microstructural details of the immediate matrix surrounding a fiber are shown in Fig. 5.1(b). One observes that very fine α phase has precipitated homogeneously within the grains as well as along the grain boundaries. The average grain size in areas surrounding the fibers is about 12 μm, which is smaller than that of the matrix material (about 50 μm). The presence of finer grains is associated with recrystallization during fabrication where large amount of viscoplastic flow occurs near the fibers [11]. The high viscoplastic strain, which is necessary to achieve complete fiber/matrix bonding, produces high dislocation densities in areas surrounding fibers which, in turn, should provide sufficient driving force for recrystallization and the formation of smaller grain sizes in these areas [12-14].

The composite plates were machined into rectangular specimens measuring 75 mm x 10 mm with a center hole of 1.575 mm in diameter. All machining was accomplished using diamond cut-off wheels and diamond drills. In order to aid crack initiation, notches were cut at opposite horizontal edges of the center hole using a diamond-coated chromium wire having a diameter of 30 μm. The change of crack length during testing was measured using the DC potential-drop technique calibrated with the means of two travelling microscopes. The test specimens were heated using 8 quartz lamps arranged in an open furnace configuration, allowing a ± 4°C maximum temperature variations along the 60 mm specimen gage length. Testing temperature was measured by two thermocouple placed on opposite ends of the specimen gage length and at a distance of 14 mm from the center hole. In addition to testing at room temperature (24°C), two other temperatures were investigated, 500°C and 650°C. The temperature of 500°C is the expected application temperature for the composite under investigation while the 650°C represents a near upper limit use of this type of Sigma fiber [14].

All specimens were gripped by flat hydraulic grips and tested using a servohydraulic testing machine equipped with computer control and data acquisition capabilities. Tests were carried out in air and in vacuum environment (10^{-7} torr) under constant load range. Loads were applied parallel to the 0° orientation of the fibers. The maximum applied stress was selected as 292 MPa with the stress ratio of 0.1. Stresses in this range were shown to produce crack bridging during the fatigue crack growth process in Ti-composites [3-5]. Specimens for low frequency tests were subjected to pre-cracking performed with a loading frequency of 10 Hz while the stress range, R ratio and temperature were set equal to values intended for use in the actual test.

Three loading frequencies were examined in this test program: 10 Hz, 0.1 Hz and 0.02 Hz. The selection of these frequencies was based on results obtained from previous work on Timetal-21S fiberless laminates [7] which showed that frequencies higher than 10 Hz produce insignificant oxidation damage at temperatures below 650 °C. Frequencies lower than 10 Hz, on the other hand, were shown to induce effects related to viscoplastic deformation and

oxidation at temperatures up to 650 °C.

Several tests were stopped before the specimen separation occurred in order to identify related fiber/matrix damage features. In each of these cases one of the specimen's surfaces was ground to a depth sufficient to reveal the near surface fiber array. This provided an opportunity to observe possible fibers bridging and the extent of fiber/matrix debonding in relation to the crack path. The fracture surfaces of all specimens were subjected to scanning electron microscopy in order to identify the features of the fracture mechanisms and the changes taking place in the fiber/matrix interface region.

5.3 RESULTS AND ANALYSIS

5.3.1 The Crack Growth Process

In all the tests, the fatigue fracture process was seen to advance mainly along a single dominant crack perpendicular to both the 0° fiber orientation and the direction of the applied load. The dominant damage mechanism associated with this single crack was crack bridging, an example of which is shown in Fig. 5.2. An advantage of the confinement of the fracture process to a single propagating crack is that the damage in the vicinity of the crack tip could be described in terms of the crack growth rate. For this purpose, plots of crack length versus cycle number for each of the tests were constructed (Fig. 5.3). The slopes of these curves, which represent the crack growth rates, were in turn plotted versus the crack length, a. These results are compared in Fig. 5.4(a) for the loading frequency of 10 Hz with different temperatures and in Figs. 5.4(b) and 5.4(c) for the temperatures 500°C and 650°C, respectively, with different loading frequencies.

Results in Figs. 5.4 show that the fatigue crack growth exhibits two distinctive sequential stages. The first is a pattern of continuously decreasing crack growth rate as the crack length increases. The crack length corresponding to this crack bridging stage, as well as its cycle number, was observed to vary between tests. The end of the crack growth retardation due to bridging is marked by the attainment of the minimum crack growth rate pertaining to the particular test condition. This minimum rate ranges from 5.6×10^{-6} mm/cycle in the case of the 24°C/10 Hz test to 2.4×10^{-7} mm/cycle in the case of the 500°C/10 Hz test. The first crack bridging stage is followed by a stage which consists of either a single or repeated events of crack growth acceleration and retardation. This pattern of two-stage crack growth has also been observed in the work of Ibbotson, et al., in the study of SCS-6/Ti-6Al-4V composite at both ambient temperature and 550 °C [5] and in the work of Walls, et al., carried out on SCS-6/Ti-15-3 composite at room temperature. In no test carried out here, however, was complete crack arrest observed.

The importance of each of these two crack growth stages described above was determined on the basis of the ratio of the number of cycles corresponding to the initial crack bridging stage to the number of cycles to failure. In each of the tests, this ratio was found to be greater than 30% of the total lifetime of the corresponding test specimen, see Fig. 5.5.

5.3.2 Fractography

The different fracture processes encountered in each of the crack growth stages mentioned above are evident in the appearance of the fracture surface features. For example, Fig. 5.6(a), which belongs to the 650°C test, shows two different fracture zones, the first is for the crack bridging stage and the second is for the repeated crack growth acceleration/retardation stage. The first zone has excessive fiber core damage, which may have resulted from the application of a large number of fatigue cycles and prolonged thermal exposure. The pull-out fibers in this zone are relatively short. The second zone shows no fiber core damage and displays longer fiber pull-out length. An example of the instable fracture zone is shown in Fig. 5.6(b); it has a high degree of matrix deformation surrounding the pull-out fibers.

The matrix cracking mode for all tests was observed to be transgranular. A typical example of the fracture surface features associated with this mode is shown in Fig. 5.6(c). They consist of cleavage facets; the size of which seems to depend on their location on the fracture surface and the corresponding crack growth rate; the higher the growth rate, the larger the cleavage facet size. Furthermore, foil-foil interfaces along the fracture surface did not interrupt the continuity of the cleavage planes. Isolated colonies of fatigue striations were found on fracture surfaces of some of these tests but did not represent a dominate fracture mode in any of the test cases.

In examining the interfacial region of the bridging fibers, it was interesting to observe that, regardless of the test temperature, debonding occurred within the carbon coating layer, see Fig. 5.6(d). This form of debonding is facilitated by the compliant nature of the carbon layer. The surface morphology of the bridging fibers in the crack bridging stage are distinct for different temperatures. At 24°C, a patch-like of residual carbon layer can be observed (see Fig. 5.7(a)), while at 500°C and 650°C, this type of layer is absent (see Fig. 5.7(b)). It is possible that the presence of this layer at room temperature be a source of an increased fiber/matrix friction during the frictional sliding of the bridging fibers. At high temperatures, this extra carbon layer would be gradually oxidized to form CO/CO_2 and would evaporate thus making the fiber/matrix interfaces smoother than that at 24°C. This speculation is supported by the fact that the carbon patch layer do exist on the surfaces of the pull-out fibers within the final failure stage of the 500°C and 650°C tests. The insufficient exposure time during the rapid fracture stage results in no oxidation of the above mentioned residual carbon layer along the fibers in this region. It is worth mentioning that the surface morphology of the bridging fibers at 650°C in vacuum is similar to the one at 24°C. In general, however, one could conclude that no radical differences exist between the surface appearances of the pulled-out fibers examined in all test cases.

The debonding nature of the bridging fibers was examined by removing the outermost matrix layer of several fractured specimens; Fig. 5.8 corresponds to the 10 Hz/ 500°C case. It can be observed that fiber breakages occurred along planes which do not coincide with the matrix crack plane. By assuming that the fiber pull-out length is proportional to the debonding length, the pull out lengths were measured along the fracture surfaces of the test specimens using a scanning electron microscope. Results, listed in Table 2, show that, under

the same applied stress range and R ratio,, the fiber pull-out length in the crack bridging region increases with temperature and inversely proportional to the loading frequency.

5.3.3 Influence of Temperature

The influence of the test temperature on the crack growth rate for the 10 Hz loading frequency is shown in Fig. 5.4(a). The crack growth rate, da/dN, for the same applied stress intensity range, ΔK_{app} (or the same crack length) decreases as the temperature increases. This indicate that the effective crack tip driving force is a decreasing function of the test temperature.

This observation is supported by the experimental work of Zhang et al [15] who investigated the use of the crack tip opening displacement range, $\Delta\delta$, to examine the relationship between the test temperature and the crack tip driving force. In this, they have used a laser displacement gage

to measure the $\Delta\delta$ at different positions along crack lengths subjected to temperatures and loading conditions similar to those described in Fig. 5.4. Their results are shown in Fig. 5.9. From this figure the crack tip opening displacement range, $\Delta\delta_{tip}$, identified as the displacement at a position located 1 μm from the crack tip, can be measured. These measured $\Delta\delta_{tip}$, when examined in relation to the corresponding da/dN (see Fig. 5.10), show that the crack growth rate is proportional to $\Delta\delta_{tip}$, thus indicating that $\Delta\delta_{tip}$ can be used as a measure of the crack tip driving force. Furthermore, for the same crack length, $\Delta\delta_{tip}$, was found to be inversely proportional to temperature. A possible reason for the decrease in the crack tip driving force as the temperatureincreases is explained on the basis of the assumption that the effective stress intensity factor range experienced by the crack tip, $\Delta K_{eff,}$ could be written as [e.g. 16-18]:

$$\Delta K_{eff} = \Delta K_{app} - \Delta K_{sh}$$

where ΔK_{sh} is the crack tip shielding provided by bridging fibers and is calculated by the following expression [19,20] :

$$\Delta K_{sh} = \frac{1}{\pi\,V_f} \int_{a_0}^{a} \Delta S_f\, \ln \left| \frac{\sqrt{a^2-x^2}\, -\, \sqrt{a^2-s^2}}{\sqrt{a^2-x^2}\, +\, \sqrt{a^2-s^2}} \right|\, ds$$

where a_0 is the initial crack length, V_f is the fiber volume fraction, x is a position along the crack length and ΔS_f is the fiber bridging stress range. For the same crack geometry and length, ΔK_{sh} is thus dictated by ΔS_f. The work of the authors [21] based on a combined analytical and experimental measurements of $\Delta\delta$ for the composite under investigation,

Table 5.2 : Average Fiber Pull-Out Length Varying with Temperatures and Frequency

Temperature (°C)	Frequency (Hz)	Av. Fiber Pull-Out Length (μm)
24	10	61
500	10	86
650	10	107
500	0.1	129
650	0.1	117
650	0.02	152

showed that ΔS_f increases as the temperature increases. The mechanisms responsible for this increase involve in addition to the test temperature, the interaction of number of factors acting along the bridged fiber/matrix debonded zone. These factors include the frictional shear stress, τ_s, the radial stress, σ_r, and the debonding length occurring during the crack bridging process. Their effects could be understood by examining the trend of τ_s which is written, assuming that the friction process in the debonding zone follows Coulomb's law, as:

$$\tau_s = \tau_0 - \mu \, \sigma_r$$

where μ is the coefficient of friction and τ_0 is an initial base level of τ_s. In this equation the decrease of the magnitude of τ_s with the increase in the test temperature is attributed mainly to the reduction of σ_r [22]. Therefore, if τ_s is viewed as the stress resisting the further debonding of the fiber/matrix interface [23-25], then as the temperature increases, the length of the debonded portion of this interface is expected to increase. This is consistent with the results concerning the fiber/matrix debonded lengths listed in Table 5.2. As this interface length increases, the associated Mode II crack tip driving force increases. If the crack tip driving force due to the applied load range is considered a simple summation of Mode I plus Mode II crack tip driving forces, one could then argue that for the same bridged crack length subjected to the same ΔK_{app}, the net Mode I effective crack tip driving force is inversely proportional to temperature. This speculation is currently under experimental as well as numerical examinations by the authors.

5.3.4 Influence of Loading Frequency

The influence of the loading frequency on the crack growth speed da/dt at both the 500°C and the 650°C cases are shown in Figs. 5.11(a) and 5.11(b). The use of da/dt instead of da/dN is based on the fact that the loading frequency represents a time-dependent component of the crack growth process. It is apparent from these figures that a decrease in the loading frequency leads to a decrease in the crack growth speed which could be explained in terms of the associated decrease in the crack tip shielding. An important feature of the low frequency loading is the increasing role of the time-dependent deformation of the matrix phase, see Fig. 5.6(b). A consequence of the matrix deformation and associated matrix stress relaxation, is the increase of the matrix-to-fiber load transfer which could result in the increase of the fiber bridging stress and consequently the crack tip shielding. Zhang and Ghonem [26] have studied the alteration of the fatigue crack tip driving force by focusing on the crack opening displacement, δ, at high and low frequency loadings including conditions where hold time durations are imposed at the maximum load level. Typical δ loops for the 0.1Hz + 10 s hold time and 0.1Hz + 100 s hold time tests in addition to the 10 Hz test are shown in Fig. 5.12. Their results revealed the presence of crack tip closure associated with low frequency loadings. At a particular test temperature and for the same crack length, the magnitude of this closure, and consequently the crack tip shielding was found to increase with the decrease in the loading frequency. The occurrence of the crack tip closure was explained as being a result of the development of a matrix flow in the composite material ahead of the crack tip. A result of which, the continuous relaxation of the matrix axial stresses without the ability of the brittle fiber to accommodate the corresponding matrix deformation could produce matrix axial compressive residual stress. This stress, when relaxed due to the matrix fracture as a result of the crack tip propagation, would close the crack surfaces behind the crack tip thus producing the observed crack closure.

5.4 CONCLUSIONS

A series of fatigue crack growth experiments were conducted on specimens made of the continuous fiber reinforced SM1240/Timetal-21S composite employing a combination of temperatures and loading frequencies. Major conclusions of this study can be summarized as follows:

1.   Under loading conditions promoting fiber bridging, the fatigue crack growth process exhibits two consecutive stages: a crack growth deceleration stage where the crack growth rate decreases continuously as the crack length increases and a crack growth acceleration stage which consists of either a single event of crack growth acceleration leading to crack instability and final failure or repeated events of growth acceleration and deceleration followed, again, by crack instability and final failure. No crack arrest was observed in the present study.

111

2. The matrix fracture mode is not significantly influenced by temperature or loading frequency. The transgranular morphology with cleavage facets is dominated for all the test cases. Furthermore, the average fiber pullout length was found to increase with temperature and with the decrease of the loading frequency.

3. The crack growth rate, da/dN, for the same applied stress intensity range, ΔK_{app} (or the same crack length) decreases as the temperature increases. This is interpreted in terms of the temperature related decrease of the effective crack tip driving force due to the enhancement of the propagation of the bridging fiber /matrix interfaces.

4. The decrease in the loading frequency results in a decrease of the fatigue crack growth speed, da/dt. The associated increase in the crack tip shielding is explained on the basis of the development of crack closure due to the relaxation of the compressive residual stress that has been built up in the matrix phase during the time-dependent loadings.

5.5 REFERENCES

[1] K. S Chan and D. L. Davidson, Fatigue Crack Growth in Fiber-Reinforced Metal-Matrix Composites, in Fatigue of Advanced Materials, eds. by R. O. Ritchie, R. H. Dauskardt and B. N. Cox, Materials and Component Engineering Publications Ltd, P. O. Box 1550, Edgbaston, Birmingham B15 2JZ (UK), 1991, pp. 325-342.

[2] P. Bowen, A. R. Ibbotson and C. J. Beevers, Characterization of Crack Growth in Continuous Fiber Reinforced Titanium Based Composites Under Cyclic Loading, in Fatigue of Advanced Materials, eds. by R. O. Ritchie, R. H. Dauskardt and B. N. Cox, Materials and Component Engineering Publications Ltd, P. O. Box 1550, Edgbaston, Birmingham B15 2JZ (UK), 1991, pp. 379-393.

[3] L. Ghosn, P. Kantzos and J. Telesman, Modelling of Crack Bridging in a Unidirectional Metal Matrix Composite, International Journal of Fracture, Vol. 54, 1992, pp. 345-357.

[4] D. Walls, G. Bao and F. Zok, Fatigue Crack Growth in A Ti/SiC Composite, in Fatigue of Advanced Materials, eds. by R. O. Ritchie, R. H. Dauskardt and B. N. Cox, Materials and Component Engineering Publications Ltd, P. O. Box 1550, Edgbaston, Birmingham B15 2JZ (UK), 1991, pp. 343-356.

[5] A. R. Ibbotson, P. Bowen and C. J. Beevers, Cyclic Fatigue Resistance of Fiber Reinforced Titanium Metal Matrix Composites at Ambient and Elevated Temperature, 7th Ti Conference, San Diego, July, 1992.

[6]   K. R. Bain and M. L. Gambone, Fatigue Crack Growth of SCS-6/Ti-64 Metal Matrix
        Composites, in Fundamental Relationships Between Microstructure & Mechanical
        properties of Metal-Matrix Composites, eds. by P. K. Liaw and M. N. Gungor, The
        Minerals, Metals & Materials Society, 1990, pp. 459-469.

[7]   H. Ghonem, Y. Wen, D. Zheng, M. Thompson and G. Linsey, Fatigue Crack Growth
        Characteristics of Ti-β21S Monolithic Laminate, Studies in Applied Mechanics 34:
        Damage in Composite Materials, ed. by G. Z. Voyiadjis, Elsevier Science Publishers
        B. V., New York, 1993, pp. 161-180.

[8]   D. L. Ball, Thermomechanical Fatigue Life Prediction of SCS-6/Beta-21S
        Composites, Workshop Proceedings of Titanium Matrix Composites, eds. by P. R.
        Smith and W. C. Revels, WL-TR-92-4035, 1991, pp. 372-390.

[9]   L. Le Petitcorps, M. Lahaye, R. Pailler and R. Naslain, Modern Boron and SiC CVD
        Filaments: A Comparative Study, Composites Science and Technology, Vol. 32, 1988,
        pp. 31-35.

[10]   D. B. Marshall, M. C. Shaw, W. L. Morris and J. Graves, Interfacial Properties and
        Residual Stresses in Titanium and Aluminide Matrix Composites, Titanium Matrix
        Components, Workshop Proceedings, eds. by P. R. Smith and W. C. Revels, Wright-
        Patterson ABF, Ohio, 1992, WL-TR-92-4035, pp. 329-347.

[11]   R. K. Everett, Diffusion Bonding, Metal Matrix Composites: Processing and
        Interfaces, eds. by R. K. Everett and R. J. Arsenault, Academic Press, Harcourt Brace
        Jovanovich, Publishers, Boston, 1991, pp. 17-42.

[12]   Robert E. Reed-Hill, Physical Metallurgy Principles. PWS-KENT Publishing
        Company, Boston, 1973.

[13]   M. Taya, M. Dunn and H. Lilholt, Long Term Properties of Metal Matrix
        Composites, Metal Matrix Composites — Processing, Microstructure and Properties,
        Proceedings of the 12th International Symposium on Materials Science, eds. by N.
        Hansen, d. J. Jensen, T. Lefferes, T. Lorentzen, A.S. Pederson, O.B. Pederson, and
        B. Ralphet, Riso0 National Laboratory, Roskilde, denmark, 1991, pp.149-171.

[14]   K. Schulte and K. Minoshima, Mechanisms of Fracture and Failure in Metal Matrix
        Composites, in Metal Matrix Composites — Processing, Microstructure and
        Properties, Proceedings of the 12th International Symposium on Materials Science,
        eds. by N. Hansen, d. J. Jensen, T. Lefferes, T. Lorentzen, A.S. Pederson, O.B.
        Pederson, and B. Ralphet, Riso0 National Laboratory, Roskilde, denmark, 1991,
        pp.123-147.

[15] T. Zhang and H. Ghonem, Crack Opening Displacement of Bridging Fatigue Cracks in Titanium metal Matrix Composites at Elevated Tempertures, Int. Conf. on Composite Engneering, New Orleans, LA, August 1994.

[16] D. B. Marshall and B. N. Cox, Tensile Fracture of Brittle Matrix Composites: Influence of Fiber Strength, Acta Metallurgica et Materialia, Vol. 35, 1987, pp. 2607-2619.

[17] D. L. Davidson, The Micromechanics of Fatigue Crack Growth at 25°C in Ti-6Al-4V Reinforced with SCS-6 Fibers, Metallurgical Transactions, Vol. 23A, 1992, pp. 865-879.

[18] J. K. Shang and R. O. Ritchie, Crack Bridging by Uncracked Ligaments during Fatigue-Crack Growth in SiC-Reinforced Aluminum-Alloy Composites, Metallurgical Transactions, Vol. 20A, 1989, pp. 897-908.

[19] R. M. McMeeking and A. G. Evens, Matrix Fatigue Cracking in Fiber Composites, Mechanics of Materials, Vol. 9, 1990, pp. 217-227.

[20] L. N. McCartney, Mechanics of Matrix Cracking in Brittle-Matrix Fiber-reinforced Composites, Proceedings of Royal Society London, Vol. 409A, 1987, pp.329-350.

[21] Zheng, D. and Ghonem, H., "High Temperature/High Frequency Fatigue Crack Growth Damage Mechanisms in Titanium Metal Matrix Composites", ASTM Symposium on Life Prediction Methodology for Titanium Matrix Composites, Crystal Sands Resort, Hilton Head Island, South Carolina, March 22-24, 1994.

[22] H. Ghonem, Y. Wen and D. Zheng, An Interactive Simulation Technique to Determine the Internal Stress State in Fiber Reinforced Metal Matrix Composites, Materials Science and Engineering, Vol. 177A, 1994, pp.125-134.

[23] M. C. Watson and T. W. Clyne, The Use of Single Fiber Pushout Testing to Investigate the Interfacial Mechanical Properties of Ti-SiC Monofilament Composites, Acta metall. mater., Vol. 40, No. 1, 1992, pp.141-148.

[24] J. G. Bakuckas, Jr. and W. S. Johnson, Application of Fiber Bridging Models to Fatigue Crack Growth in Unidirectional Titanium Matrix Composites, Journal of Composite Technology & Research, Vol. 15, No. 3, 1993, pp.242-255.

[25] D. L. Davidson, K. S. Chan, A. McMinn and G. R. Leverant, Micromechanics and Fatigue Crack Growth in an Alumina-Fiber-Reinforced Magnesium Alloy Composite, Metallurgical Transactions, Vol. 20 A, 1989, pp. 2369-2378.

[26]   T. Zhang and H. Ghonem, Time-Dependent Fatigue Crack Growth Mechanisms in Titanium Metal Matrix Composites, Fatigue fract. Engng Mater. Struct. Vol. 18, No. 11, 1995, pp. 1249 - 1262.
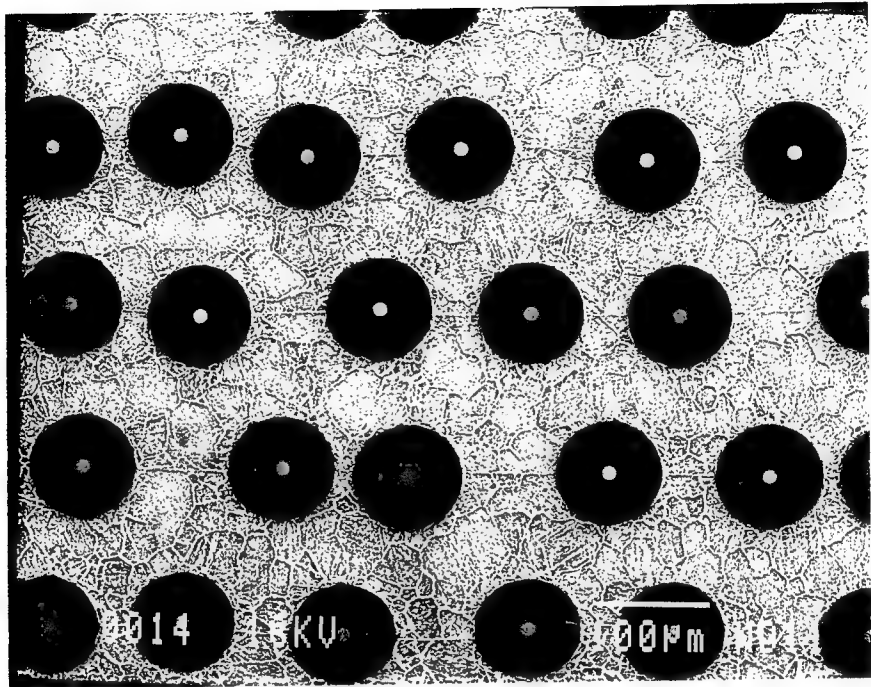
Fig. 5.1(a)   A cross section of the as-fabricated SM1240/Ti-β21S composite specimen
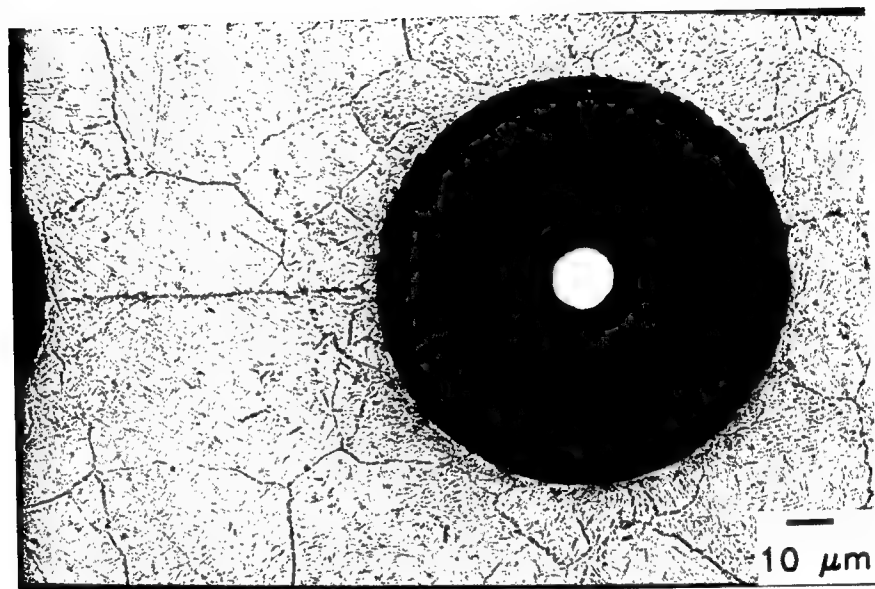
Fig. 5.1(b)   Microstructure details of the Ti-β21S matrix in the fiber surrounding region.
Note the fine matrix grains in the immediate area surrounding the fiber/matrix
interface.

117
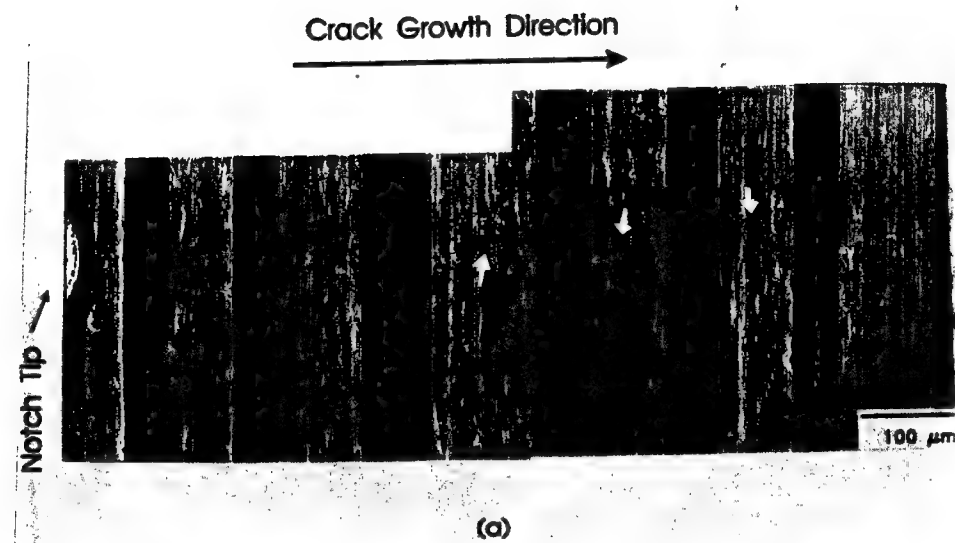
Fig. 5.2 (a) Polished surfaces of test specimens showing crack bridging and positions of
fiber fracture: 24°C/10 Hz test stopped after the crack growth bridging stage-
arrows indicate matrix cracks.

118
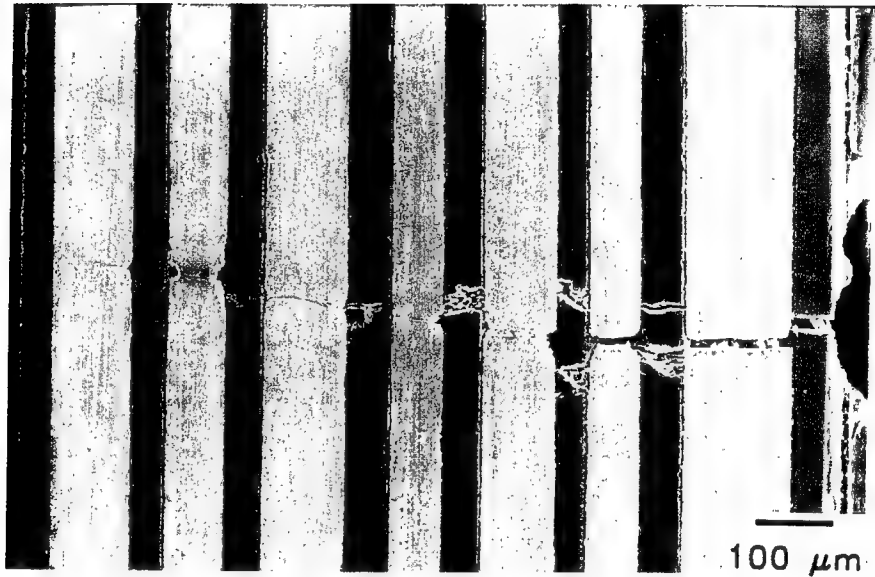
Fig. 5.2(b)   Polished surfaces of test specimens showing crack bridging and positions of fiber fracture: 650 °C/ 0.1 Hz test stopped during the unstable fracture stage.
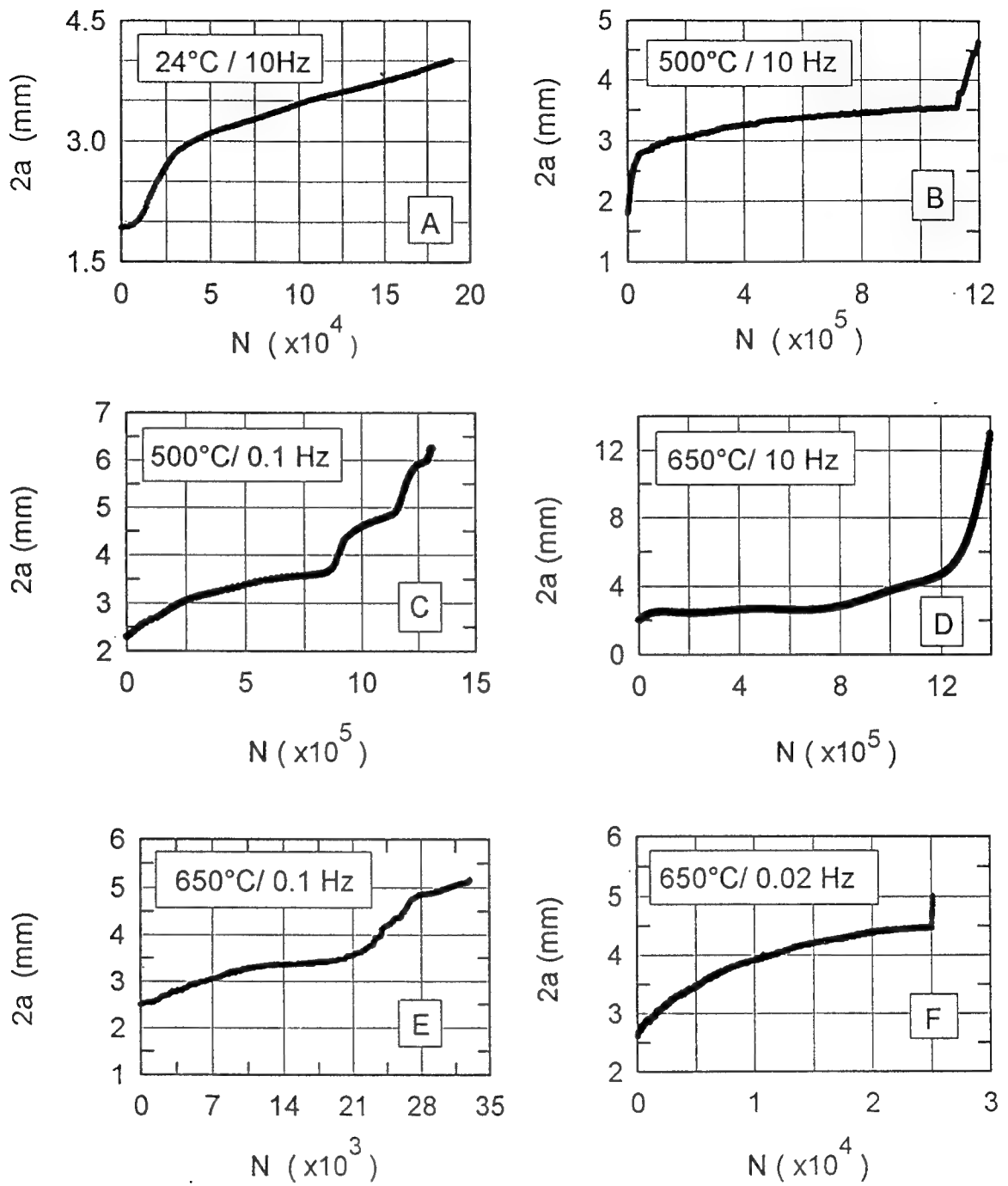
Fig. 5.3   Variation of the crack length, 2a, with the number of fatigue cycles, N, for different test conditions.   (a) 24 °C/10 Hz; (b) 500 °C/10 Hz; (c) 500°C/0.1Hz; (d) 650 °C/10 Hz; (e) 650 °C/0.1 Hz; (f) 650 °C/ 0.02 Hz.

120
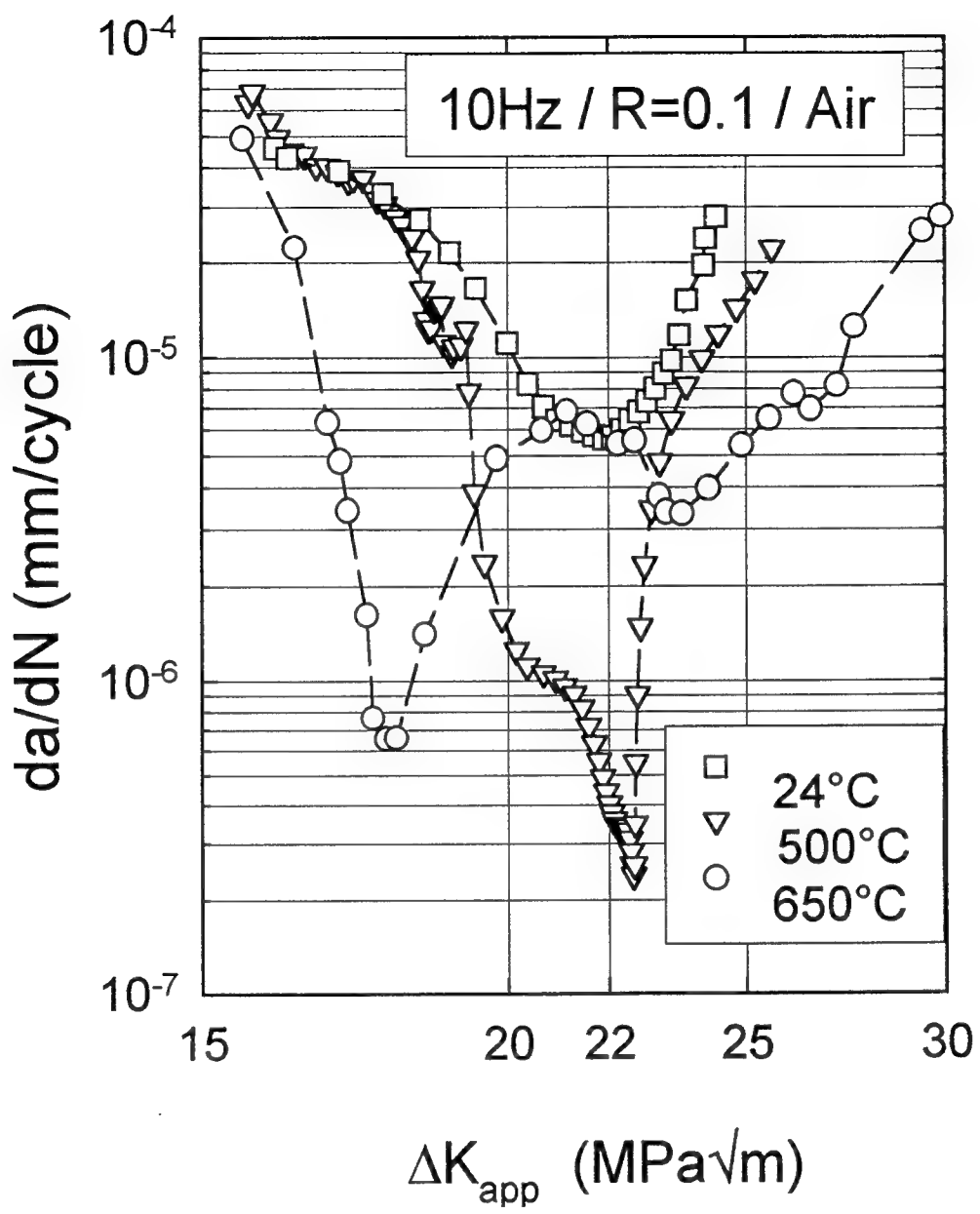
Fig. 5.4(a)   Fatigue crack growth rate, da/dN, versus crack length, 2a, for different test
temperatures
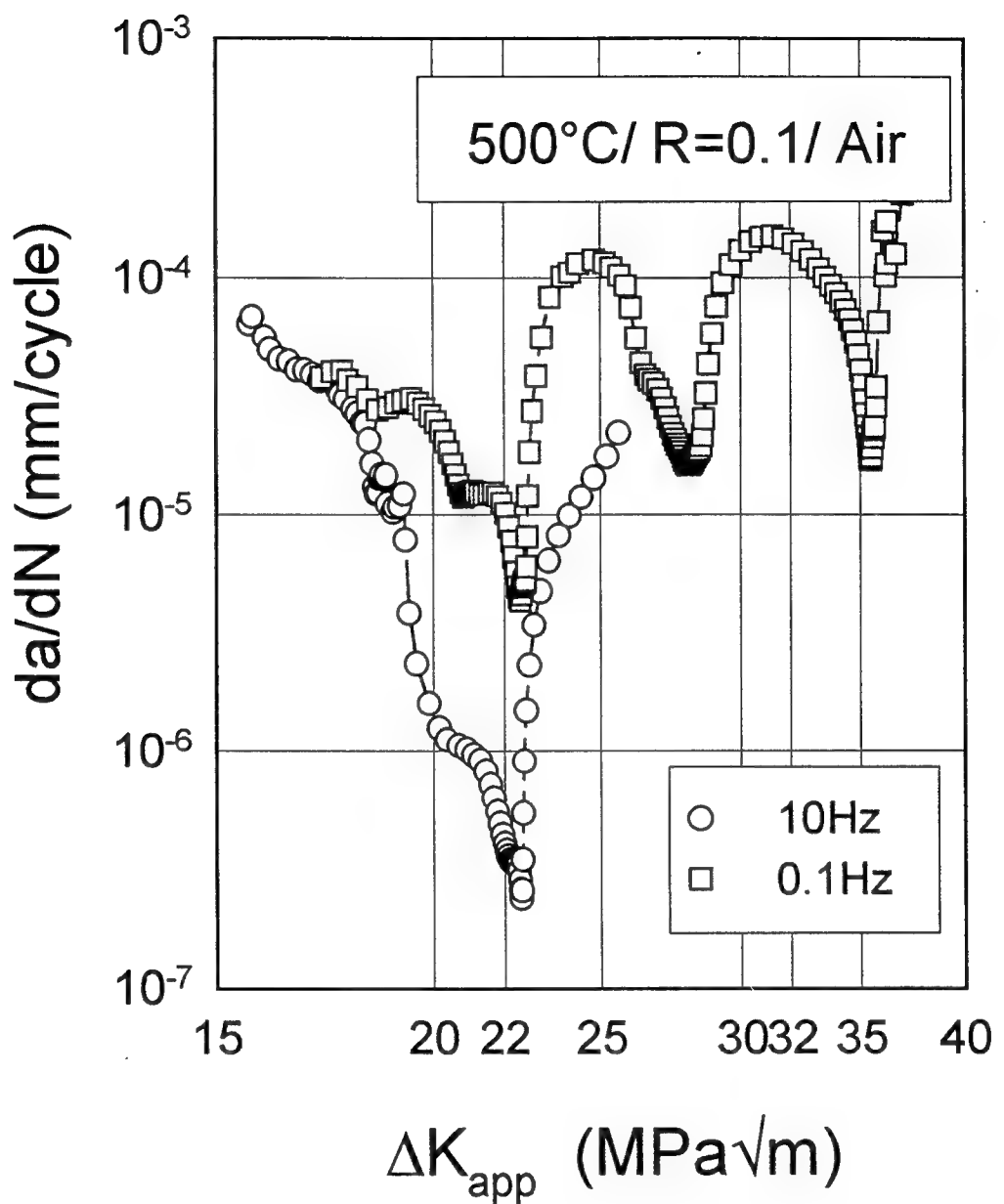
Fig. 5.4(b)   Fatigue crack growth rate, da/dN, versus crack length, 2a, for different loading frequencies at 500 °C
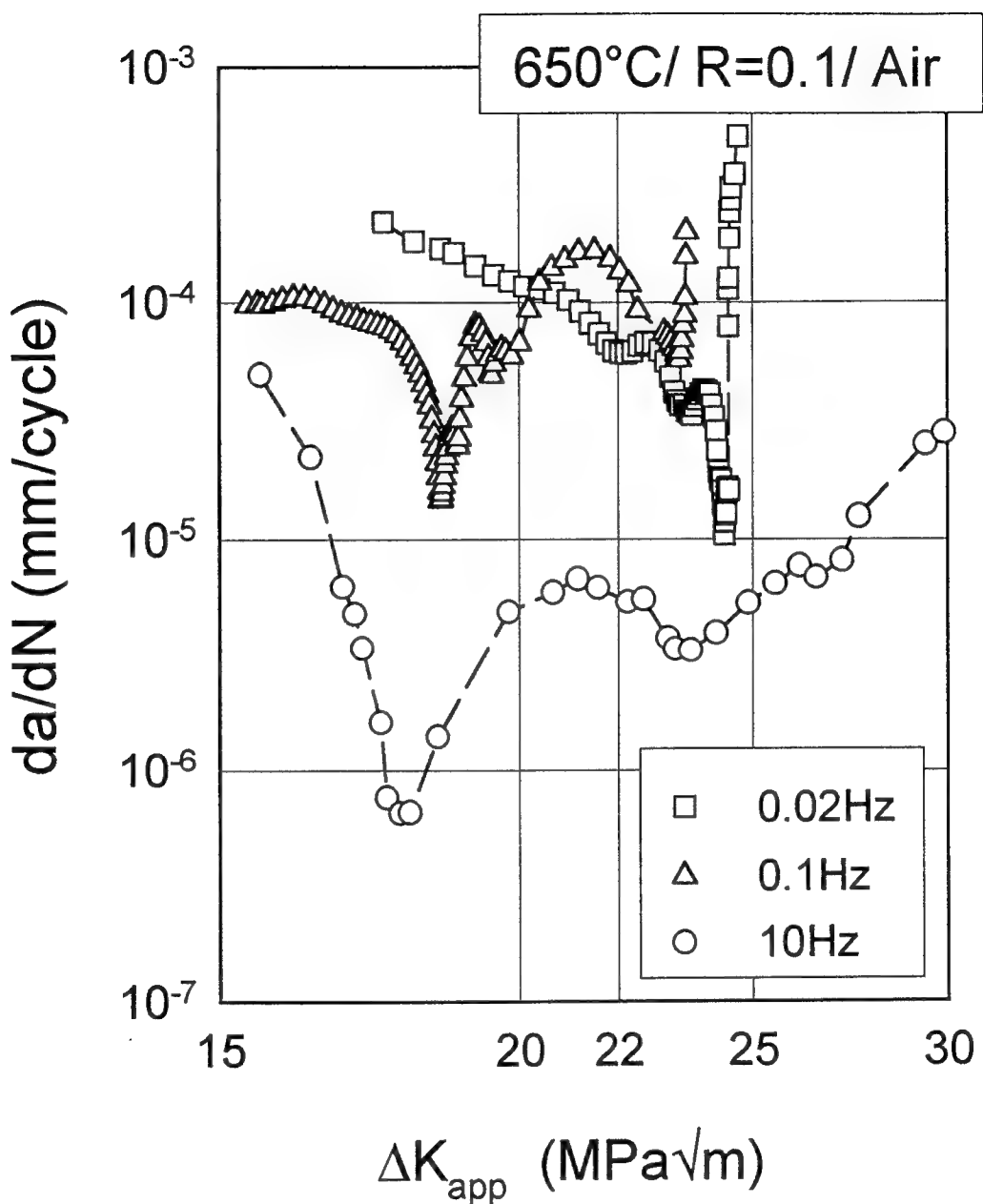
Fig. 5.4(c)   Fatigue crack growth rate, da/dN, versus crack length, 2a, for different loading frequencies at 650 °C.
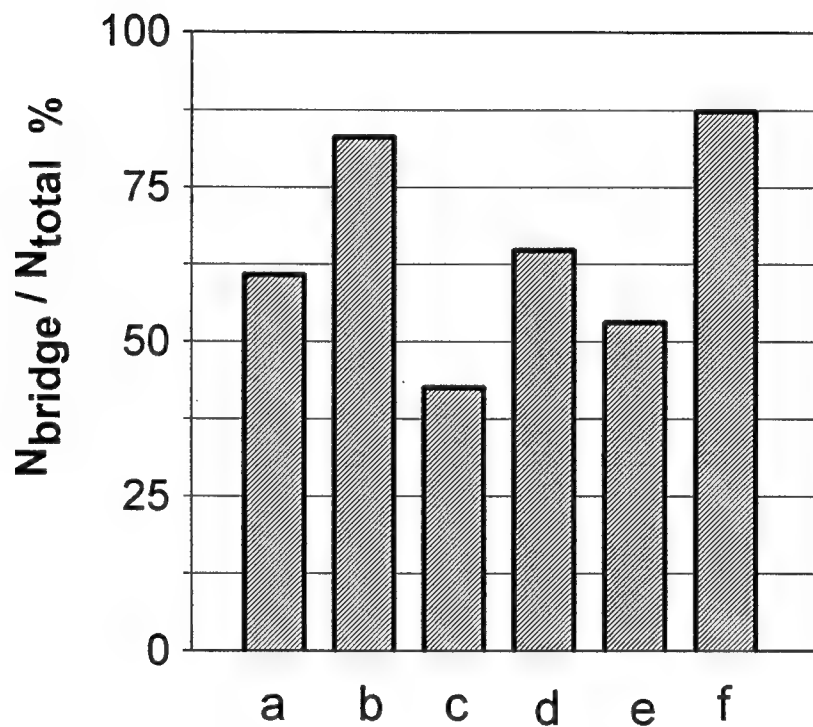
Fig. 5.5   The ratio of the number of cycles of the first crack bridging stage, N_{bridge} to the total number of cycles of the corresponding test, N_{total} (a) 24°C/10Hz; (b) 500°C/10Hz; (c) 500°C/0.1Hz; (d) 650°C/10Hz; (e) 650°C/0.1Hz; (f) 650°C/0.02Hz.
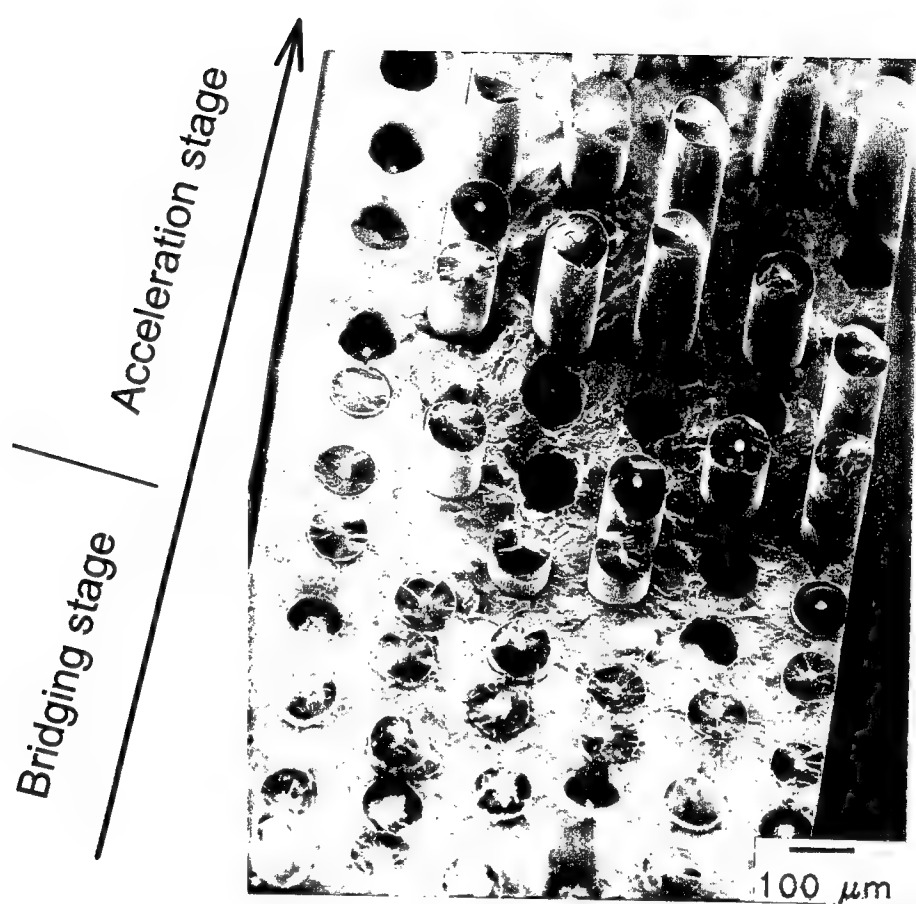
Fig. 5.6(a)   Typical fracture surface showing the crack bridging stage and the crack growth acceleration stage. (650°C/10 Hz).

125
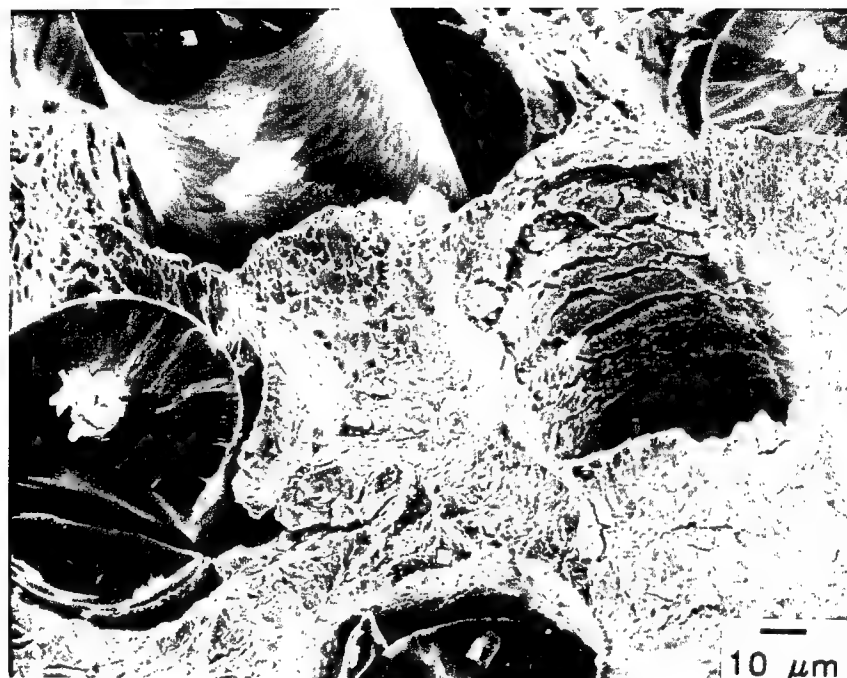
Fig. 5.6(b)   Matrix flow surrounding a pull-out fiber in the unstable fracture region (650 °C/0.02 Hz).
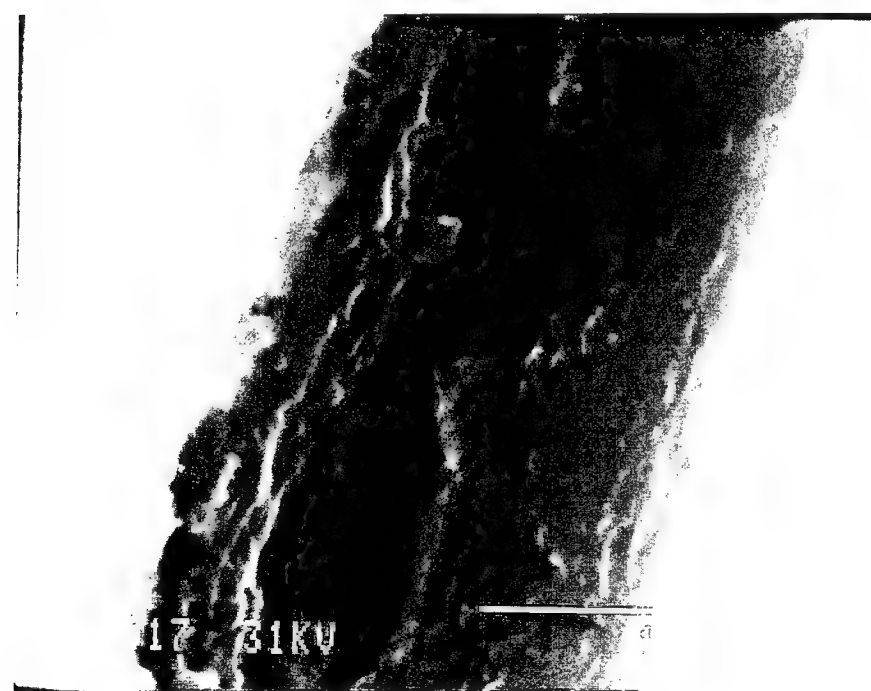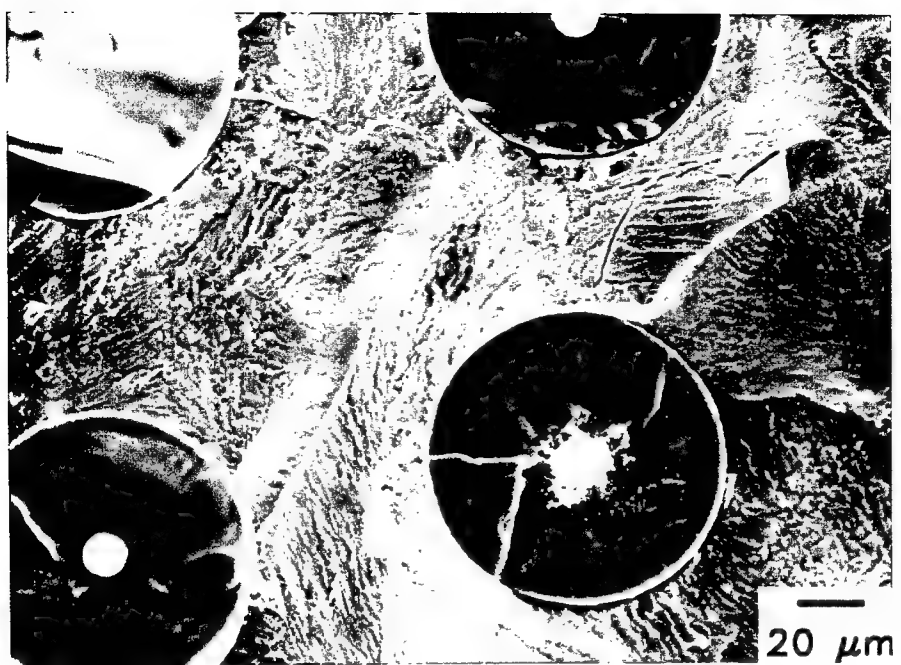
Fig. 5.6   (c) Typical matrix transgranular fracture features as observed in all test conditions; and (d) Matrix/Fiber debonding occuring within the carbon coating layers (650°C/10 Hz test).

Fig. 5.7(a)   Typical surface appearance of bridging fibers showing a patch-like of residual carbon layer at 24°C

Fig. 5.7(b)   Typical surface appearance of bridging fibers showing a smooth surface at 500°C or 650 °C
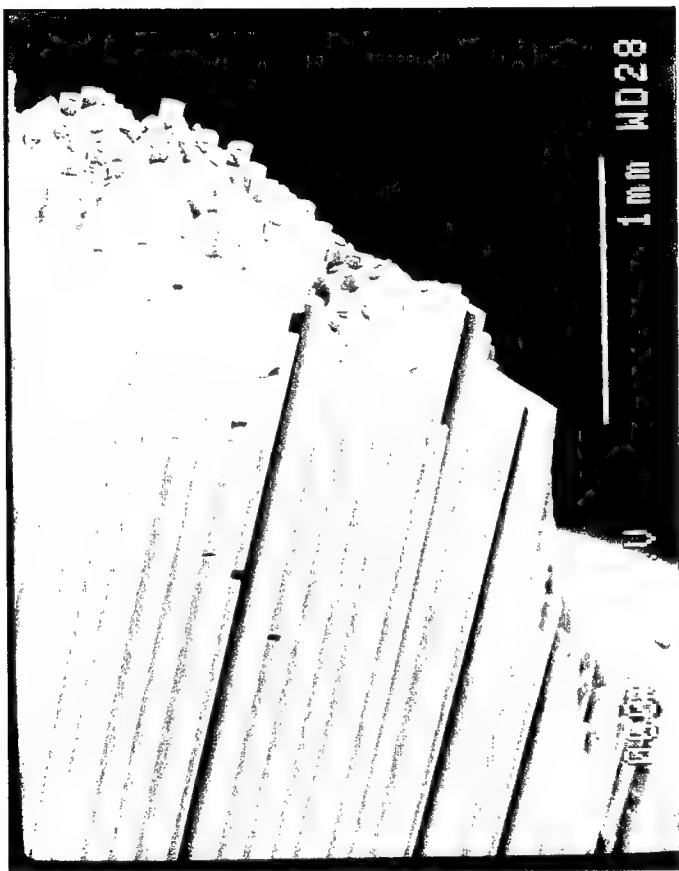
Fig. 5.8   Ground and polished lateral surface of a test specimen showing locations of bridging fiber fractures (650°C/10 Hz).

130
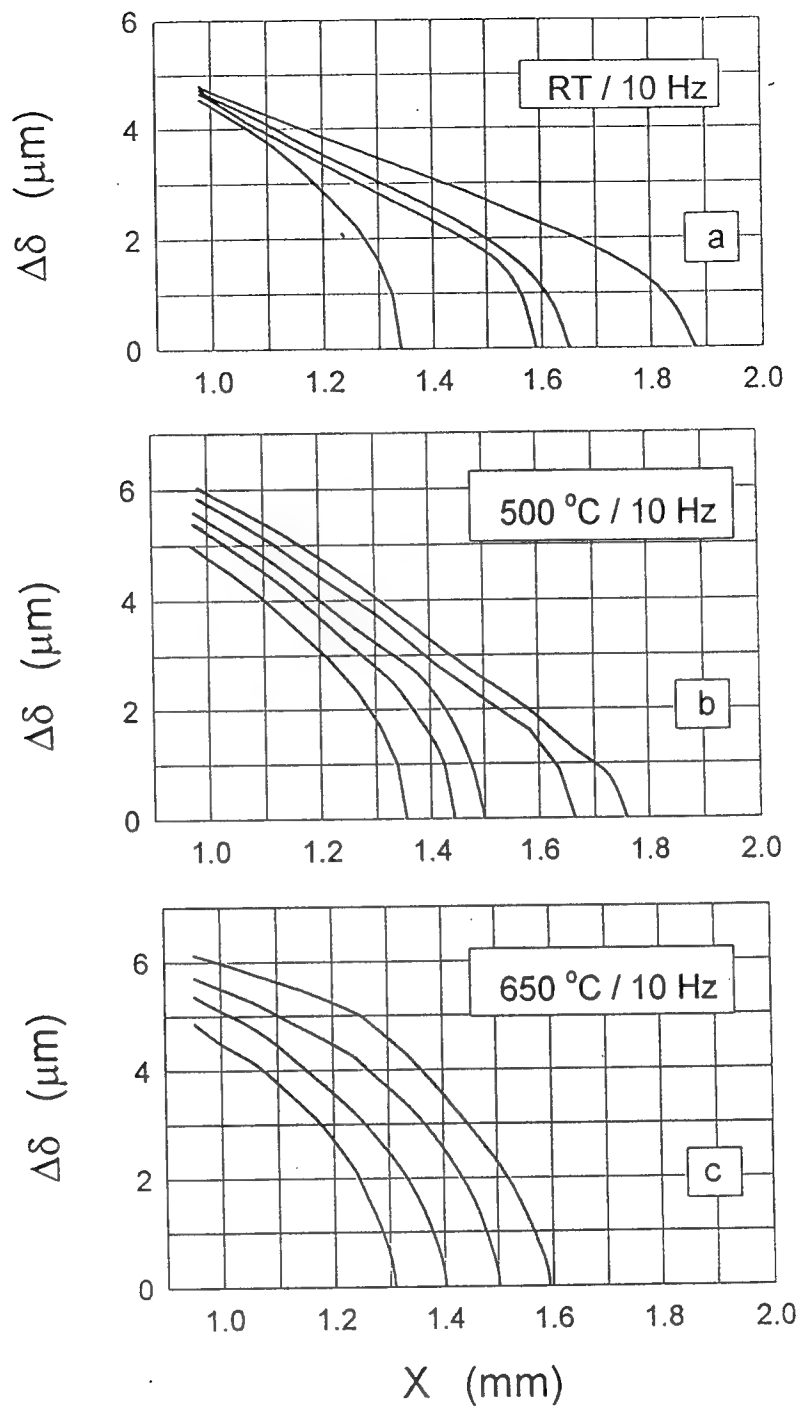
Fig. 5.9   The Crack Opening Displacement range $\Delta\delta$ as a function of temperature for the loading frequency 10 Hz (15).

131
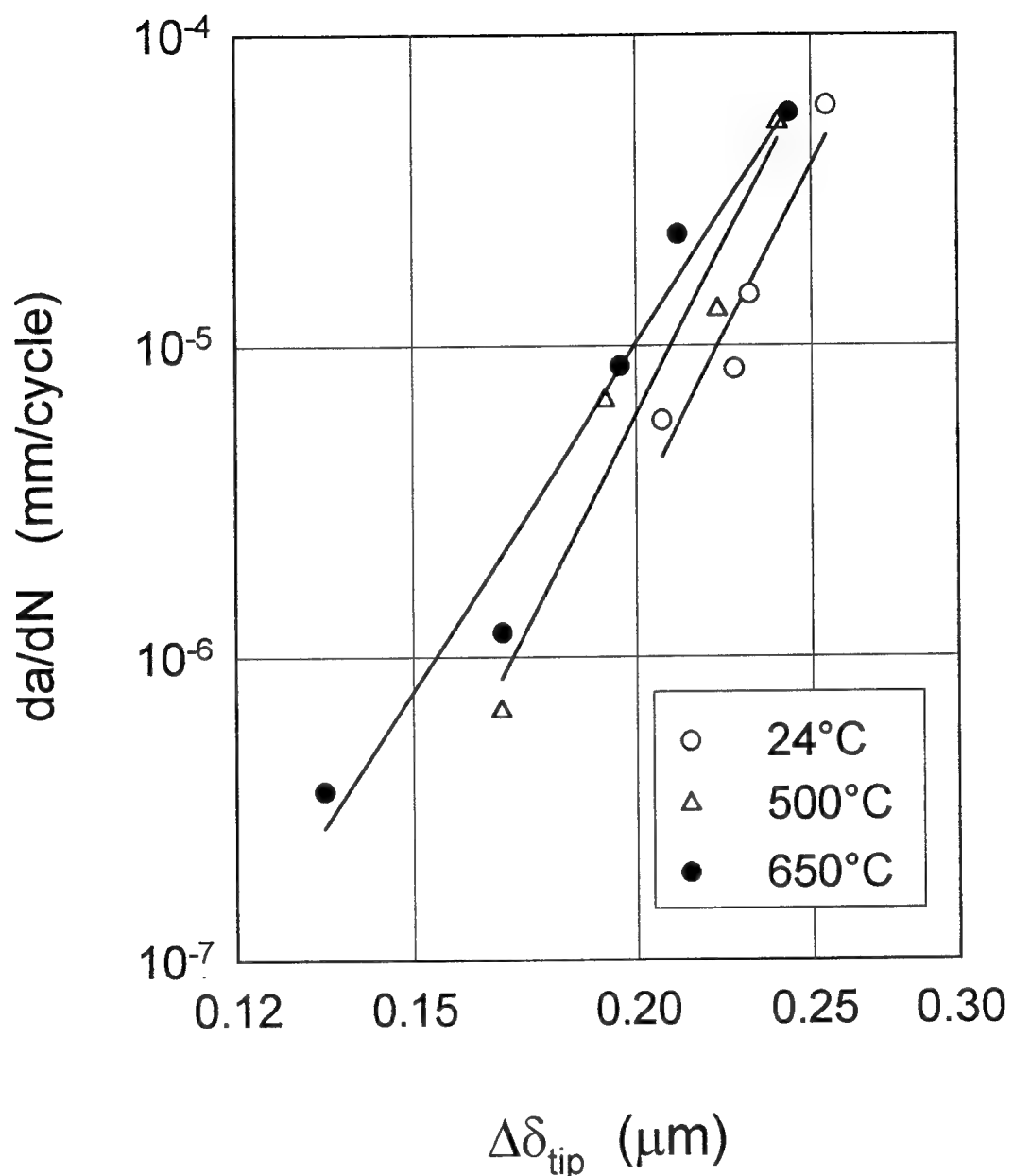
Fig. 5.10   Crack Tip Opening Displacement range, $\Delta\delta_{tip}$, versus the corresponding crack growth rate, da/dN (15).
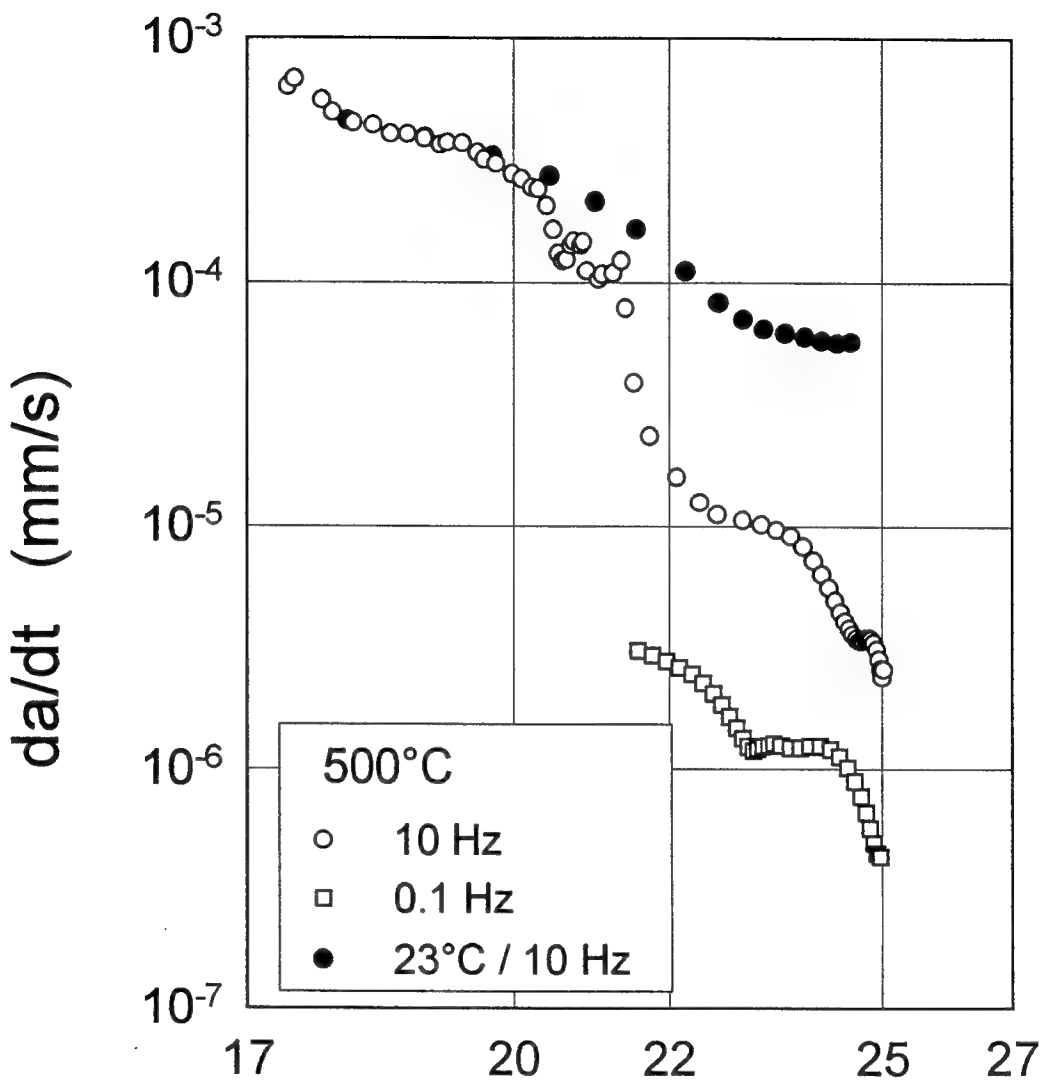
Fig. 5.11(a) Fatigue crack growth rate, da/dt, versus the maximum applied stress intensity factor range, K_{max}, for different loading frequencies at 500°C.

133
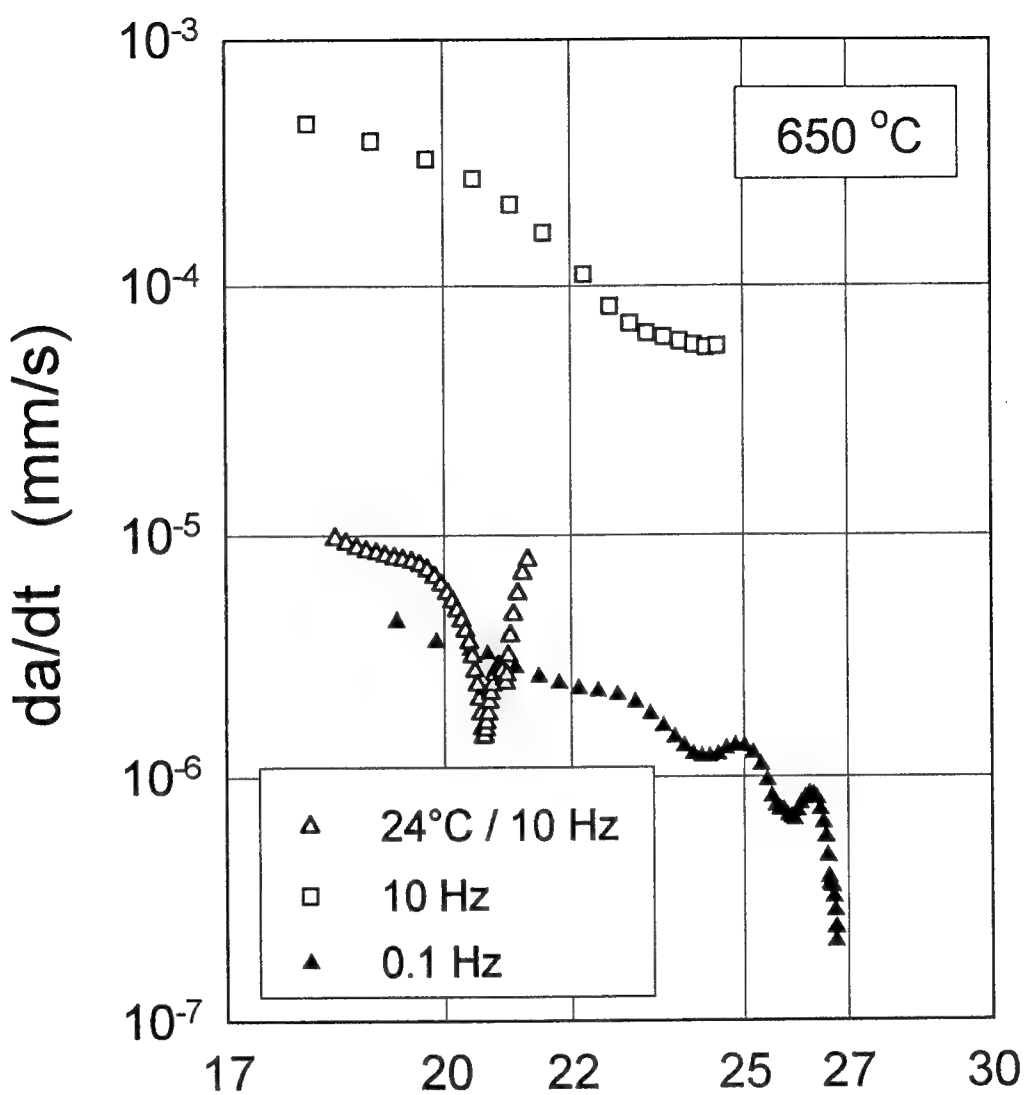
Fig. 5.11(b)   Fatigue crack growth rate, da/dt, versus the maximum applied stress intensity factor range, K_{max}, for different loading frequencies at 650 °C.
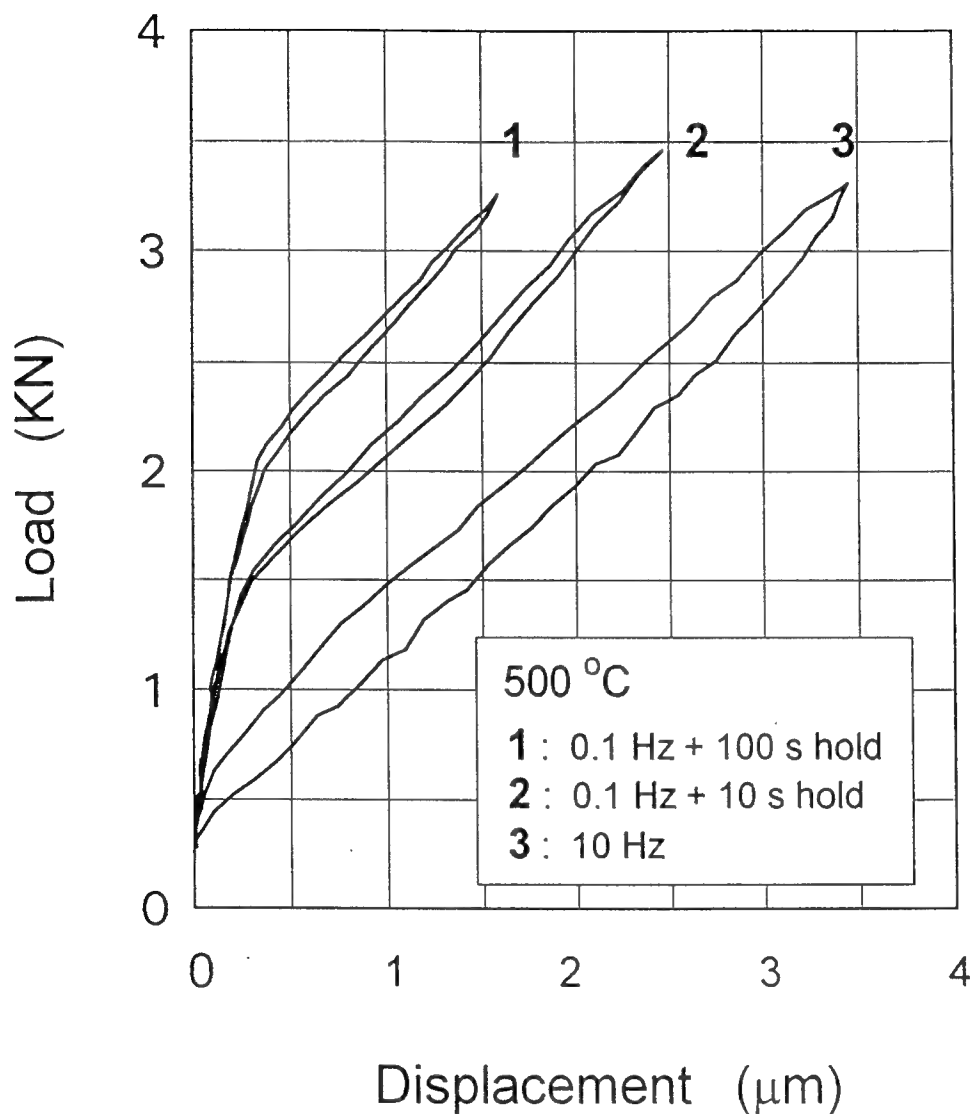
Fig. 5.12   Crack Opening displacement, δ, versus load for test conditions 10Hz, 0.1Hz + 10 s hold time and 0.1Hz + 100 s hold time (26). Notice the relation between the closure stress level and the loading frequency.

SECTION 6

HIGH TEMPERATURE/HIGH FREQUENCY FATIGUE CRACK GROWTH DAMAGE MECHANISMS IN TITANIUM METAL MATRIX COMPOSITES [6]

ABSTRACT

An experimental study was conducted to examine the effects of high temperature/ high frequency loading on the crack growth behavior in titanium composites. Fatigue crack growth tests were performed on the unidirectional SM1240/Timetal-21S composite in air environment at three different temperatures: 24°C, 500°C and 650°C with a loading frequency of 10 Hz and a stress ratio of 0.1. Tests were also carried out in vacuum and on aged specimens. In all the tests, the crack length was measured continuously while the crack opening displacement (COD) was measured at discrete positions along the crack length. Results show that, at all temperatures, the crack progresses in two sequential stages; a stage in which the crack growth rate decreases as the crack length increases followed by a stage characterized by an accelerated crack growth rate. The first stage corresponds to a crack bridging condition and is the focus of the analysis in this paper. In additional to COD measurements, the microstructural features associated with the fracture process during this stage was examined by scanning electron microscopy with emphasis being placed on the matrix crack morphology, debonding location, temperature and environmental influences on the fiber coatings. An analytical procedure, employing concepts of the theory of fracture mechanics and micromechanics analysis of the stress state along bridging fibers, was applied in order to calculate the fiber bridging stress, the frictional shear stress and the effective stress intensity factor. Results of this work suggest that the fiber bridging stress and the frictional shear stress are variables along the crack length and are test temperature dependents. Furthermore, it was concluded that both the crack tip opening displacement and the effective stress intensity factor can be used as measurements of the crack tip driving force in the crack bridging stage. Based on the experimental and analytical results collected in this study, a bridging damage mechanism under the loading condition specified here is suggested. This mechanism argues that the effect of temperature on the high frequency crack growth process is established through the temperature related modification of the frictional shear stress and the resulting adjustment of the internal stress state in the debonded regions of the bridging fibers.

6.1 INTRODUCTION

An important factor in the development of continuous fiber reinforced metal matrix composites (FRMMC) is the understanding of the fatigue crack growth mechanisms and governing factors. The focus on the crack growth stage stems from the fact that the different methods used to fabricate this class of composites inevitably lead to the formation of microscopic defects. The presence of these defects in applications involving load reversals and high temperature environment lead to a significant reduction in the crack initiation life of the corresponding composite. Furthermore, the damage tolerance procedure employed in aerospace applications, for which FRMMC are candidate materials, is based on fracture mechanics concepts aimed at describing the growth behavior of an existing crack in the material under consideration. In the case of titanium matrix composites, fatigue crack growth occurs by mechanisms involving fiber-matrix debonding, matrix cracking and fiber breakage. For load levels which are not sufficient to produce immediate fiber breakage at the crack tip, the fatigue crack growth is dominated by matrix fracture and fiber bridging. This mode of damage is facilitated by the fact that the SiC type fibers used to reinforce titanium matrices are coated with one or more carbon-rich layers designed to accommodate fiber/matrix debonding and sliding which occur during the matrix cracking. In a bridging crack condition, the crack tip is shielded by the amount of the load carried by the bridging fibers. As a result, the crack tip driving force is minimized leading to a crack growth rate lower than that of the matrix material when subjected to the same externally applied load. Efforts have been made to identify the different factors influencing the crack bridging process with the aim of determining the crack tip driving force. These efforts have largely followed models which employ concepts of linear fracture mechanics coupled with micromechanical interpretation of balance of forces acting on the debonded region of bridging fibers [1-8]. While the majority of these models may not be directly applicable to fatigue crack growth in composites with ductile matrices, they do, however, identify the crack opening displacement range, $\Delta\delta$, the fiber bridging stress range, Δp, and the fiber/matrix frictional shear stress, τ_s, as being the critical governing parameters of the fatigue crack bridging process. Efforts have been made to study each of these parameters and their form of correlations with mechanical and material properties of the composite. In this, the crack opening displacement, $\Delta\delta$, particularly that of the near crack tip region, is viewed, on the basis of the experience gained from studying the fracture processes of high strength monolithic materials, to be a measure of the crack tip driving force. In addition, $\Delta\delta$ has the advantage, in spite of its expected small magnitude in bridging cracks, of being a measurable parameter. This provides the possibility of establishing an experimentally based methodology to analyze the crack bridging behavior. A number of studies have been carried out in this regard. For example, Davidson [5], using a stereo-imaging technique, measured the $\Delta\delta$ caused by cyclic loading of discontinuously grown cracks in SCS-6/Ti-6Al-4V and SCS-6/Ti-14Al-21Nb The crack tip driving force and the slip length were then correlated with $\Delta\delta$ measurements in order to compute crack growth rates using fracture mechanics concepts. Telesman et al. [9] used a loading stage mounted inside a scanning electron microscope chamber to measure the $\Delta\delta$ profiles of cracks propagating in SCS-6/Ti-24Al-11Nb. These measurements were then used to develop an experimentally

based approach to calculate the fatigue crack growth driving force for bridged cracks. Hartman and Nicholas [10] developed an automated laser interferometric displacement gage system which was then used by Jira and. Kleismet [11] to measure the $\Delta\delta$ at different positions along a bridged crack length in SCS-6/Ti-24Al-11Nb. John et al. [12] utilized these measurements to examine the validity of different crack bridging models applied to unidirectional titanium matrix composites. Aside from the above mentioned studies, knowledge related to the evolution of $\Delta\delta$ as function of the crack length is non existent. Equally absent in the literature is the influence of high temperature on the $\Delta\delta$ in titanium matrix composites.

The second important crack bridging parameter is the fiber bridging stress, Δp, which has a direct influence on the crack tip shielding and the consequent effect on the reduction of the crack tip driving force. The calculation of Δp, which is not amenable to experimental measurements, has relied on micromechanical concepts dealing with the balance of forces acting on the debonded region of bridging fibers [5,7,12,13]. Once Δp is determined, the effective stress intensity factor, ΔK_{eff}, of the corresponding bridged crack could be calculated by considering the crack to be propagating in a matrix material with an imposed closure pressure distributed along the crack length. Davidson [5] estimated Δp through the computed fiber stress by measuring the fiber strain. The work of Telesman et al. [6] and John et al. [12] calculated Δp based on either an elementary strength of materials approach (they term it fiber pressure model) or an approach assuming that σ_b has a power-law form. These types of Δp calculations are not associated with parameters such as the frictional shear stress, τ_s, or the crack opening displacement, $\Delta\delta$. Furthermore, the distribution of the fiber bridging stress obtained from various techniques are quite different. In the work of Davidson, for example, an assumption was made that Δp is approximately constant. The simple shear-lag analysis, however, indicates that Δp is proportional to the square of the crack opening displacement, $\Delta\delta$. This implies that Δp vanishes at the crack tip and the bridging fibers at the crack tip carry no load [8,13]. Chiang et al. [8] applied a modified shear-lag model and showed that Δp attains a finite value at the crack tip. Although a significant amount of research has been made in relation to the fiber bridging stress distribution in metal matrix composites, no single calculation of Δp distribution for high temperature conditions exists. Moreover, the available information for Δp distribution at room temperature, does not discuss the effect of the crack length, for example, on the nature of the distribution.

Among the three bridging parameters mentioned above, the frictional shear stress, τ_s, has been the parameter most studied [4,13,15,16]. This is due to the recognition that the mechanics of the fiber/matrix interface region is critical for the understanding of the composite behavior. Different methods of measurement have been applied to determine the magnitude of τ_s. The most common of these is the use of fiber push-out/pull-out tests to measure τ_s in terms of the stress required to cause fiber/matrix slippage in as-received specimens of the composite under investigation [17-21]. These methods however view τ_s as being a single material constant. This view has been utilized in variety of bridging models to predict the crack tip driving force, the debonding length and the crack opening displacement. The existence of a gap between the results of these models and corresponding experimental data has focused the attention on examining the characteristics of τ_s and the validity of extending its single value as measured from pre-fatigued specimens to conditions under which

fiber/matrix interfacial damage accumulates [5,6,13]. Recent work in this area has shown that repeated sliding on a fiber/matrix interface may lead to deterioration of that interface either by fracture of fiber coatings [22,23], wear of asperities [18] or plastic relaxation of the friction stress on the interface [18]. Indeed, available fiber push-out/pull-out tests have revealed reduced interface frictional stress in metal-, intermetallic and ceramic composites after a few loading/unloading cycles. However, push-out tests performed on fatigued composite specimens have shown either further decease or limited increase in the value of τ_s when compared with the that obtained from as-received specimens. Furthermore, the variation in debonding mechanisms along the interface as discussed by Bakuckas and Johnson [13] indicates that the value of τ_s is apparently a function of the fiber location along the debond length and crack length. These results led Chan [15], Bukuckas and Johnson [13] and Zheng and Ghonem [24] to suggest that τ_s is not a material constant but should rather be viewed as a variable which depends on loading conditions (applied stress level, temperature and frequency), debonding mechanisms, viscoplastic deformation of surrounding matrix and environmental attack of the fiber/matrix interface region. Eldridge [19] measured the frictional shear stress in titanium matrix composites at different high temperatures in vacuum controlled environment. This work showed that the increase in temperature causes a decrease in the value of τ_s. In contrast, pull-out tests by Marshall et al. [25] and push-out tests by Clyne [26] both applied to SM1240/Timetal-21S, at room temperature, have showed that high temperature aging prior to testing leads to an increase in the as-received τ_s. These contradictory results imply that τ_s is a condition sensitive parameter. Examining the state-of-art data base for τ_s indicate that the distributions of τ_s along the bridging zone under both room (ambient) temperature and elevated temperatures are not available.

The objective of the present study is to identify the evolution of $\Delta\delta$, Δp and τ_s, in terms of both crack length and test temperature. This has been achieved using an experimental approach to measure $\Delta\delta$ which was then used through an analytical approach to determine both Δp and τ_s. This paper discusses the main characteristics of these three parameters and describes their interdependent relationships as well as their individual and combined effects on the crack bridging mechanism at selected elevated temperatures.

6.2 MATERIAL AND EXPERIMENTAL PROCEDURE

The material used in this study is the SM1240/Timetal-21S composite. The matrix material is the metastable β titanium alloy Timetal-21S. The composition of this alloy (in wt%) is 0.1 Fe, 16.0 Mo, 3.06 Al, 2.9 Nb, 0.2 S, 0.22 C, 0.12 O, 0.005 N with the balance being Ti. The SM1240 (SiC) fiber (100μm in diameter) consists of 10μm diameter tungsten-cored SiC monofilament with dual vapor-deposited coatings of carbon and boron-rich titanium diboride at the surface. The thickness of each of these layers is about 1 μm. The composite material is made of eight plies of Timetal-21S foils, each 112 μm in thickness, with continuous SM1240 fibers having approximately a 35% volume fraction and oriented along the 0° direction. Table 6.1 lists the basic properties of both the fiber and the matrix material. The composite was consolidated using vacuum hot pressing employing per-established critical

processing parameters. All consolidated plates, measuring 900 mm x 100 mm x 1 mm, received a stabilization heat treatment (621 °C/8 hours) in a dynamic vacuum furnace. Fig. 5.1 is a chemically etched cross-section of the as-fabricated composite showing a hexagonal fiber arrangement and traces of the foil to foil interfaces. The average center-to-center fiber spacing is approximately 150 μm.

The plates were machined into rectangular specimens measuring 75 mm x 10 mm with a center hole of 1.575 mm in diameter. Notches were cut at opposite horizontal edges of the center. In addition to testing at room temperature, two other temperatures have been investigated, 500°C and 650°C. The temperature of 500°C is the expected application

Table 6.1: Mechanical Properties of the Fiber and the Matrix

Property	24 (°C)	500 (°C)	650 (°C)
E_m(GPa)	98.2	72.4	47.6
ν_m	0.35	0.35	0.35
$\sigma_{Y,m}$ (MPa)	1043	552	245
$\sigma_{U,m}$ (MPa)	1089	641	289
$\epsilon_{F,m}$ (%)	>3.9	>10.5	50-55
E_f (GPa)	390	390	390
ν_f	0.3	0.3	0.3
$\sigma_{U,f}$ (MPa)	3340	3340	3340
$\epsilon_{F,f}$ (%)	1	1	1

temperature while 650°C represents a near upper limit use of this type of Sigma fiber [27]. In addition to tests in air environment, one vacuum test (10^{-7} torr) was performed at 650°C/10 Hz. High temperature tests were carried out using two-zone resistance furnace and allowing a ± 4°C maximum temperature variations along the 40 mm specimen gage length.

All specimens were gripped by a flat ended hydraulic grip and tested using a servohydraulic material testing machine equipped with computer control and data acquisition capabilities. Tests were carried out under constant load range with the stress ratio of 0.1. In all cases, the applied stress range was 273 ± 3 MPa.

As the objective of this work was to identify the role of temperature on the crack growth mechanism without introducing significant time-dependent deformation effects, the loading frequency was selected to be 10Hz for all test conditions performed here. This selection is based on results obtained from previous work on Timetal-21S fiberless laminates [28] which showed that frequencies higher than 10 Hz produce insignificant oxidation damage and creep deformation at temperatures below 650°C. Frequencies lower than 10 Hz, on the other hand, were shown to induce effects related to viscoplastic deformation and oxidation at temperatures up to 650°C. In addition, a 500°C test was carried out in air using a loading frequency of 20 Hz. To asses the role of the fiber/matrix interface aging during the high temperature crack growth testing several specimens were aged for durations ranging from 40 - 600 hours at 650°C and 720°C. These specimens were then subjected to crack growth testing at room temperature.

In all the tests, the crack length was measured continuously using the direct current potential drop technique supported by optical measurements using travelling microscopes. Furthermore, the crack opening displacement, $\Delta \delta$, was measured by calculating the difference between the maximum and minimum values of the displacement-load loops of the measuring position near the crack tip. This loop which corresponds to a full loading cycle was obtained using a linear array laser interferometric displacement gage system with a resolution of 10 nm. As this technique depends on the fringe pattern obtained from a laser reflection of two microhardness indents placed above and below the crack surfaces at the location of interest, the COD measurements were collected at discrete crack lengths with the condition that a measurement be performed only when the crack tip advances a distance of at least 600 μm from the previous measuring position. This was to isolate the fringe pattern of the current measuring position from reflection interference caused by indents of a neighboring measuring position. No COD measurements were carried out for vacuum tests.

Several tests were stopped before the specimen final separation occurred in order to identify related fiber/matrix damage features. In each of these cases one of the specimen's surfaces parallel to the fiber direction was ground to a depth sufficient to uncover the near surface fiber array. This provided an opportunity to observe possible fiber bridging and the extent of fiber/matrix debonding in relation to the crack path.

Post test examinations included fractographic analysis of the fracture surface in order to identify features of the fracture mechanisms and changes taking place in the fiber/matrix interface region. The fiber/matrix interfacial growth at several temperatures and for different exposure durations was also studied using scanning electron microscopy.

6.3 RESULTS AND ANALYSIS

The purpose of the analysis carried out in this section is to determine the evolution characteristics of the parameters governing the crack bridging mechanism, in particular, the crack growth rate, the fiber bridging stress, the frictional shear stress and the crack tip driving force. The success in identifying the characteristics of these parameters for the test temperatures used here will lay the ground for a proposed high temperature crack growth damage mechanism of crack bridging to be described in the next section.

6.3.1 The Crack Growth Rate

The curves representing the crack growth rate versus the applied stress intensity factor for all test conditions are shown in Fig. 5.4(a). The common feature of theses curves is the presence of an initial crack bridging stage signified by the continuous decrease in the crack growth rate as applied stress intensity factor ΔK_a (or the crack length) increases. In this case, unlike the monolithic materials, ΔK_a cannot, therefore, be treated as a crack tip driving force. This crack bridging stage is followed by a stage which consists of repeated events of crack growth acceleration and retardation leading ultimately to crack instability and final failure of the test specimen In no test condition performed here was full crack arrest observed.

Focusing on the initial crack bridging stage, which occupies not less than 30% of the fatigue life of any of the test specimens, it is observed that for a particular crack length the crack growth rate decreases as the temperature increases thus signifying the dependency of the crack tip shielding force on temperature. At 500°C, it was observed that the crack growth rates at 10Hz (air) and 20 Hz (air) are identical. The role of environment is noticeable in the difference between the 650°C crack growth rates in air and in vacuum. The slope of the crack growth rate curve corresponding to the first crack bridging stage, which could be considered a measure of the build up rate of the crack tip shielding force, is lowest in the 24°C test and highest in the 650°C air test. This observation reinforces the fact that the crack tip shielding force increases as temperature increases. The end of the crack bridging stage is marked by the lowest crack growth rate attained in each of the tests. This rate ranges from 5.6×10^{-6} mm/cycle in the room temperature test to 2.4×10^{7} mm/cycle in the 500°C. The crack length at the end of this stage, which marks a transition from decelerated to accelerated crack growth rate, decreases as the temperature increases. This length is, however, similar in the 500°C and 650°C (vacuum) tests.

As will be detailed later, the analysis in this paper will focus only on the initial crack bridging stage of each of the tests carried out here. This stage is hereafter termed the crack bridging stage.

6.3.2 Fractography

The different fracture processes encountered in each of these crack growth stages are

evident in the appearance of the fracture surface features. For example, Fig. 6.1, which belongs to the 500°C test, shows two different fracture zones, the first for the crack bridging stage and the second for the repeated crack growth acceleration/retardation stage. The first zone has excessive fiber core damage, which may have resulted from the application of a large number of fatigue cycles and prolonged thermal exposure. The pull-out fibers in this zone are relatively short. The second zone shows no fiber core damage and displays longer fiber pull-out length. An example of the unstable fracture zone is shown in Fig. 6.2; it has a high degree of matrix deformation surrounding the pull-out fibers.

The matrix cracking mode for all tests was observed to be transgranular. A typical example of the fracture surface features associated with this mode is shown in Fig. 5.6(c). They consist of cleavage facets; the size of which seems to depend on their location on the fracture surface and the corresponding crack growth rate; the higher the growth rate, the larger the cleavage facet size. Furthermore, foil to foil interfaces along the fracture surface are difficult to identify and did not interrupt the continuity of the cleavage planes. Isolated colonies of fatigue striations were found on fracture surfaces of some of these tests but did not represent a dominate fracture mode in any of the test cases.

In examining the interfacial region of the bridging fibers, it was interesting to observe that, regardless of the test temperature, debonding always occurred within the carbon coating layer or between the carbon and the TiB_2 layers. Fig. 5.6(d) shows an example of a debonding crack in the carbon layer immediately under the fracture surface of a 24°C test. The debonding that occurred at these locations is possibly due to the compliant nature of the carbon layer.

The surface morphology of the bridging fibers in the crack bridging stage are distinct for different temperatures. At 24°C, a patch-like of residual carbon layer can be observed (see Fig. 5.7(a)), while at 500°C and 650°C, this type of layer is absent (see Fig. 5.7(b)). It is possible that the presence of this layer at room temperature be a source of an increased fiber/matrix friction during the frictional sliding of the bridging fibers. This may in fact be the cause of the groove-shape traces observed on the debonded surface of pull-out fibers at 24°C, see Fig. 6.3(a). At high temperature, this extra carbon layer would be gradually oxidized to form CO/CO_2 and would evaporate, thus making the fiber/matrix interfaces smoother than that at 24°C. This speculation is supported by the fact that the carbon patch layer do exist on the surfaces of the pull-out fibers within the final failure stage of the 500°C and 650°C tests (see Fig. 6.3(b)). The insufficient exposure time during the rapid fracture stage results in no oxidation of the above mentioned residual carbon layer along the fibers in this region. It is worth mentioning that the surface morphology of the bridging fibers at 650°C in vacuum is similar to the one at 24°C (see Fig. 6.3(c)).

The debonding length of fibers along the crack length was examined by removing the outermost matrix layer in several fractured specimens; Fig. 5.8 shows the debonding length for 650°C. It can be seen that fiber breakage occurred in the bridging fibers, which indicates that the fiber pull-out length could be proportional to the debonding length. By carefully measuring the fiber pull-out length from the fracture surface using scanning electron microscope, it is found that the average fiber pull-out length in the crack bridging stage increases as the temperature increases (see Table 6.2). In fact when comparing the trend of these lengths with that of the crack growth rate one could conclude that the higher the crack

143

growth rate, the lower the average fiber pull-out length.

Table 6. 2 Average Fiber Pull-Out Length

Temperature (°C)	Average Fiber Pull-Out Length (μm)
24 (air)	61
500 (air)	86
650 (air)	107
650 (vacuum)	96

6.3.3 The Crack Opening Displacement, $\Delta\delta(x)$

The range of the crack opening displacements, $\Delta\delta$, were obtained at positions x measured from the center of the bridged crack length during the 24°C, 500°C and 650°C (air) tests. These discrete data points for different (half) crack length, in addition to those obtained by setting $\Delta\delta$ at the crack tip at zero, are shown in Figs. 5.9(a-c). The smooth curves connecting the points tn these curves were generated by using a spline curve fitting procedure. The general trend of these curves is that, for the same crack length, $\Delta\delta(x)$ increases as the distance from the crack tip increases; a trend similar to that observed in unbridged cracks. The influence of bridging fibers on the crack opening displacement is, however, apparent in the fact that the measured values of $\Delta\delta(x)$ are much smaller than those of monolithic materials [4] and in the weak dependency of $\Delta\delta(x)$ on the increase of the crack length. In the case of the 24°C test, for example, the advance of the half crack length from 1.39 mm to 1.88 mm leads to 0.3 μm increase in the $\Delta\delta$ measured at the notch mouth. The increase in the test temperature produces, however, higher values of $\Delta\delta$. This is evident in the 24°C test results when compared with those of 650°C.

6.3.4 Fiber Bridging Stress, $\Delta p(x)$

In this study, the bridging crack length is considered a short crack falling within the transient region mentioned by Chiang et al. [8]. Here, the stress and strain fields are complex on both sides of the crack tip, and the discrete bridging traction of the bridging fibers supposedly control the crack tip driving force. This section focuses on determining the fiber bridging stress and its relationship with temperature and crack length.

With reference to the previous section, the measured crack opening displacement,

$\Delta\delta(x)$ is equal to the difference between the crack opening displacement, $\Delta\delta_a(x)$, which is proportional to the externally applied stress, $\Delta\sigma_a$, and the crack opening displacement, $\Delta\delta_b(x)$, which is related to the fiber bridging stress, $\Delta p(x)$. $\Delta\delta(x)$ can thus be written as:

$$\Delta\delta(x) = \Delta\delta_a(x) + \Delta\delta_b(x) \tag{1}$$

where on the basis of the linear elastic fracture mechanics concepts, both $\Delta\delta_a(x)$ and $\Delta\delta_b(x)$ can be written as [31]:

$$\Delta\delta_a(x) = \frac{4\Phi}{E_c} \Delta\sigma_a \sqrt{a^2 - x^2} \tag{2}$$

and

$$\delta_b(x) = \frac{4\Phi}{E_c\pi} \int_{a_0}^{a} \Delta p(t) \ln\left|\frac{\sqrt{a^2 - x^2} + \sqrt{a^2 - t^2}}{\sqrt{a^2 - x^2} - \sqrt{a^2 - t^2}}\right| dt \tag{3}$$

Φ is a correction factor accounting for the finite width [32] and is given as:

$$\Phi = \ln\left(\frac{1 + \sin(\pi a/W)}{\cos(\pi a/W)}\right) \bigg/ \frac{\pi a}{W} \tag{4}$$

By setting

$$\int_{a_0}^{a} \Delta p(t) \ln\left|\frac{\sqrt{a^2 - x^2} + \sqrt{a^2 - t^2}}{\sqrt{a^2 - x^2} - \sqrt{a^2 - t^2}}\right| dt = F(x) \tag{5}$$

Eq.(3) could thus be written as:

$$F(x) = \pi \Delta\sigma_a \sqrt{a^2 - x^2} - \frac{\pi E_c \Delta\delta(x)}{4\Phi} \tag{6}$$

Eq.(6) is a typical Fredholm equation of the first kind which can be solved numerically by the least-square method using the singular value decomposition technique [33,34]. This solution, yields values of $\Delta p(x)$ as a function of the crack length, a. Results for the three temperature levels 24°C, 500°C and 650°C are shown in Figs. 6.4(a), (b) and (c), respectively. A feature of these distributions is the presence in all test cases of a minimum

145

finite value of Δp at the crack tip. Also, the average values of $\Delta p(x)$ increase proportionally to both the increase in the temperature and the crack length. Considering the fiber bridging stresses to be the principal contributor to the shielding of the crack tip driving force, this result explains the decrease in the crack growth rate associated with the increase in both temperature and crack length. Furthermore, for the same test temperature, the difference between the maximum and minimum fiber bridging stress at a particular crack length decreases as the crack length increases. This tendency of $\Delta p(x)$ to approach a uniform level is also influenced by the temperature as can be seen in Fig. 6.4.

Once the fiber bridging stress distribution, $\Delta p(x)$, is determined, the discrete fiber traction, ΔS_f, acting on the individual bridging fibers can be calculated as:

$$\Delta S_f(x) = \Delta p(x) \,/\, V_f \qquad\qquad (7)$$

where V_f is the fiber volume fraction. The maximum value of ΔS_f is reached at the end of the crack bridging stage and acts on the first fiber located at the crack mouth. These values for the three temperatures are 776 MPa (24°C), 873 MPa (500°C) and 877 MPa (650°C). Fig. 6.5 shows the evolution of ΔS_f calculated at the crack mouth as a function of the crack length and at different temperatures. This figure shows that the dependency of ΔS_f on temperature is not significant while its dependency on the crack length decreases as the temperature increases. Fig. 6.5 moreover, indicates that while ΔS_f increases with increasing crack length and temperature, its value seems to converge to an upper limit of about 900 MPa. Since these crack-mouth bridging fibers are most likely to be the first to fracture at the end of the crack bridging stage, the 900 MPa, would represent the fracture strength of the Sigma fibers. This value is much lower than the monotonic tensile strength of this type of fiber which is estimated as 3000 MPa level [35]. This significant discrepancy could be primarily related to the fact that the fatigue fracture strength of a SiC fibers is lower than its monotonic fracture strength. The mechanical damage induced in the fiber surface due to load reversibility and fiber/matrix frictional wear effects could also be seen as another factor accelerating the fibers failure at a lower traction stress.

6.3.5 Frictional Shear Stress $\tau_s(x)$

When the tip of the matrix crack bypasses a fiber during crack bridging, neglecting the details of the fiber/matrix interfacial debonding process, the loading part of the fatigue cycle is assumed to produce a maximum debonding length, L_{max} along the bridging fiber. The subsequent unloading of the cycle will introduce, within L_{max}, a reversed frictional sliding, L_R, along which the interface degradation would expect to alter the average frictional sliding stress, τ_s. The change in τ_s, could, in turn, affect the reversed sliding length, L_R. However, once τ_s is stabilized within a few loading cycles [6,12], L_{max} and L_R could also reach stable lengths. This steady state condition is maintained until the crack tip advances and involves a new fiber. Focusing on this condition for an arbitrary location, x, along the crack length

146

a, a geometric model, based on the work of Budiansky, Hutchinson and Evans [36], has been developed by the authors [37] to identify the stress states in three regions along the loading axis of the fiber/matrix interface. These regions are bonded zone ($z > L_{max}$), initial debonded zone ($L_R < z \leq L_{max}$) and frictional sliding zone ($0 \leq z \leq I_R$) , see Fig. 6.6   This model takes into account the influence of the axial fiber and matrix residual stresses, σ^R_f and σ^{R0}_m, respectively, as well as effects of the mean load. The formulation of this model leads to the determination of $\tau_s(x)$ in terms of the crack opening displacement range, $\Delta\delta(x)$. This is expressed as:

$$\tau_s(x) \;=\; \frac{(B_1 + B_2)}{\Delta\delta(x) - B_3} \tag{8}$$

where B_1, B_2 and B_3 are explicit functions of material properties, fiber volume fraction, fiber bridging stress, $\Delta p(x)$, applied stress $\Delta\sigma_a$, residual stresses of fiber, σ^{R0}_f, and matrix, σ^{R0}_m, as well as the initial frictional shear stress τ_0. The input requirements to execute the above expression, in particular, the values of σ^{R0}_f and σ^{R0}_m , were obtained from data generated in the work of Ghonem et al. [38] on the same composite material; these values are listed in Table 6.3. Furthermore, τ_0 was measured using a room temperature fiber push-out procedure carried out on thin composite specimens which have been previously aged (100 hours) in air at elevated temperatures for different durations. Results of this work, detailed in Ref [39], show that τ_0 has the values 67 MPa, 34 MPa and 22 MPa for the 24°C, 500°C and 650°C tests, respectively (these results are being examined by the authors in order to confirm their validity when both aging and push-out procedures are performed in high temperature / vaccum conditions). Now, with the use of $\Delta\delta(x)$ profiles, the frictional shear stress $\tau_s(x)$ for various crack lengths at the different test temperatures can be determined from Eq. (8). Results for three different crack length at the three temperatures under consideration are shown in Fig. 6.7 . It can be seen that the frictional shear stress, τ_s does not have a single value but is a variable along the crack length. The relative variation of $\tau_s(x)$ in terms of the temperature, T, and the half crack length, a, can be written as follows:

$$\tau_s(x) \;=\; \tau_0(T)\ \exp\{-\beta\ a^{-2}\ T^{-0.05}[1 - (x/a)^\alpha]\} \tag{9}$$

where β is a material related parameter which could encompass factors such as matrix material properties, fiber diameter and fiber volume fraction. In the current study, β is approximately equal to 1.09. The exponent α is the prime controlling factor of the above equation and depends on both the crack length and the temperature via the following expression:

$$\alpha = (C_1 + C_2 T)\ a^{-4.145} \tag{10}$$

where C_1 and C_2 are constants equal to 54.33 and 0.0253; respectively.

Table 6.3 Thermal Residual Stress of the Matrix

Temperature (°C)	24	500	650
σ^{RO}_m (MPa)	200	47	21

6.3.6 Crack Tip Driving Force

It has been shown above that ΔK_a cannot be considered an effective crack tip driving force due to the presence of a crack tip shielding force exerted by the fiber traction. A correction of ΔK_a, which yields an effective stress intensity factor ΔK_{eff} can be calculated by subtracting from ΔK_a the shielding component produced by fiber bridging stress. This is expressed as:

$$\Delta K_{eff} = Y \, \Delta\sigma_a\sqrt{\pi a} - 2Y\sqrt{a/\pi} \int_{a_0}^{a} \frac{\Delta p(x)}{\sqrt{a^2 - x^2}} dx \tag{11}$$

where a_0 is the initial half crack length, and Y is a geometric factor for finite width correction:

$$Y = \left(\sec(\pi \, a/2W) \right)^{\frac{1}{2}}$$

The use of Eq. (11) to calculate ΔK_{eff} depends only on the knowledge of $\Delta p(x)$ which in turn, was calculated on the basis of the experimentally determined $\Delta\delta(x)$. This equation in conjunction with results shown in Fig. 6.4, was applied to various bridged crack lengths for the three test temperatures. Results in the form of ΔK_{eff} versus the crack growth rate, da/dN, are plotted in Fig. 6.8. It shows that da/dN is proportional to ΔK_{eff}, and for the same ΔK_{eff}, da/dN increases as the temperature increases. The trends of these results are similar to those observed in monolithic materials. The curves shown in Fig.4.14 could be expressed in a Paris-type equation written as follows:

148

$$\frac{da}{dN} = C(T) \ \Delta K_{eff}^{n(T)} \tag{12}$$

where both the coefficient C and the exponent n are temperature dependents.

The influence of crack length and test temperature on the effective stress intensity factor are further examined in Fig. 6.9. It shows that ΔK_{eff} is inversely proportional to both a and T. For comparison between the behavior of ΔK_{eff} and that of the crack tip opening displacement, see Ref. [39].

6.4 DISCUSSION

The work in this paper has focussed on the influence of high temperature on the bridging fatigue crack growth in the SM-1240/Timetal-21S composite when subjected to high frequency loading. The basic conclusion is that, in the range from 24°C to 65°C; an increase in the test temperature leads to a decrease in the fatigue crack growth rate. This result was supported by experimental and analytical work identifying the evolutionary behavior of the fatigue crack opening displacement and the distributions of both the fiber bridging stress and the frictional shear stress. Results of this work show that the temperature related reduction in the crack growth rate is primarily due to events taking place in the debonding zone of bridging fibers leading to an increase in the crack tip shielding. In an attempt to formulate, on the basis of these results, a damage mechanism capable of interpreting the observed response of the bridging crack to the temperature, one should recall the following important observations:

- Debonding of bridging fibers, regardless of the test temperature, occurs within the carbon coating layer or between the carbon and the TiB_2 layers. The occurrence of this at room temperature is possibly due to the compliant nature of the carbon layer. At high temperatures, however, this may be also due to the degradation of this layer by means of carbon diffusion outward through the TiB_2 layer or the formation of new phases such as TiC at TiB_2/C interface. The work of Osborne and Ghonem [30] on the interfacial kinetics of this composite has demonstrated, however, that the thickness change of the TiB_2 layer as well as the outward diffusion of the carbon are insignificant up to 650°C.

- The average fiber pull-out length increases as the temperature increases. This result in addition to the fact that the crack opening displacement, particularly at the crack mouth, increases with an increase in temperature, means that the debonded length along a bridging fiber, i.e the mode II crack, is temperature dependent.

- The role of environmental effects on the crack growth behavior at 500°C is negligible. This is due to the fact that crack growth rates of the 10 Hz and the 20 Hz tests are identical. At 650°C, the role of environment seems to play a role due to the observation that there exists a certain difference between the crack growth rates of the corresponding air and vacuum tests. This influence is primarily through the modification of the surface morphology of the debonded area in the bridging fibers to alter the frictional shear stress.

149

On the basis of these observations, a crack bridging damage mechanism could be established. Here, an assumption is made that the initial debonding under the same external loadings is approximately identical in all temperatures. Two important factors will, however, influence the ensuing events. They are: a) the mode II fracture toughness, K_{II}, of the fiber carbon coating layer, and b) the magnitude of the radial stress acting on the boundary of the would-be debonded and debonded regions. It is documented that the carbon becomes more brittle as the temperature increases up to 1000°C [40,41]. Based on concepts of fracture mechanics, in general, the more brittle the material has lower fracture toughness. This implies that for the same applied ΔK_{II} acting at the tip of the initially debonded region (mode II crack) on the bridging fiber, a relatively longer debonded length within the more brittle carbon layer would be generated at higher temperatures. The relative movement between the two surfaces of this mode II crack is governed primarily by the frictional shear stress, τ_s, acting along these surfaces. τ_s is, in fact, a function of both the surface roughness characteristics and the clamping force provided by the radial stress, σ_r, acting perpendicular to the frictional surfaces. One could then express τ_s as:

$$\tau_s = \tau_o - \mu \, \sigma_r \tag{13}$$

where τ_0 is the initial frictional shear stress of the frictional surfaces, and μ is the coefficient of friction. Tamin and Ghonem [42], have shown, on the basis of a time-dependent finite element study performed on the same composite, that the Poisson's ratio related radial stress, σ_r, decreases as the temperature increases. It is, therefore, possible to assume that τ_s, being a variable, decreases with the increase in temperature. This assumption has, in fact, been verified in this study. Now, a relatively longer debonding length with a reduced frictional shear stress between its surfaces would permit, for the same applied ΔK_{II}, a larger surfaces movement which is translated as a larger crack opening displacement of the main bridging crack. This larger movement between the surfaces of the debonded region would, in turn, result in a higher shear stress and consequently higher ΔK_{II}, at the corresponding mode II crack tip. At the steady stage which the debonding length is stable, a combination of larger relative displacement of the frictional surfaces and higher (mode II) crack tip shear stress necessitates, for achieving a balance of axial forces, a higher fiber traction. For higher temperature test conditions, this traction, when integrated along the bridged crack length, produces a crack tip shielding stress higher than that in lower temperature test conditions and thus a lower crack growth rate. This mechanism is therefore based on the notion that the temperature related reduction in the crack growth rate is traced to the associated stress state variation with respect to temperature. In this, temperature related effects in the form of phase changes or growth of the fiber/matrix interface are assumed to play a minor role. In order to examine the validity of this concept a specimen was aged for 40 hours at 650°C. This duration is equal of that required to complete the crack growth test at this temperature. After aging , the specimen was tested at 24°C. The resulting crack growth rate versus ΔK_a is shown in Fig. 6.10 and compared to the results of the non-aged 24°C test. The similar crack growth rates suggest that the fiber/matrix interfacial related modification has little influence

on the bridging crack growth behavior, which is consistent with the result of interfacial reaction kinetics study.

6.5 CONCLUSIONS

The experimental and analytical studies in this work have been performed in order examine the high temperature fatigue crack damage mechanisms in the titanium metal matrix composites. The SM1240/Timetal-21S composite was used as a test material. The results of this work show that the fatigue crack growth rate of the composite at all temperatures consists of a deceleration crack growth stage followed by the acceleration crack growth stage. The present work has focused on the understanding of the controlling parameters and the damage events occurring in the initial crack bridging stage. The major conclusions of these efforts are as follows:

1. For the 10Hz fatigue loading condition, based on the presentation of the crack growth rate versus applied stress intensity factor, the fatigue crack growth rate decreases with the increase of the temperature.

2. The crack opening displacement, $\Delta\delta(x)$, at a position farthest from the crack tip increases as the crack length or the temperature increases, while the crack opening tip displacement near the crack tip, $\Delta\delta_T$, is found to decrease as the both crack length and the temperature increase.

3. The fiber bridging stress, $\Delta p(x)$, is a variable along the crack length with a decreasing distribution from the crack mouth to the crack tip. At the crack tip, $\Delta p(x)$ is a finite value. Its magnitude increases as the crack length or the temperature increases, the longer the crack length or the higher the temperature, the more uniformly distributed is the fiber bridging stress, $\Delta p(x)$.

4. The frictional shear stress, $\tau_s(x)$, is not a single value; instead it varies along the crack length with the lowest value at the crack mouth. As the crack length or the temperature increase, $\tau_s(x)$ increases and is more uniformly distributed along the crack length.

5. The present study indicates that both the crack tip opening displacement, $\Delta\delta_T$, and the effective stress intensity factor, ΔK_{eff}, are the proper measurements of the crack tip driving force in the condition of crack bridging.

6. The temperature influence is primarily expressed through the alternation of the internal stress state which, in turn, affects the frictional shear stress. This results in the modification of the crack tip driving force through the corresponding adjustment of the fiber bridging stress. The effect of environment is apparently shown by further

151

modifying the surface morphology of the sliding region, which also directly changes the frictional shear stress.

6.6 REFERENCES

[1]   Marshall, D. B., Cox, B. N. and A. G. Evans, "The Mechanics of Matrix Cracking in Brittle-Matrix Fiber Composites", Acta metall, Vol. 33, 1985, pp.2013-2021.

[2]   McCartney, L. N., "Mechanics of Matrix Cracking in Brittle-Matrix Fiber-reinforced Composites", Proceedings of Royal Society Londan, Vol. 409A, 1987, pp329-350.

[3]   McMeeking, R. M. and Evans A. G., "Matrix Fatigue Cracking in Fiber Composites", Mechanics of Materials, Vol. 9,1990, pp.217-227.

[4]   Ghosn, L., Kantzos, P. and Telesman J., "Modelling of Crack Bridging in a Unidirectional Metal Matrix Composite", International Journal of Fracture, Vol. 54, 1992, pp.345-357.

[5]   Davidson, D. L., "The Micromechanics of Fatigue Crack Growth at 25°C in Ti-6Al-4V Reinforced with SCS-6 Fibers", Metallurgical Transactions, Vol. 23A, 1992, pp.865-879.

[6]   Telesman, J., Ghosn, L. J. and Kantzos, P. , "Methodology for Prediction of Fiber Bridging Effects in Composites", Journal of Composites Technology & Research, Vol. 15, 1993, pp.234-241.

[7]   Walls, D. P., Bag and Zok, W. , "Mode I Fatigue Cracking in a Fiber Reinforced metal Matrix Composite", Acta metall. mater., Vol. 41, 1993, pp. 2061-2071.

[8]   Chiang, Y-C.,Wang, A. S. and Chou, T-W,"On Matrix Cracking in Fiber Reinforced Ceramics". Journal of Mechanics and Physics of Solids, Vol. 41, 1993, pp.1137-1154.

[9]   Telesman, J.,Kantzos, P. and Brewer, D., "In Situ Fatigue Loading Stage Inside Scanning Electron Microscope", Lewis Structures Technology-1988, NASA CP 3003, Vol. 3, May 1988, pp.161-172.

[10]   Hartman, G. A. and Nicholas, T. , "An Enhanced Laser Interferometer for Precise Displacement Measurements. Experimental Techniques", SEM, Vol. 11, No.2, 1987, pp.24-26.

[11]   Jira, J. R. and Kleismet, R.,"Crack Opening Displacement Measurements in

Unidirectional Metal Matrix Composites",. 1993.

[12]   John, R., Kaldon, S. G. and Ashbaugh, N. E., "Applicability of Fiber Bridging Models to describe Crack Growth in Unidirectional Titanium Matrix Composites",Titanium Metal Matrix Composites II, Proceedings of Titanium Metal Matrix Composites II Workshop, June, 1993, WL-TR-93-4105, pp.270-290.

[13]   Bakuckas Jr, J. G. . and Johnson, W. S., "Application of Fiber Bridging Models to Fatigue Crack Growth in Unidirectional Titanium Matrix Composites", Journal of Composites Technology & Research, Vol. 15, 1993, pp.242-255.

[15]   Chan, K. S. , "Effects of Interface Degradation on Fiber Bridging of Composite Fatigue Cracks", Acta metall. mater., Vol. 41, 1993, pp.761-768.

[16]   Thouless, M. D., Sbaizro, O. , Sigl. L. S. and Evans, A. G., "Effect of Interface Mechanical Properties on Pullout in a SiC-Fiber-Reinforced Lithium Aluminum Silicate Glass-Ceramic", J. Am. Ceram. Soc., Vol. 72, 1989, pp.525-532.

[17]   Marshall D. B. and Oliver, W. C.," Measurement of Interfacial Mechanical Properties in Fiber-Reinforced Ceramic Composites", Journal of American Ceramic Society, Vol. 70, 1987, pp.542-548.

[18]   Mackin, T. J. ,Warren, P. D and Evans, A. G., "Effects of Fiber Roughness on interface Sliding in Composites", Acta metall mater., Vol. 40, 1992, pp.1251-1257.

[19]   Eldridge, J., "Fiber Push-Out Testing of Intermetallic Matrix Composites at Elevated Temperatures", Materials Research Society Symposium Proceedings, Vol. 273, eds. by D. Miracle, J. Graves and D. Anton, 1992, pp.325-330.

[20]   Marshall, D. B. , Shaw, M. C. Morris, W. L. and Graves, J. ,"Interfacial Properties and Residual Stresses in Titanium and Titanium Aluminide Matrix Composites", Workshop proceedings for Titanium matrix Composites, eds. by P. R. Smith and W. C. Revelos, Wright-Patterson AFB, Ohio, 1991, pp.329-347.

[21]   Watson M. C. and Clyne, T. W. , "The Use of Single Fiber Pushout Testing to Explore Interfacial Mechanics in SiC monofilament-Reinforced Ti — II. Application of the Tests to Composite Material", Acta metall. mater., Vol. 40, 1992, pp.141-148.

[22]   Kantzos, P. , Ghosn, L. and Telesman, J. ,"The Effect of Degradation of the Interface and Fiber Properties on Crack Bridging", HITEMP Review 1992, Vol. II, Cleveland, Ohio, 1992, pp.32-1 - 32-14

[23]   Warren, P.D., Mackin T. J and Evans, A. G.,"Design, Analysis and Application of An Improved Push-through Test for the Measurement of Interface Properties in

Composites", Acta metall. mater., Vol. 40, 1992, pp.1243-1249

[24] Ghonem, H., Zheng, D., Tamin, M. N. and Zhang, T., "Investigation of High Temperature Crack Bridging Mechanisms in SM1240/Timetal-21S", Annual Report prepared for AFOSR, Bolling Air Force Base, DC, April, 1994

[25] Cox, B. N. and Marshall, D. B. ,"The Determination of Crack Bridging Forces", International Journal of Fatigue, Vol. 49, 1991, pp.159-176

[26] Clyne, T. W. and Withers, P. J.,"An Introduction to Metal Matrix Composites", Cambridge University Press, London, 1993

[27] Schulte, K. and Minoshima, K., "Mechanisms of Fracture and Failure in Metal Matrix Composites, Metal Matrix Composites - Processing, Microstructure and Properties", N. Hansen et al., Eds. RISO National Laboratory, Roskilde, Denmark, 1991, pp. 129-147.

[28] Ghonem, H., Wen, Y. , Zheng, D., Thompson, M. and Linsey, G., "Effects of Temperature and Frequency on Fatigue Crack Growth in Ti-β21S Monolithic Laminate", Materials Science and Engineering, Vol. 161, 1993, pp.45-53.

[29] Warwick, C. M. and Smith, J. E., "Interfacial Reactions in Titanium Alloys Reinforced with C/TiB$_2$-Coated SiC Monofilament", Metal Matrix Composites - Processing, Microstructure and Properties, N. Hansen et al, Eds. ,RISO National Laboratory, Roskilde, Denmark, 1991, pp. 735-740.

[30] Osborne, D. and Ghonem, H. "On the Interfacial Reaction Kinetics of Timetal-21S Reinforced with SM1240 and SCS-6 Continuous Fibers", submitted to Materials Science and Engineering, March 1995.

[31] McCartney, L. N., "General Solution of A Certain Mixed Boundary Value Crack Problem", International Journal of Engineering Science, Vol. 21, 1983, pp.131-142

[32] Sneddon, I. N. and Lowengrub, M., "Crack Problems in the Classical Theory of Elasticity", Wiley, New York, 1969

[33] Marti, J. T., "An Algorithm for Computing Minimum Norm Solutions of Fredholm Integral Equations of the First Kind", SIAM Journal on Numerical Analysis, Vol. 15, pp.1071-1076, 1978

[34] Baker, C. T. H.," The Numerical Treatment of Integral Equations", Oxford University Press, Walton Street, Oxford, Great Britain, 1977

[35] Le petitcorps, Y., Lahaye, M., Pailler R. and Naslain, R., "Modern Boron and SiC

CVD Filaments: A Comparative Study", Composites Science and technology, Vol. 32, 1988, pp.31-55

[36] Budiansky, B., Hutchinson, J. W. and Evans, A. G., "Matrix Fracture in Fiber-Reinforced Ceramics", Journal of Mechanics and Physics of Solids, Vol. 34, 1986, pp.167-189.

[37] Zheng, D. and Ghonem, H., "A Model for High Temperature Fatigue Crack Bridging in Metal Matrix Composites", Annual Report prepared for AFOSR, Bolling Air Force Base, DC, July, 1995.

[38] Ghonem, H., Wen, Y. and Zheng, D. , "An Interactive Simulation Technique to Determine the internal Stress States in Fiber Reinforced Metal Matrix Composites", Materials Science and Engineering, A177, 1994, pp. 125-134.

[39] Zhang T. and Ghonem H., "Fatigue - Creep Interaction in Titanium Metal Matrix Composites", submitted to Int J. Fatigue and Fracture of Engineering materials, January 9, 1995.

[40] Buesking, K. W., Young J. L. and Reynolds, G. H., "Status of Advanced Filament Development for Titanium Alloy and Titanium Intermetallic Matrix Composites". Workshop proceedings for Titanium matrix Composites, eds. by P. R. Smith and W. C. Revelos, Wright-Patterson AFB, Ohio, 1991, pp.25-64.

[41] Blackman, L. C. F.," Modern Aspects of Graphite Technology", Academic Press Inc., London, 1970.

[42] Tamin M. N., Zheng, D. and Ghonem, H., "The Determination of the Stress State Variation during High Temperature Crack Bridging Process in MMCs", Damage of Metal Matrix Composites, 3rd Symposium on Advances in Fatigue, Lifetime Predictive techniques, Montreal, Canada, May, 1994.
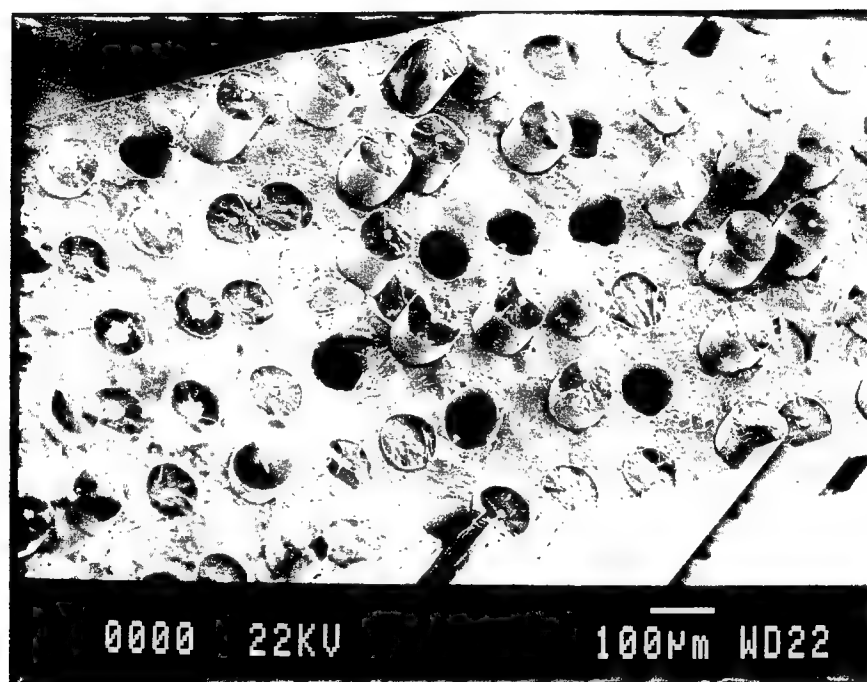
Fig. 6.1   Typical view of fracture surface obtained from 500°C/10 Hz test showing distinctive regions which related to the crack bridging and the crack acceleration stages.
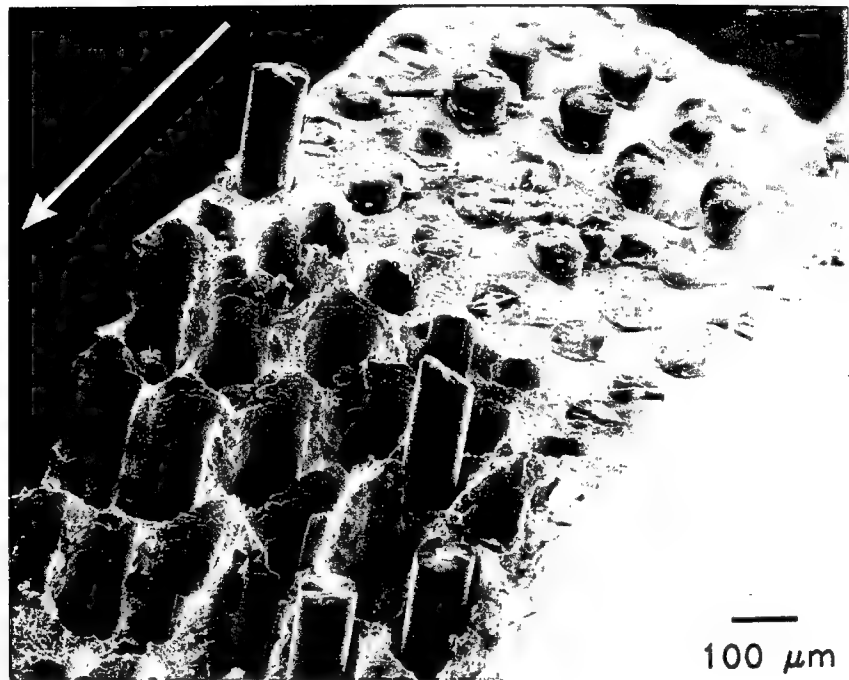
Fig. 6.2   View of final fracture region at low magnification (650°C/10Hz, arrow
            indicates the crack growth direction and the lower part of the fracture surface
            is the final fracture region.

Fig. 6.3(a)   Evidence of sliding grooves on the debonded surface at 24°C.

Fig. 6.3(b)   Surface morphology of the fiber in the final fracture region at 650°C showing intact parts of the carbon coating layer.

159

Fig. 6.3(c)   Surface morphology of the fiber in the bridging region at 650°C (vacuum).
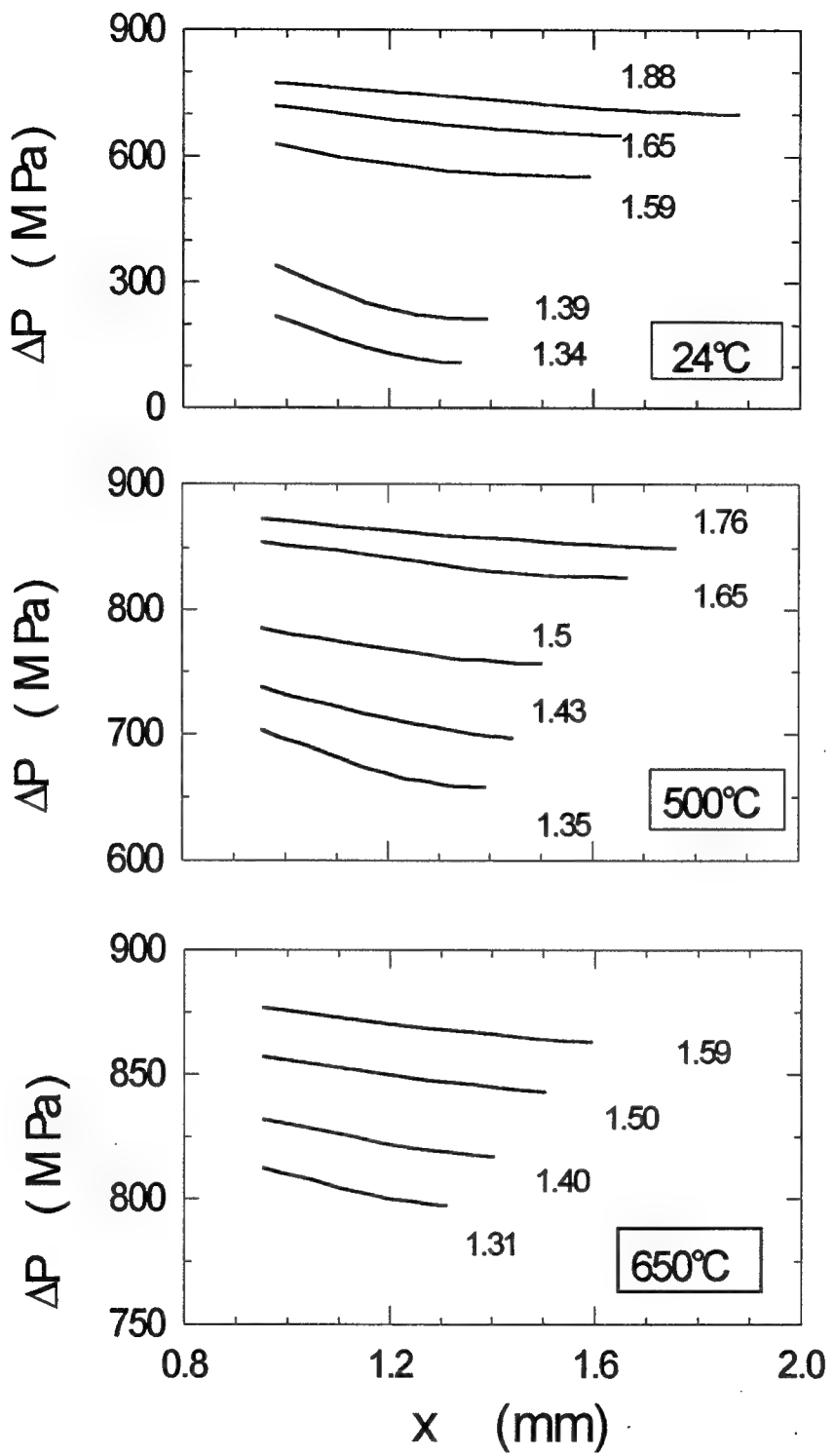
Fig. 6.4   Fiber bridging stress distributions for different crack lengths at: (a) 24°C; (b) 500°C; (c) 650°C. X is the distance measured fro the crack tip to the center of the machined hole.
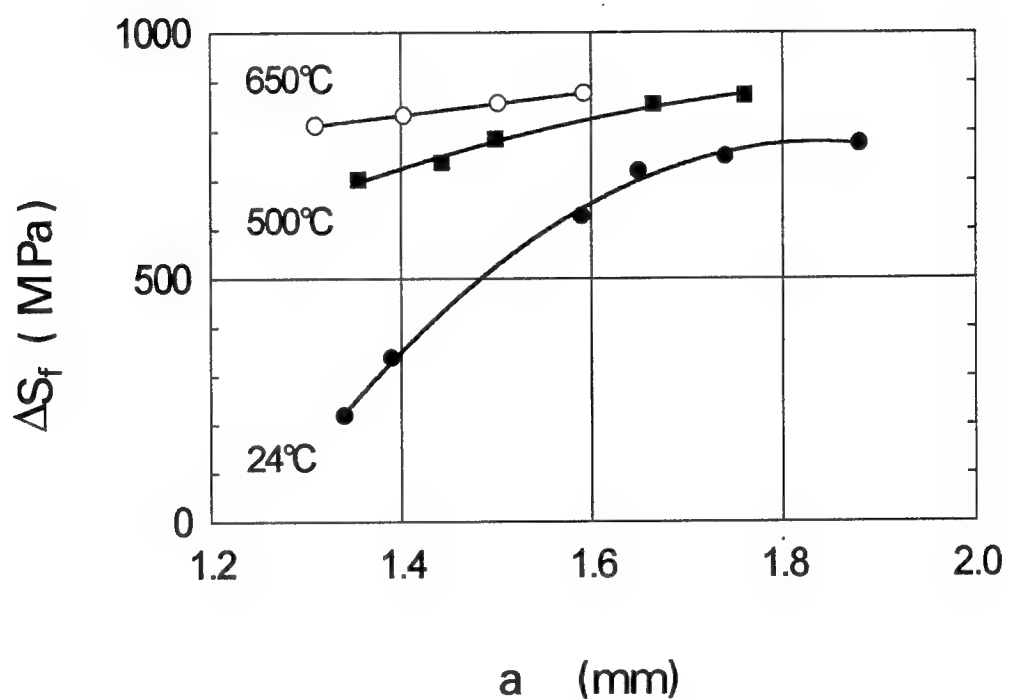
Fig. 6.5   Fiber bridging traction at the crack mouth as function of crack length
(measured from the center of the hole) and temperature.
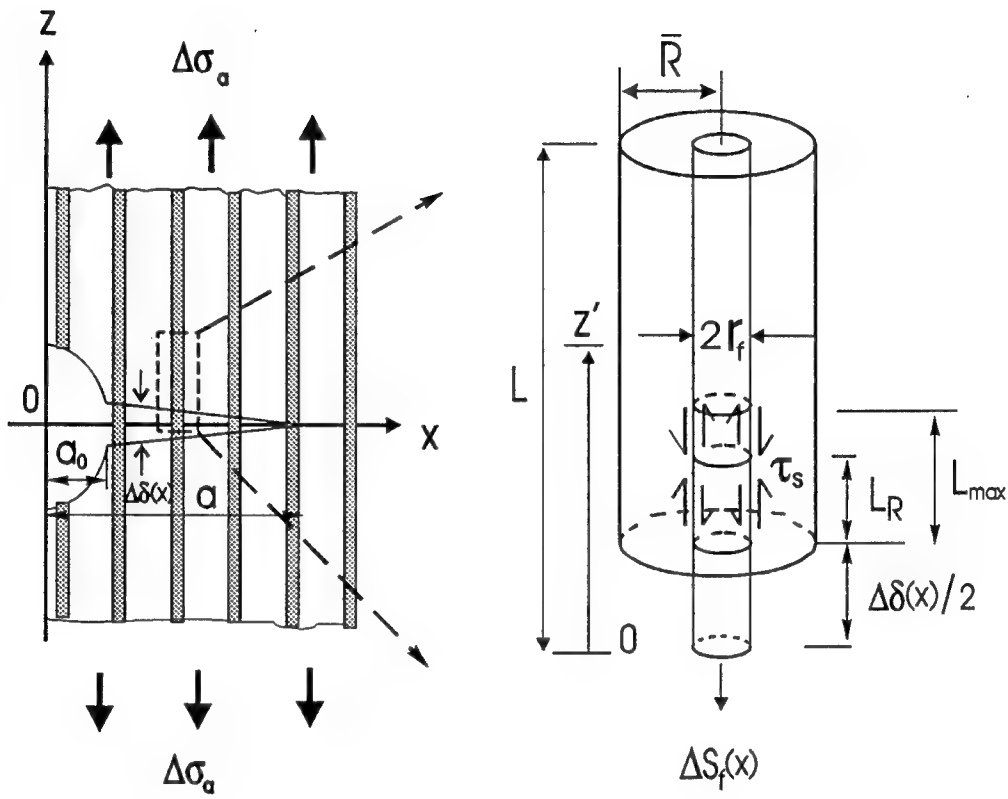
Fig. 6.6   A geometric configuration of the proposed micromechanical model.
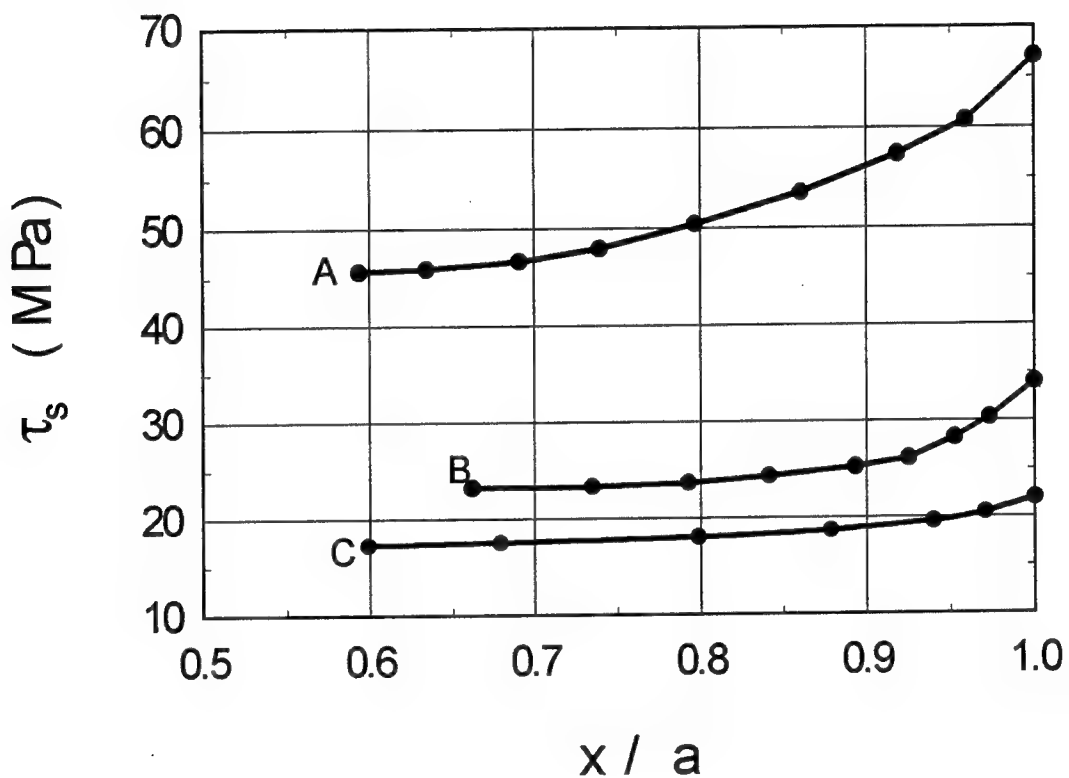
Fig. 6.7   Frictional shear stress for different crack lengths and temperatures; **A)** 1.65 mm / 24°C,   **B)** 1.665 mm / 500°C and **C)** 1.593 mm / 650°C
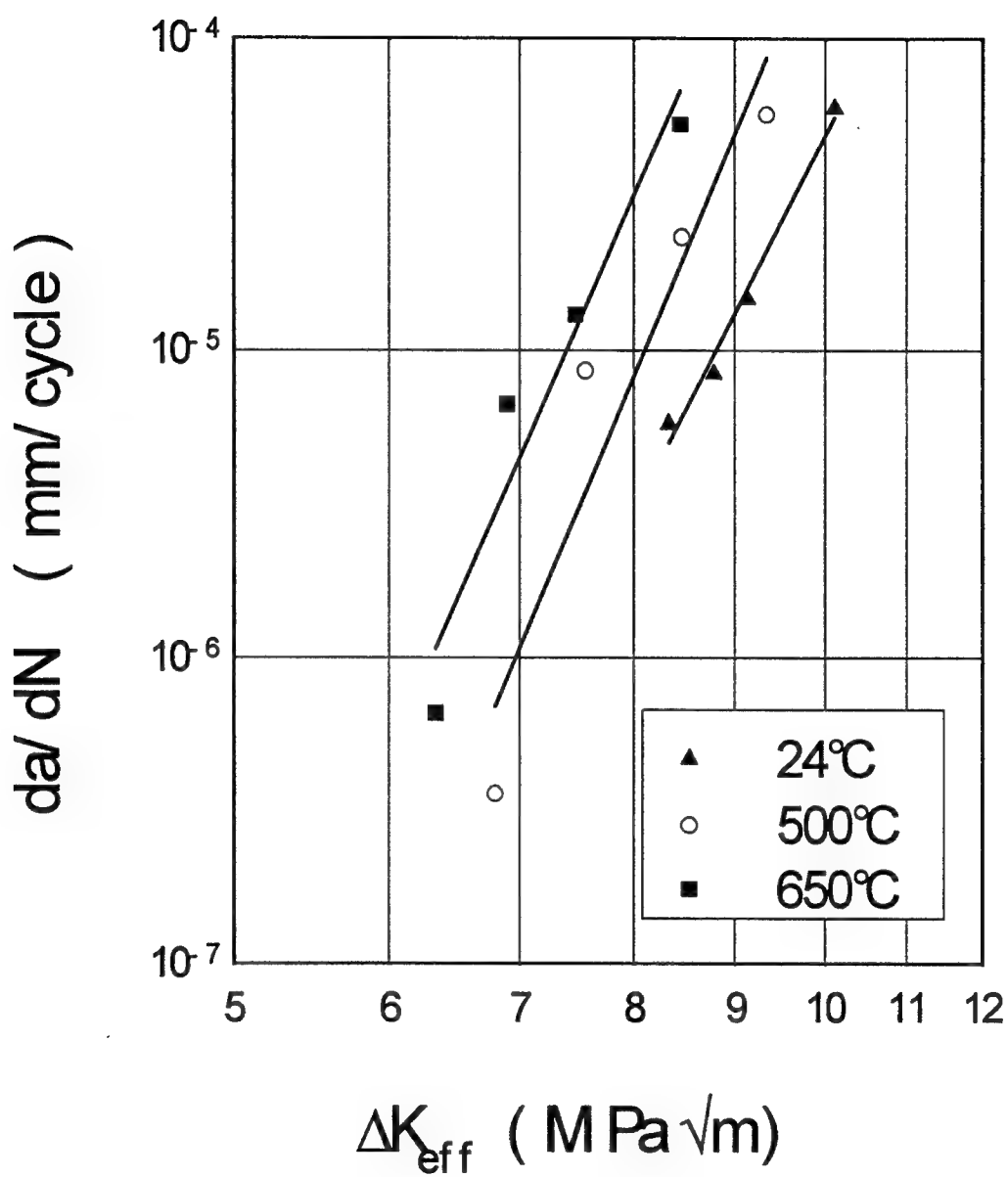
Fig. 6.8 ΔK_{eff} versus crack growth rate for different temperatures.
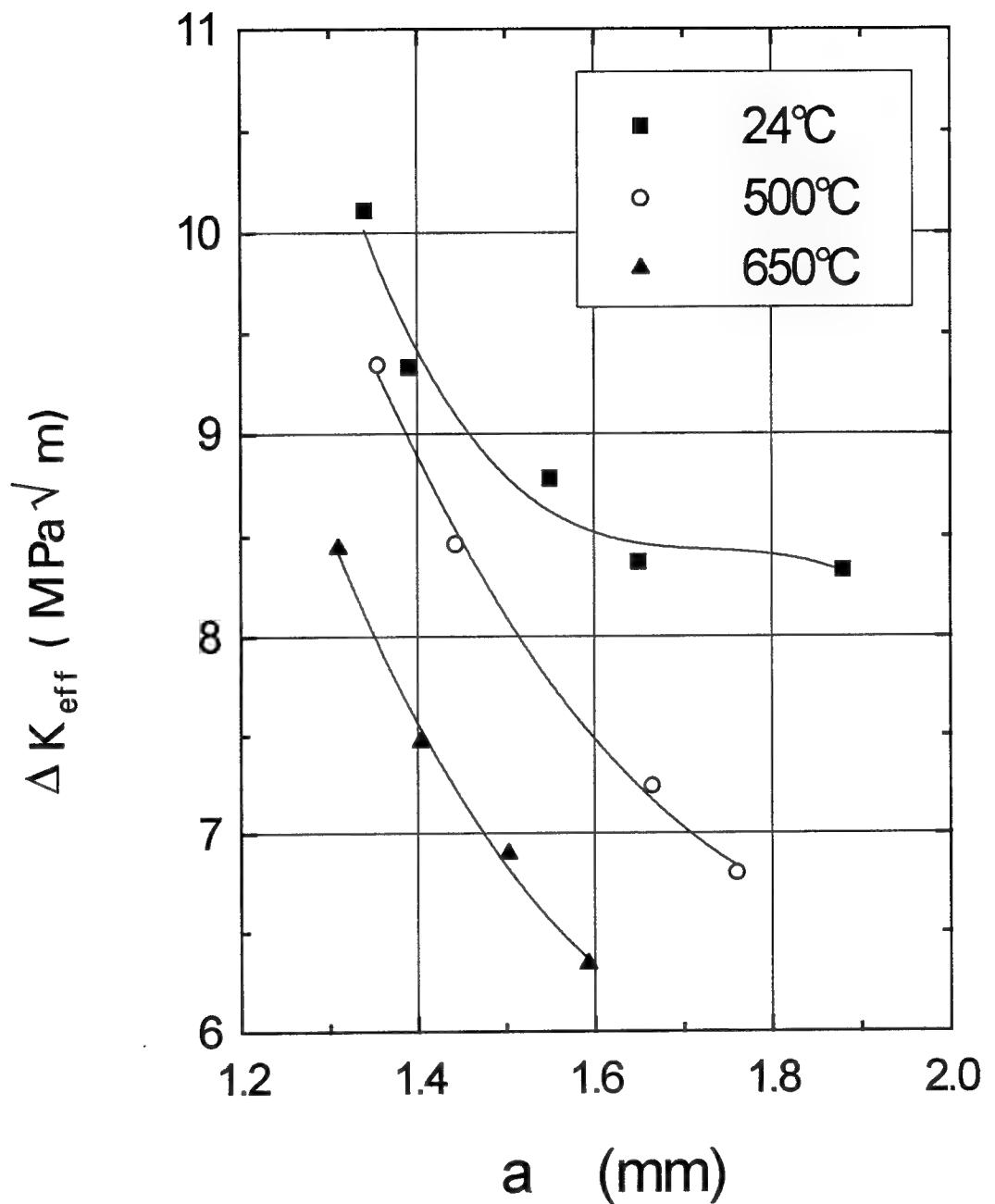
Fig. 6.9 ΔK_{eff} versus crack length for different temperatures.
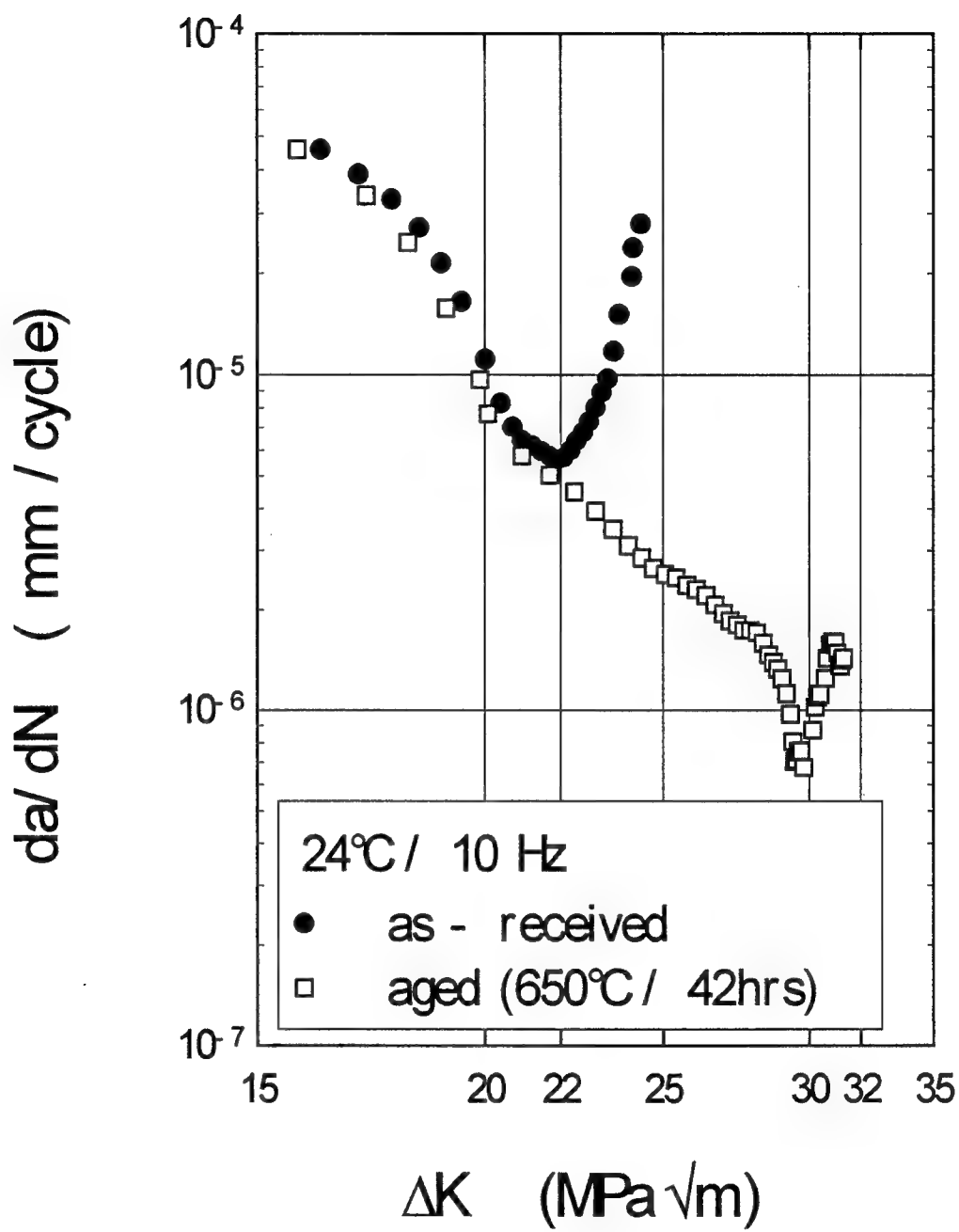
Fig. 6.10   The crack growth rates for as-received and aged specimens (24°C/10Hz).

SECTION 7

TIME-DEPENDENT FATIGUE CRACK GROWTH
IN TITANIUM METAL MATRIX COMPOSITES [7]

ABSTRACT

The interaction of fatigue and creep in a titanium metal matrix composite was studied by employing loading frequencies of 10 Hz (in both air and vacuum environment) and 0.1 Hz with and without hold times (in air) at 500 °C. It was shown that, for the same loading frequency, the crack growth rate is lower in vacuum than in air. In air environment, however, where the influence of load-related creep and environmental effects exist, it was shown that a decrease in the loading frequency leads to a decrease in the crack growth rate. This behavior is interpreted in terms of the redistribution of fiber and matrix stresses occurring in response to the creep-related relaxation of matrix stresses. The result of this stress redistribution is the generation of a compressive axial residual stress in the matrix phase in the region of the composite ahead of the crack tip. As the crack bridges the fibers in this region, the release of the matrix residual compressive stress leads to the closure of the matrix fractured surfaces at the crack tip, thus leading to a decrease in the crack tip driving force. To support this concept, experimental measurements of the crack opening displacement at different loading frequencies are presented. In addition, a simple model is proposed to describe the nature of the residual stresses developed in the matrix phase during cyclic loading. Results of this model have been examined using finite element analysis. The influence of time-dependent effects during a fatigue cycle was, furthermore, investigated by carrying out high frequency fatigue tests on specimens which have been previously subjected to creep deformation. Results of these tests in terms of the crack growth rate and associated crack closure, support the conclusion that a predeformed matrix produces a decrease in the crack growth rate of the corresponding composite.

7.1 INTRODUCTION

Fiber-reinforced titanium metal matrix composites are promising materials for high temperature aerospace applications. They offer improved combinations of various properties such as strength, oxidation resistance, density and high temperature capabilities. In anticipation of their use as high temperature structural components, efforts have to be made

---

[7]   Appeared as "Time-dependent Fatigue Crack Growth in Titanium Metal Matrix Composites," T. Zhang and H. Ghonem , Int J. Fatigue and Fracture of Engineering Materials, pp. 1249-1262, 1995.

in understanding their fatigue and crack growth behavior under loading conditions promoting time-dependent damage effects. These effects are significant due to the fact that although deformation response of the SiC-fibers reinforcement for temperatures up to 800 °C remains elastic, the titanium alloy matrix readily flows at temperatures as low as 400 °C [1]. Tamin and Ghonem [2,3] suggested that the failure of fibers in the SM1240/Timetal 21S composite at 500 °C and 650 °C depends on both the continuous fiber strength degradation and fiber stress buildup. These two factors were shown to be both cycle- and time-dependent. A number of experimental studies have been done in this regard. These studies can be classified into two groups according to whether fatigue life or crack growth rate was used as the measure of the fatigue damage. In the first group of studies, Gabb and Gayda [4], for example, evaluated the creep-fatigue-environment interactions on SiC/Ti-14Al-21Nb composite at the temperature of 650 °C and the frequency of 0.33 Hz with a hold time imposed at the maximum load levels. They concluded that creep and environmental attack considerably reduce the fatigue life of the composite by fiber overloading, due to load shedding from the matrix to the fibers. At higher loads, the fatigue life is dominated by creep, while environmental attack became more significant at lower load levels. In a different study [5] conducted on the SCS-6/Ti-15-3 composite at 300 °C and 550 °C, it was shown that at high cyclic stress and strain, the fatigue resistance of the composite was substantially lower at 550 °C than that at 300 °C. This observation was attributed to the inability of the matrix to support the cyclic mean stress at 550 °C. Nicholas and Russ [6] performed a study on SCS-6/Ti-24Al-11Nb at 650 °C using several loading frequencies. Their study demonstrated that the fatigue life measured in terms of the number of fatigue cycles was reduced by a factor of approximately 10 when the fatigue loading frequency was decreased from 3 Hz to 0.00278 Hz. Further reduction of the fatigue life was observed when periods of hold-time were imposed at the maximum stress levels. There are other studies which have dealt with the same topics [7-11] and all these studies reach the same conclusion that the fatigue life of the titanium matrix composite degrades as the temperature and hold time increase and as the frequency decreases.

In the second group of studies, the time-dependent fatigue behavior was investigated in terms of the crack growth rate. Bain et al [12] worked on SCS-6/Ti-6Al-4V at 318 °C subjected to loading frequencies of 20 Hz, 0.33 Hz and 0.033 Hz. Their results showed that, while there was no significant difference in the fatigue crack growth rates for the first two frequencies, the fatigue crack growth rate for the 0.033 Hz testing increased by a factor of 40. This increase was attributed to environmental damage affecting the Ti-6Al-4V matrix material. They did not, however, observe changes in the fracture surface features of specimens tested at the three different frequencies. Ibboston et al. [13] studied the crack growth response of the same above-mentioned composite using single edge notched specimens. Tests were carried out at both room temperature and 550 °C for two loading frequencies; 10 Hz and 0.5 Hz. They observed that the crack growth rate increases with an increase in temperature and a decrease in the loading frequency. Barney et al [14] performed a study The tests were carried out at a frequency of 10Hz, $\Delta K_a = 12 MPa\sqrt{m}$, R= 0.5 and at room temperature as well as at 500 °C. At room temperature, the da/dN was found to decrease as the crack length increased until the crack was arrested, indicating that significant fiber bridging had occurred. At 500 °C, while the da/dN was higher than that at room

temperature, it increased rapidly with the increase in the crack length thus indicating very limited, if any, fiber bridging involved. Zheng and Ghonem [15] studied the crack growth process in the SM1240/Timetal-21S at 24°C, 500° C and 650° C in air environment at frequencies ranging from 20 Hz to 0.03 Hz. It was observed that in the high frequency range (>10 Hz), the crack growth rate in the crack bridging stage decreases as the temperature increase. At loading frequencies lower than 10 Hz, it was similarly shown that the decrease in the loading frequency leads to a decrease in the crack growth rate. While these results seem to be contradictory to those mentioned above, an important difference exists between the test conditions used in Ref. [15], and those used, for example, in Refs. [12-14]. While the former used an applied load range low enough to produce a crack growth process with significant fiber bridging, the latter employed a fatigue load with a level at which fiber bridging was limited or completely eliminated. The combined influence of temperature and fiber bridging is illustrated in a study carried out by John et al. [16]. In their work, it was shown that the fatigue crack of SCS-6/Ti-24Al-11Nb composite at 650°C propagates with very limited fiber bridging at relatively low load levels, while at room temperature significant fiber bridging could be found during crack growth at all the applied load levels. At 650°C, a region of crack bridging ocurred at a stress level of 450 MPa . In this region the crack growth rate was almost aidentical to that at room temperature. However, for non-bridging crack growth at 500°C, the crack growth rate for identical loading conditions increased by one to two orders of magnitude.

On the basis of the above mentioned results, it could be stated that the fatigue resistance of titanium matrix composites, described in terms of fatigue life or in terms of the crack growth rate, is strongly time-dependent where creep and/or environmental attack are considered important parameters. For the crack growth process with either limited or no fiber bridging, the crack growth rate increases as the temperature increases and frequency decreases . However, when significant fiber bridging is involved during crack growth, the same conclusions may not hold true as suggested by the results of Refs. [15,16]. Because environmental attack is always detrimental to the crack growth process, these results suggest that, under the condition of fiber bridging at elevated temperatures, the creep component of the loading cycle could produce crack growth rate retardation effects. The objective of this work is to investigate the validity of this suggestion by focusing on the time dependent crack growth behavior of titanium matrix composites in the presence of fiber bridging. In this, an attempt will be made to determine the crack growth mechanisms associated with creep loading. This is achieved by measuring the crack growth rate of the SM1240/Timetal-21S composite subjected to loading profiles combining both creep and fatigue components with the load level promoting significant fiber bridging. The ability of this type of loading to modify the redistribution of stresses in the matrix and fiber phases of the composite was analyzed. The nature of the matrix stresses was linked to local deformation events taking place at the crack tip, and, consequently, influencing the crack growth process. For this purpose, the crack opening displacement was measured as a function of both temperature and loading frequency. To support the experimental results, a simple analytical model is proposed to describe the nature of the residual stresses developed in the matrix phase during cyclic loading. Results of this model have been examined using finite element analysis.

7.2 MATERIAL AND EXPERIMENTAL PROCEDURE

The material used in this study is the SM1240/Timetal-21S composite. The matrix material is the metastable-ß titanium alloy, Timetal-21S (in wt%: 0.1 Fe, 16.0 Mo, 3.06 Al, 2.9 Nb, 0.2 S, 0.22 C, 0.12 O, 0.005 N and balance Ti). The SM1240 fiber (100 μm in diameter) consists of 10 μm diameter tungsten-cored SiC monofilament with dual vapor-deposited coatings of carbon (1 μm) and boron-rich titanium di-boride (1 μm) on the surface. The composite material is made of seven plies of Timetal-21S foil, each 112 μm, in thickness and 6 layers of SM1240 fibers, i.e. $[0]_6$ lay up. The composite with a fiber volume fraction of 35%, was consolidated using a vacuum hot press producing plates measuring 900 mm x 100 mm x 1 mm, all of which have received a stabilization heat treatment (621°C/8 hours) in a dynamic vacuum furnace. Test specimens were cut into rectangular coupons (75 mm x 10 mm) with the fibers oriented along the loading direction, 0°. A center hole with horizontal side notches producing an average initial crack length, $2a_o$, measuring 1.89 mm, was machined in each of the crack growth specimens.

Fatigue tests were carried out using a servohydraulic testing machine equipped with a computer controlled waveform and data acquisition system. The specimens were gripped with end tabs made of waspalloy and an alignment procedure was performed prior to each test. During each of the fatigue tests, the crack length was measured continuously using the direct current potential drop method supported by optical measurements using traveling microscopes. The loading frequencies included 10 Hz, 0.1 Hz and 0.1 Hz with both 10- and 100- second hold times imposed at the maximum stress level. All the fatigue tests were carried out under constant load range with a maximum level of 300 MPa and a stress ratio, R, of 0.1. This loading condition, in the work of Zheng and Ghonem [19], is shown to produce bridging fatigue cracks in the composite under study. Furthermore, in order to asses the role of environment, a single test was carried out in vacuum conditions (10^{-7} torr / 10Hz). In addition, several notch-free specimens were independently subjected to accelerated creep loading at 500 °C in order to introduce an amount of inelastic deformation in the matrix phase of each. The creep strain was achieved using a servohydraulic testing machine and measured using a water-cooled extensometer with quartz rods. These "pre-deformed " specimens, after machining the center notch in each, were subsequently subjected to pure fatigue loading in order to identify the effect of predeformation on the crack growth behavior. Heating of all the test specimens was achieved with an open furnace using radiant heating lamps. The temperature was controlled with two thermocouples spot-welded to the specimen about 10 mm above and below the center of the specimen. Temperature variations along the specimen gage length were less than 2 °C. The loading parameters and the testing environment for each of fatigue tests are listed in Table 7.1. Furthermore, the crack opening displacement, $\Delta\delta$, for selected discrete crack lengths in each fatigue test was determined. This was done by calculating the difference between the maximum and minimum value of the displacement-load loops at the crack position where the measurements are taken. This loop which corresponds to a full loading cycle, was obtained using a linear array laser interferometric displacement gage system with a resolution of 10 nm. The crack opening displacement (COD) measurements were conducted by using a loading cycle with a frequency of 0.03 Hz. No

COD measurements were carried out for the vacuum test.

Table 7.1: Description of Fatigue Tests[†]

No. of Tests	Description of Test in Text	Test Environment	Frequency (Hz)	Hold time[††] (seconds)
2	10 Hz	air	10	none
1	0.1 Hz	air	0.1	none
1	0.1 Hz (vac)	vacuum	0.1	none
1	0.1 Hz + 10sh	air	0.1	10
1	0.1 Hz + 100sh	air	0.1	100
2	pre-creep[†††]	air	0.1	none
1	aging-only[††††]	air	0.1	none

†   All fatigue tests were carried out at temperature = 500 °C, σ_{max} = 300 MPa and R= 0.1.

††   The hold time is imposed at the maximum load level of the loading cycle

†††   The pre-deformed specimens were subjected to creep loading of 600 MPa/120 hours at 500 °C prior to the fatigue test.

††††   The aging-only specimen was subjected to thermal aging in air for 120 hours at 500 °C prior to the fatigue test.

7.3 RESULTS AND ANALYSES

7.3.1 Crack Growth Behavior

Experimental results in the form of the crack growth rate, da/dN, versus the applied stress intensity factor, ΔK_a, for the five fatigue tests discussed above are shown in Fig. 7.1(a). The common feature of these growth curves is the presence of an initial crack bridging stage indicated by the continuous decrease in the crack growth rate as the applied stress intensity factor ΔK_a (or the crack length) increases. This crack bridging stage is followed, as in the case of the 10 Hz
test, by a single growth acceleration stage, while in the 0.1 Hz test (air), it is followed by a stage which consists of repeated events of growth acceleration and deceleration leading ultimately to crack instability and final failure of the test specimen. Detailed analysis of the crack growth behavior of this composite is discussed in Ref. [15]. Focusing only on the first crack bridging stage of each testing condition, the crack growth results were plotted in Fig.5.1(b) in the form of the crack growth speed, da/dt, which takes into account the variations in the cycle time for the different loading frequencies, versus the maximum applied stress intensity factor, K_{max}. The detrimental influence of environment is evident when comparing both the 0.1 Hz air and vacuum conditions; the absence of air environment has produced a lower crack growth rate. For air tests, the decrease of the loading frequency from 10 Hz to 0.1 Hz has resulted in a decrease in the crack growth rate. A further decrease in the loading frequency to 0.1 Hz + 10 seconds hold time and 0.1 Hz + 100 seconds hold time produced a further decrease in the crack growth rate. Since an increase of the cycle time duration permits the time-dependent related effects, namely environment and creep, to influence the crack growth rate behavior, the above results would suggest that the presence of creep, contrary to environmental effects, leads to a decrease in the crack growth rate. This effect of creep loading could be due to a possible related reduction of the crack tip driving force. This conclusion is supported by results in Fig. 7.2 which show the COD loops for the 10 Hz and the two hold time tests. These loops are obtained at positions located 220 μm behind the crack tip in the 10Hz and 0.1Hz + 10sh tests and 70 μm in the 0.1Hz + 100sh test. The COD loops for the 0.1 Hz +10 sh and the 0.1 Hz +100 sh exhibit crack closure at load levels of 2 KN and 1.5 KN, respectively. The net applied load range in these cases becomes as small as 1.3 KN and 1.8 KN, which is lower than that experienced by the crack tip in the 0.1 Hz test case (It should be noted that while the crack growth rate of the 0.1 Hz +100 sh test is lower than 0.1 Hz, it is higher than that of the 0.1Hz + 10sh test. This could be interpreted in terms of a stronger environmental role as the hold time becomes as excessive as 100 seconds. The competition between the influence of creep effects versus those of the environment as a function of the hold time duration is under investigation by the authors). The reason for this closure phenomena could be understood by examining the stress distribution in the matrix and fiber phases in regions ahead of the crack tip when subjected to a low frequency loading. In the next section, a simplified model is developed to describe the evolution of these stresses, particularly of the matrix, in a notch-free specimen subjected to creep loading.

173

7.3.2 Matrix Residual Stress due to Creep Loading

In this analysis, it is assumed that a composite specimen is subjected to an isothermal loading cycle in which a hold time, t_h, is imposed with a maximum constant stress σ_c, see Fig.3. It is also assumed that the stress distribution between the fiber and matrix phases obeys the law of mixture and a full bonding of the fiber/matrix interface holds throughout the analysis. The strain rate of the matrix at any time, t , during the hold time period is given by:

$$\dot{\varepsilon}_{\tilde{A}} = B(T) \ \sigma_{\tilde{A}}^{\hat{a}}$$

which could be rewritten as:

$$d\varepsilon_{\tilde{A}} = B(T) \ \sigma_{\tilde{A}}^{\hat{a}} \ dt \tag{1}$$

where B(T) and n are temperature- and material-dependent variables and σ_m is the stress developed in the matrix at time t. The corresponding fiber stress, σ_f , is then calculated as:

$$\sigma_{\hat{u}} = \frac{\sigma_{\hat{U}} - \sigma_{\tilde{A}} (1 - V_{\hat{u}})}{V_{\hat{u}}} \tag{2}$$

where V_f is the fiber volume fraction. Because of the perfect fiber/matrix bond assumption, the variations in the fiber and matrix iso-strains, $d\varepsilon_f$ and $d\varepsilon_m$, respectively, are written in incremental form as:

$$d\varepsilon_{\hat{u}} = \frac{d\sigma_{\hat{u}}}{E_{\hat{u}}} = d\varepsilon_{\tilde{A}} \tag{3}$$

Where E_f is the Young's modulus of the fiber. Substituting Eqs. (1) and (2) into (3) gives:

$$d\varepsilon_{\hat{u}} = - \frac{(1 - V_{\hat{u}})}{V_{\hat{u}} \ E_{\hat{u}}} \ d\sigma_{\tilde{A}} = B(T) \ \sigma_{\tilde{A}}^{\hat{a}} \ dt \tag{4}$$

By rearranging the two right-hand side terms, one obtains:

$$\sigma_{\tilde{A}}^{-\tilde{a}} \ d\sigma_{\tilde{A}} = \frac{V_{\hat{u}} \ E_{\hat{u}}}{(1 - V_{\hat{u}})} \ B(T) \ dt \tag{5}$$

Integrating Eq. (5) for the limits of σ_m and t, the following expression is obtained:

$$\sigma_{\tilde{A}} = (\alpha \ t + \beta)^{-\frac{\cdot}{\tilde{a} - \cdot}} \tag{6}$$

where

$$\alpha = \frac{B(T) \ (n-1) \ V_f \ E_f}{1 - V_f} > 0$$

$$\beta = (\sigma_m^0)^{-(n-1)}$$

and $\sigma_m{}^0$ is the matrix stress occurring at the moment of applying the composite stress, σ_c , i.e. at $t_h = 0$ (position 1 indicated on Fig. 7.3). Eq. (6) could then be used to calculate the matrix stress in terms of the hold time t_h. These calculations show that three possibilities exist regarding σ_m . Each of these possibilities depends on the duration of t_h . These are:

$$
\begin{array}{lllll}
\text{a)} & t_{\hat{u}} = 0 & , & \sigma_{\tilde{A}} = \sigma_{\tilde{A}}^{D} ; \\
\text{b)} & t_{\hat{u}} > 0 & , & \sigma_{\tilde{A}} < \sigma_{\tilde{A}}^{D} ; & \tag{7} \\
\text{c)} & t_{\hat{u}} \to \infty & , & \sigma_{\tilde{A}} \to 0
\end{array}
$$

Upon unloading at the end of the hold time period (position 2 in Fig.3) and reaching the applied load level of zero, the sum of the residual stress in both the matrix and fiber, $\sigma_m{}^*$ and $\sigma_f{}^*$, respectively, at position 3, is written as:

$$\sigma_{\hat{u}}^{*} \ V_{\hat{u}} + \sigma_{\tilde{A}}^{*} \ (1 - V_{\hat{u}}) = 0 \tag{8}$$

At this position, the fiber and matrix iso-strain condition dictates that:

$$\frac{\sigma_{\tilde{A}} - \sigma_{\tilde{A}}^{*}}{E_{\tilde{A}}} = \frac{\sigma_{\hat{u}} - \sigma_{\hat{u}}^{*}}{E_{\hat{u}}} \tag{9}$$

where E_m is the Young's modulus of the matrix. Substituting Eq. (8) into (9) gives:

$$\sigma_{\tilde{A}}^* = \frac{V_{\hat{u}}(E_{\hat{u}}\,\sigma_{\tilde{A}} - E_{\tilde{A}}\,\sigma_{\hat{u}})}{E_{\dot{U}}} \tag{10}$$

Now, consider the balance of fiber and matrix stresses at the two positions labeled 1 and 2 in Fig, 7.3. These could be written as:

$$\sigma_{\tilde{A}}^{\textrm{Ð}}\,(1 - V_{\hat{u}}) + \sigma_{\hat{u}}^{\textrm{Ð}}\,V_{\hat{u}} = \sigma_{\dot{U}} \tag{11}$$

$$\sigma_{\tilde{A}}\,(1 - V_{\hat{u}}) + \sigma_{\hat{u}}\,V_{\hat{u}} = \sigma_{\dot{U}} \tag{12}$$

Thus, the difference between the above two equations becomes:

$$(\sigma_{\tilde{A}}^{\textrm{Ð}} - \sigma_{\tilde{A}})\,(1 - V_{\hat{u}}) = (\sigma_{\hat{u}} - \sigma_{\hat{u}}^{\textrm{Ð}})\,V_{\hat{u}} \tag{13}$$

Substituting Eq. (13) into (10) gives:

$$\sigma_{\tilde{A}}^* = \sigma_{\tilde{A}} - \sigma_{\tilde{A}}^{\textrm{Ð}} \tag{14}$$

Eqs. (7) and (14) indicate clearly that the matrix residual stress due to the application and the subsequent removal of a creep load is always compressive. However, when, considering the consolidation-induced matrix residual stress $\sigma_m{}^R$, the net matrix residual stress becomes $\sigma_m{}^*$ + $\sigma_m{}^R$. As will be detailed later, under the loading and temperature conditions used in the above mentioned crack growth experiments, $\sigma_m{}^*$ is calculated using a finite element model, see Appendix I, and is found to be larger in magnitude and opposite in sign to $\sigma_m{}^R$. This, therefore, leads to the conclusion that the net matrix residual stress in regions ahead of the crack tip, due to the creep component of a low frequency loading, could be compressive in nature.

7.4 PROPOSED MECHANISM

On the basis of the crack growth results and the residual stress analysis described above, a concept is proposed to explain the observed influence of the low frequency loading on the high-temperature bridging fatigue crack growth behavior. During a low frequency loading cycle, time-dependent flow and associated stress relaxation occur in the matrix phase. This is aided by the fact that matrix grains surrounding fibers are smaller than the average matrix grain size due to consolidation-induced recrystallization, see Fig. 7.4. The matrix

176

stress relaxation leads to an increase of the matrix-to-fiber load transfer which results in an increase of the fiber bridging stress and, consequently, the crack tip shielding. The complex aspect of the matrix time-dependent deformation during a low frequency loading occurs, however, in the composite region ahead of the crack tip. In this region, a condition of matrix/fiber iso-strain is required in order to maintain the fiber/matrix bonding. Depending on the degree of the inability of the fiber to accommodate the matrix strain, a compressive residual stress could be developed in the matrix phase of this region. This stress when relaxed due to the matrix fracture as it is reached by the propagating bridging crack, would result in a matrix surface displacement producing a crack tip closure. This closure, which occurs at an applied stress level higher than that corresponding to the minimum load of the fatigue cycle, results in a decrease of the applied stress range and, consequently, the crack tip driving force. The basic idea behind this concept is that the redistribution of stresses in the matrix phase of the composite due to time-dependent loading leads to a crack tip closure and consequently to a lower crack growth rate. Viewing the low frequency loading as being a combined creep-fatigue process, this concept was investigated through an experimental procedure in which the influence of prior creep-deformation on the subsequent fatigue crack growth behavior was examined. This was achieved by subjecting a notch-free specimen to a static loading at 500 °C in order to develop matrix creep deformation which would, for the reasons discussed above, introduce a compressive residual stress into the matrix phase. This was followed by cooling the specimen to room temperature in order to machine a center hole with notch starters identical to those used in the fatigue specimens. The temperature was then raised to the 500 °C level where the specimen is supposed to regain the level of the residual stress developed during the previous creep loading. The test specimen was subjected to a 10 Hz fatigue loading cycle which was assumed to promote none or minimum creep related effects. The crack growth rate of this specimen was then compared with that of the 10 Hz/500 °C crack growth curve (shown in Fig. 7.1) which belongs to a specimen without prior creep deformation.

For the specimen which was subjected to creep loading, a permanent inelastic strain of 0.13% was achieved by applying a constant stress level of 600 MPa for a duration of 120 hours. The corresponding creep curve is shown in Fig. 7.5. A numerical analysis using a finite element model was carried out in order to identify the nature of the residual stress, due to the pre-deformation process, in both the fiber and the matrix phases of this specimen. This work, detailed in Appendix I, shows that the matrix residual stress at the test temperature 500 °C, is -40 MPa. Fatigue results of this pre-deformed specimen (10 Hz/500 °C), in the form of the number of cycles versus the crack length are shown in Fig. 7.6a which is compared with that of the as-received specimen, i.e. without prior creep deformation, in Fig. 7.6b. These figures show that the number of fatigue cycles required to achieve the same crack length is larger in the pre-deformed specimen. The crack growth rate versus the crack length and versus the applied stress intensity factor for the pre-deformed specimen are shown in 7.7(a) and 7.7(b), respectively. The presence of a complex stress field ahead of the crack tip in this pre-deformed specimen is evident in the number of repeated crack bridging events following the first crack bridging stage. As shown in Fig. 7.7(a), the distance between each deceleration/acceleration pair, positions A, B, C and D, is approximately 100 μm which is within the range of the fiber spacing in this composite. The mechanism leading to this

177

repetition of deceleration/acceleration growth events could be explained as follows. As the crack tip bridges the first encountered fiber array, the matrix material surrounding these fibers is cracked, thus releasing its compressive stress which, in turn, causes crack tip closure. This is evident in the appearance of the COD loops taken at different crack length of this pre-deformed specimen, see Fig. 7.8. The presence of closure in these loops produces a decrease in the effective crack tip driving force, ΔK_{eff}, thus giving rise to the apparent crack tip arrest as indicated by positions A, B, C and D in Fig 7.7. The temporary arrest of the crack at one fiber position permits, through a Mode II fatigue process, a longer fiber/matrix interface debonding which assists in a further decrease of the ΔK_{eff} and, consequently, a further delay in the propagation of the Mode-I crack tip. As the number of fatigue cycles increases, the bridging stresses acting along all or some of the bridging fibers could reach their corresponding residual strength, see the work of Tamin and Ghonem [2]. The failure, or partial failure, of the first fiber array triggers a stage of crack growth acceleration thus advancing the crack tip to the next fiber array where events of crack closure and subsequent acceleration are to be repeated. As a result of this complex crack growth process, the number of cycles required to propagate a crack length of 3.39 mm, measured from the notch tip of the pre-deformed specimen, is approximately seven times higher than that experienced by the specimen without the pre-creep deformation, see Figs. 7. 6(a) and 7.6(b). Comparisons of the crack growth rate versus the applied stress intensity factor for these two specimens are shown in Fig. 7.7. Here, it is noted that during the single bridging stage occurring in the as-received specimen, multiple acceleration/deceleration events took place in the pre-deformed specimen. A similar pattern is also observed in the 0.1Hz + 10 sh specimen, see Fig. 7.1.

Furthermore, in order to insure that aging alone is not the reason behind the crack growth response of the pre-deformed specimen, a crack growth test was carried out on a specimen which was aged (without pre-deformation) at 500 °C for 120 hours (a duration equal to that experienced by the predeformed specimens during the creep loading) prior to the fatigue testing. The crack growth curve of this aged-only specimen, again compared with that of the as-received specimen, is shown in Fig. 7.9. This figure indicates that although aging has some influence on the crack growth rate, it is not the reason for the distinct fatigue behavior of the pre-deformed specimen. The COD loops recorded at two different crack lengths in the aged-only specimen are shown in Fig. 7.10. Here, the closure feature observed in Fig. 7.8 is absent.

The series of tests carried out on the pre-deformed specimen was duplicated in order to examine the repeatability of the observations outlined above. Results of the crack growth rate versus the applied stress intensity factor for the two identical pre-deformed tests indicate clearly that the response of the low-frequency bridging fatigue crack growth, as shown above, is a repeated phenomenon.

7.5 CONCLUSIONS

A series of fatigue tests was performed on a SM1240 / Timetal-21S metal matrix composite at a temperature of 500 °C focusing on the low frequency loading in order to

identify the influence of time dependent effects on crack growth behavior. Under loading conditions promoting crack bridging in the above mentioned composite and focusing on the crack bridging stage, the following conclusions could be made:

(1) For the 0.1 Hz loading frequency, the absence of air environment results in a lower crack growth rate. The decrease in the loading frequency from 10 Hz to 0.1 Hz in air results in an increase of the crack growth rate. A further decrease in the frequency particularly when involving hold times at the maximum load level, however, results in a decrease in the crack growth rate. The influence of aging-only was found not to produce significant variations in the crack growth rate of the first crack bridging stage. The corresponding COD loops did not show features indicating crack tip closure.

(2) The decrease in the low frequency crack growth rate is explained on the basis of a mechanism which views the low frequency loading as being a combined creep-fatigue process. The creep related effects are exhibited in the form of time-dependent flow and associated compressive residual stress in the matrix phase in the region of the composite ahead of the crack tip. This stress, when relaxed due to the matrix fracture as it is reached by the propagating bridging crack, could result in a matrix surface displacement which produces a crack tip closure. This closure is shown to be responsible for the decrease of the applied stress range and consequently the crack tip driving force. This concept is supported by results of an analytical model and finite element analysis which were employed to identify the nature of the matrix residual stress due to time-dependent loading. Furthermore, the proposed concept was examined using a sequential creep-fatigue testing procedure.

7.6 REFERENCES

[1] P. K. Wright (1992), "Creep Behavior and Modeling of SCS-6 / Titanium MMC", Proceedings of Titanium Matrix Components Workshop, P. R. Smith and W. C. Revelos, eds., WL-TR-92-4035, 251-276.

[2] M. N. Tamin, and H. Ghonem (1994),"A Fracture Criterion for Bridging Fibers in Titanium Metal Matrix Composites ar Elevated Temperature", in Durability of Composite Materials, Robert C. Wetherhold, ed, proceedings of 1994 International Mechanical Engineering Congress and Exposition, Chicago, 51-58.

[3] M. N. Tamin, D. Zheng and H. Ghonem (1994), "Evolution of Bridging Fiber Stress in Titanium Metal Matrix Composite at Elevated Temperature", ASTM Third Symposium on Advances in Fatigue Lifetime Predictive Technique, Montreal, Quebec, Canada, May 16-17, 1994.

[4] T. P. Gabb and J. Gayda (1992), "Isothermal and Nonisothermal Fatigue Damage /

Failure Mechanism", in proceedings of Titanium Matrix Components Workshop, P. R. Smith and W. C. Revelos, ed., Report: WL-TR-92-4035, Materials Directorate, Wright Laboratory, 292-305.

[5]   T. P. Gabb, J. Gayda, and R. A. MacKay (1990), "Isothermal and Nonisothermal Fatigue Behavior of a Metal Matrix Composite", Journal of Composite Materials, Vol.24, 667-689.

[6]   T. Nicholas and S. M. Russ (1992), "Elevated Temperature Fatigue Behavior of SCS-6 / Ti-24Al-11Nb", Materials Science and Engineering, A153, 514-519.

[7]   T. Nicholas, S. M. Russ, N. Schehl and A. Cheney (1993), "Frequency and Stress Ratio Effects on Fatigue of Unidirectional SCS-6 / Ti-24Al-11Nb Composite at 650°C", Fatigue 93, Volume II, J. -P. Bailon and J. I. Dickson, ed., EMAS, 995-1000.

[8]   P. J. Cotterill and P. Bowen (1993), "Fatigue Crack Growth in a Fiber-reinforced Titanium MMC at Ambient and Elevated Temperatures", Composites, Vol.24(3), 214-221.

[9]   S. M. Russ and D. G. Hanson (1993), "Fatigue and Thermomechanical Fatigue of a SiC/Titanium $[0/90]_{2s}$ Composite", Fatigue 93, Vollume II, J. -P. Bailon and J. I. Dickson, ed., EMAS, 969-974.

[10]   M. Mirdamadi and W. S. Johnson (1993), "Fatigue of $[0/90]_{2s}$ SCS-6/Ti-15-3 Composite under Generic Hypersonic Vehicle Flight Simulation", Fatigue 93, Volume II, J. -P. Bailon and J. I. Dickson, ed., EMAS, 951-956.

[11]   S. M. Jeng and J. -M. Yang (1992), "Damage mechanisms of SCS-6/Ti-6Al-4V Composites under Thermal-mechanical Fatigue", Materials Science and Engineering, A156, 117-124.

[12]   K. R. Bain and M. L. Gambone (1990), "Fatigue Crack Growth of SCS-6/Ti-64 Metal Matrix Composites", in Fundamental Relationships Between Microstructure & Mechanical properties of Metal-Matrix Composites, ed. by P. K. Liaw and M. N. Gungor, The Minerals, Metals & Materials Society, 459-469.

[13]   A. R. Ibboston, C. J. Beevers and P. Bowen (1993), "Damage Assessment and Lifing of Continuous Fiber-reinforced Metal-matrix Composites", Composites, 24(3), 241-247.

[14]   C. Barney, C. J. Beevers and P. Bowen (1993), "Fatigue Crack Growth in SiC Continuous Fiber Reinforced Ti-6Al-4V Alloy Metal Matrix Composites", Fatigue 93, Vollume II, J. -P. Bailon and J. I. Dickson, ed., EMAS, 1073-1078.

[15]   D. Zheng, and H. Ghonem (1995), "High Temperature Fatigue Crack Growth of the Continuous Fiber Reinforced Titanium Metal Matrix Composite SM1240/Timetal-21S",   Metallurgical and Material Transaction, in print.

[16]   R. John, J. R. Jira, J. M. Larsen, and N. E. Ashbaugh (1994), "Fatigue Crack Growth in Unidirectional SCS-6/Ti-24Al-11Nb Composite Containing a Circular Hole (Part II)", in Mechanical Behavior of High Temperature Structural Materials, N. E. Ashbaugh, ed., Report: WL-TR-94-4059, Materials Directorate, Wright Laboratory, 466-517.

[17]   Y. L. Petitcorp, M. Lahaye, R. Pailler and R. Naslain (1988), "Modern Boron and SiC CVD Filaments: A Comparative Study", Composites Science and Technology, Vol.32, .31-55.

[18]   SIGMA Monofilament Products, Information Sheets, BP Metal Composites Limited, RAE Road, Farnborough, Hampshire GU146XE, England.

APPENDIX I

A finite element method was utilized to calculate the stress distribution in the constituents of the composite due to post-processing cool down and subsequent creep loading. In this analysis, the fiber distribution was idealized as a hexagonal array architecture with a unit cell being modelled as a concentric cylinder of a fiber with radius, r_f, embedded in the matrix phase with an outer radius of $r_m = r_f / \sqrt{v_f}$, where $v_f = 0.35$ is the fiber volume fraction of the composite. The outer surface of the axisymmetric was assumed to be stress free. The SiC fiber, SM1240, was assumed to behave elastically for all loading conditions with elastic modulus, $E_f = 400$ GPa, Poisson's ratio, $v = 0.22$ and temperature dependent coefficient of thermal expansion (CTE) [17,18]. The constitutive behavior of the Timetal-21S matrix was formulated using the unified theory of elastic-viscoplasticity with Bodner-Partom model. The fiber/matrix interface was assumed to be perfectly bonded throughout the analysis.

The load history employed in the analysis consisted of initial cool down from consolidation temperature to the test temperature at a rate of 0.1°C/sec, followed by instantaneous loading to 600 MPa. This creep load was sustained for a time duration of 140 hours. At the end of the creep test, the model was unloaded completely and cooled to room temperature at the same cooling rate of 0.1 °C/sec.   This load sequence is illustrated in Fig. A-1. The calculated evolution of the axial stress in matrix phase at a location in the immediate vicinity of the fiber/matrix interface is shown in Fig. A-2. The tensile residual stress induced in the matrix during initial cool down enhances the creep deformation of the matrix and the subsequent load transfer to the reinforcing fiber. It is noted that upon unloading at the end of the creep test duration, the matrix residual stress is compressive. This compressive residual stress at the test temperature depends on variables such as consolidation temperature

and cooling rate, and the creep loading conditions including temperature level, duration of loading time and magnitude of the applied load. On further cool down to room temperature, this pre-creep procedure would lower the residual stress level in the matrix phase of the composite.
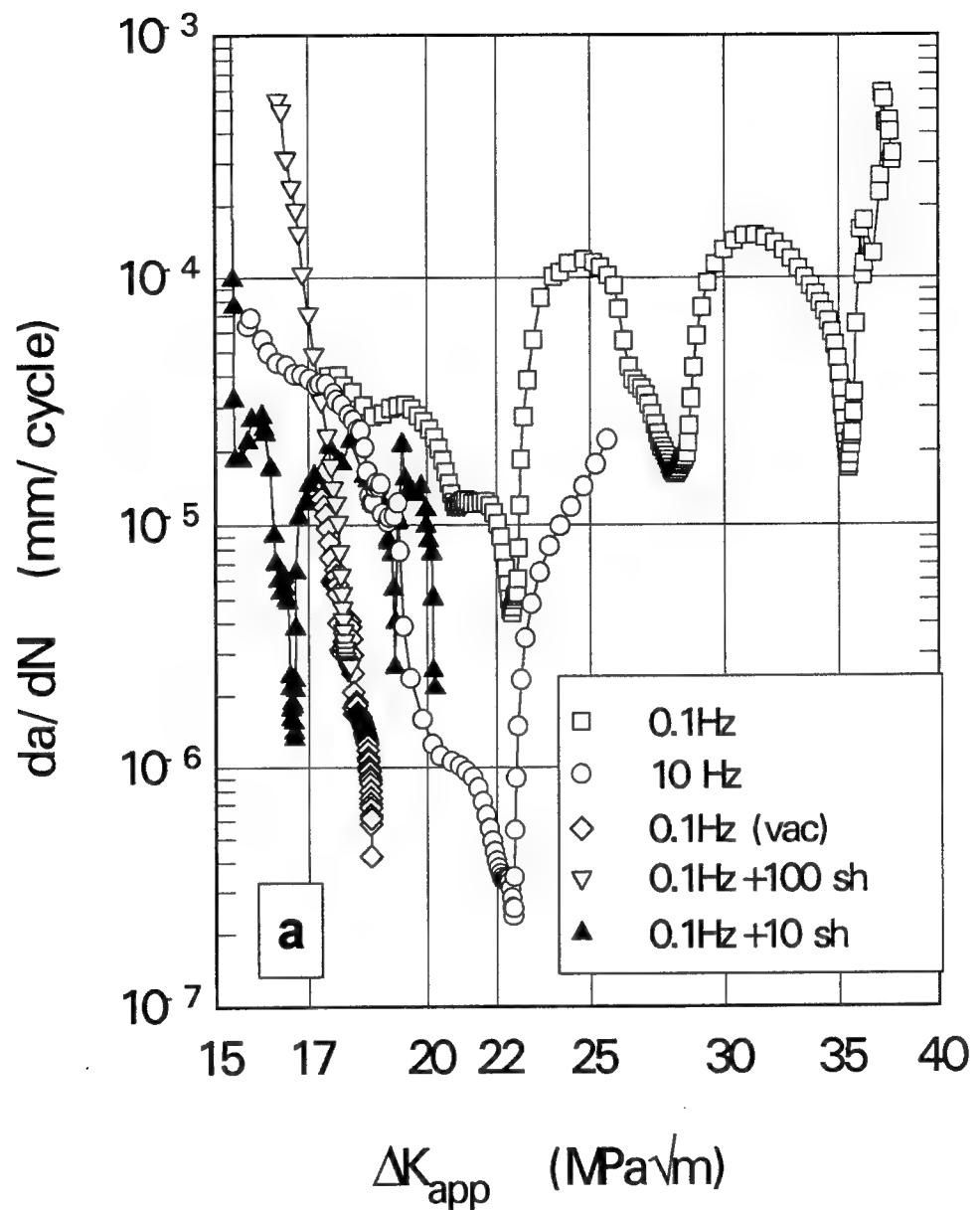
Fig. 7.1(a)   Crack growth rate versus the applied stress intensity factor for five different test conditions
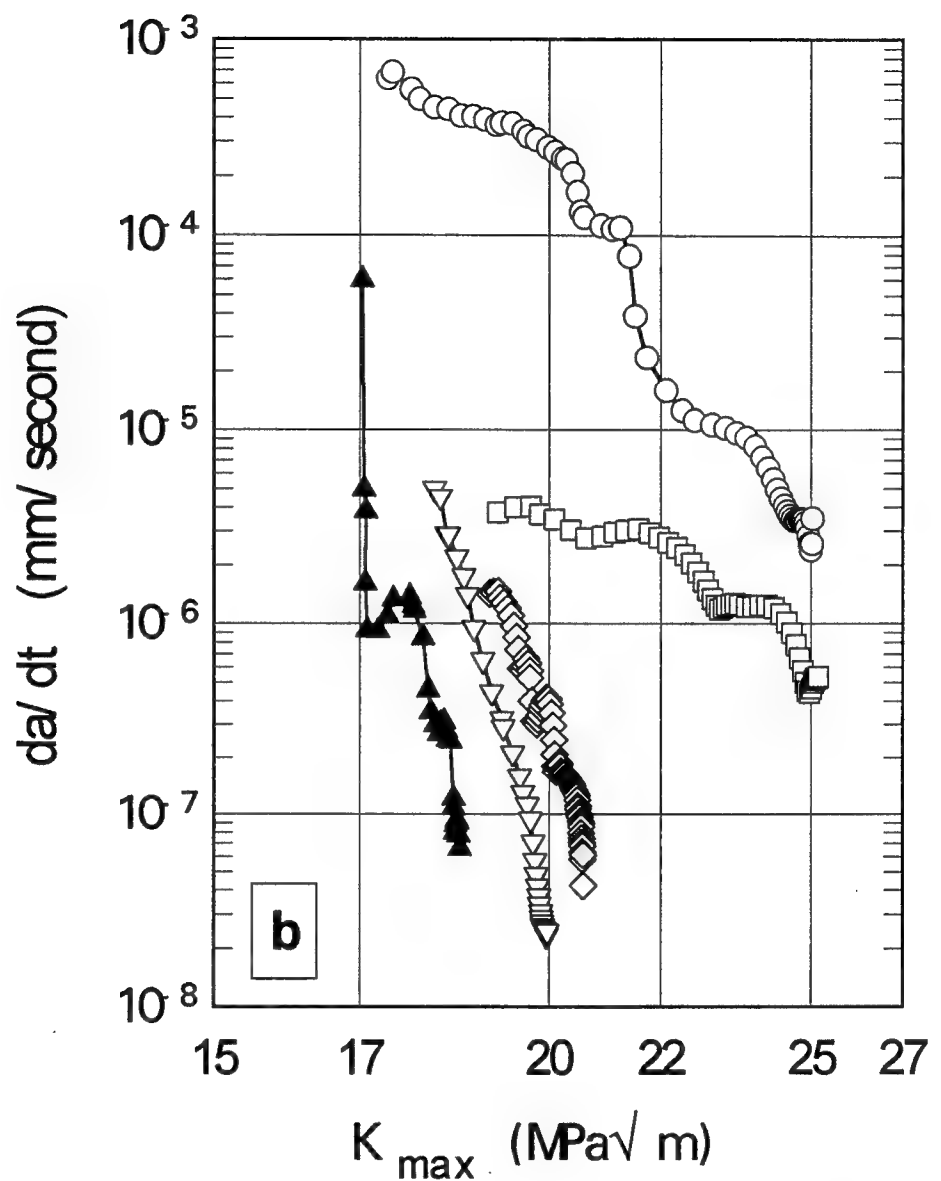
Fig. 7.1(b)   Crack growth speed versus the maximum applied stress intensity factor corresponding to the first crack bridging stage for the conditions shown in Fig. 7.1(a).
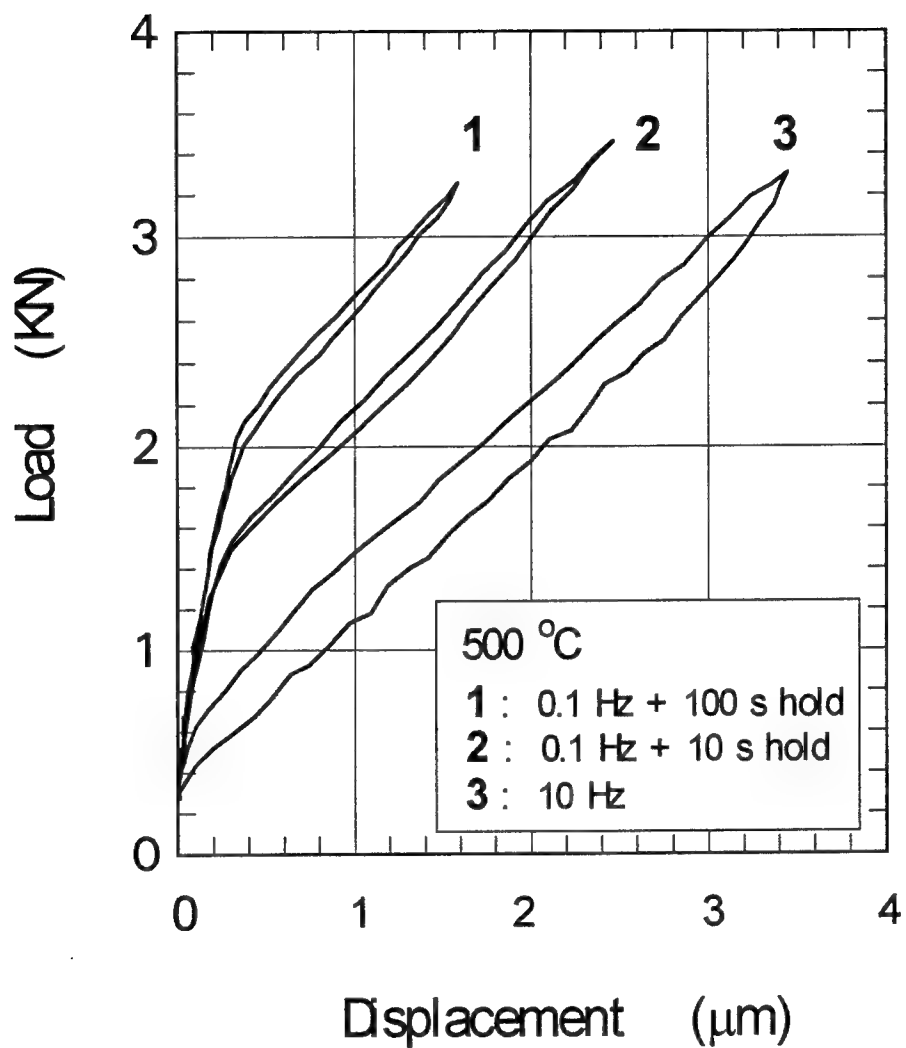
Fig. 7.2. Crack opening displacement loops for three tests: **1**: 0.1 Hz + 100 s hold, **2**: 0.1 Hz + 10 s hold and **3**: 10 Hz. The distance between the location at which these loops are measured and the crack tip for the three tests are 70μm (crack length = 2.55 mm), 220μm (crack length = 3.41 mm) and 220 μm (crack length = 2.69 mm), respectively.
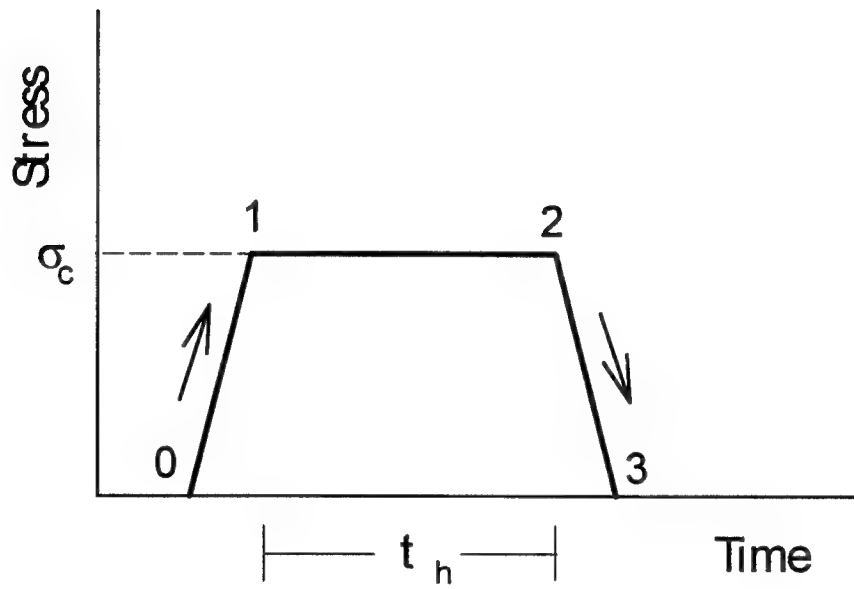
Fig. 7.3. A loading cycle profile including fatigue and creep components. **0-1**: loading part of the cycle (fatigue), **1-2**: hold time duration (creep), and **2-3**: unloading part of the cycle (fatigue).
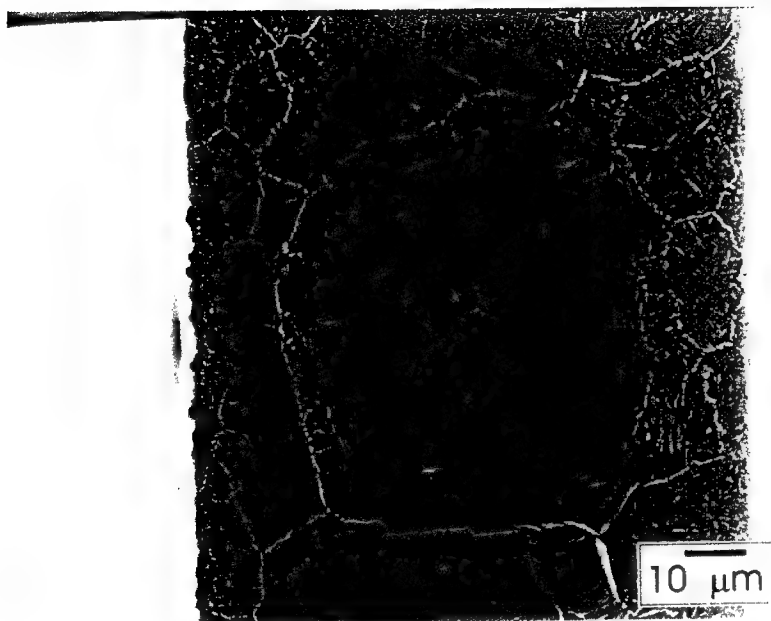
Fig. 7.4. Non-uniform distribution of the matrix grain size in the composite
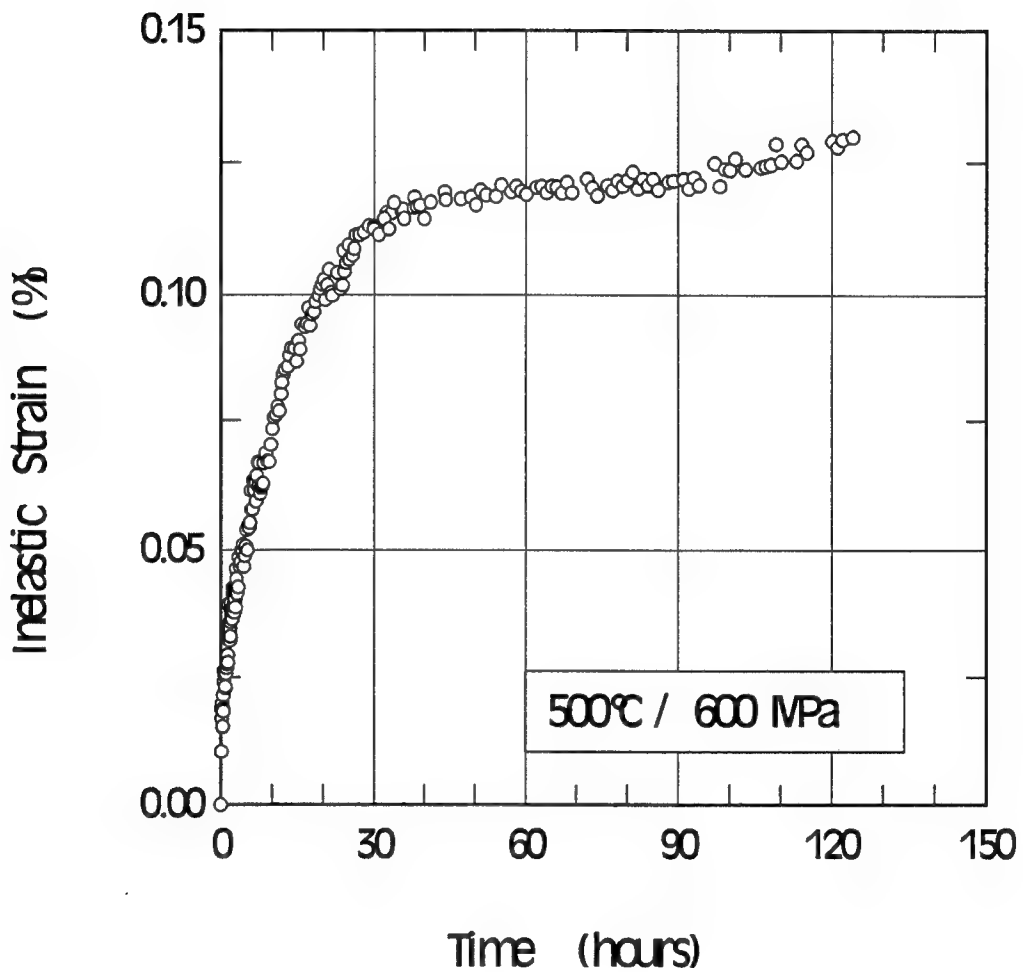
Fig. 7.5. Creep strain developed in the pre-creep specimen as function of time.

188
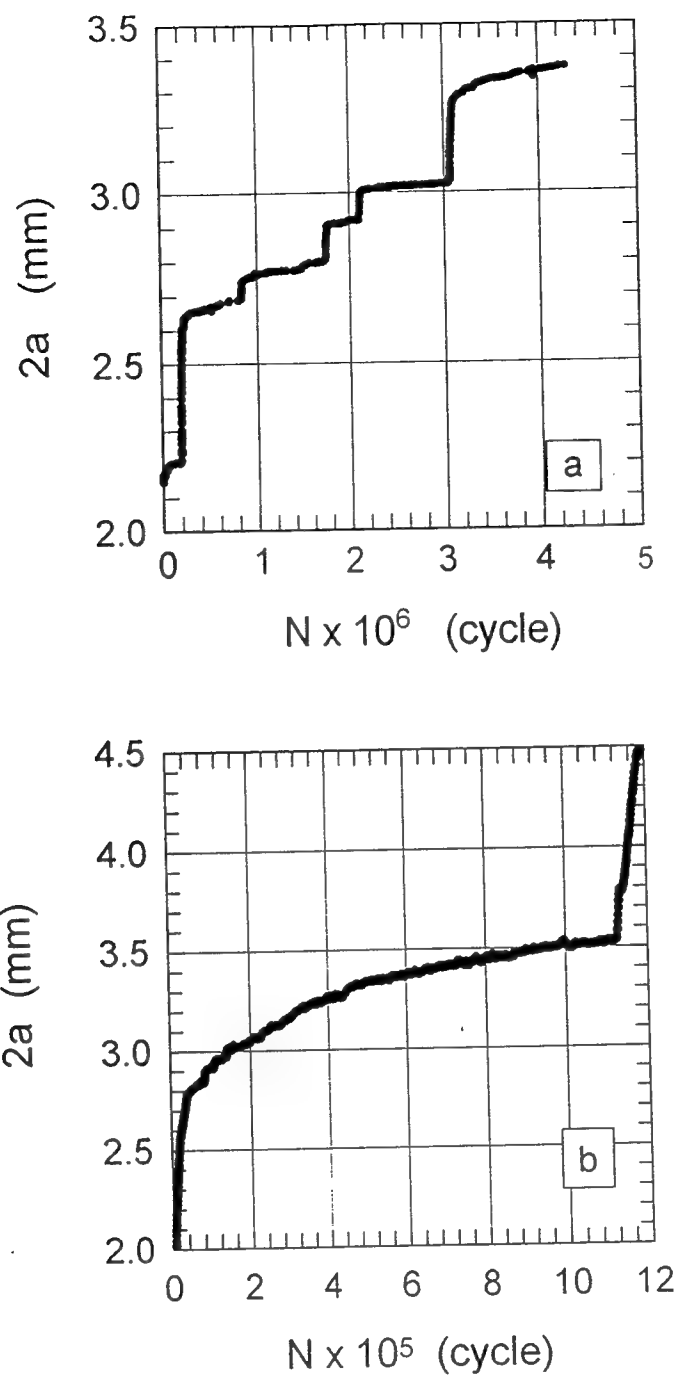
Fig. 7.6. Crack length versus number of cycles; a) pre-deformed specimen, b) as-received specimen
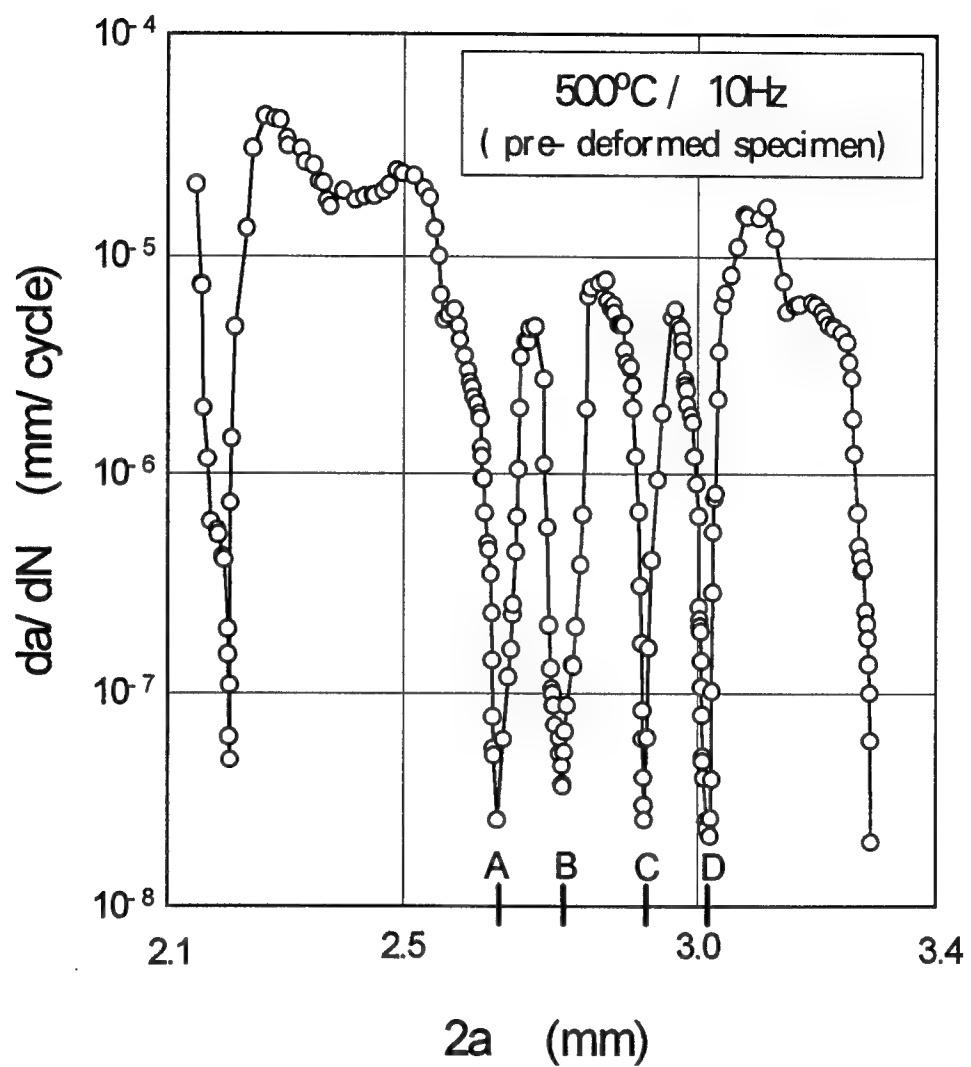
Fig. 7.7(a)   Crack growth rate versus the crack length for the pre-deformed specimen.

190
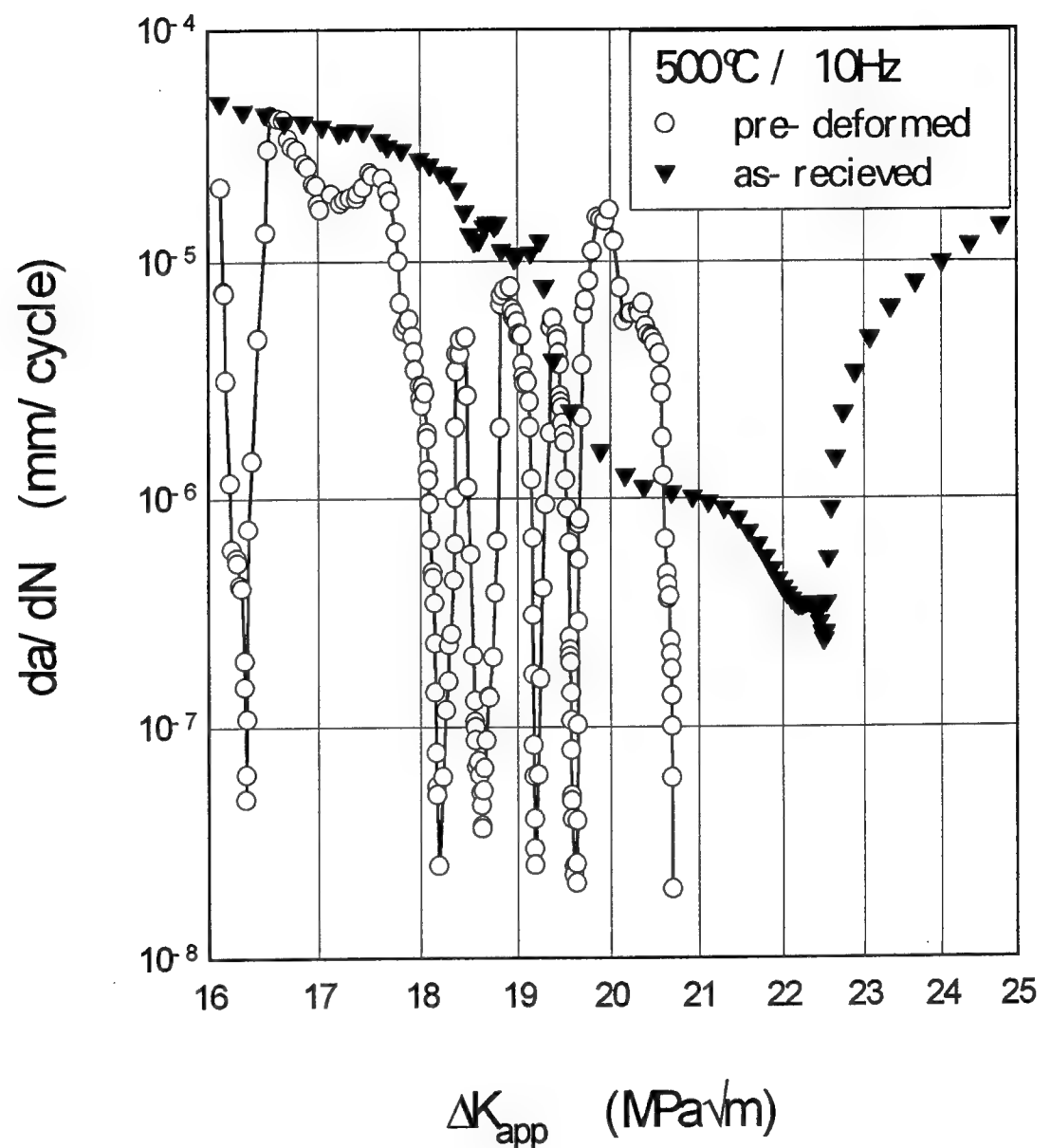
Fig. 7.7(b)   Crack growth rate versus the applied stress intensity factor for both the pre-deformed and the as-received specimens.
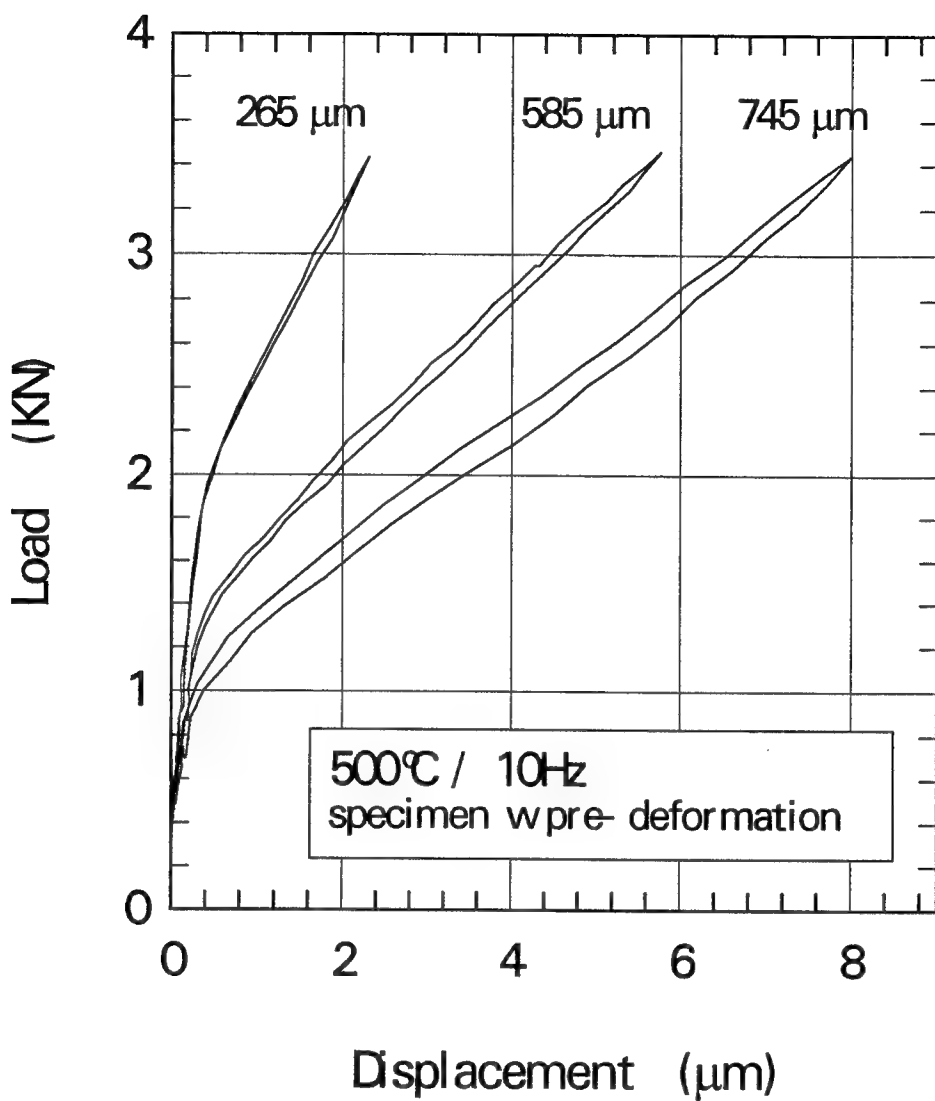
Fig. 7.8. Crack opening displacement loops for the pre-deformed specimen. Numbers at the top of each loop represents the crack length (distance from the crack tip to notch) at which the loop is recorded. The measurement position in the three cases was located 26 μm from the notch.

192
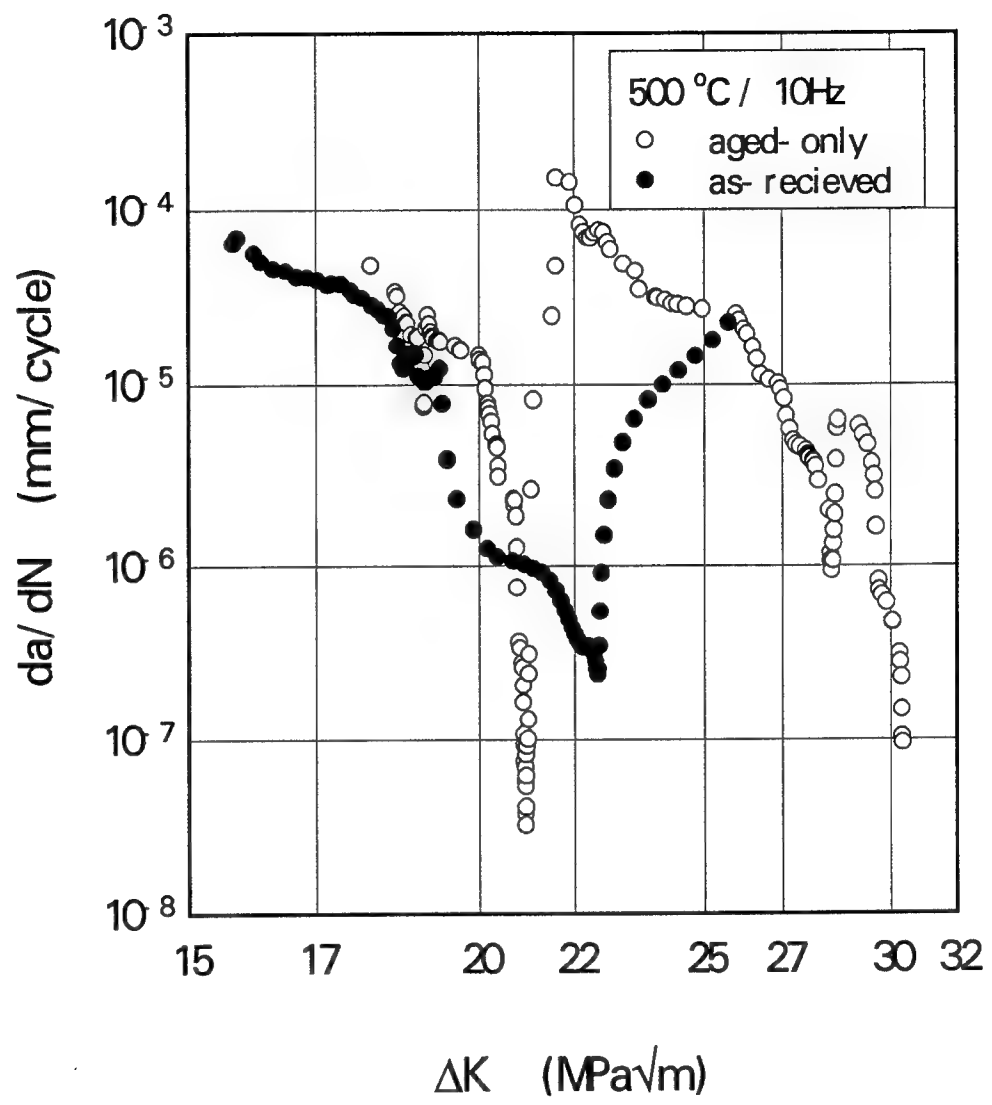
Fig. 7.9. Crack growth rate versus the applied stress intensity factor for both the aged-only and the as-received specimens.
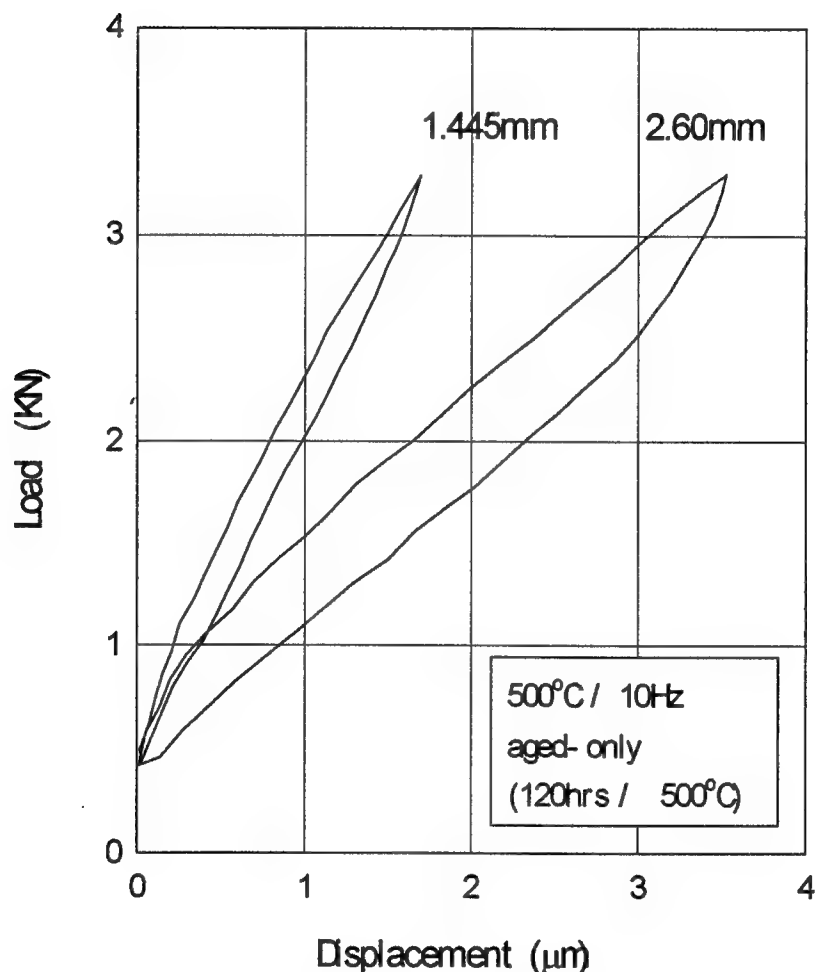
Fig. 7.10. Crack Opening Displacement loops at two different crack lengths in the aged-only specimen. Numbers at the top of each loop represents the crack length (distance from the crack tip to notch) at which the loop is recorded. The measurement position in the two cases was 400 μm from the notch.
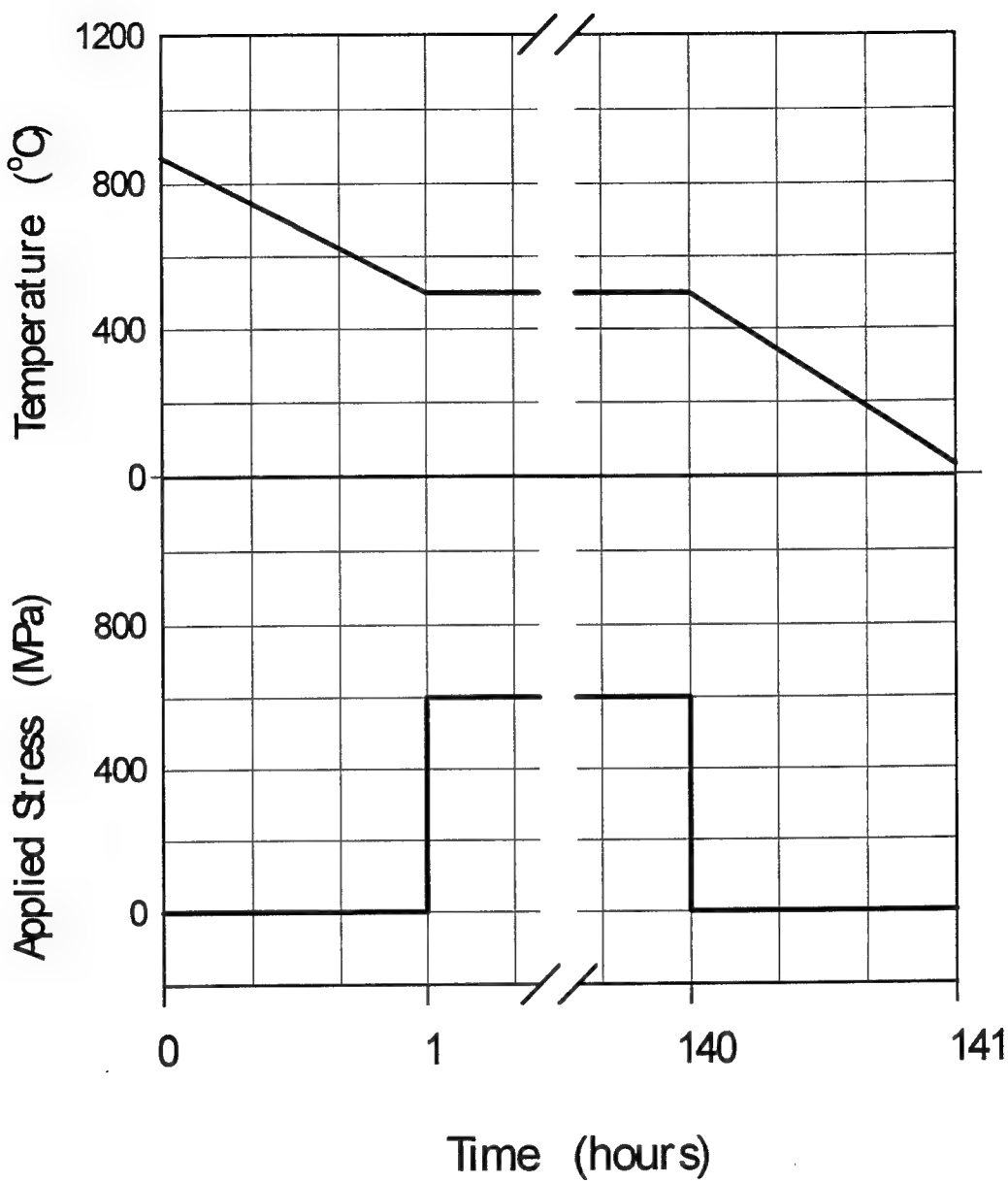
Fig. 7A-1 Combined applied load and temperature sequence employed on the pre-creep specimen prior to subjecting it to fatigue testing.
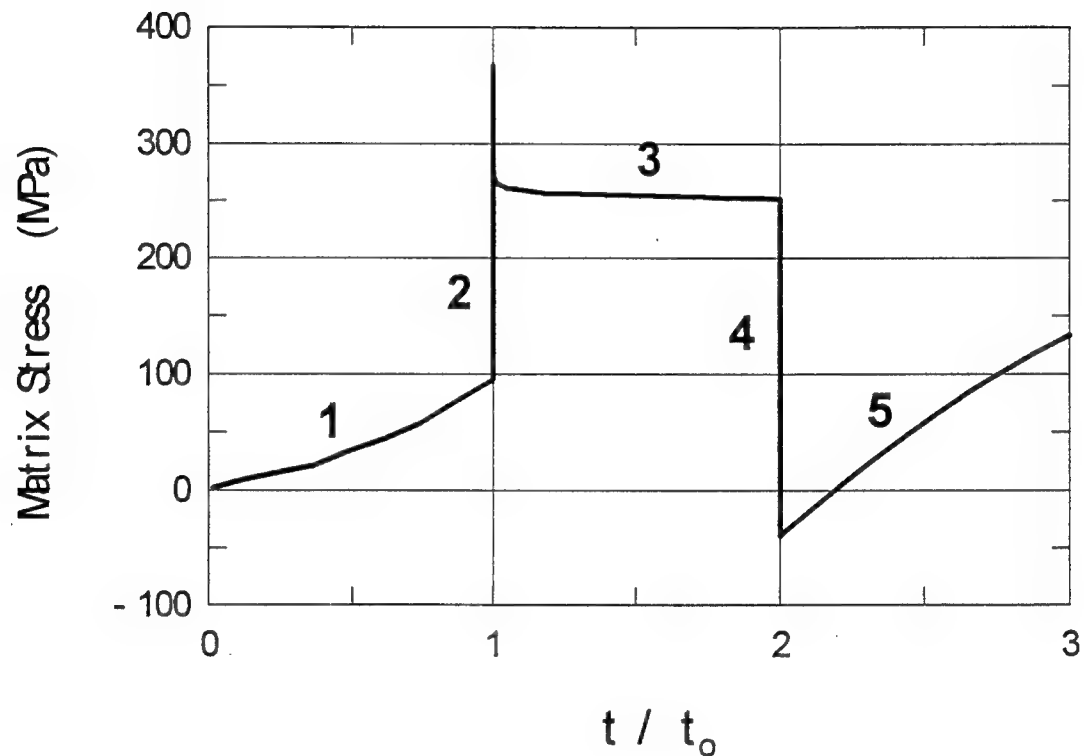
Fig. 7A-2 Axial stress response in the matrix phase of the pre-creep specimen due to the load and temperature cycle shown in Fig. 7A-1. This stress is calculated at a matrix position in the immediate vicinity of the fiber/matrix interface. **1**: cooling from consolidation temperature to 500 °C during the time duration t_o, **2**: loading to 600 MPa, **3**: hold time at maximum load level, **4**: unloading, and **5**: cooling from 500 °C to room temperature.

196

SECTION 8

EVOLUTION OF BRIDGING FIBER STRESS IN TITANIUM METAL MATRIX COMPOSITES AT ELEVATED TEMPERATURE [8]

ABSTRACT

This paper deals with the determination of the stress evolution in bridging fibers during the fatigue crack growth in SM1240/Timetal-21S composite using the finite element method. Several parameters affecting this evolution were considered; namely, the process-induced residual stress, the creep characteristics of the matrix layer surrounding the fiber, the test temperature and the loading frequency. In support of these calculations, a series of elevated temperature fatigue crack growth tests was conducted in order to identify the crack growth behavior of the composite when subjected to different temperatures at both high and low loading frequencies. Results of this numerical/experimental work were then utilized in conjunction with a postulated fiber fracture criterion based on the notion that a competition exists between the increase in the axial fiber stress and the continuous degradation of the fiber strength due to cyclic wear induced by the interface frictional shear stress. The conclusions of this study show that the axial stress in the bridging fibers increases with the increase in temperature and with the decrease in both the loading frequency and the matrix grain size. A combination of high temperature, low frequency and small matrix grain size would enhance creep deformation of the matrix, thus leading to an increase in the rate of the load transfer from the matrix to the bridging fibers. Furthermore, the presence of a compressive residual stress state in the bridging fibers retards the time-dependent increase of their axial stress. The fatigue strength of the bridging fibers was estimated to range from 720 MPa to 870 MPa within the temperature range of 500 °C to 650 °C. This strength was found to depend on both the temperature and the loading frequency.

8.1 INTRODUCTION

Previous studies on several unidirectional fiber-reinforced metal matrix composites (MMCs) including SCS-6/Ti-6Al-4V, SCS-6/Ti-15V-3Al-3Cr-3Sn, SCS-6/Ti-24Al-11Nb and SCS-6/25Al-10Nb-3Cr-1Mo indicated that fiber bridging is an operative damage mechanism under loading conditions of practical interest [1-8]. Fiber bridging occurs when the fiber

---

strength is sufficiently high that a fatigue crack extends through the matrix leaving unbroken fibers in the crack wake [9-11]. Bridging fibers can improve the fatigue crack growth properties by carrying part of the applied load, thus shielding the crack tip driving force. Silicon carbide (SiC) fibers used as reinforcement in these composites have several carbon-rich coatings to accommodate fiber/matrix sliding and debonding [12,13]. Cyclic loading the composites with SiC fibers causes debonding to occur between the carbon-rich coating and the SiC part of the fiber while the existence of carbon-rich region permits slippage to occur within the coating [14]. During fiber bridging, the crack tip driving force is modified by the presence of crack tip shielding force as the result of load transfer from the matrix to the fibers. Thermal residual stresses arising from the mismatch of the coefficients of thermal expansion (CTEs) of the composite constituents during initial cool down may influence the load transfer characteristics by altering the fiber/matrix interfacial strength. The combination of chemical bonding and thermally induced clamping results in high interfacial shear strength especially at low temperature. The transfer of load is further modified by various inelastic processes occurring at or in the vicinity of fiber/matrix interface such as matrix plasticity, interfacial debonding and frictional sliding. The stress experienced by a bridging fiber is a function of applied load, crack length, number of bridging fibers, the load partition between uncracked and cracked regions of the composite as well as the frictional shear stress present in the fiber/matrix interface region. The fiber surface frictional-related damage could result in a severe deterioration of the fiber strength and thus decrease its ability to carry the evolving load. The objective of this work is to determine the evolution characteristics of the stress in the bridging fibers as influenced by temperature, loading frequency, residual stress state and material variables. A link will then be established between the fiber bridging damage mechanisms and the fiber stress state for the purpose of determining the influence of the aforementioned parameters on the bridging fiber strength.

In the next section, the composite material used and the experimental procedures employed in fatigue crack growth tests are briefly outlined. This will be followed by a description of the resulting crack growth characteristics. The stress evolution of the bridging fiber will be calculated using the finite element method and the results will be applied in a proposed fiber fracture criterion.

8.2 MATERIAL AND EXPERIMENTAL PROCEDURES

Fatigue crack growth tests were conducted on SM1240/Timetal-21S composite specimens. The chemical composition of the metastable β titanium alloy, Timetal-21S is (in wt%): 0.1 Fe, 16.0 Mo, 3.06 Al, 2.9 Nb, 0.2 Si, 0.22 C, 0.12 O, 0.005 N with the balance being Ti. The SM1240 fiber with a diameter of 100 μm consists of chemically vapor deposited SiC on a 10-μm tungsten monofilament. A dual coating of carbon and titanium diboride, each layer having a thickness of 1 μm, is deposited on the surface. The consolidated, eight-ply, unidirectional composite, ($[0°]_{(8)}$), has a nominal fiber volume fraction of 35%.

Center-hole rectangular specimens measuring 75 mm X 4 mm, with notches cut at

opposite horizontal sides of the 1.577 mm diameter hole, were used in fatigue crack growth tests. The tests were carried out at room temperature as well as 500 °C and 650 °C. The room temperature tests established the baseline crack growth behavior. The 500 °C, on the other hand, is the expected service temperature while the 650 °C represents the near upper limit use of the matrix material. All tests were carried out under a constant applied stress range of 270±5 MPa with the load ratio, R, of 0.1. The two loading frequencies considered in this study were 10 Hz and 0.1 Hz. The selection of these frequencies is based on earlier work on Timetal-21S fiberless laminates which showed that frequencies higher than 10 Hz produced insignificant oxidation damage effect at temperatures below 650 °C, while those lower than 10 Hz showed effects related to viscoplastic deformation and oxidation at temperatures up to 650°C [15].

Fig. 5.1(a) shows a polished and chemically etched cross section of the as-fabricated composite. The fibers are aligned in a hexagonal array with an average center-to-center distance of 150 μm. The microstructure of the heat treated matrix alloy consists of distinctive β grains with an average size of 80 μm containing Widmanstatten acicular α phase and a continuous grain boundary α material with a thickness of about 0.8 μm. The micrograph also reveals a distribution of small equiaxed grains immediately surrounding each fiber with an average grain diameter of 15 μm, see Fi.g 5.1(b). This fine grain structure could have been the result of recrystallization during fabrication of the composite [16]. In high temperature loadings, this zone with small grain size around the fibers will experience a creep deformation with a rate higher than that of the larger grain base matrix material. The effect of enhancement of creep deformation due to the existence of the duplex microstructure on the efficiency of load transfer to the fiber at elevated temperature loading is considered in this study.

8.3 THE CRACK GROWTH PROCESS

In all the tests, the fatigue fracture process was seen to advance along a single dominant crack perpendicular to both the 0° fiber orientation and the direction of the applied load. The growth of the single crack was found to follow a trend in which the crack growth rate decreases continuously with increasing applied stress intensity factor (or crack length). The work in Ref [16] has associated this decrease in the crack growth rate with an increase in the number of fibers bridging the crack wake. The end of this stage is marked by the attainment of the minimum crack growth rate pertaining to the particular test condition. The first decelerated growth stage is followed by a transition to a stage which consists of repeated events of crack growth acceleration and retardation leading ultimately to crack instability and final failure of the test specimen. The crack growth rate versus the applied stress intensity factor curves limited to the first accelerated and decelerated stages in each test are shown in Fig.5.4(a).

The 500 °C/10 Hz test was repeated twice to establish the reproducibility of the observed behavior. Two additional 500 °C/ 10 Hz tests were interrupted; one while in the initial crack growth deceleration stage and the other while in the following crack growth

acceleration stage. A typical crack growth curve for this load case is shown in Fig. 5.4(a). The specimens were ground to the first layer of fibers and examined using optical microscopy to identify fractured fibers and the location of the fracture sites. Results of this work showed that all bridging fibers are intact while in the bridging stage. During the accelerated growth stage, however, several fibers at locations farthest away from the crack tip were broken along planes not coinciding with the matrix crack plane. These observations indicate that the crack growth transition from decelerated to accelerated growth is associated with the breakage of bridging fibers. In this, the fibers located near the crack mouth are the ones that have experienced the largest number of fatigue cycles, thus the greatest frictional surface wear which in turn may result in extensive fiber strength degradation [17]. As the bridged crack propagates, a competition is set between the increase in the axial stress at a critical fiber cross-section and the continuous decrease of the fiber strength. The failure of any of the bridging fibers would result in a decrease of the crack tip shielding force thus triggering a condition of crack growth acceleration. As will be discussed in the following section, the frictional shear stress, the component responsible for the surface wear damage of bridging fibers, is uniformly distributed along the fiber/matrix interface region. Emphasis will then be placed on estimating the stress evolution in the bridging fibers at a plane coinciding with the tip of the debonded interface since at this position bridging fibers experience the largest stress gradient due to the presence of large stresses at the crack tip.

8.4 STRESS DISTRIBUTION IN BRIDGING FIBERS

The stress distribution in the constituents of the composite and the evolution of fiber stress in the bridging fibers are predicted using the finite element method. Based on the fiber arrangement in this composite (see Fig. 5.1(a)), the fiber distribution is idealized as a hexagonal array architecture. A unit cell is then modelled as two concentric cylinders of a fiber with radius, r_f and a matrix phase with an outer radius of $r_m = r_f/\sqrt{v_f}$, where $v_f = 0.35$ is the fiber volume fraction of the composite. A section of this axisymmetric cylinder is discretized into finite elements with the mesh shown in Fig. 8.1. The SiC fiber, SM1240 is assumed to behave elastically for all loading conditions with elastic modulus, $E_f = 400$ GPa, Poisson ratio, $v = 0.22$, tensile strength, $\sigma_u = 3750$ MPa and temperature dependent coefficient of thermal expansion (CTE) [13,18], (See Fig. 8.2). The elastic modulus, CTE and yield limit of the Timetal-21S matrix alloy were also considered to be temperature-dependent [15], as shown in Fig. 8.2. The creep properties of the matrix alloy are based on limited experimental data [19,20], and the creep behavior is represented by the Bailey-Norton's equation in the transient and the steady state stages of creep deformation [21]. The effect of duplex microstructure of the matrix phase is approximated through the assumption that the strain rate varies inversely proportional to the square of the grain diameter for self-diffusion creep [22].

The loading sequence of the present simulation includes cool down from consolidation temperature to room temperature at a rate of 0.1 °C/sec, followed by reheating to the test temperature and the application of cyclic loading. The fiber/matrix interface is assumed to

be perfectly bonded throughout cool down from fabrication to room temperature and subsequent reheating to the test temperature. At the test temperature, the matrix crack and fiber/matrix debonding are introduced simultaneously. The outer surface of the matrix is maintained vertical in order to preserve the displacement compatibility of the unit cell with the surrounding composite. Schematic diagram of the model is illustrated in Fig. 8.3 defining the length of the debonded interface, L_d and the distance, z along the fiber measured from the plane coinciding with the matrix crack plane. These notations will be used in subsequent figures. Frictional effects are assumed to act along the fiber/matrix debonded length in the presence of compressive radial stress. The debonded length and the coefficient of friction required for use with the Coulomb law are selected so that the resulting crack opening displacement (COD) at a particular crack length matches that experimentally obtained [14]. This value of COD is assumed not to vary throughout the duration of the loading cycles. This assumption corresponds to the steady state stage of the bridged crack growth where the debonded length is assumed to be stable [23].

Table 8.1 summarizes the test cases considered in this study. The variables being investigated are temperature, loading frequency, residual stress state and the grain size of the fiber-surrounding matrix material. When the bridged crack reaches a length at which deceleration/acceleration crack growth transition occurs, the axial stress in the bridging fiber closest to the crack mouth is believed to have reached a maximum value. The finite element results show that the maximum axial stress in the bridging fiber is at the section coinciding with the matrix crack plane as illustrated in Fig. 8.2. However, fractographic analysis of SM1240/Timetal-21S composite specimens subjected to isothermal fatigue loadings showed that bridging fibers fractured at planes located above and below the matrix crack plane (see Fig. 5.2(a)). Studies on other MMCs such as SCS-6/Ti-6-4 and SCS-6/Ti-15-3-3 also reported a similar fracture feature of bridging fibers [1,24]. Furthermore, work by Thouless et al. [25] has suggested that the fracture plane of bridging fibers is at a distance from the matrix crack plane and the location depends on the magnitude of the frictional shear stress along the fiber/matrix interface.

Typical distributions of radial and shear stress components along the fiber/matrix interface are illustrated in Figs. 8.5 and 8.6, respectively. It is noted that only small variation of frictional shear stress occurred along the slip length of the fiber/matrix interface, with an average value of 3.5 MPa. Consequently, it can be assumed that degradation of the fiber strength resulting from the frictional wear of the surface of the fiber is uniform, and the location of most probable failure site is determined from statistical consideration. In the crack tip region of the debonding length, the shear stress gradient is the highest due to the transition from debonded region to fully bonded region along the fiber/matrix interface. In addition, the evolution of the bridging fiber axial stress is most pronounced at cross sections in the vicinity of the Mode II crack tip because the residual stress state is less affected by the matrix crack and the debonding interface. Consequently, the evolution of axial stress at a bridging fiber plane coinciding with the tip of the fiber/matrix interface is addressed in this study.

TABLE 8.1 - Test Parameters for the Cases Used in the Finite Element Calculations

Test Case	Temp ($^\circ$C)	Frequency (Hz)	d^{++}
1A	500	10	1
1B	500	0.1	1
1C$^+$	500	10	1
1D$^+$	500	0.1	1
1E	500	10	0.3
1F	500	0.1	0.3
2A	650	10	1
2B	650	0.1	1
2C$^+$	650	10	1
2D$^+$	650	0.1	1
2E	650	10	0.3
2F	650	0.1	0.3

$+$ A case in which the process-induced residual stresses are not considered in the FE calculations.

$++$ $d = d_1/d_2$ (where d_1 is grain size of the matrix layer in the immediate vicinity of the fiber and d_2 is the grain size of the basic matrix material)

8.5 STRESS EVOLUTION IN BRIDGING FIBERS

The evolution of the axial bridging fiber stress at the cross-section coinciding with the tip of the fiber/matrix debonded region during fatigue loading for test cases listed in Table 8.1 is shown in Fig. 8.7(a) and 8.7(b), for loading frequencies of 0.1 Hz and 10 Hz, respectively. As the loading cycles proceed, the matrix undergoes creep deformation and subsequent stress relaxation resulting in a load transfer to the fiber. A higher level of axial fiber stress is predicted for a composite in which the fabrication-related compressive residual stress in the composite is not considered. Similarly, the fiber stress was found to increase when the layer of the matrix surrounding the fiber was assumed to consist of grain size smaller than that in the remaining of the matrix material. The presence of fine grains in the direct vicinity of the fiber enhances the stress relaxation of the matrix phase through creep deformation, thus, increases the load being transferred to the bridging fiber.

Furthermore, comparison of the stress evolution curves for the 650 °C and 500 °C indicates that the level of bridging fiber stress reached after the application of a certain number of load cycles is lower at lower temperature. This could be attributed to the rapid transfer of load from the matrix to the bridging fiber at higher temperature level. For the same temperature, the material experienced the higher portion of the applied stress for a longer duration of time at a lower frequency, thus greater contribution to matrix creep deformation resulting in higher level of bridging fiber stress. This contribution is also apparent in the higher slope of the evolution curve at lower frequency, which reflected higher rate of load transfer to the bridging fiber due to stress relaxation of the matrix phase. The evolution of the fiber stress during isothermal fatigue is therefore dictated by the time-dependent deformation of the matrix which is significant at lower frequency.

8.5 FATIGUE STRENGTH OF BRIDGING FIBERS

As mentioned above, the transition from decelerated to accelerated crack growth is a result of the breakage of bridging fibers located near the crack mouth. The fracture of these fibers is assumed to occur when the evolving fiber stress level reached the value of the continuously decreasing fiber residual strength. This concept forms the basis for the fracture criterion of bridging fibers at elevated temperature [26]. The fatigue strength, S_f, is determined by locating along the fiber stress evolution curve, the stress level corresponding to the cycle number, or the equivalent time, at which the first transition to accelerated crack growth occurred, as indicated in Fig. 8.7(a) and (b) for 0.1 Hz and 10 Hz test cases, respectively. The resulting fatigue strength, S_f, of the bridging fibers ranges from 720 MPa to 870 MPa for the two temperature levels considered. It is further noted that the fatigue strength of the bridging fiber is both time- and cycle-dependent. The fiber strength at the test condition of 650 °C, 10 Hz, for example, is determined as 760 MPa. As seen from Fig. 8.7(b), assuming that this strength is unique for the particular bridging fiber, it is then apparent that for a matrix with a uniform grain size, the presence of residual stresses due to consolidation could prolong the fatigue life of the bridging fibers. On the other hand, the absence of residual stresses would decrease the fiber life.

The influence of elevated temperatures and loading frequencies on the bridging fiber strength is summarized in Fig. 8.8. For the same temperature level, the bridging fiber strength increases as the frequency decreases. The decrease in frequency and the associated increase in the matrix creep rate permit the fiber stress to evolve to a higher level before the fiber surface wear generated by cyclic frictional sliding causes fiber failure. This type of competition between the fiber stress evolution and the fiber strength degradation due to frictional surface effects could also be used to interpret the observation that the number of loading cycles, and thus the fiber strength, decreases as the frequency increases, as indicated in Fig. 8.8. Experimental observation indicated that the number of fatigue cycles at the transition point for loading frequency of 10 Hz is about two order of magnitude higher than that for the low frequency of 0.1 Hz. At any frequency, the strength of the bridging fiber increases with increasing temperature level. This is due to the fact that the frictional shear

stress which represents the degree of surface wear of the fiber is lower at higher temperature level. The temperature dependency of interfacial shear stress for several titanium MMC is reported elsewhere [27,28]. Based on the evolution characteristics of the bridging fiber stress and its postulated strength degradation during the fiber bridging process, it is noted that the evolution of the bridging fiber stress is time-dependent in nature while the bridging fiber strength is primarily cycle dependent.

8.6 CONCLUSIONS

An attempt was made to determine the evolution of stress in bridging fibers during the fatigue crack growth in SM1240/Timetal-21S composite using the finite element method. Several parameters affecting this evolution were considered; namely, the presence of the process-induced residual stress, the creep behavior of the matrix layer surrounding the fiber, the test temperature and the loading frequency. In support of these calculations, a series of elevated temperature fatigue crack growth tests was conducted in order to identify the crack growth behavior of the composite when subjected to different temperatures at both high and low loading frequencies. Results of this numerical/experimental work were then utilized in conjunction with a postulated bridging fiber fracture criterion based on the notion that a competition exists between the increase in the axial fiber stress and the continuous degradation of the fiber strength due to cyclic wear induced by the interface frictional shear stress. The conclusions of this study are summarized as follows:

1. The stress in the bridging fibers increases with increasing temperature level and with the decrease of both the loading frequency and the fiber-surrounding matrix grain size. The rate of increase in the stress is proportional to the temperature but inversely proportional to the loading frequency and the matrix grain size. A combination of high temperature, low frequency and small matrix grain size enhances creep deformation of the matrix, thus leading to an increase in the load being transferred to the bridging fiber. The evolution of the bridging fiber stress basically is time-dependent.

2. The fiber compressive residual stress state induced during consolidation of the composite retards the time-dependent increase of the axial stress in the bridging fiber. This residual stress state decreases with increasing temperature level and number of fatigue cycles.

3. The fatigue strength of bridging fibers ranges from 720 MPa to 870 MPa within the temperature range of 500 °C to 650° C and the strength depends on both the temperature and loading frequency.

8.7 REFERENCES

[1]   Davidson, D. L., "The Micromechanics of Fatigue Crack Growth at 25 C in Ti-6Al-4V Reinforced with SCS-6 Fibers", *Metallurgical Transactions A*, Vol. 23A, March 1992, pp. 865-879.

[2]   Telesman, J., Ghosn, L. J. and Kantzos, P., "Methodology for Prediction of Fiber Bridging Effects in Composites", *Journal of Composites Technology & Research*, Vol. 15, No. 3, Fall 1993, pp. 234-241.

[3]   Bakuckas, J. G. and Johnson, W. S., "Application of Fiber Bridging Model in Fatigue Crack Growth in Unidirectional Titanium Matrix Composites", *Journal of Composite Technology & Research*, Vol. 15, No. 3, Fall 1993, pp. 242-255.

[4]   Jeng, S. M., Allassoeur, P. and Yang, J. -M., "Fracture Mechanisms of Fiber-reinforced Titanium Alloy Matrix Composites, V: Fatigue Crack Propagation", *Materials Science and Engineering*", A154, 1992, pp. 11-19.

[5]   Sensmeier, M. D. and Wright, P. K., "The Effect of Fiber Bridging on Fatigue Crack Growth in Titanium Matrix Composites", in Fundamental Relationships Between Microstructure & Mechanical Properties of Metal-Matrix Composites, P. K. Liaw and M. N. Gungor, eds., *The Minerals, Metals & Materials Society*, 1990, pp. 441-457.

[6]   Bowen, P., Ibbotson, A. R. and Beevers, C. J., "Characterization of Crack Growth in Continuous Fiber Reinforced Titanium Based Composites Under Cyclic Loading", in Fatigue of Advanced Materials, R. O. Ritchie, Dauskardt, R. H. and Cox, B. N., eds., Materials and Component Engineering Publications Ltd., P. O. Box 1550, Edgbaston, Birmingham B15 2JZ, England, 1991, pp. 379-393.

[7]   Ibbotson, A. R., Bowen, P. and Beevers, C. J., "Cyclic Fatigue Resistance of Fiber Reinforced Titanium Metal Matrix Composites at Ambient and Elevated Temperature", 7th Titanium Conference, San Diego, July, 1992.

[8]   Brindley, P. K., Draper, S. L., Eldridge, J. I., Nathal, M. V. and Arnold, S. M. "The Effect of Temperature on the Deformation and Fracture of SiC/Ti-24Al-11Nb", *Metallurgical Transactions*, Vol. 23A, 1992, pp. 2527-2540.

[9]   Evans, A. G. and He, M. Y., "Interface Debonding and Fiber Cracking in Brittle Matrix Composites", *Journal of the American Ceramic Society*, Vol. 72[12], 1989, pp. 2300-2303.

[10]   Marshall, D. B., Cox, B. N. and Evans, A. G., "The Mechanics of Matrix Cracking in Brittle-Matrix Fiber Composites", *Acta Metallurgica*, Vol. 33, No. 11, 1985, pp.

2013-2021.

[11] Cox, B. N. and Lo, C. S., "Load Ratio, Notch, and Scale Effects for Bridged Cracks in Fibrous Composites", *Acta Metall. Mater.*, Vol. 40, No. 1, 1992, pp. 69-80.

[12] Lerch, B. A., Hull, D. R. and Leonhardt, T. A., "Microstructure of a SiC/Ti-15-3 Composites", *Composites*, Vol. 21, No. 3, May 1990, pp. 216-224.

[13] Petitcorp, Y. L., Lahaye, M., Pailler, R. and Naslain, R., "Modern Boron and SiC CVD Filaments: A Comparative Study", *Composites Science and Technology*, 32, 1988, pp. 31-55.

[14] Zheng, D. and Ghonem, H., "High Temperature/High Frequency Fatigue Crack Growth Damage Mechanisms in Titanium Metal Matrix Composites", *Symposium on Life Prediction Methodology for Titanium Matrix Composites*, Crystal Sands Resort, Hilton Head Island, South Carolina, March 22-24, 1994.

[15] Ghonem, H., Wen, Y., Zheng, D., Thompson, M. and Linsey, G., "Effects of Temperature and Frequency on Fatigue Crack Growth in Ti-β21S Monolithic Laminate", *Materials Science and Engineering*, Vol. 161, 1993, pp. 45-53.

[16] Zheng, D. and Ghonem, H., "Fatigue Crack Growth in Titanium Metal Matrix Composites", *Metallurgical Transaction*, (accepted for publication).

[17] Chan, K. S., "Effects of Interface Degradation on Fiber Bridging of Composite Fatigue Cracks", *Acta Metall. Mater.*, Vol. 41, No. 3, 1993, pp. 761-768.

[18] SIGMA Monofilament Products, Information Sheets, BP Metal Composites Limited, RAE Road, Farnborough, Hampshire GU14 6XE, England.

[19] Khobaib, M. and Ashbaugh, N., University of Dayton Research Institute, Dayton, OH, October 1991, Unpublished work.

[20] Martin, P. L., Bingel, W. H. and Mahoney, M. W., "SiC-Reinforced β-21S Creep Properties", in *Workshop Proceedings on Titanium Matrix Components*, P. R. Smith and W. C. Revelos, eds., April 1992, WL-TR-92-4035, pp. 277-291.

[21] Tamin, M.N., Zheng, D. and Ghonem, H., "Time-Dependent Behavior of Continuous-Fiber-Reinforced Metal Matrix Composites: Modeling and Applications", *Journal of Composites Technology & Research*, Vol. 16, No. 4, October 1994, pp. 314-322.

[22] Reed-Hill, E.E., "Physical Metallurgy Principles", Van Nostrand, New York and London, 1964.

[23]   Zheng, D. and Ghonem, H., "Fatigue Crack Tip Shielding Effects in Metal Matrix Composites", *Fatigue and Fracture of Engineering Materials and Structures*, (submitted for publication).`

[24]   Jeng, S. M., Nguyen, T. -H. B., Dana, O. and Yang, J. M., "Fatigue Cracking of Fiber Reinforced Titanium Matrix Composites", *Journal of Composite Technology & Research*, Vol. 15, No. 3, Fall 1993, pp. 217-224.

[25]   Thouless, M. D., Sbaizero, O., Sigl, L. S. and Evans, A. G., "Effect of Interface Mechanical Properties on Pullout in a SiC-Fiber-Reinforced Lithium Aluminum Silicate Glass Ceramic", *Journal of the American Ceramic Society*, 72[4], 1989, pp. 525-532.

[26]   Tamin, M.N. and Ghonem, H., "A Fracture Criterion for Bridging Fibers in Titanium Metal Matrix Composites at Elevated Temperature", *Symposium on Durability of Composite Materials*, R.C. Wetherhold (ed.), ASME Winter Annual Meeting, Chicago, IL, Nov. 6-11, 1994, MD-Vol. 51, pp. 51-58.

[27]   Eldridge, J. I. and Ebihara, B. T., "Fiber Push-out Testing Apparatus for Elevated Temperatures", *Journal of Materials Research*, Vol. 9, No. 4, April 1994, pp. 1035-1042.

[28]   Osborne, D. and Ghonem, H., "Determination of Frictional Shear Stress of SM1240/Timetal-21S at Elevated Temperature", Internal Report, University of Rhode Island, 1994.
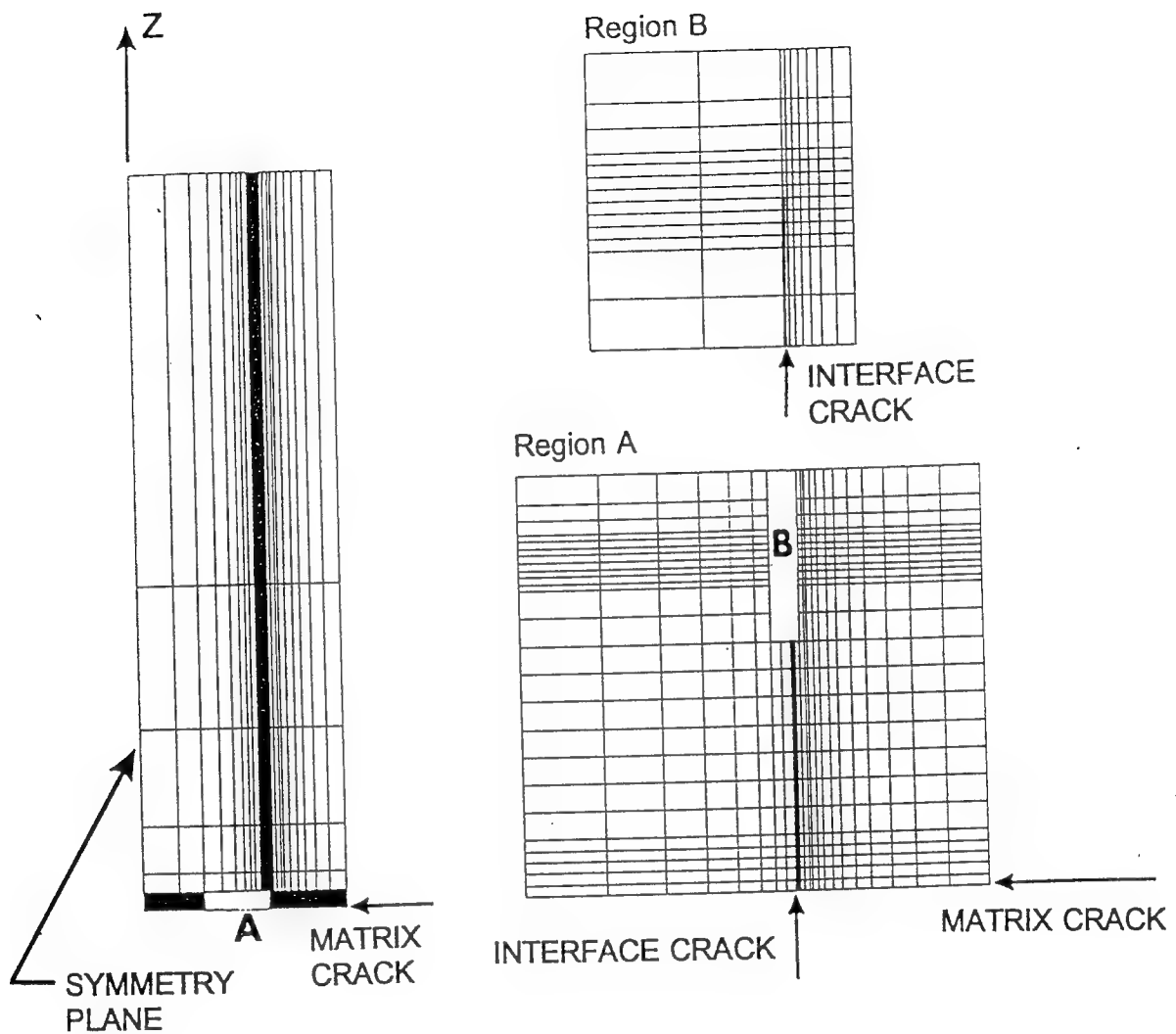
Fig. 8.1   Finite element mesh employed in modelling the response of bridging fiber under cyclic loading.
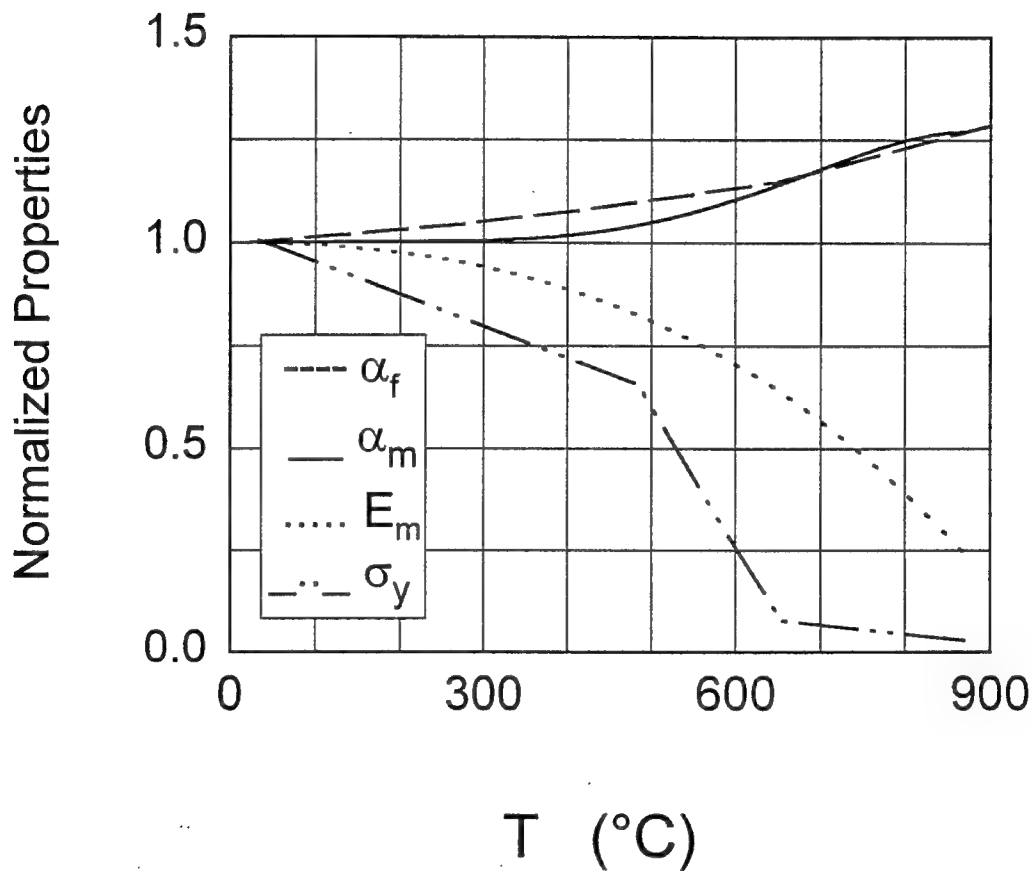
Fig. 8.2   Young's modulus, E, yield strength, σ_Y, and coefficient of thermal expansion, α_m, for Timetal-21S matrix alloy, and coefficient of thermal expansion, α_f, for SM1240 fiber. The properties are normalized by their respective values at 24°C : $E_{RT} = 94$ GPa, $\sigma_{Y,RT} = 1040$ MPa, $\alpha_{m,RT} = 8.41$ X 10^6 /° C, and $\alpha_{f,RT} = 4.72$ X 10^{-6} / °C.
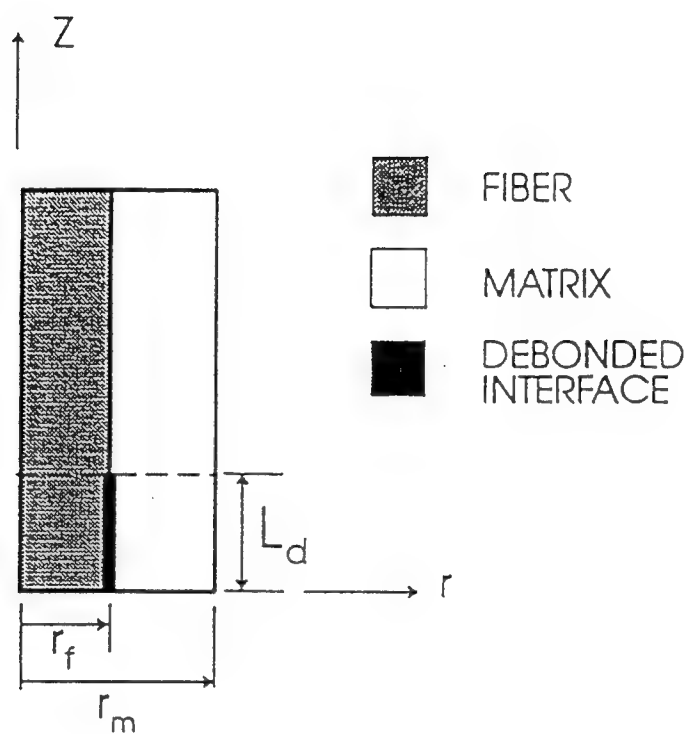
Fig. 8.3   Cross section of the axisymmetric model showing the debonded length, L_d, radius of fiber, r_f and radius of matrix cylinder, r_m. z and r are the axial and radial coordinate axes, respectively.
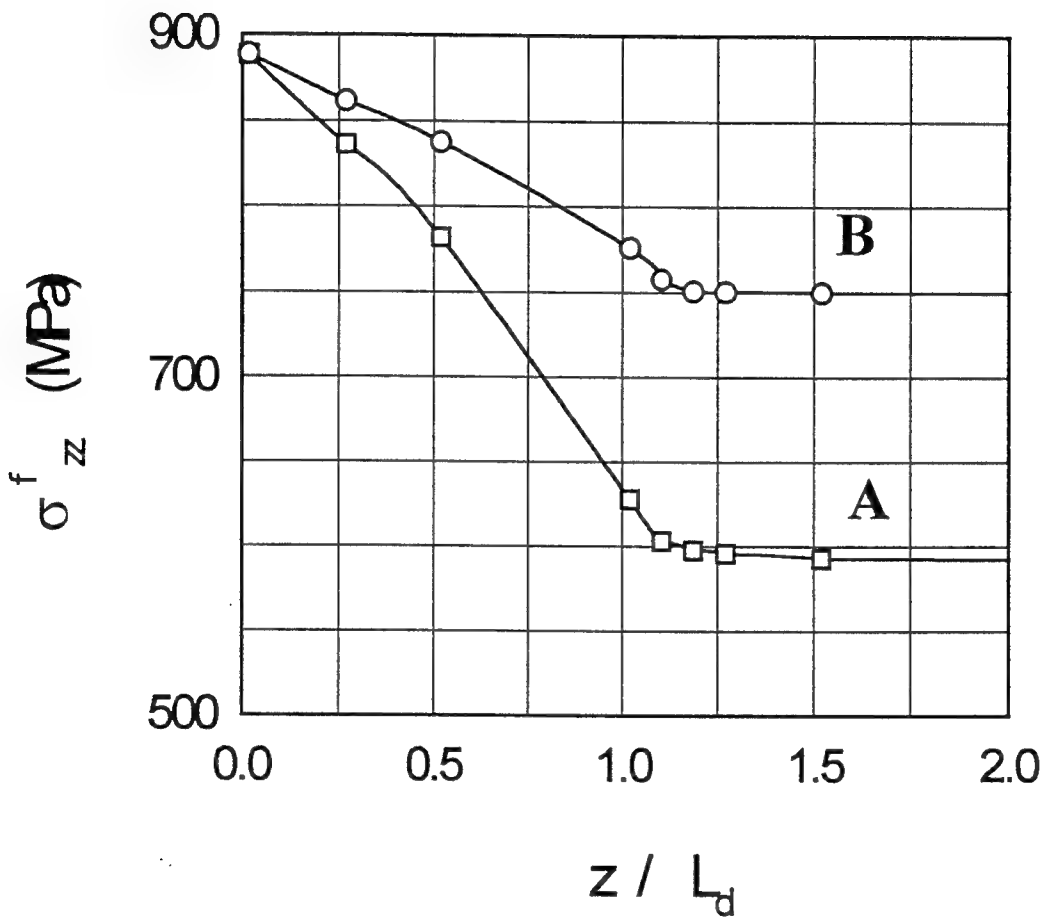
Fig. 8.4   Variation of axial stress along the bridging fiber at different loading cycles.
Curve A represents the stress variation after 1 load cycle while curve B is the
variation at the end of 500 load cycles. The debonded length, L_d = 1200 μm.
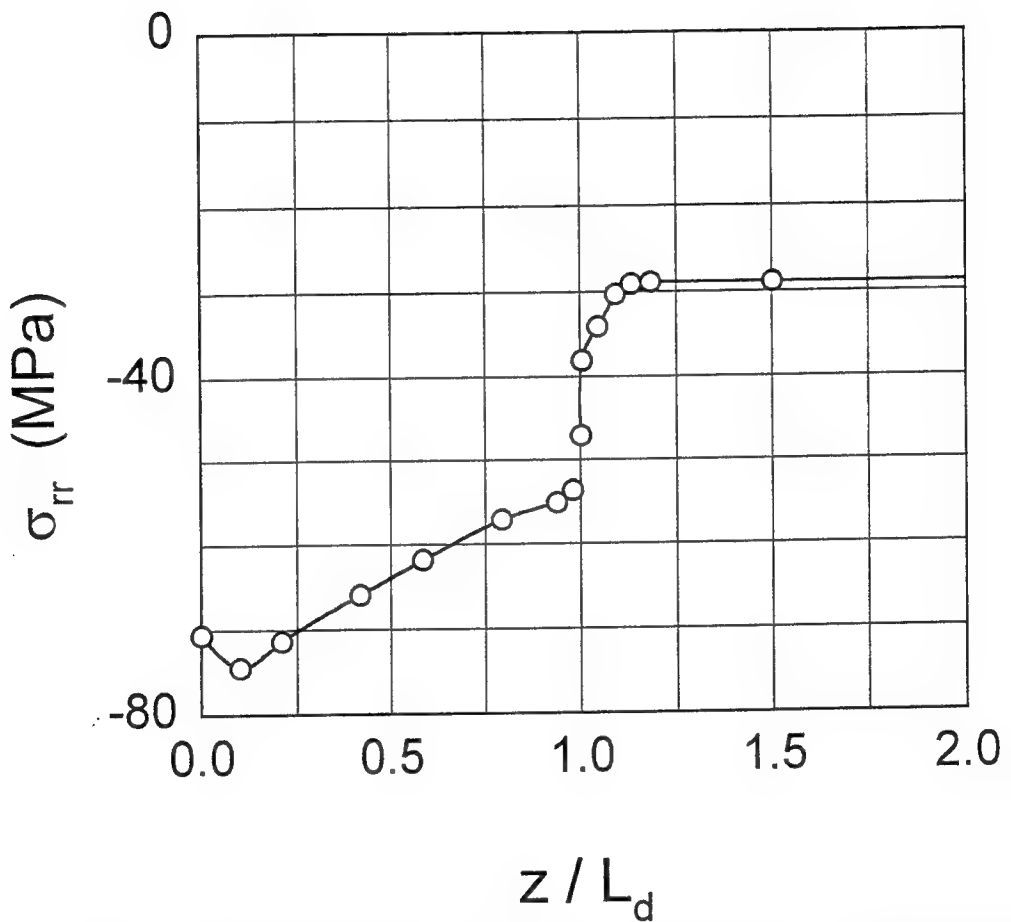
Fig. 8.5   Variation of radial stress along the fiber/matrix interface at the peak of the first applied load cycle. The temperature is 650 °C and the debonded length, L_d = 1200 μm.
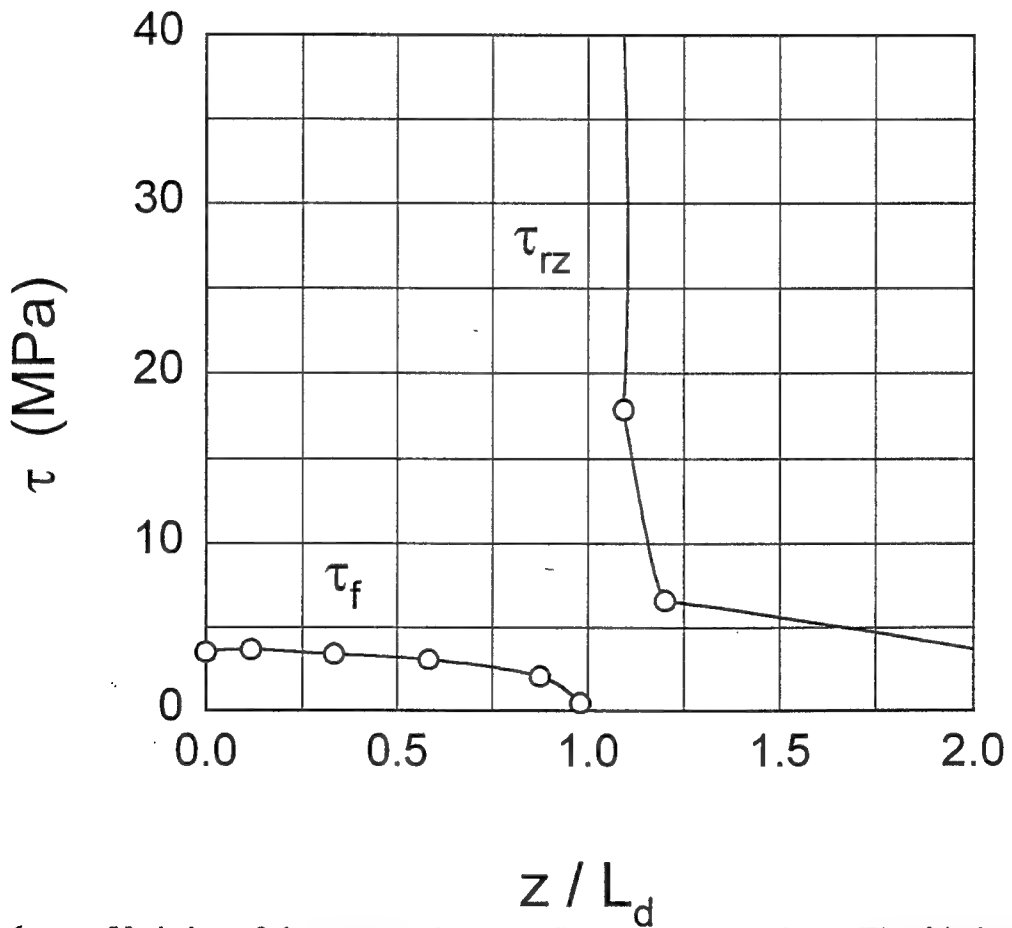
Fig. 8.6   Variation of shear stress along the fiber/matrix interface. The frictional shear stress, τ_f, acts along the slip length, $L = 950$ μm, with the coefficient of friction, $\upsilon = 0.05$ at test temperature 650 °C. The debonded length, $L_d = 1200$ μm.
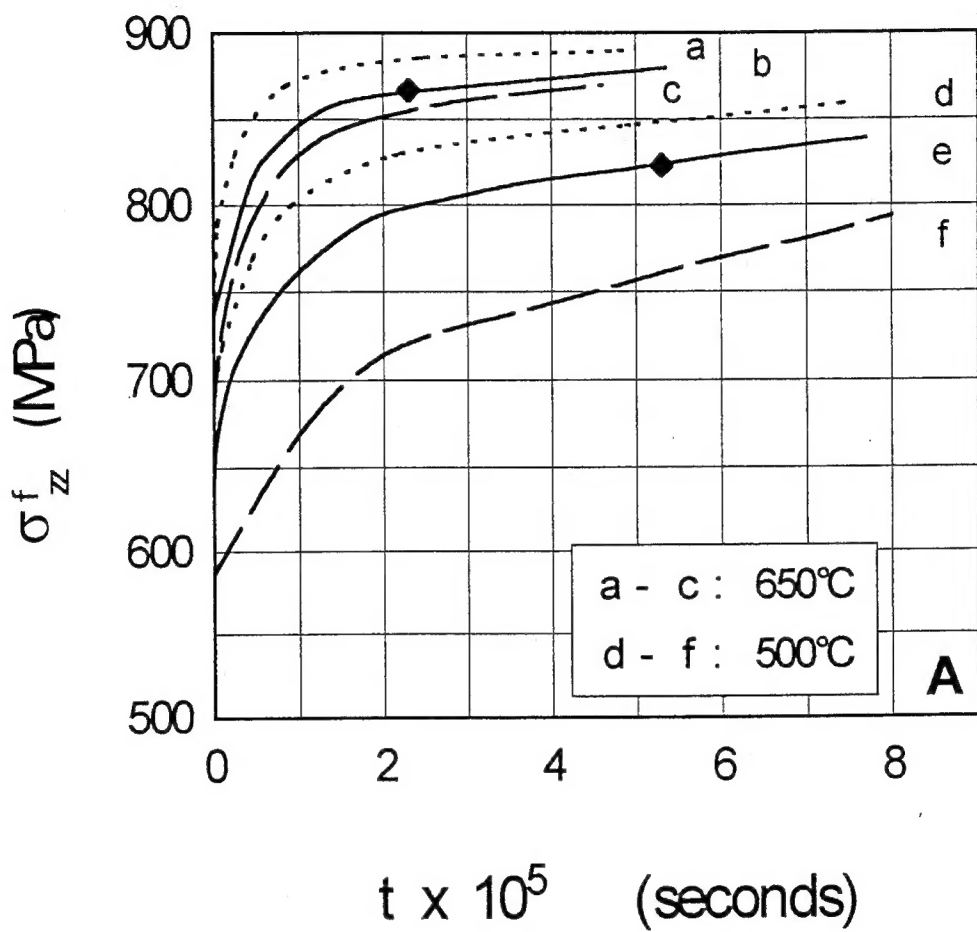
Fig. 8.7(a)   Evolution of axial stress in the bridging fiber at the loading frequencies of 0.1 Hz. – – – – – without process induced residual stress and with uniform large matrix grain size, ————— with residual stress and duplex microstructure of the matrix phase, – — — — with residual stress and uniform large matrix grain size.   The filled diamond symbols on curves b and e represent the fatigue strength, S_f of the bridging fibers.

214

This page is left blank
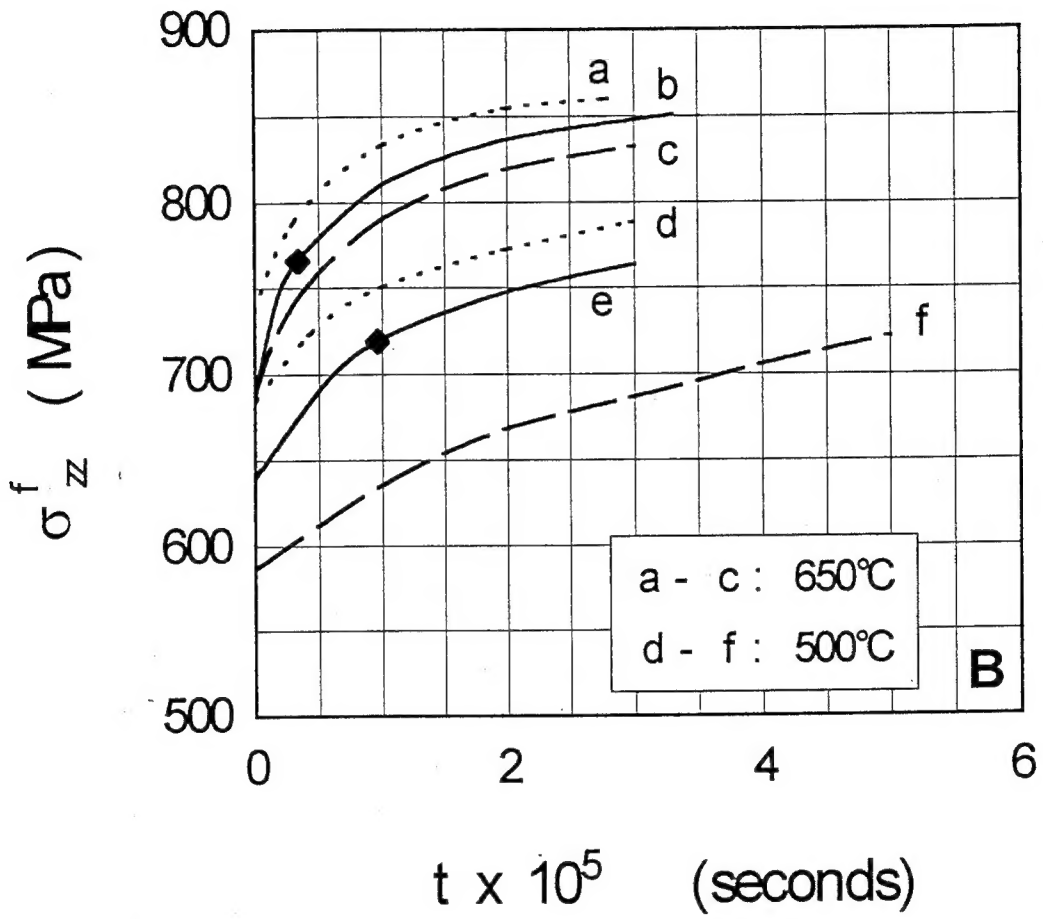
Fig. 8.7(b)   Evolution of axial stress in the bridging fiber at the loading frequencies of 10 Hz. – – – – – without process induced residual stress and with uniform large matrix grain size, ———— with residual stress and duplex microstructure of the matrix phase, — — — — with residual stress and uniform large matrix grain size. The filled diamond symbols on curves b and e represent the fatigue strength, S_f of the bridging fibers.
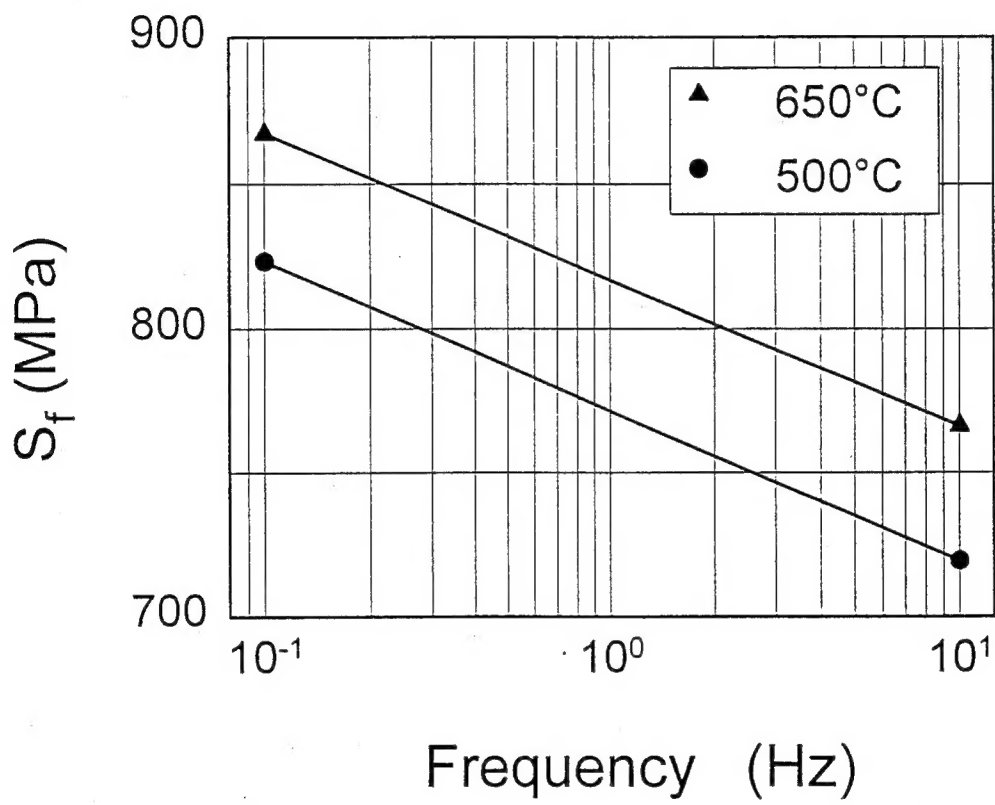
Fig. 8.8 The influence of temperature and loading frequency on the fatigue strength of bridging fiber in SM1240/Timetal-21S composite.